2015

Direct Numerical Simulation Of Ablative Boundaries In Turbulent And Laminar Flows

Ryan Campbell Crocker
University of Vermont, rcrocker@uvm.edu

DIRECT NUMERICAL SIMULATION OF ABLATIVE BOUNDARIES IN TURBULENT AND LAMINAR FLOWS

A DissertationPresented

by

Ryan Campbell Crocker

to

The Faculty of the Graduate College

of

The University of Vermont

In Partial Fulfillment of the Requirements
for the Degree of Doctor of Philosophy
Specializing in Mechanical Engineering

October, 2015

Defense date: July 27, 2015
Dissertation Examination Committee:

Yves C. Dubief, Ph.D., Advisor
Mandar Dewoolkar, Ph.D, Chairperson
Darren Hitt, Ph.D.
Douglas Fletcher, Ph.D
Cynthia J. Forehand, Ph.D., Dean of the Graduate College

Abstract

Rapid surface ablation by a turbulent flow creates complex flow and surface phenomena arising from the evolving boundary topography and its interaction with a turbulent flow that transports the ablative agent onto the surface. The dynamic nature of ablative flow boundaries generate unsteady flow dynamics and thermodynamics occurring over a wide range of scales. The non-equilibrium nature of these phenomena pose a major challenge to the current fundamental understanding of turbulence, which is mostly derived from equilibrium flows, and to Computational Fluid Dynamics (CFD). The simulation of moving boundaries is a necessary tradeoff between computational speed and accuracy. The most accurate methods use surface-conforming grids, forcing the grid to move and deform in time at a high computational cost. The technique used in this study, immersed boundary methods, removes the need for a surface-conforming grid, typically at the expense of numerical accuracy. The objectives of the present study are (i) to develop an Energy Immersed Boundary Method (EIBM) to simulate conjugate heat transfer and phase change with a spatial order of accuracy larger than one, and (ii) use the EIBM to study the dynamics of ablative flows.

A generalized finite volume (FV) flow solver with second-order accuracy in time and space and energy conserving schemes is the basis of the EIBM algorithm development. The EIBM combines level-set method for the definition and transport of the fluid/solid interface with an immersed boundary method, i.e. a modification of the transport equation to enforce the proper boundary conditions at the solid surface. The proposed algorithm is shown to be second order accurate in space in the simulation of conjugate heat transfer flows. The validation also included comparison with phase-change (melting) experiments where it was shown to correlate very well to previous experiments of a rectangular slab of gallium melted from one side. As well as showing second order convergence for the mass loss and the ablated shape of a cylinder in a melting cross flow.

The EIBM is applied to an investigation of the interactions between turbulence and an erodible surface. The study first focuses on the response of a turbulent flow over a receding wall, with constant recession velocity. It is found that wall recession velocities, near the small scale, the Kolmorgorov microscale, velocity of the buffer layer, produce minute shear free layers near the wall which both enhanced and stretched out the low and high velocity streaks near the wall. The larger streak area produced larger turbulent intensities on the dynamic boundary side of the channel, and far more semi-streamwise vortices. In the Second study the EIBM is applied to the ablation of a generic slab in a turbulent channel heated from one side in the absence of gravity. The study focuses on the characterization of the surface topography in relation to the evolution of coherent structures in the flow as ablation proceeds. The produced surface topology is linked to the flow topology and the turbulent generating and dissipating forces inside the turbulent flow. It is shown that the streaks for stefan numbers producing average ablation velocities slightly smaller than the Kolmorgorov microscale create groves in which the high speed buffer layer streaks sit, and their sinus motion in the spanwise direction is reduced.

Dedication

This work is dedicated to my grandfather, Weyman Crocker for inspiring me to be an engineer, to my father, Richard Crocker for giving me a love of building things, and to Polly Perkins for all her love and support through this entire crazy ride. I couldn't have done it without her.

Acknowledgements

Firstly, I would like to thank my committee professors: Darren Hitt, Douglas Fletcher, and Mandar Dewoolkar for showing up so early on a rainy Friday morning, and my Advisor Professor Yves Dubief for all his guidance, friendship, and for always finding a way to keep me funded for all these years. I would like the thank Olivier Desjardins and his research group at Cornell University for the use, and help with, the NGA-ARTS flow solver. I would also like to thank Nagi Manour for the office space, direction, and time to finish a large amount of this work at NASA-AMES. Finally I would like to thank Dr. Max Dougherty for his help bolstering the overall sanity needed to write code and to track down problems, such as seals. This project was funded by the grants: NSF-0967857 and NASA-11-EPSCoR-0004-NNH11ZHA003C

Table of Contents

List of Tables

List of Figures

List of Symbols

Units
All dimensioned quantities in: MKS

Roman Symbols

ℓ	Kolmorgorov length scale
$\mathfrak{F}$	Generic function for reinitializing the level set field
C	Cold side
c_p	Specific heat capacity
D	Cylinder diameter
G	Level set field
H	Hot side
i	Index in x
j	Index in$y$
k	Index in z
L_2	Euclidian error norm
L_∞	Maximum error norm
L_s	Latent heat of melting
L_x	Domain length in x
L_y	Domain length in y
L_z	Domain length in z
N	A counting variable for summations
N_x	Number of computational nodes in x
N_y	Number of computational nodes in y
N_z	Number of computational nodes in z
NU	Nusselt Number
P	Pressure
Pr	Prandtl number
Q	Q criteria
R	Ablated cylinder radius from the centroid
r	Radius
$R_{i,o,m}$	Co-annular cylinder radii
Ra	Rayleigh number
Re	Reynolds number
S	Strain rate or surface area

Ste . . . . . Stefan number
u . . . . . Velocity in x
U_∞ . . . . . Far field or boundary velocity
u_τ . . . . . Friction velocity
V . . . . . Volume
v . . . . . Velocity in y, or normal to Γ
V_{ext} . . . . . FFM extension velocity
w . . . . . Velocity in z
x . . . . . X-axis or direction
y . . . . . Y-axis or direction
z . . . . . Z-axis or direction

Abbreviations

ADIM . . . . . Alternating Direction Implicit Methods
CFL . . . . . Courant-Friedrichs-Lewy condition
CHT . . . . . Conjugate Heat Transfer
CHTIB . . . . . Conjugate Heat Transfer Immersed Boundary
CHTIBM . . . . . Conjugate Heat Transfer Immersed Boundary Method
DNS . . . . . Direct Numerical Simulation
EHIB . . . . . Energy Immersed Boundary Method
ENO . . . . . Essentially Non-Oscillatory
FMM . . . . . Fast Marching Method
FV . . . . . Finite Volume
FVM . . . . . Finite Volume Method
GTE . . . . . General transport equation
HOUC . . . . . High Order Upstream Centered
HT . . . . . Heat Transfer
IB . . . . . Immersed Boundary
IBM . . . . . Immersed Boundary Method
IC . . . . . Initial Condition/Conditions
LES . . . . . Large Eddy Simulaion
LHS . . . . . Left hand side
LLNL . . . . . Lawrence Livermore National Laboratory
MPI . . . . . Message Passing Interface
PBM . . . . . Projected boundary method
PDE . . . . . Partial differential equation
RANS . . . . . Reynolds-Averaged Navier-Stokes
RHS . . . . . Right hand side
TKE . . . . . Turbulent Kinetic Energy
TPS . . . . . Thermal protection systems
WENO . . . . . Weighted Essentially Non-Oscillatory

Greek Symbols

α . . . . . Thermal diffusivity
β . . . . . Mixing fraction or the coefficient of thermal expansion

Δt . . . . . Time step
ϵ . . . . . Turbulent dissipation
η . . . . . Pseudo pressure of the fractional step method
Γ . . . . . Fluid-Solid interface, $G = 0$ isosurface
γ . . . . . Interpolation or stencil separation
κ . . . . . Thermal conductivity
$\mathcal{P}$ . . . . . Turbulent production
μ . . . . . Dynamic viscosity
ν . . . . . Kienamatic viscosity
ν . . . . . Pseudo Pressure
Ω . . . . . Rotation rate
ϕ . . . . . Transported scalar
Ψ . . . . . Coherence width
ψ . . . . . Intermediat WENO variable
ρ . . . . . Density
σ . . . . . Deviatoric stress tensor
Υ . . . . . A general mixed quantity for the IBM
ϖ . . . . . Coherence center distance to Γ_{high}

Subscripts

u . . . . . Denotes the momentum source term
$\mathscr{I}$ . . . . . Integral scale
ϕ . . . . . Denotes the energy source term
τ . . . . . A parameter based on the friction velocity
n . . . . . A quantity normal to Γ
u . . . . . Velocity source term
exact . . . . . Analytical or experimental value
high . . . . . Highest area of ablation referenced from the wall start
low . . . . . Lowest area of ablation referenced from the wall start
c . . . . . Centerline
c . . . . . The area under a hydrostatic fluid column
CS . . . . . Coherent Structure
D . . . . . Based on the diameter
d . . . . . Dynamic pressure
f . . . . . Solid domain
G . . . . . Non-Linear flux for G
K . . . . . Kolmorgorov scale
o . . . . . Initial value or reference value
rms . . . . . Root-Mean-Square
s . . . . . Fluid domain
st . . . . . Static pressure
t . . . . . Derivative with respect to time
2 . . . . . Denoting the L_2 error norm

Superscripts

$\intercal$ . . . . . Transpose
k . . . . . Sub-iteration index (Newton-Raphson Method)
n . . . . . Time step index at time, t
$n+1$ . . . . . Time step index at time, $t + \Delta t$

Vectors

$\boldsymbol{\omega}$ . . . . . Vorticity vector
$\boldsymbol{\Theta}$ . . . . . Generic source term
$\boldsymbol{g}$ . . . . . Gravity field
$\mathbb{I}$ . . . . . Identity matrix or vector
$\mathbf{F}$ . . . . . Nonlinear flux
$\mathbf{n}$ . . . . . Normal vector
$\mathbf{u}$ . . . . . Velocity vector
$\hat{\boldsymbol{\imath}}$ . . . . . Unit vector in x
$\hat{\boldsymbol{\jmath}}$ . . . . . Unit vector in y
$\hat{\mathbf{k}}$ . . . . . Unit vector in z

Mathematical Symbols

$\cdot$ . . . . . Dot Product or multiplication
δ_Γ . . . . . The difference between
$\dot{(\cdot)}$ . . . . . Temporal derivative, source term, rate
∞ . . . . . Error norm for maximum error, or the far field value
$(\cdot)'$ . . . . . Fluctuating term
$(\cdot)^*$ . . . . . Dimensionless quantity
$(\cdot)^+$ . . . . . Wall units or the positive derivative side for WENO
$\lvert(\cdot)\rvert$ . . . . . Absolute value, Euclidian norm
$\mathcal{F}$ . . . . . Linear discretized operators i.e. $\boldsymbol{\nabla}$ and $\boldsymbol{\nabla} \cdot \boldsymbol{\nabla}$
∇ . . . . . Gradient operator
$\otimes$ . . . . . Tensor poroduct
$\overline{(\cdot)}$ . . . . . Average term
∂ . . . . . Partial derivative
BOLD . . . . . Emboldened symbols denote vector quantities
$\widehat{(\cdot)}$ . . . . . Projected Boundary Method interpolation
$\widetilde{(\cdot)}$ . . . . . CHTIBM interpolation
$D(\cdot)/Dt$ . . . . . Material derivative
max . . . . . Field maximum
min . . . . . Field minimum
$sign$ . . . . . Returns the the sign of the input

Chapter 1

INTRODUCTION

Erosive processes occur when a fluid flow transports an erosive medium (force, concentration, or temperature) onto an erodible substrate, where here erosion is considered any ablative or souring process whereby a fluid removes material from the surface over which it flows. Erosion induced by fluid flow spans a wide range of phenomena from the mechanical erosion of sediment beds around bridge abutments and piers to the ablation of thermal protection systems (TPS), or heat shields, on spacecraft entering atmosphere from orbit. It is a multi-billion dollar engineering problem with scales ranging from the molecular (viscosity) to the space shuttle to entire coast lines. One of the major problems associated with erosive and ablative flows is that the scale discrepancies and the unknown physics associated with them can make it nearly impossible to accurately simulate or model. This is an issues because erosive process can be the source of major engineering failures and the cause of expensive engineering problems. The cost alone of coastal erosion because of sea level rise alone could cost well into the trillions if current projections are realized for the European Union and [18], [19], [20], and the United States [21] and [22]. The ablation of TPS is a problem where the tools of CFD are more readily applied. This is advantageous because TPS typically need to be tested in situ ([23] and [24]) to determine the measure of heat

shield loss, exactly. This can be costly because in situ results would necessarily require the re-entry and recovery of a spacecraft [25]. A substantially less costly option would be to run a simulation of the TPS and other erosive processes with CFD tools.

The purpose of this study is to develop simulation techniques and methods, for fast erosion processes at relatively small scales and based on a continuum approach of the flow, solid and fluid/solid interface. The scales of systems to be simulated are constrained by our desire to simulate the flow and the dynamics of the erodable wall as accurately as possible, i.e. by explicitly simulating the small scales. This constraint suits the overarching objective of the present research to simulate the ablation of TPS samples subjected to a plasma jet. Such experiments are used to characterize the behavior of TPS under realistic atmospheric entry conditions. The present research is however confined to much simpler applications in order to focus on the development of robust and accurate methods for the simulation of the fluid/solid interface of an erodible wall. Specifically, this manuscript describes algorithms for the simulation of heat transfer and ablation by melting of solid by heated flow. The resulting algorithm is the Energy Immersed Boundary Method (EIBM), built in a multi physics direct numerical simulation (DNS) flow solver. The DNS flow solver discretizes flows on a Cartesian structured grid, for higher fidelity in terms of conservation of mass and energy. The EIBM is a modification of the transport equation of momentum and energy to model solid surfaces of complex geometries on non-conforming grids. The algorithm will eventually be coupled with the chemical models used in [26] to simulate the inductively coupled plasma torch at the University of Vermont, [27].

DNS has been a robust tool in numerical simulation and validation of new algorithms for fluid flow and heat transfer by comparing experimental and DNS results [28]. Much attention has been paid to canonical flows, such as the DNS of fully developed turbulent channels in, [29] and [30], in these validation studies. Fully developed flow and heat transfer have been studied experimentally in [31], [32], [33], and with DNS [34], [35], [36],

and [37], where numerical simulations were correlated with experimental data giving the proper scaling and simulation parameters for turbulent, heated, flows. Building on these early DNS studies Reynolds Averaged Navier-Stokes (RANS) and Large Eddy Simulations (LES developed by Deardorff in the 1970's [38]) can be used to model the smallest scales that constrain DNS allowing for large scaling up of flow simulations from centimeters to meters by sacrificing some accuracy and adaptability. The drawback of RANS and LES, for this study, is their reliance on models that are derived from statistical properties of equilibrium flows. This limits RANS and LES models to slow ablative environments where the multi-physics and the erosion modeling can be predicted, such as the combustion model of Mahesh et. al 2004 [39] and 2006 [40]. During rapid ablation the boundaries will be dynamic causing non-equilibrium effects in the flow that will create large inaccuracies in statistics based models requiring the use of DNS.

During ablation the boundaries will move from a collocated positions on a structured grid to non-collocated positions (see the ablation patters in figure 1.1). To properly define non-mesh conforming boundary conditions, IBMs, have been used. The IBM was development by Peskin in 1972 [41], to simulate complex geometries with low Reynolds numbers, specifically to simulate heart valves. Yusof et. al 1997 expanded the idea of IBs and developed the direct forcing method, [42], eliminating velocity stability issues associated with indirect forcing IBMs. The final issues with stability linked to small cut cells and pressure oscillations defined by Seo et. al 2011 [43] and Lee et. all 2011 [44] were solved by the reconstruction or cut-cell IBMs where multiple methods were developed: cell merging [45], mixed cell linking/merging [46], cell linking [47], and cell mixing [48] methods, all of which show second order error in their results for low to moderate Reynolds numbers. In this study the sharp representation of boundaries is done through a mixing method modified from [48]. The method was developed by Brady et. al 2014 [49] and uses a combination cell mixing of derived cell quantities, such as face fluxes, and cell face areas to the surrounding area. These mixed values are kept consistent on both sides of the momentum, and pressure,

solutions of the Navier-Stokes and Poisson pressure equations making it implicit, robust and stable over a wide range of Reynolds numbers.

The EIBM will also be applied to the energy equation through conjugate heat transfer (CHT) and the calculation of the ablation velocity at the surface. The addition of CHT to DNS heat transfer studies greatly complicates the analysis of developed flows and initial research into the subject suffered from a lack of an adequate order of error. For example, [50] and [51] derived first order in space methods. Recently, advances in the interpolation schemes of curvilinear flow solvers have been shown to generate solutions with second order error convergence [12]. However, this was done only for small ratios of thermal conductivity and was not applied to the solution implicitly or in a way easily applicable to cartesian finite volume (FV) solvers with complex, non-mesh conforming boundary conditions. To that end a conjugate heat transfer immersed boundary (CHTIB) algorithm, a subset of an EIBM, is developed and used in this study. The calculation of the ablation velocity is handled with overset grid methods and high order interpolations that produce computational stencils capable of reproduction of second order derivatives in any direction. These are used in a Stefan condition that computes the surface ablation velocity by the fluid and solid parameters and the balance of thermal fluxes normal to solid-fluid interface.

The solid-fluid interface is tracked using level set methods that were developed by Sethian et al. 1988 [52] to track and analyze an interface's position and motion in three dimensions. Level set fields are defined as a set of equidistant iso-surfaces of some real value (for example a topographical map) and they have very nice properties when it comes to tracking them in cut-cell methods. Their normal and volumetric geometry are readily available if the level set field is a signed distance function, [53], as shown by Owkes et. al 2014 [54]. Time evolution of the level set field is done by a simple explicit transport equation followed by a velocity extension done with the fast marching method (FMM) [55]. The result is a well behaved fluid-solid interface that can be manipulated by flow condition

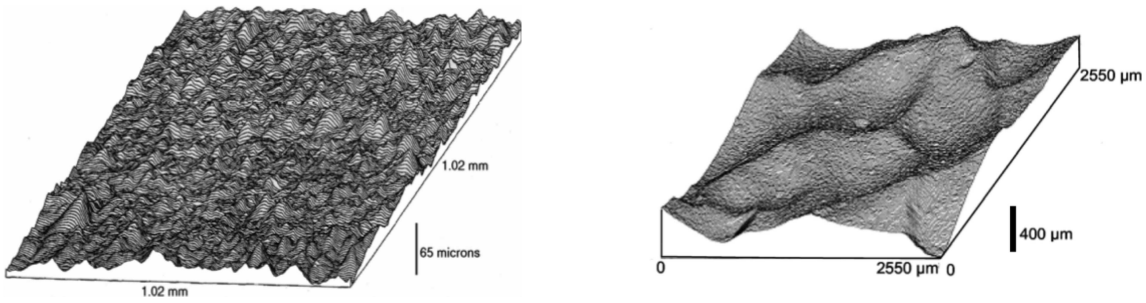

(a) (b)

Figure 1.1: Data taken from [7] and [8] a.) A surface of carbon composite ablated by laminar flow. b.) A surface of carbon composite ablated by turbulent flow.

in any direction and will always return accurate, conservative geometries to be used for the IBMs.

The DNS flow solver, NGA-ARTS, used in this work was developed by Desjardins et. al [56] and is based off of the flow solver developed by Pierce et. al in 2004 [57] for progressive variable simulations of LES combustion. It couples IBMs for momentum, in addition to the EIBM developed in this study, with surface tracking through conservative level set methods. It is used to validate the EIBM for both CHT and ablation using two canonical flows and experimental results. It is also used to simulate both an isothermal channel with one dynamic boundary moving at different constant velocities and a heated channel with one ablative boundary. The flow structures, flow dynamics, and surface geometry, and their relationships with each other, are studied for both channels.

Chapter 2

GOVERNING EQUATIONS

2.1 Momentum Transport and Mass Conservation

The governing equations of fluid flow are two sets of vector equations. The continuity equation,

$$\partial_t \rho + \boldsymbol{\nabla} \cdot (\rho \mathbf{u}) = 0, \tag{2.1}$$

and Navier-Stokes set of equations,

$$\begin{aligned} &\frac{D\mathbf{u}}{Dt} = \partial_t (\rho \mathbf{u}) + \boldsymbol{\nabla} \cdot (\rho \mathbf{u} \otimes \mathbf{u}) = \\ &- \boldsymbol{\nabla} \cdot \mathbb{I} P + \boldsymbol{\nabla} \cdot \underbrace{\left[\mu(\boldsymbol{\nabla}\mathbf{u} + \boldsymbol{\nabla}^{\intercal}\mathbf{u}) - \frac{2}{3}\mu (\boldsymbol{\nabla} \cdot \mathbf{u}) \mathbb{I} \right]}_{\text{deviatoric stress tensor, } \sigma} + \dot{\Theta}_{\mathbf{u}}, \end{aligned} \tag{2.2}$$

are written in fully conservative form. In equations 2.1, and 2.2, bold terms are vectors, $\mathbf{u}$ is the velocity vector with $\mathbf{u} = u\hat{\boldsymbol{\imath}} + v\hat{\boldsymbol{\jmath}} + w\hat{\mathbf{k}}$, P is the pressure, μ is the dynamic viscosity, ∂_t is the temporal derivative, $\boldsymbol{\nabla} = \frac{\partial}{\partial x}\hat{\boldsymbol{\imath}} + \frac{\partial}{\partial y}\hat{\boldsymbol{\jmath}} + \frac{\partial}{\partial z}\hat{\mathbf{k}}$, $\dot{\Theta}_{\mathbf{u}}$ is a source term, and $\mathbb{I}$ is the identity matrix. The continuity equation conserves mass globally and the Navier-Stokes equations transport momentum via convection and diffusion. Equation 2.2 is kept in a fully general and conservative form to increase numerical accuracy after discretization. A discretized non-

dimensional form of equation 2.2 will be developed for each numerical experiment consistent with the proper physical scales inherent to the numerical experiments.

2.2 Scalar Transport

Energy is transported as a passive scalar in the flow as,

$$\partial_t \phi + \boldsymbol{\nabla} \cdot (\mathbf{u}\phi) = \boldsymbol{\nabla} \cdot (\alpha_f \boldsymbol{\nabla}\phi) + \dot{\Theta}_\phi \tag{2.3}$$

where ϕ is any transported scalar (concentration, temperature, etc), α is the diffusivity of the scalar, $\dot{\Theta}_\phi$ is a source term, and the subscript f denotes that it is in the fluid medium. Like equation 2.2, equation 2.3 is kept in its fully conservative form, and is non-dimensionalized in subsequent chapters. The solid portion of the domain requires an additional scalar transport equation:

$$\partial_t \phi = \boldsymbol{\nabla} \cdot (\alpha_s \boldsymbol{\nabla}\phi)\,. \tag{2.4}$$

The only differences between the two forms given in equations 2.3 and 2.4 are the absence of the convective term in equation 2.4, the absence of the source term, and the use of the solid diffusivity, α_s in the solid domain.

2.3 Level Set

Level set functions, G, are smooth, Lipschitz continuous, functions in four dimensions, $f(x, y, z, t)$. They are typically used to separate two different physical regions in a computational domain. Such as the different regions in multiphase flows. An interface, Γ, separates the two different regions through the sign of G (see figure 2.1). The motion of G and the interfaces (there may be multiple in any general simulation) are defined by their velocity field, $\mathbf{v}_\Gamma$, which can depend on both local and global physics, and simulation parameters.

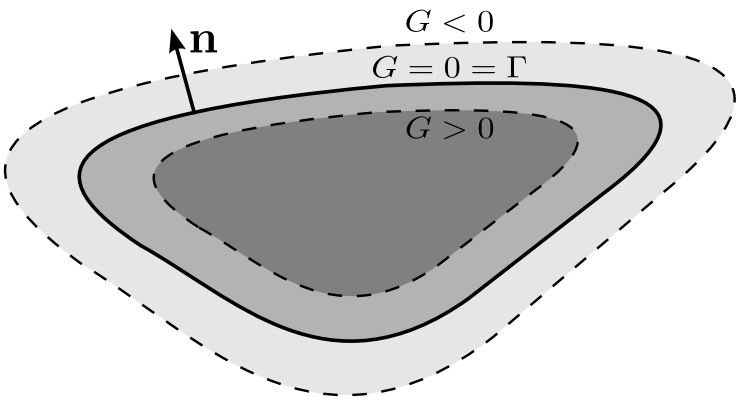

Figure 2.1: A level set function with normal and the interface shown.

The most general form of the evolution equation for G is given by the Hamilton-Jacobi form of the level set transport equation,

$$\partial_t G + \mathbf{v}_\Gamma \cdot \boldsymbol{\nabla} G = 0. \tag{2.5}$$

The level set function has the properties, $G > 0$ defines one region and $G < 0$ defines another region separated by $\Gamma(x, y, z, t) = \{(x, y, z) | G(x, y, x, t) = 0\}$, and $\mathbf{v}_\Gamma$ is defined only at Γ; elsewhere $\mathbf{v}_\Gamma = 0$. When G is in the form of a signed distance function, $|\boldsymbol{\nabla} G| = 1$, equation 2.5 can be simplified to

$$\partial_t G + v_{\mathbf{n}} |\boldsymbol{\nabla} G| = 0, \tag{2.6}$$

where $v_{\mathbf{n}}$ is the velocity normal to Γ. The normal vector at any point in G is given by $\mathbf{n} = \boldsymbol{\nabla} G / |\boldsymbol{\nabla} G|$, which can be used to define the curvature of G, $G_{\text{curve}} = \boldsymbol{\nabla} \cdot (\mathbf{n}/|\mathbf{n}|)$, and the normal velocity of Γ, $v_{\mathbf{n}} = \mathbf{n} \cdot \mathbf{v}_\Gamma$. Osher et. al 2011 [58] showed that equation 2.6 needs only to be evaluated locally, near Γ, which greatly simplifies equation 2.5, thereby reducing computational overhead for the evolution equation of G.

Another advantage of equation 2.6 is the simplicity of computations in areas of interfacial splitting and merging, as in [59], because the interface is found for all t by locating where $\Gamma(t)$ gives $G = 0$ [60]. This can cause problems with the formulation of the moving interfaces. The first problem is that the level set field will not stay a signed

distance function for $v_{\mathbf{n}} > 0$ unless $v_{\mathbf{n}}$ is uniform throughout the level set field which would lead to only very simple motions of Γ (see the wall dropping experiment in chapter 5). The second problem with the formulation of the level set transport equation given by equation 2.5, G is not explicitly conserved, which can lead to oscillatory solutions. These problems will be addressed by reinitialization of the level set field (section 2.3.1) to keep the field either locally or globally (depending on the application) a signed distance function and well behaved.

2.3.1 Reinitialization of Level Set Functions

If the velocity normal to Γ is non-zero, movement of the interface will distort G in a way that causes large gradients in G, or no gradient in G, which can be just as numerically debilitating, as both cause the loss of a smooth and continuous Γ. With this loss of smoothness, small perturbations in the interface velocity and in G can cause large, non-physical changes in the location of the interface. The reason for this behavior is the loss of one of the defining characteristics of a level set function, namely that $|\boldsymbol{\nabla} G|$ is no longer equal to unity. Reinitialization of the level set function around the position of the interface in the absence of large gradients can reproduce a signed distance function to the interface at some $t + \Delta t$ and retrieve $|\boldsymbol{\nabla} G| = 1$.

A common reinitialization method utilizes the viscosity solution of the Eikonal equation [61]. The form of the Eikonal equation given by Sussman et al. 1994 [62] is one of the most common forms of viscosity solution of level set field reinitialization equations,

$$\frac{\partial G}{\partial t^*} + sign(G_o)(|\boldsymbol{\nabla} G| - 1) = 0, \tag{2.7}$$

where $G_o = G(x, y, z, 0)$, $sign$ is a function which gives -1 if the argument is negative and 1 if the argument is positive, and t^* is a pesudo time used for an iterative solution to 2.7. Equation 2.7 works under the assumption that in between small simulation time

steps the change in the position from Γ^n to Γ^{n+1} is small (the solution process is given in depth in [63]). In the case of small Γ^n-Γ^{n+1}, equation 2.7, will converge quickly and efficiently. If there are large discrepancies in the $v_{\mathbf{n}}$ and the similarity between Γ^n to Γ^{n+1} is reduced, then the level set function will need to be reinitialized at every simulation time step. This can become very costly. During this research, re-initializations were used only for the initialization of level set geometries used to make up the boundary conditions for the momentum and energy equations by specifying an initial location for Γ and fitting a crude level set field to the rest of the computational domain. When this field is reinitialized it forms the signed distance function about the interface giving a usable level set field, with $|\boldsymbol{\nabla} G| = 1$, for subsequent simulations of that geometry.

The viscous reinitialization procedure will not be covered in depth here because a more computationally efficient method, the fast marching method (FMM), is used and covered in section 2.3.2 (see [64], [65], and [66] for an in depth studies on level set reinitialization).

2.3.2 Fast Marching Method and Velocity Extention

The FFM was introduced by Sethian in 1990 [55]. It is essentially a subset of fast Hamilton-Jacobi equation solvers. Use of the FMM yields results that are equivalent to the reinitialization methods mentioned in section 2.3. Both reinitialization andHuygen the FMM solve a form of the non-linear Eikonal equation turning level set fields into signed distance functions. A general form of the Eikonal equation is,

$$|\boldsymbol{\nabla} G| = \mathfrak{F}\left(x, y, z\right), \tag{2.8}$$

where $\mathfrak{F}\left(x, y, z\right)$ is a scalar function in three dimensions. The difference is that strict reinitialization methods will iterate over an entire domain while the FMM only reinitializes the level set field in an area "near" where $G = 0$.

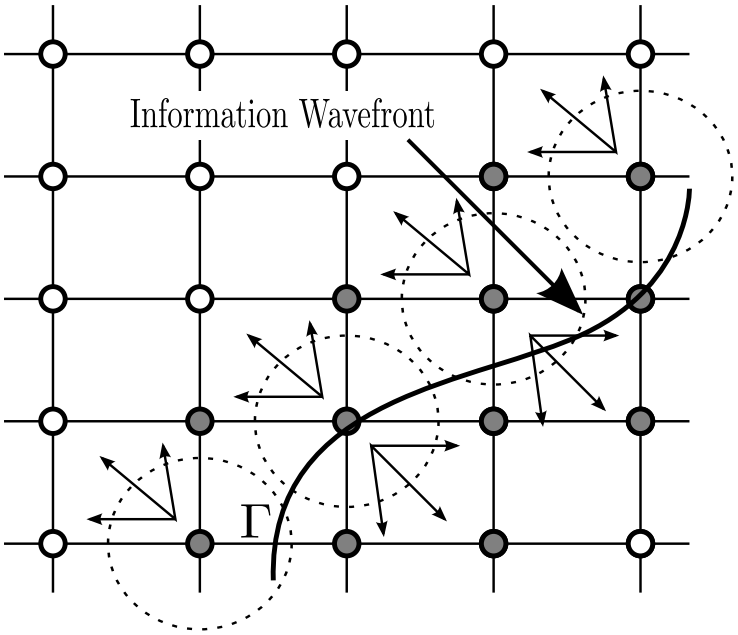

Figure 2.2: A propagating front used to update computational points with the FMM using Huygen's principle. The circles are the search area for the trial points, and the grey circles are the points near or on the interface. The dashed line represents the propagation of information from the interface, Γ, to the surrounding points. The order of the propagation of information is determined by the FMM.

The FMM works by extending the solution of Eikonal equation, equation 2.7, in a downwind manner, away from the interface. The method begins by finding a discrete node which has the minimum value of G in the set of computational nodes on either side of $G = 0$ (which may not be collocated on the Γ nodes). The perturbation is propagated like a wave front to all other nodes surrounding the initial node. This is also numerically known as Huygen's principle where each computation node in the perturbation wave is now the discrete point of perturbation for all of their surrounding points (see figure 2.2). The FMM is covered extensively in [67] but the basic algorithm begins by placing all computational nodes into three sets. They are either **close**, **far** or **old**. Any nodes within one grid spacing

of the interface are **old**. All nodes within grid spacing of the **old** nodes are **near** nodes. Any nodes not in either **near** or **old** are considered **far**. The iteration loop begins as,

1. Find the minimum value of G in the **near** group and call that the **trial** node.
2. The new **trial** node is now moved into **old**.
3. The neighboring nodes of the **trial** node that are in the **far** group are also added to the **near** group.
4. Solve equation 2.8 locally for the **trial** node at all it's **near** neighbors. Any points that are in the **far** group and the **near** group are treated as if they were ∞.
5. Repeat the loop.

While the FMM is a fast method for reinitializing level set fields to signed distance functions it can suffer from non-physical bunching or spreading of level set isosurfaces in velocity fields consistent with fluid flow. This can cause discontinuities and non-physical interface formulation, as shown by Chang et al. 1996 [68]. Also, over reinitialization of level set fields can cause the front, Γ, to perturb and "wiggle".

To avoid the numerical issues associated with the FMM Adalsteinsson et al. 1998 [69] added extension velocities to its formulation, which is the preferred technique in this work. The purpose of extension velocities is to spread the velocity out to the nodes in the narrow band around the interface while also keeping the level set field a signed distance function (see figure 2.3). This is accomplished with the solution to equation 2.9 with $|G_{temp}| = 1$,

$$\boldsymbol{\nabla} G_{temp} \cdot \boldsymbol{\nabla} \mathrm{V}_{ext} = 0 \tag{2.9}$$

if $|G_{temp}| = 1$ and V_{ext} are an extension velocity matching $v_{\mathbf{n}}$ at the interface, built on that signed distance function, and G_{temp} is a temporary level set field that has the same zero level set as G. Following the logic, if the velocity and level set field are smooth, then $|G_{temp}| = 1$ is true for all time [53].

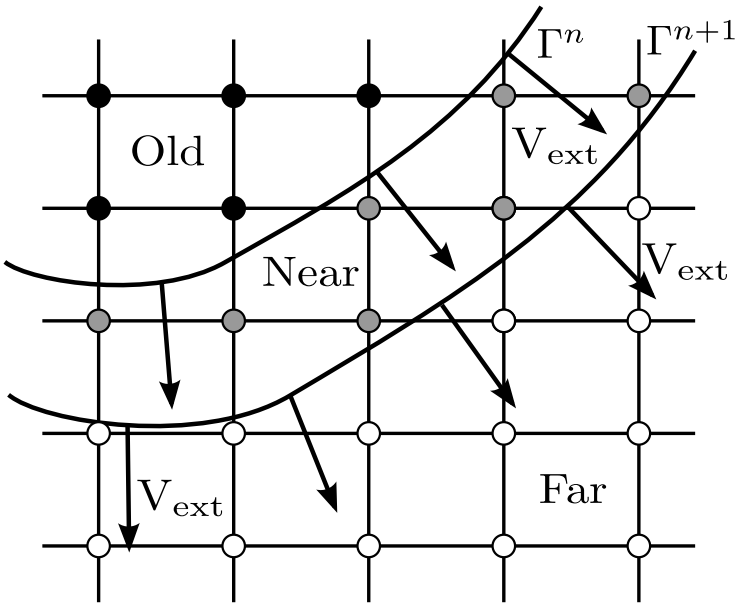

Figure 2.3: A propagating front used to update computational nodes with the FMM. V_{ext} is the extension of the velocity. The normal, and wave front movement, are defined by the vectors at the front. Black filled nodes are the "accepted" values. Grey nodes are "close" nodes where equation 2.9 is to be solved. Open circles are far from the interface and will be handled when the information wave front reaches them.

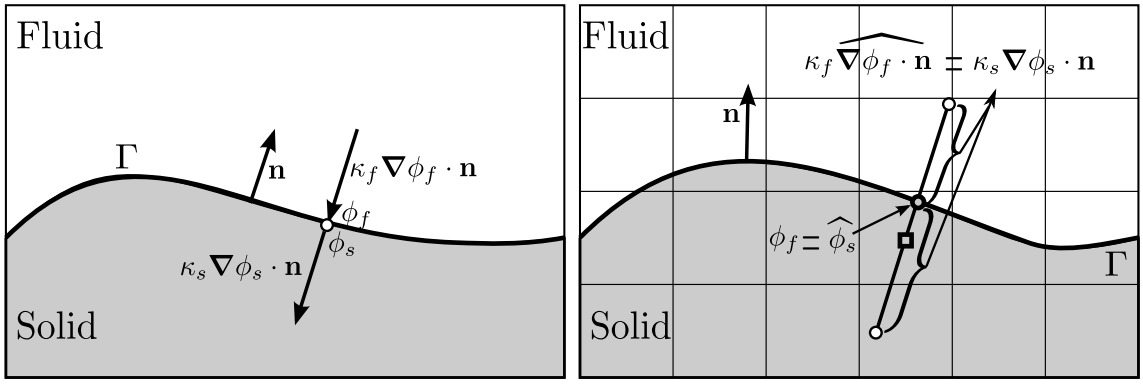

(a) **(b)**

Figure 2.4: a.) A schematic representation of CHT between a fluid and solid with the interface point at ◯. b.) The Projected Boundary Method showing the interpolation stencil and cell center, □, and interface interpolation point at ◯.

After the front advances, the velocity at the front is extended to the surrounding narrow band nodes. Following the FMM, each node is updated so that $|G_{temp}| = 1$ then the solution to equation 2.9 is used to apply V_{ext} to that node. Once the velocity is extended away from the interface, the level set field is updated through equation 2.6. This updates the narrowband level set near the interface and keeps G a signed distance function (see figure 2.3).

2.4 Conjugate Heat Transfer

In CHT two boundary conditions must be satisfied. The first is the continuity of temperature at Γ,

$$\phi_s = \phi_f, \tag{2.10}$$

and the second is the flux balance across Γ

$$\kappa_s \nabla \phi_s \cdot \mathbf{n} = \kappa_f \nabla \phi_f \cdot \mathbf{n}, \tag{2.11}$$

where the subscripts f and s stand for the conductive fluid and solid media, respectively, and $\kappa = \alpha c_p \rho$ is the thermal conductivity [70]. CHT does not necessarily need to be between to materials in different phases but in this work one phase will always be solid (the ablative or melting boundary) the other will be a fluid. The boundary conditions in equations 2.10 and 2.11 are asymmetrically satisfied and numerically stiff when discretized. They lead to solutions of the scalar evolution equation that can only be computed iteratively which can greatly increase computational overhead.

Some of the first work on the subject of CHT was conducted by making assumptions about the materials at the boundaries. It is called the Projected Boundary Method or PBM, used in [50], [71], and [72], and it is capable of symmetrically satisfying the CHT boundary conditions with non-grid-conforming boundary conditions; like the IBM for momentum (see section 3.4.1). The PBM works by decoupling each of the different materials, here the fluid and solid domains, and then interpolating information from one domain to the other domain. The modified boundary conditions given in equations 2.12 and 2.13 are the continuity of temperature at Γ,

$$\widehat{\phi_s} = \phi_f, \tag{2.12}$$

and the flux balance across the interface,

$$\kappa_f \widehat{\boldsymbol{\nabla}\phi_f \cdot \mathbf{n}} = \kappa_s \boldsymbol{\nabla}\phi_s \cdot \mathbf{n}, \tag{2.13}$$

where $\widehat{(\cdot)}$ denotes interpolated values. The Dirichlet condition is used on the fluid side as it is more naturally stable, see figure 2.4. In previous work, the Neumann condition is used on the solid side as the solid diffusivity is much larger than the diffusivity of the fluid [51].

The PBM proves to show only a first order decline in error, so it is not used in this work. In section 3.4.4 both equations 2.10 and 2.11 are applied implicitly on Γ, after discretization, giving a sharply defined boundary condition to the interfacial nodes, which

is applicable for a large range of Reynolds number, and ones with κ_s and κ_f orders of magnitude apart. It also shows second order error reduction.

2.5 Stefan Condition

The thermal ablation, or melting, of a solid at the solid fluid interface is described through the balance of heat fluxes at the interface, or the Stefan-Condition, developed by Joseph Stefan in 1891 [73],

$$\mathbf{v}_\Gamma = \frac{1}{L_s \rho_s}\left[\kappa_s \frac{\partial \phi}{\partial \mathbf{n}_{\Gamma s}} - \kappa_f \frac{\partial \phi}{\partial \mathbf{n}_{\Gamma f}}\right] \quad \text{if} \quad \phi_\Gamma \geq \phi_m \tag{2.14}$$

where L_s is the latent heat of melting for the solid and ϕ_m is the melting temperature; taken from [74]. The particular formulation given in equation 2.14 assumes only melting of the solid takes place when $\phi_\Gamma \geq \phi_m$. Until the melting criterion is met conjugate heat transfer occurs and interfacial energy transport is handled with equations 2.10 and 2.11. Rearranging equation 2.14 gives the Stefan-Condition for solidification,

$$\mathbf{v}_\Gamma = \frac{1}{L_f \rho_s}\left[\kappa_f \frac{\partial \phi}{\partial \mathbf{n}_{\Gamma f}} - \kappa_s \frac{\partial \phi}{\partial \mathbf{n}_{\Gamma s}}\right] \quad \text{if} \quad \phi_\Gamma \leq \phi_{\text{solid}} \tag{2.15}$$

where L_f is the latent heat of solidification of the fluid and ϕ_{solid} is the solidification temperature. In this work only equation 2.14 will be used to model melting/ablation. The solidification at Γ is of note because often TPS experience a cool down period after initial re-entry, [75]. This was shown to be the case with NASA's Stardust program when the heat shield was recovered, as seen in [76] and [77]. Later models of the work presented here will include both ablating/melting and solidification regimes during simulations.

Chapter 3

NUMERICAL METHODS

3.1 Momentum Transport and Mass Conservation

The momentum transport equation, equation 2.2, is discretized using a second order, finite volume (FV) method (FVM) on a pressure-velocity staggered grid. The fractional step method, developed by Kim et al. 1985 [78], is used to enforce mass conservation by applying the anelastic, low mach number, incompressible continuity equation, $\boldsymbol{\nabla} \cdot \mathbf{u} = 0$ to the discretized version of equation 2.2, with the same corresponding approximations; keeping $\mathbf{u}$ solenoidal. This is done by projecting the pressure gradient onto an intermediate velocity field using predictor-corrector steps during time advancement.

The FVM is derived from a generic conservation equation,

$$\partial_t \mathbf{u} + \boldsymbol{\nabla} \cdot \mathbf{F} = 0. \tag{3.1}$$

In equation 3.1, $\mathbf{F}$ is the nonlinear flux that combines the convective, pressure, and diffusive terms in equation 2.2. The definition of the nonlinear flux is

$$\mathbf{F} = \mathbf{u} \otimes \mathbf{u} + \mathbb{I}P - \nu \boldsymbol{\nabla} \mathbf{u} \rightarrow \boldsymbol{\nabla} \cdot \mathbf{F}\left(\mathbf{u}, P\right) \tag{3.2}$$

where $\nu = \mu/\rho$ is the kinematic viscosity.

At this point some note must be taken of the procedure to calculate the convective fluxes because of the staggered grid arrangement of P, u, v, and w. Expanding the convective flux term in 2.2,

$$\boldsymbol{\nabla} \cdot [\mathbf{u} \otimes \mathbf{u}]\, \hat{\boldsymbol{\imath}} = \frac{\partial uu}{\partial x} + \frac{\partial uv}{\partial y} + \frac{\partial uw}{\partial z} \tag{3.3}$$

for the x direction, lying on the $\{i - \frac{1}{2}, j, k\}$ and $\{i + \frac{1}{2}, j, k\}$ faces of the computational cell as the pressure node in the cell center is considered $\{i, j, k\}$ (see figure 3.1). The other velocities, v and w, do not lie on the same computational node as u, see figure 3.1. Therefore, some of the values, by necessity, must be interpolated from adjacent points on the computational cell. To do this the interpolation procedure from [79] and [56] is used keeping to second order accuracy with both the staggered differential and staggered interpolation operators. The advantages of second order staggered interpolation operators are:

1. There are no dispersion errors caused by central differencing
2. The insurance of better primary conservation (mass and momentum)
3. Secondary conservation (kinetic energy); both globally and locally.

Substituting equation 3.2 into equation 3.1, and keeping with the laws of conservation, the volume integral of the fluxes around the surface of any computation cell (figure 3.1) with Gauss's theorem yields

$$\partial_t \int_{\mathrm{dV}} \mathbf{u}\mathrm{dV} = \oint_{\mathrm{dS}} \nu \boldsymbol{\nabla}\mathbf{u} \cdot \mathbf{n}\mathrm{dS} - \oint_{\mathrm{dS}} \mathbb{I}P \cdot \mathbf{n}\mathrm{dS} - \oint_{\mathrm{dS}} \mathbf{n} \cdot \mathbf{u} \otimes \mathbf{u}\mathrm{dS}, \tag{3.4}$$

where dS is the area of the face perpendicular to $\mathbf{n}$ (Δx and Δy from figure 3.1), where here $\mathbf{n}$ is the face normal of the computational cell. Using the volumetric average of $\mathbf{u}$, $\overline{\mathbf{u}} = 1/V \int_{\mathrm{dV}} \mathbf{u}$, and integrating 3.4 forward in time, $t \to t + \Delta t$, gives the FV discretization of equation 3.1 as

$$\frac{\overline{\mathbf{u}}^{n+1} - \overline{\mathbf{u}}^{n}}{\Delta t} = \frac{1}{V} \oint_{\mathrm{S}} \mathbf{n} \cdot \mathbf{F}\left(\overline{\mathbf{u}}^{n}, P^{n}\right) \mathrm{dS}, \tag{3.5}$$

where the superscript n is at the current time step and $n+1$ is at the time step (see $t + \Delta t$ [80]). Solving for the velocity at $n + 1$, in equation 3.4, and applying Newton-Raphson

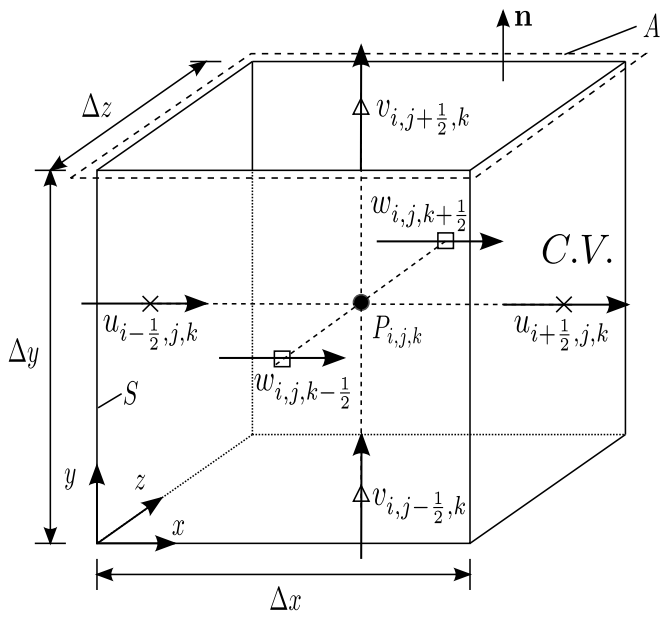

Figure 3.1: A computational cell that shows the staggering of velocity and pressure.

sub-steps between t and $t + \Delta t$, gives the time evolution equation for the velocity,

$$\mathbf{u}^{k+1,n+1} = -\mathbf{u}^{k=0,n} - \mathbf{u}^{k+1,n} + \Delta t \frac{1}{V} \oint_{\mathrm{S}} \mathbf{n} \cdot \mathbf{F} \left(\mathbf{u}^*, P \right)^{n,k} \mathrm{dS}. \tag{3.6}$$

The $(\cdot)^*$ superscript in equation 3.6 that replaced $n+1$ denotes the intermediate velocity in the fractional step method and k, as a superscript, is the sub-iteration of the intermediate time steps from the Newton-Raphson method, and the over-bars representing the time averages have been omitted.

Time advancement at each sub-step in equation 3.6 is done by use of a tri-directional, semi-implicit, second order in time Crank-Nicholson-like [81] time evolution scheme, with approximate factorization [82]. As well as a form of alternating direction implicit methods (ADIM), which consists of a system of second order trilinear equations. The solution of which is readily expanded to three dimensions and to codes written in parallel with message passing interfaces (MPI), as shown in [83]. Substituting the progressive variable velocity, $\tilde{\mathbf{u}} = \left(\mathbf{u}^{n+1} + \mathbf{u}^{n} \right) / 2$, from [57] into equation 3.6, using the procedure outlined

in appendix B, discretizing, and then integrating equation 3.6 gives the residual form of the time evolution equation,

$$\begin{aligned}\left(\mathbf{u}^{k+1,n+1}-\mathbf{u}^{k,n+1}\right)\left[1-\frac{\Delta t}{2}\frac{\partial\mathcal{F}}{\partial\tilde{\mathbf{u}}}\right]=\mathbf{u}^{k=0,n}-\mathbf{u}^{k,n+1}+\\ \Delta t\left(\frac{1}{\Delta x}\left[\tilde{\mathbf{F}}\mathbf{x}^{n}_{i+\frac{1}{2},j,k}-\tilde{\mathbf{F}}\mathbf{x}^{n}_{i-\frac{1}{2},j,k}\right]+\right.\\ \frac{1}{\Delta y}\left[\tilde{\mathbf{F}}\mathbf{y}^{n}_{i,j+\frac{1}{2},k}-\tilde{\mathbf{F}}\mathbf{y}^{n}_{i,j-\frac{1}{2},k}\right]+\\ \left.\frac{1}{\Delta z}\left[\tilde{\mathbf{F}}\mathbf{z}^{n}_{i,j,k+\frac{1}{2}}-\tilde{\mathbf{F}}\mathbf{z}^{n}_{i,j,k-\frac{1}{2}}\right]\right)\end{aligned} \tag{3.7}$$

where $\mathcal{F}$ are the discretized linear operators (discretized gradient and divergence metrics) in $\mathbf{F}$ from equation 3.2, consistent with a second order finite difference stencils on a cartesian grid, and $\tilde{\mathbf{u}}$ has been substituted into equation 3.6, giving equation 3.7, and $\tilde{F}\left(\tilde{u},P\right)$. The intermediate velocity, $\mathbf{u}^{*}=\mathbf{u}^{k+1,n+1}$, is not divergence free after the evolution in equation 3.7 has been applied to the equation 2.2. The procedure is the same as that used by [56], inspired by [84], and in combination with scalar transport (see appendix B.1).

A divergence free velocity field is obtained by projecting the pressure gradient onto the intermediate velocity field by the solution of Poisson's Equation in equation 3.8,

$$\boldsymbol{\nabla}\cdot\boldsymbol{\nabla}\eta=\frac{\boldsymbol{\nabla}\cdot\mathbf{u}^{*}}{\Delta t}\quad\rightarrow\quad\mathbf{u}^{n+1}=\mathbf{u}^{*}-\Delta t\boldsymbol{\nabla}\eta. \tag{3.8}$$

The Poisson-pressure equation is solved with either a Boomerang Algebraic Multi-Grid (BoomerAMG) from [85] or the General Minimum RESidual (GMRES) solver from [86], depending on the symmetry of the Laplacian coefficient matrix (see figure 3.11b). Both Poisson solvers are from the Hypre suite of solvers [87]. The pseudo-pressure, η, is an increment in pressure to guarantee a solenoidal velocity field. The gradient of the pseudo-pressure in equation 3.8, subtracted from the velocity at the current time step, n, gives a divergence free velocity field at the next time step, $n+1$. The pressure can then be updated to the next time step using

$$P^{n+1}=P^{n}+\eta. \tag{3.9}$$

3.2 Scalar Transport

Scalar transport is discretized similarly to the momentum equations in section 3.1, using second order FVM for diffusive terms, but differs by the use of a third order scheme for the convective terms. The the scalar values are held at the center of the computational cell (see figure 3.1) with the pressure. The transport equation of the scalars in conservative form is given as

$$\partial_t \phi + \nabla \cdot \mathbf{F} = 0. \tag{3.10}$$

The non-linear flux is given as

$$\mathbf{F} = \mathbf{u}\phi - \alpha \nabla \ \phi \rightarrow \boldsymbol{\nabla} \cdot \mathbf{F}\left(\mathbf{u}, \phi\right). \tag{3.11}$$

Substituting equation 3.11 into equation 3.10, and then taking the integral around the computational cell and using Gauss's theorem gives

$$\partial_t \int_{\mathrm{dV}} \phi \mathrm{dV} + \oint_{\mathrm{dS}} (\mathbf{u}\phi) \cdot \mathbf{n} \mathrm{dS} = - \oint_{\mathrm{S}} \alpha \boldsymbol{\nabla} \phi \cdot \mathbf{n} \mathrm{dS}. \tag{3.12}$$

Substituting the volumetric average of ϕ, $\overline{\phi} = 1/V \int_{\mathrm{dV}} \phi$, into equation 3.12 and integrating forward in time, $t \rightarrow t + \Delta t$ gives the finite volume discretization of equation 3.10,

$$\frac{\overline{\phi}^{n+1} - \overline{\phi}^{n}}{\Delta t} = \frac{1}{V} \oint_{\mathrm{S}} \mathbf{n} \cdot \mathbf{F}\left(\overline{\phi}^{n}, \mathbf{u}^{n},\right) \mathrm{dS}, \tag{3.13}$$

where the superscript, n, is at the current time step and $n+1$ is at the time step (see $t + \Delta t$ [80]). Solving for the velocity at $n+1$ in equation 3.13, and applying Newton-Raphson sub-steps between t and $t + \Delta t$, gives the time evolution equation for the scalars in the fluid domain,

$$\overline{\phi}^{k+1,n+1} = \overline{\phi}^{k=0,n} - \overline{\phi}^{k,n+1} + \Delta t \frac{1}{V} \oint_{\mathrm{S}} \mathbf{n} \cdot \mathbf{F}\left(\overline{\phi}, \mathbf{u}\right)^{k,n} \mathrm{dS}. \tag{3.14}$$

where the $(\cdot)^k$ superscript denotes the sub-step scalar value of the k order Newton-Raphson scheme, and $\phi^{*,0}$ is the initial value of the scalar field at the beginning of the n to $n+1$ time step. The FVMs, in both solid and fluid domains, are advanced in time, semi-implicitly,

in all three spacial directions by a second order Crank-Nicholson method with approximate factorization (see appendix A and B). Integrating 3.14, just as in section 3.1 with equation 3.6, in two dimensions gives

$$\begin{aligned}\left(\phi^{k+1,n+1}-\phi^{k,n+1}\right)\left[1-\frac{\Delta t}{2}\frac{\partial\mathcal{F}}{\partial\tilde{\phi}}\right] = \phi^{k=0,n}-\phi^{k,n+1}+\\ \Delta t\Bigg(\frac{1}{\Delta x}\left[\tilde{\mathbf{F}}^{n}_{i+\frac{1}{2},j,k}-\tilde{\mathbf{F}}^{n}_{i-\frac{1}{2},j,k}\right]+\\ \frac{1}{\Delta y}\left[\tilde{\mathbf{F}}^{n}_{i,j+\frac{1}{2},k}-\tilde{\mathbf{F}}^{n}_{i,j-\frac{1}{2},k}\right]+\\ \frac{1}{\Delta z}\left[\tilde{\mathbf{F}}^{n}_{i,j,k+\frac{1}{2}}-\tilde{\mathbf{F}}^{n}_{i,j,k-\frac{1}{2}}\right]\Bigg),\end{aligned} \tag{3.15}$$

where again $\mathcal{F}$ are the discretized linear operators in $\mathbf{F}$ from equation 3.11, consistent with a second order finite difference stencil on a cartesian grid, using the progressive variable, $\tilde{\phi}=\left(\phi^{n+1}+\phi^{n}\right)/2$, the procedure from section 3.1, where $\mathbf{F}\left(\tilde{\phi},u\right)$. Discretization of the scalar terms is not quite complete. The hyperbolic term in 3.12 causes solution oscillations even while sub-stepping with a Newton-Raphson method. Second order centered difference schemes, such as the one used for the momentum equations, produce a numerically stable solution of equation 3.15. Without any other treatment of the scheme referred to by equation 3.14 would have prohibitively small time steps to avoid solution oscillations. To avoid small time steps and to produce a numerically stable solution upwinding is used, as in [88]. For this research a third order scheme, the High Order Upstream Centered (HOUC developed by Nourgaliev et al. 2007 [89]), is applied to equation 3.15 in the same manner as was done by Desjardins et al. 2008 [90]. The HOUC scheme is derived from Leonard's quadratic upstream interpolation for convective kinematics or, QUICK scheme [91]. The HOUC first interpolates the scalar onto the adjacent computational cell faces using a second order polynomial. Figure 3.2 shows the stencil used for the interpolation. After interpolation to the cell faces the gradient of the total flux at $i+\frac{1}{2}$ from figure 3.2 is readily computed as

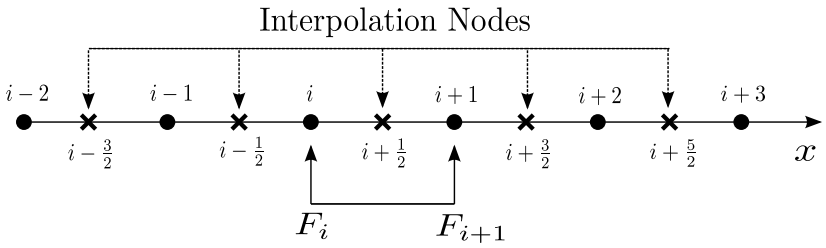

Figure 3.2: A one dimensional computational grid the solid circles are cell faces, Xs are the cell centers, the dotted lines show the cell centers used for interpolation onto positions i and $i+1$ for HOUC scheme.

in [92],

$$\begin{aligned}\nabla \cdot \mathbf{F} =& \frac{1}{2}\mathbf{u}_{i+\frac{1}{2}} \left(\frac{\widetilde{\phi}_{i+1} - \widetilde{\phi}_i}{x_{i+1} - x_i} \right) + \\ & \alpha \left(\frac{\phi_{i+\frac{3}{2}} - \phi_{i+\frac{1}{2}}}{x_{i+\frac{3}{2}} - x_{i+\frac{3}{2}}} - \frac{\phi_{i+\frac{1}{2}} - \phi_{i-\frac{1}{2}}}{x_{i+\frac{1}{2}} - x_{i-\frac{1}{4}}} \right) \frac{1}{x_{i+1} - x_i},\end{aligned} \tag{3.16}$$

where the $\widetilde{(\cdot)}$ denotes HOUC interpolated terms. The direction of the interpolation, either using backward $\{i-2, i-1, i\}$ or forward $\{i-1, i, i+1\}$ stencils referenced from figure 3.2, is dependent on the direction of the velocity at the point i given in equation 3.17, as.

$$\begin{aligned}|u_i| - u_i = 0 \rightarrow \text{backward stencil} \\ |u_i| + u_i = 0 \rightarrow \text{forward stencil}\end{aligned} \tag{3.17}$$

Boundary conditions will be unique to each application and will be discussed later in this work.

3.3 Level Set Methods

The algorithm to update the level set field at each new time step is:

1. Use the FMM to set the level set field from the previous time step to a signed distance function

2. Calculate the new normals at the interface with a high order Weighted Non-Oscillatory Method (WENO)

3. Find the interface velocity given by either thermal or chemical interface ablation or melting conditions

4. Apply the velocity with the time evolution equation, equation 3.18, and advance the interface

5. Return to step 1

The level set field, in the case of the work presented here, only experiences velocities at the interface. The FMM keeps computational nodes near the interface as signed distance functions simplifies the level set time evolution equation to

$$\frac{G^{n+1} - G^n}{\Delta t} = -\mathrm{v}_{\mathbf{n}} \cdot |\nabla G| \rightarrow G^{n+1} = G^n - \Delta t \mathrm{v}_{\mathbf{n}} \cdot |\nabla G|. \tag{3.18}$$

This simplified equation does not convect (the ablated/melted domain is solid) the level set field itself, but keeps the interface moving as a narrow band. Multiple fluid phase flows would typically require high order methods, such as weighted essentially non-oscillatory (WENO) or essentially non-oscillatory (ENO) schemes, [59]. The higher order methods are avoided here by updating the level set field with the FMM at every time step, which keeps the near interface level set field a signed distance function, [93].

The calculation of the normals of the interface does require a high order scheme. This is due to the need of highly accurate normal vectors to calculate data from when treating the fluid/solid interface. For this purpose a WENO scheme is chosen and is briefly described here in one dimension in the form

$$\partial_x^- G_i = \omega_1 \left(\partial_x G\right)_1 + \omega_2 \left(\partial_x G\right)_2 + \omega_3 \left(\partial_x G\right)_3 . \tag{3.19}$$

Equation 3.19 is the most general representation of a WENO scheme, where the weights $\omega_{\{1,2,3\}}$ are the weights based on how smooth and continuous the level set field is; $\omega_1 + \omega_2 +$

$\omega_3 = 1$. The derivatives of G in equation 3.19 are given based on the ENO approximations of the derivatives, which choose the smoothest possible polynomial interpolation of G. For a five point stencil from $i-2$ to $i+2$, where ∂_x^- is a backward finite difference, and $\xi_1 = \partial_x^- G_{i-2}$, $\xi_2 = \partial_x^- G_{i-1}$, $\xi_3 = \partial_x^- G_i$, $\xi_4 = \partial_x^- G_{i+1}$, $\xi_5 = \xi_x^- G_{i+2}$, equations 3.20-3.22 give the convex combination of 3 interpolation equations,

$$(\partial_x G)_1 = \frac{\xi_1}{3} - \frac{7\xi_2}{6} + \frac{11\xi_3}{6} \tag{3.20}$$

$$(\partial_x G)_2 = -\frac{\xi_2}{6} + \frac{5\xi_3}{6} + \frac{\xi_4}{3} \tag{3.21}$$

$$(\partial_x G)_3 = \frac{\xi_3}{3} - \frac{5\xi_4}{6} - \frac{\xi_5}{6}. \tag{3.22}$$

The weights in equation 3.19 are determined using equations 3.26-3.28, the smoothness stencils, $\{S_{s1}, S_{s2}, S_{s3}\}$ from [94], and $\epsilon = max\{\xi_1, \xi_2, \xi_3, \xi_4, \xi_5\}10^{-6}$.

$$\psi_1 = \frac{0.1}{(S_{s1} + \epsilon)^2} \tag{3.23}$$

$$\psi_2 = \frac{0.6}{(S_{s2} + \epsilon)^2} \tag{3.24}$$

$$\psi_3 = \frac{0.3}{(S_{s3} + \epsilon)^2} \tag{3.25}$$

The weights are then given using by equations 3.26-3.28 as

$$\omega_1 = \frac{\psi 1}{\psi 1 + \psi 2 + \psi 3} \tag{3.26}$$

$$\omega_2 = \frac{\psi 2}{\psi 1 + \psi 2 + \psi 3} \tag{3.27}$$

$$\omega_3 = \frac{\psi 3}{\psi 1 + \psi 2 + \psi 3}. \tag{3.28}$$

Substituting in the weights from equations 3.26-3.28 gives a 5th order approximation for the derivative of the level set field at the interface. The positive derivative, $\partial_x^+ G_i$, is found using the same procedure as above exchanging backward difference for forward differences. For a more in depth look at WENO schemes see [95] and [60].

After the level set field is redefined by the FMM, and the normals are redefined for the new level set field at $n+1$, which is a signed distance function. The solution is then advanced with the new interface velocities. The time evolution equation for the level set field, as mentioned in section 2.3, has the form given in 2.6 if the level set field follows $|\nabla G| = 1$. Applying this, simplifying equation 2.6, and discretizing the temporal derivative gives

$$\frac{\partial G}{\partial t} + v_{\mathbf{n}} \nabla G = 0 \rightarrow G^{n+1} = G^n - \Delta t \mathbf{F}_G, \tag{3.29}$$

which is explicit Euler time stepping. Sethian [96] has shown that this time stepping does not greatly effect solution oscillations or accuracy especially when used with HOUC high order methods and the Newton-Raphson method to advance the solution of G. The final discretized equation for 3.29 is given as,

$$G^{n+1,k+1} = G^{n,k=0} - \Delta t \mathbf{F}_G^{n,k}. \tag{3.30}$$

The iteration constants given in equation 3.7 have the same properties as those given in sections 3.1 and 3.2 for the momentum and scalar transport equations in two dimensions. G is located at the center of the computational cells with the pressure. The HOUC metrics used to interpolate the level set values to the velocity nodes, and to calculate the face fluxes are also the same as those used in section 3.2 in equation 3.16.

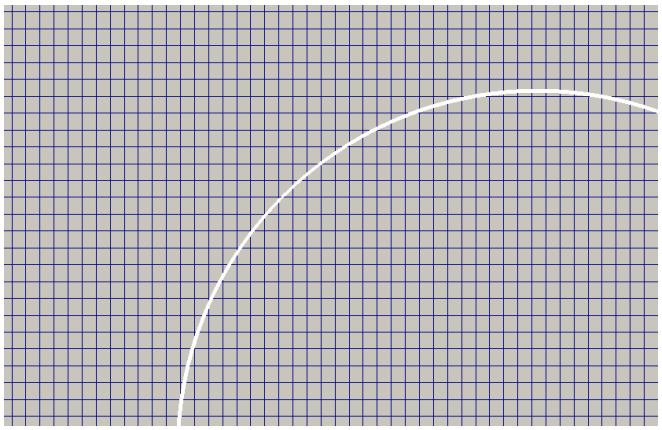

Figure 3.3: An IB, the white line, applied to a cartesian grid used in the cylinder cross flow numerical experiments.

3.4 Interface Treatment

3.4.1 Immersed Boundary Method for Momentum

The Immersed Boundary Method (IBM) is a numerical technique to apply non-grid conforming boundary conditions to time evolution equations by reconstructing the cells near a boundary interface. Figure 3.3 shows a portion of a curved boundary applied to a cartesian grid, which is used in this research. The basis of the IBM comes from the flux form of the FVM,

$$\begin{aligned}\partial_t(\rho\mathbf{u}) = \frac{1}{V}\Bigg[&\left(\mathbf{Fx}_{i+\frac{1}{2},j,k}A_{i+\frac{1}{2},j,k} - \mathbf{Fx}_{i-\frac{1}{2},j,k}A_{i-\frac{1}{2},j,k}\right)\cdot\mathbf{n}_x \\ &+ \left(\mathbf{Fy}_{i,j+\frac{1}{2},k}A_{i,j+\frac{1}{2},k} - \mathbf{Fy}_{i,j-\frac{1}{2},k}A_{i,j-\frac{1}{2},k}\right)\cdot\mathbf{n}_y \\ &+ \left(\mathbf{Fz}_{i,j,k+\frac{1}{2}}A_{i,j,k+\frac{1}{2}} - \mathbf{Fz}_{i,j,k-\frac{1}{2}}A_{i,j,k-\frac{1}{2}}\right)\cdot\mathbf{n}_z\Bigg].\end{aligned} \tag{3.31}$$

Equation 3.31 is derived by integrating, expanding, and discretizing equation 3.4. The areas, $A_{i\pm\frac{1}{2},j,k} = \Delta y\Delta z$, $A_{i,j\pm\frac{1}{2},k} = \Delta x\Delta z$, $A_{i,j,k\pm\frac{1}{2}} = \Delta x\Delta y$, volume, $V = \Delta x\Delta y\Delta z$, and dimensions, Δx, Δy, and Δz are given in figure 3.1. The boundary between domains (fluid and solid) are defined by the zero level set isosurface ($G = 0$ from figure 2.1). Each cells through which the $G = 0$ isosurface passes is said to be "cut" by the isosurface. The

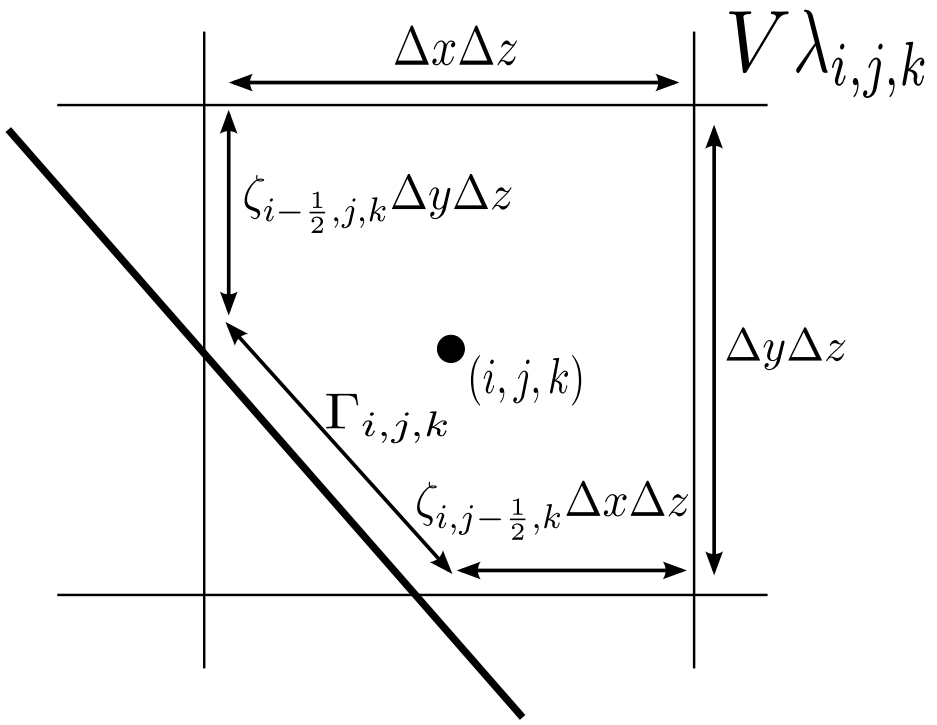

Figure 3.4: A schematic of a cell cut by the boundary, Γ, used in the IB method.

cut cells will have a shape similar to the schematic cut cells in figure 3.4. The cut cell IB method described by [46] and [48] uses the new face created by the interface cell cut to re-derive the volume integral, equation 3.4 (equation 3.31 without any cut cells), and enforce concentration of mass, equation 3.8. The new terms in the momentum equations, from the new IB area of the cell, are viscous, D, and momentum, C, source terms that enforce the no-slip condition in the tangental and normal directions to the cut cell face plane. The cut cell aperture size, $\zeta_{i,j,k}$, and the cut cell volume fraction, λ where $V_{i,j,k} = \lambda_{i,j,k} \Delta x \Delta y \Delta z$ along with the addition source terms, when added to equation 3.31, account for cell movement

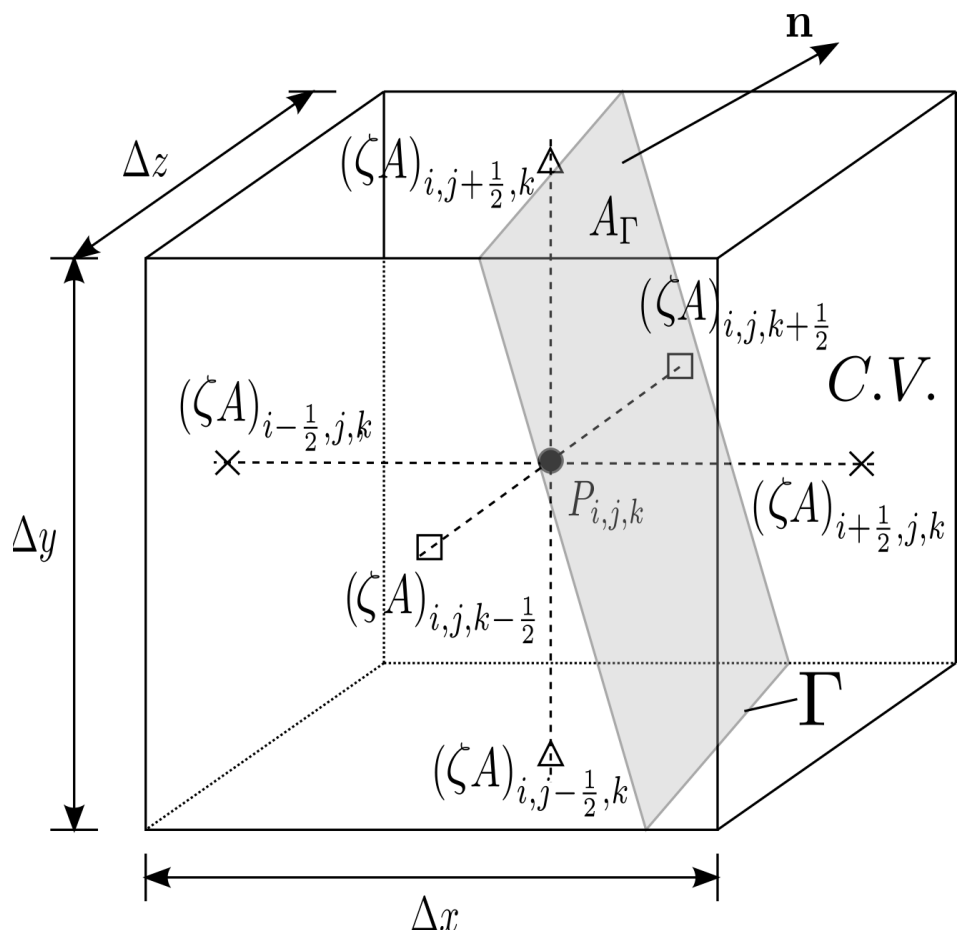

Figure 3.5: A schematic of a three dimensional cell cut by the boundary, Γ, used in the IB method.

and the no-slip condition at the interface between fluid and solid,

$$\begin{aligned} u^* = u^n &+ \frac{\Delta t}{\lambda_{i,j,k}\Delta x}\left((\zeta A)_{i+\frac{1}{2},j,k}\,\mathbf{Fx}^n_{i+\frac{1}{2},j,k} - (\zeta A)_{i-\frac{1}{2},j,k}\,\mathbf{Fx}^n_{i-\frac{1}{2},j,k}\right)\cdot\mathbf{n}_x \\ &+ \frac{\Delta t}{\lambda_{i,j,k}\Delta y}\left((\zeta A)_{i,j+\frac{1}{2},k}\,\mathbf{Fy}^n_{i,j+\frac{1}{2},k} - (\zeta A)_{i,j-\frac{1}{2},k}\,\mathbf{Fy}^n_{i,j-\frac{1}{2},k}\right)\cdot\mathbf{n}_y \\ &+ \frac{\Delta t}{\lambda_{i,j,k}\Delta z}\left((\zeta A)_{i,j,k+\frac{1}{2}}\,\mathbf{Fz}^n_{i,j,k+\frac{1}{2}} - (\zeta A)_{i,j,k-\frac{1}{2}}\,\mathbf{Fz}^n_{i,j,k-\frac{1}{2}}\right)\cdot\mathbf{n}_z \\ &+ \frac{\Delta t}{\lambda_{i,j,k}V_{i,j,k}}\left(C+D\right). \end{aligned} \tag{3.32}$$

Both $\zeta_{i,j,k}$ and $\lambda_{i,j,k}$ are between 0 and 1 and represent the fraction of the cell face and volume lost owing to the cell cut (see figure 3.5).

The viscous term added by the IB method, D, comes from the integration of the equation 3.4, taking into account the interface $\Gamma_{i,j,k}$, from figure 3.5, and giving

$$\int_{\Gamma_{i,j,k}} \nu D = \int \nu \left(\nabla \mathbf{u}\right) \cdot \mathbf{n} dS \tag{3.33}$$

Equation 3.33 accounts for the no slip boundary condition at the surface cut by the boundary. The momentum exchange term, C, accounts for any motion of the interface cut. If the boundary is moving, C has the form

$$C = v_{\mathbf{n}} \frac{V_{i,j,k}}{\Delta t}. \tag{3.34}$$

If the interface boundary is not moving and is impervious, then $C = 0$. When the boundary is in motion the wall normal velocity, $v_{\mathbf{n}}$, imposes the wall velocity as a boundary condition on the flow of an equal and opposite velocity.

Using the same cut cell area and volume fractions from the fully discretized Poisson-pressure equation is written as equation 3.35,

$$\begin{aligned}
&\frac{1}{\Delta x}\left[(\zeta A)_{i+\frac{1}{2},j,k}\left.\frac{\partial \eta}{\partial x}\right|_{i+\frac{1}{2},j,k} - (\zeta A)_{i-\frac{1}{2},j,k}\left.\frac{\partial \eta}{\partial x}\right|_{i-\frac{1}{2},j,k}\right] \\
&\frac{1}{\Delta y}\left[(\zeta A)_{i,j+\frac{1}{2},k}\left.\frac{\partial \eta}{\partial y}\right|_{i,j+\frac{1}{2},k} - (\zeta A)_{i,j-\frac{1}{2},k}\left.\frac{\partial \eta}{\partial y}\right|_{i,j-\frac{1}{2},k}\right] \\
+&\frac{1}{\Delta z}\left[(\zeta A)_{i,j,k+\frac{1}{2}}\left.\frac{\partial \eta}{\partial z}\right|_{i,j,k+\frac{1}{2}} - (\zeta A)_{i,j,k-\frac{1}{2}}\left.\frac{\partial \eta}{\partial z}\right|_{i,j,k-\frac{1}{2}}\right] - \frac{\lambda_{i,j,k}\Gamma_{i,j,k}\nabla\eta\cdot\mathbf{n}}{V_{i,j,k}} \\
=&-\frac{1}{\Delta x \Delta t}\left[(\zeta A)_{i+\frac{1}{2}j,k}\, u^*_{i+\frac{1}{2},j,k} - (\zeta A)_{i-\frac{1}{2},j,k}\, u^*_{i-\frac{1}{2},j,k}\right] \\
&-\frac{1}{\Delta y \Delta t}\left[(\zeta A)_{i,j+\frac{1}{2},k}\, v^*_{i,j+\frac{1}{2},k} - (\zeta A)_{i,j-\frac{1}{2},k}\, v^*_{i,j-\frac{1}{2},k}\right] \\
&-\frac{1}{\Delta z \Delta t}\left[(\zeta A)_{i,j,k+\frac{1}{2}}\, w^*_{i,j,k+\frac{1}{2}} - (\zeta A)_{i,j,k-\frac{1}{2}}\, w^*_{i,j,k-\frac{1}{2}}\right] + \frac{\lambda_{i,j,k}\Gamma_{i,j,k}\mathrm{v}_{\mathbf{n}}}{V_{i,j,k}}.
\end{aligned} \tag{3.35}$$

The discretization of the gradient and divergence operators, following [48], are a simple geometric re-scaling of the original FV operators. This keeps the gradient and divergence (in the IB affected cells) consistent with the global FV solution process. Uniquely

to the method proposed by Brady et al. 2014 [49], and used here, this scaling constancy allows for the solution of the IB cut cells, with their source terms, implicitly. It is called the Fictitious Cell Merging (FCM) method.

The IB geometry can be quite complex and must be updated dynamically while a simulation is progressing. This means that at any given step the volume and area fractions must be updated and provided to the fluid and scalar solvers to re-scale the gradient and divergence operators. This is accomplished by a tetrahedra-marching-algorithm that was developed by Lorensen et al. [97] to process complex 3D medical data with level set methods. The algorithm works by moving a cube through a data field and determining the cube corner intersections with the data field at a given value ($G = 0$ here). The intersections and basic geometry are then used to find the volumes and wetted surface area of each cell. Though initially used for visualization applications, it updates the new geometry of the evolved level set field quite nicely. The actual computational algorithm is complex and outside the scope of this work. Comprehensive reviews can be found in [49] and [54]; as well as expansions of the original marching tetrahedra algorithm in [98], [99], [100], and [101].

3.4.2 Immersed Boundary Mixing for Momentum

The application of the cut-cell IBM can lead to very small cell volumes when compared to the rest of the computational cell volumes. By not taking account these small cells the momentum solutions will be numerically unstable without small, and computationally prohibitive, time steps. The most efficient and stable numerical treatment of the small cells is by merging them with the surrounding cut cells and un-cut cells but this does not lend itself easily to implementation in complex 3D geometries [102]. Kirkpatric et al. 2003 [47] considered cell-linking which sets the larger cell next to a small cell as the master cell, and the small cell as the slave cell. The coordinates of the small cells are shifted to be collocated with the master cell and a strong flux between the two cells comes from of the new Jacobian

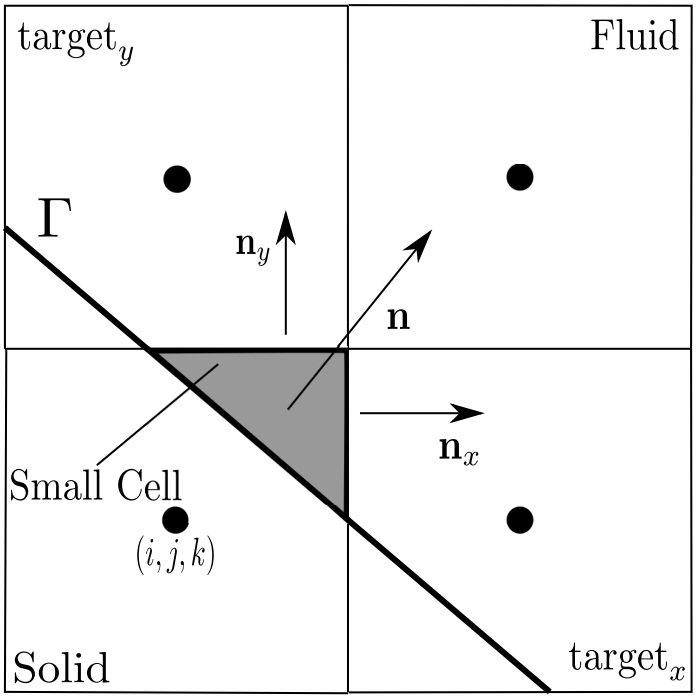

Figure 3.6: A schematic of a small cut cell and the target cells to mix with during the solution process.

of their momentum discretizaton. The strong flux, for all intents and purposes, sets the slave cell velocity to the large cells. This is not totally mass conserving and requires continuous alterations to the momentum Jacobian and monitoring of the solution stability. A more versatile method is to mix small cell momentum fluxes with the cells that surround them, such as the method used in [103]. The mixing method is altered to fit a staggered grid and follows the method in [48]. The mixing fraction, $\beta^i_{i,j,k}$ and the exchange variable, and ξ_i are given in the x direction with the conservative mixing variable, Υ, in equation 3.36

$$\xi_x = \frac{\beta^x_{i,j,k}}{\beta^x_{i,j,k} V_{i,j,k} + V_{\text{target}_x}} \left(V_{i,j,k} \Upsilon^*_{\text{target}_x} - V_{\text{target}_x} \Upsilon^*_{\text{target}_x} \right). \tag{3.36}$$

Mixing fractions, $\beta^i_{i,j,k}$ are a combination of the normal vector to the target cell and $\lambda_{i,j,k}$, which, in two dimensions, is

$$\beta^i_{i,j,k} = \mathbf{n}_i^2 \lambda_{i,j,k} \rightarrow \quad \beta^x_{i,j,k} = \mathbf{n}_x^2 \lambda^{\text{target}_x}_{i,j,k} \quad \beta^y_{i,j,k} = \mathbf{n}_y^2 \lambda^{\text{target}_y}_{i,j,k} \quad \beta^{xy}_{i,j,k} = \mathbf{n}_x \mathbf{n}_y \lambda^{\text{target}_{xy}}_{i,j,k}, \tag{3.37}$$

where $\beta_{i,j,k}^{\text{target}_{\text{direction}}}$ is the mixing coefficients to the larger cells and enhancing numerical stability. The cut-off for cells to be considered small for this work is $\lambda_{i,j,k} \leq \lambda_{\text{C}} = 0.5$, and the condition that the sum of all of the mixing fractions be normalized so that $\sum_{i=1,n}^{n} \beta_{i,j,k}^{i} = 1$, where n is the number of target cells. The values for Υ are mixed to the surrounding cells from the small cells by equation 3.38.

$$\Upsilon = \Upsilon^{*} + \frac{1}{V_{i,j,k}} \sum_{i=1,N}^{N} \xi_{i}, \tag{3.38}$$

where in this case Υ^{*} is the variable to be mixed to before mixing, and N is the number of surrounding cells to the small cell. The form of Υ^{*} that gives the best solution to the pressure is

$$\Upsilon^{*} = \frac{1}{V_{i,j,k}} \int_{V_{i,j,k}} \mathbf{F} \cdot \mathbf{n}, \tag{3.39}$$

and is the provided method by which the small cell conservative fluxes are mixed to their neighbors. The small cells volumes are then set to zero and they are removed from the computation at their particular node positions, as their momentum information has been passed to the surrounding large cells.

The mixing of the momentum cell face fluxes, equation 3.2, in both this study and in [48] was found to provide the most stable and accurate solutions over a wide range of Reynolds numbers and geometries. It should also be noted, as it is pertinent to the time stepping, that the mixing of the face flux, at each cell face, is no different than adding a strong surface forcing to the existing flux,

$$\mathbf{Fx}_{i,j,k} = \mathbf{Fx}_{i,j,k} - \frac{\Upsilon_{i+1,j,k}^{x}}{\Delta t \left(\zeta A\right)_{i+\frac{1}{2},j,k}}, \tag{3.40}$$

in the x direction if the cells at $i+1$ are small and i was a normal cell. As equation 3.39 is now part of the evolution equation there is a CFL associated with it, as there also is with cell linking [47]. The absence of this CFL constraint can lead to divergence of, and oscillation in, the solutions when the number of small cells is large.

3.4.3 Immersed Boundary Merging/Mixing for Pressure

The momentum flux terms do not require more mixing than the volumetric treatment given in section 3.4.2 for their small cells. The Poisson-pressure equation, however, does require more mixing on both the LHS and RHS of equation 3.35. When mixing and operator rescaling are relegated to only the RHS of equation 3.35 the solutions are numerically stable, but not mass conserving [104]. This is caused by the use of different divergence operators existing on the LHS and RHS of equation 3.35, due to uneven mixing of the small cells.

Alterations to equation 3.35 are also not confined to only equation 3.35, as the operator for pressure is also on the LHS of equation 3.31. If the pressure operators in only one equation, 3.31 or 3.35, were rescaled, or mixed, discrete mass conservation could not be assured. Therefore, following Brady et al. 2014 [49], both the LHS and RHS of equation 3.35 will be mixed, volumetrically as in section 3.4.2 with the addition of the mixing of the cell face aperture area at the intersecting plane of the large and small cells. The procedure similar to that in section 3.4.2, from equations 3.36 - 3.37 with the modification that now the direction of the mixing is based on the target cell volume in that direction,

$$\beta_{i,j,k;x}^{l,0,0;\mathrm{pre}} = \begin{cases} \left(\zeta_{i\pm\frac{l}{2},j,k}\right)^2 \lambda_{i\pm l,j,k}, & \text{if} \quad \lambda_{i+l,j,k} > \lambda_C \\ 0 & \text{else} \end{cases} \tag{3.41}$$

$$\beta_{i,j,k;y}^{0,m,0;\mathrm{pre}} = \begin{cases} \left(\zeta_{i,j\pm\frac{m}{2},k}\right)^2 \lambda_{i,j\pm m,k}, & \text{if} \quad \lambda_{i,j+m,k} > \lambda_C \\ 0 & \text{else} \end{cases} \tag{3.42}$$

$$\beta_{i,j,k;z}^{0,0,n;\mathrm{pre}} = \begin{cases} \left(\zeta_{i,j,k\pm\frac{n}{2}}\right)^2 \lambda_{i,j,k\pm n}, & \text{if} \quad \lambda_{i,j,k+n} > \lambda_C \\ 0 & \text{else,} \end{cases} \tag{3.43}$$

where $n, m, l = -1, 0, 1$ with indexing over the $\{i, j, k\}$ directions from the small cell to its neighbors (see figure 3.7). The new mixing fraction in x, $\beta_{i,j,k}^{l,0,0;\mathrm{pre}}$ is the Poisson-pressure mixing term based on the cell volume of the small cell and the geometry of its

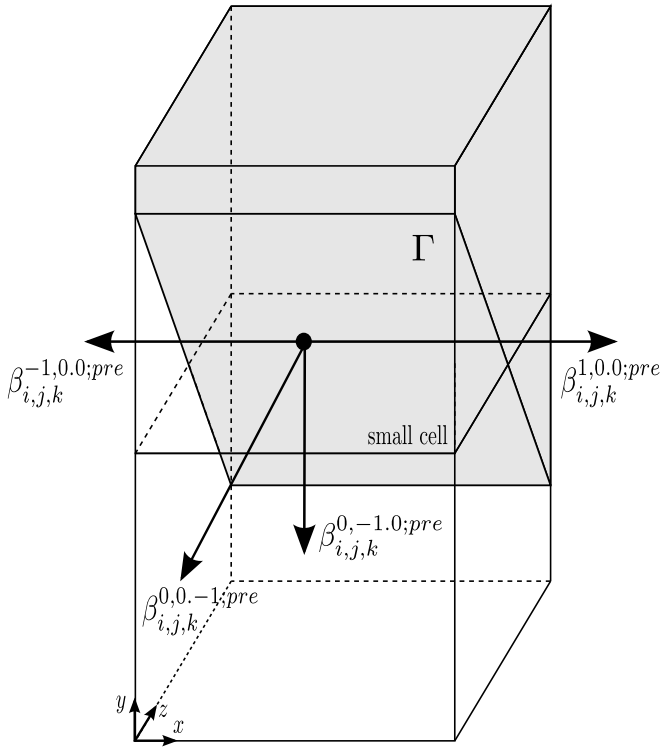

Figure 3.7: A schematic of the pressure volume mixing directions used to determine the mixing fractions from equations 3.41-3.43 for the FCM method

surrounding cells. It is different from the volumetric mixing fraction in section 3.4.2 because it contains the direction and the amount of geometric information to pass to the surrounding cells. The mixing fractions in equations 3.41-3.43 are then normalized by $= \beta_{i,j,k}^{l,m,n;\text{pre}} = \beta_{i,j,k}^{l,m,n;\text{pre}} / \sum \beta_{i,j,k}^{l,m,n;\text{pre}}$. The volumetric mixing coefficients are then used to modify the volume fractions in equation 3.35 with

$$\lambda_{i+l,j+m,k+n} = \lambda_{i+l,j+m,k+n} + \beta_{i,j,k}^{l,m,n;\text{pre}} \lambda_{i,j,k} \frac{V_{i,j,k}}{V_{i+l,j+m,k+n}}, \tag{3.44}$$

where each direction, l, m, n, is assessed and added to its neighbors. After mixing the small cell, its volume at $\{i, j, k\}$ is set to zero; removing it from the solution of equation 3.35.

The gradient and divergence operators in equation 3.35 still need to mix the face aperture area fractions to keep the FCM scheme consistent. To mix the face aperture areas

new mixing coefficients are found for the small cells and their surrounding larger cells, using the volumetric mixing coefficients from equations 3.41-3.43,

$$\beta_{i,j,k}^{m,n;fx} = \begin{cases} \zeta_{i-\frac{1}{2},j,k}\zeta_{i+\frac{1}{2},j+l,k+n}\Lambda_{i,j,k}^{m,n;fx} & \text{if} \quad \lambda_{i\pm1,j+m,k+n} > \lambda_C \\ 0 & \text{else} \end{cases} \tag{3.45}$$

$$\beta_{i,j,k}^{l,n;fy} = \begin{cases} \zeta_{i,j-\frac{1}{2},k}\zeta_{i+l,j+\frac{1}{2},k+n}\Lambda_{i,j,k}^{l,n;fy} & \text{if} \quad \lambda_{i+l,j\pm1,k+n} > \lambda_C \\ 0 & \text{else} \end{cases} \tag{3.46}$$

$$\beta_{i,j,k}^{l,m;fz} = \begin{cases} \zeta_{i,j,k+\frac{1}{2}}\zeta_{i+l,j+m,k-\frac{1}{2}}\Lambda_{i,j,k}^{l,m;fz} & \text{if} \quad \lambda_{i+l,j+n,k\pm1} > \lambda_C \\ 0 & \text{else} \end{cases} \tag{3.47}$$

where,

$$\begin{aligned} \Lambda_{i,j,k}^{m,n;fx} &= \sqrt{\left(\beta_{i,j,k}^{0,m,n;\text{pre}}\right)^2 + \left(\beta_{i\pm1,j,k}^{0,m,n;,\text{pre}}\right)^2} \\ \Lambda_{i,j,k}^{l,n;fy} &= \sqrt{\left(\beta_{i,j,k}^{l,0,n;\text{pre}}\right)^2 + \left(\beta_{i,j\pm1,k}^{l,0,n;\text{pre}}\right)^2} \\ \Lambda_{i,j,k}^{l,m;fz} &= \sqrt{\left(\beta_{i,j,k}^{l,m,0;\text{pre}}\right)^2 + \left(\beta_{i,j,k\pm1}^{l,m,0;\text{pre}}\right)^2}. \end{aligned} \tag{3.48}$$

Figure 3.8 shows the face mixing fractions and their directions using the same cut cell example from figure 3.7.

The area mixing fractions are then added to the surrounding large cells and the area of the small cell is set to zero

$$\zeta_{i\pm\frac{1}{2},j+m,k+n} = \zeta_{i\pm\frac{1}{2},j+m,k+n} + \beta_{i\pm\frac{1}{2},j,k}^{m,n;fx}\zeta_{i\pm\frac{1}{2},j,k}\frac{A_{i\pm\frac{1}{2},j,k}}{A_{i\pm\frac{1}{2},j+m,k+n}} \tag{3.49}$$

$$\zeta_{i+l,j\pm\frac{1}{2},k+n} = \zeta_{i+l,j\pm\frac{1}{2},k+n} + \beta_{i,j\pm\frac{1}{2},k}^{l,n;fy}\zeta_{i,j\pm\frac{1}{2},k}\frac{A_{i,j\pm\frac{1}{2},k}}{A_{i+l,j\pm\frac{1}{2},k+n}} \tag{3.50}$$

$$\zeta_{i+l,j+m,k\pm\frac{1}{2}} = \zeta_{i+l,j+m,k\pm\frac{1}{2}} + \beta_{i,j,k\pm\frac{1}{2}}^{l,m;fz}\zeta_{i,j,k\pm\frac{1}{2}}\frac{A_{i,j,k\pm\frac{1}{2}}}{A_{i+l,j+m,k\pm\frac{1}{2}}}. \tag{3.51}$$

The FCM procedure outlined in this section was developed by Brady et al. 2014 [49], and this work draws heavily on that previous research. It has been shown to be highly

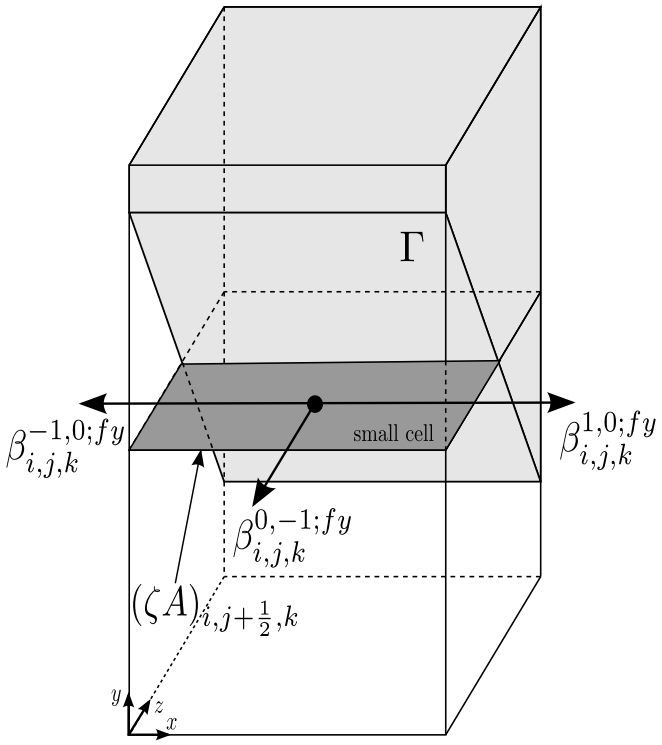

Figure 3.8: A schematic of the pressure face mixing directions used to determine the mixing directions from equations 3.45-3.47 using the example given in figure 3.7 for the FCM method

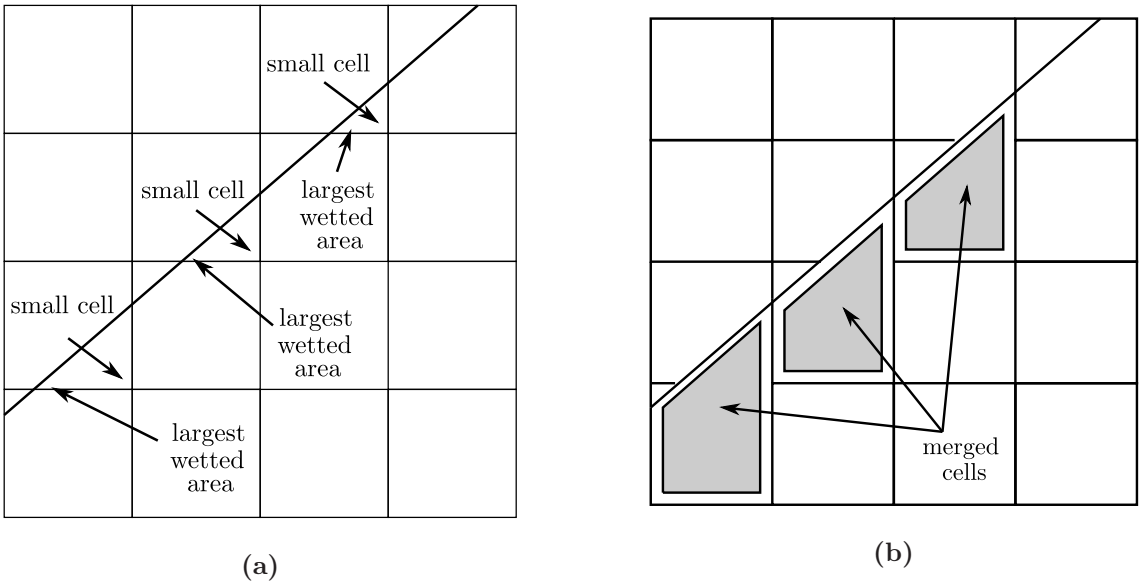

Figure 3.9: a.) Non-merged IB border cells; b.) Cells merged after using IB pressure mixing.

robust, accurate, and stable, on non-coarse grids. A schematic FCM is shown in figure 3.9.

Though the FCM does a very good job at conditioning of the Poisson-pressure Laplacian it can still leave the issue of well-posedness of Poisson's equation system. It is possible to have velocity cells with only one associated pressure cell, which could reside mostly, or all the way, in the IB (shown in figure 3.10). This situation typically only arrises in very complex geometries, but it can make the calculation of the pressure gradient impossible. This was discussed by Kirkpatrick et al. 2003 [47] and alluded to by Meyer et al. 2010 [48], where it is mentioned that some small pressure cells must be left out of the Poisson-pressure solver. This can lead to mass loss and will cause pressure oscillations near the IB interface [104]. Here though, the modification of 3.35, by rescaling with RHS and LHS mixing, will allow for the the compatibility condition: $\boldsymbol{\nabla} P_\Gamma \cdot \mathbf{n}_\Gamma = 0$ [105], to hold true, even at poorly posed small cells. Thereby ensuring discrete mass conservation and stable pressure solutions.

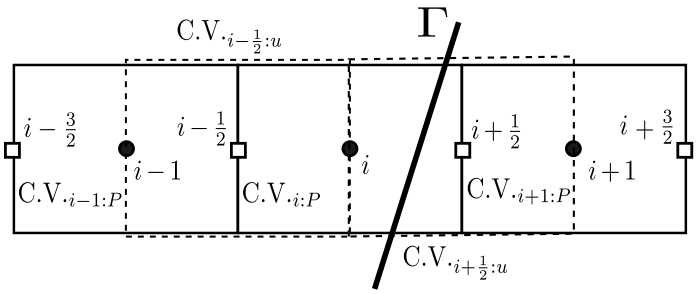

Figure 3.10: A schematic of a small cut cell which would cause an ill-posed Poisson-pressure equation because the C.V. for u at $i+\frac{1}{2}$ has an associated pressure C.V. at $i+1$ that is completely inside the IB.

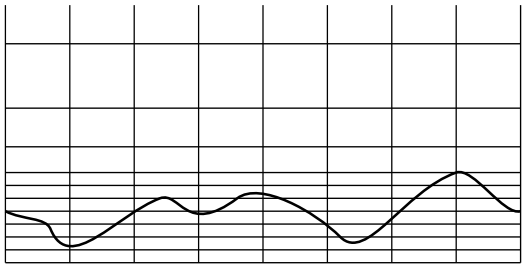

(a)

$$\begin{bmatrix} a_{m-1,n-1} & a_{m-1,n-2} & a_{m-1,n-3} & a_{m-1,n-4} \\ 0 & 1 & 0 & 0 \\ a_{m-3,n-1} & 0 & a_{m-3,n-3} & a_{m-3,n-4} \\ a_{m-4,n-1} & a_{m-4,n-2} & a_{m-4,n-3} & a_{m-4,n-4} \end{bmatrix}$$

(b)

Figure 3.11: a.) A schematic of ablated surface, and b.) an arbitrary non-symmetric Laplacian.

The final issue with the solution to equation 3.35 with the IB-FCM method is that complex, dynamic boundaries (like those for turbulent ablation in section 6.1) can cause the passing of very ugly pressure Laplacians to the pressure solver (see figure 3.11). This requires the relaxation of the iterative method, as the non-symmetric Laplacians also preclude FFTs solutions to pressure even on periodic domains. This is typically handled with a non-symmetric Red-Black-Gauss-Seidel (RBGS) method, which is what is used in this work when the Laplacian becomes non-symmetric.

3.4.4 Immersed Boundary Method for Scalars

The thermal IB (TIB) is derived from the conjugate heat transfer boundary conditions at the interface of two dissimilar substances, in the absence of contact resistance. Those boundary conditions are the continuity of the normal surface flux rates at Γ (also discretized),

$$\kappa_s \frac{\partial \phi}{\partial \mathbf{n}_{\Gamma s}} = \kappa_f \frac{\partial \phi}{\partial \mathbf{n}_{\Gamma f}} \rightarrow \kappa_s \frac{3\phi_{\Gamma s} - 4\tilde{\phi}_{s1} + \tilde{\phi}_{s2}}{\partial \mathbf{n}_{\Gamma s}} = \kappa_f \frac{-3\phi_{\Gamma f} + 4\tilde{\phi}_{f1} - \tilde{\phi}_{f2}}{\partial \mathbf{n}_{\Gamma f}}, \tag{3.52}$$

and the continuity of temperature at Γ,

$$\phi_{\Gamma s} = \phi_{\Gamma f} = \phi_{\Gamma}, \tag{3.53}$$

where the $\sim$ terms are interpolated equidistant (spaced at γ_{int}) from the interface on either side of the domain with κ is the thermal conductivity. The discretized forms of the CHT boundary conditions, given in equations 3.52 and 3.53, are used to form an implicit, single boundary condition for any cut cell. Substituting equation 3.53, and the relationship $\mathbf{n}_{\Gamma s} = -\mathbf{n}_{\Gamma f} = \mathbf{n}_{\Gamma}$, into equation 3.52 gives the new flux condition,

$$\kappa_s \frac{3\phi_{\Gamma} - 4\tilde{\phi}_{s1} + \tilde{\phi}_{s2}}{\partial \mathbf{n}_{\Gamma}}\bigg|_s = \kappa_f \frac{-3\phi_{\Gamma} + 4\tilde{\phi}_{f1} - \tilde{\phi}_{f2}}{\partial \mathbf{n}_{\Gamma}}\bigg|_f. \tag{3.54}$$

The interpolation functions used to find the interface quantities in equations 3.52-3.54 are second order Lagrange polynomials (see figure 3.12a for a one dimensional schematic of the interpolation stencil). The left and right stencils used in the interpolation are then used to derive an equation for ϕ_{Γ} with second order backward and forward differences shown in equation 3.54. The CHTIB is implemented in the same manner as embedded FV boundary conditions (see appendix A). Solving for ϕ_{Γ} using the interface distance, γ from figure 3.12a, the Crank-Nicholson, semi-implicit form, of the scalar transport equation is

$$\partial_t \phi = \boldsymbol{\nabla} \cdot (\boldsymbol{\nabla} \alpha \phi) - \boldsymbol{\nabla} \cdot (\mathbf{u}\phi) \rightarrow a_i \phi_{i-1}^{n+1} + b_i \phi_i^{n+1} + c_i \phi_{i+1}^{n+1} = a_i \phi_{i-1}^{n} + b_i \phi_i^{n} + c_i \phi_{i+1}^{n} \tag{3.55}$$

The embedded boundary condition for figure 3.12b in one dimension is then

$$\phi_{i+1} = \phi_{\Gamma} \frac{\Delta x_i}{\gamma} + \phi_i \left(1 - \frac{\Delta x_i}{\gamma}\right), \tag{3.56}$$

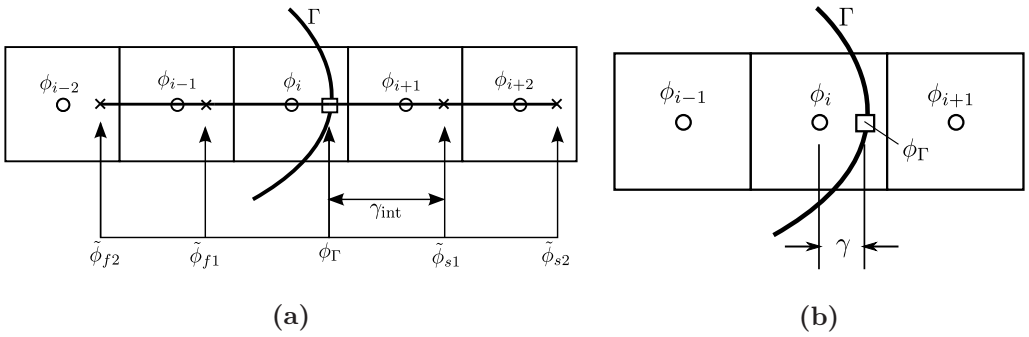

Figure 3.12: a.) One dimensional interpolation stencils used to find ϕ_Γ. b.) One dimensional stencil used to apply the boundary condition from Γ to ϕ_i.

which the implicit,

$$a_i\phi_{i-1}^{n+1} + \phi_i^{n+1}\left[b_i - \left(1 - \frac{\Delta x_i}{\gamma}\right)\right] \rightarrow c_i = 0, \tag{3.57}$$

and explicit (equation 3.58) forms of the RHS and LHS of equation 3.55,

$$\boldsymbol{\nabla}\cdot(\boldsymbol{\nabla}\alpha\phi) - \boldsymbol{\nabla}\cdot(\mathbf{u}\phi) \quad \text{with} \quad \phi_{i+1}^n = \phi_\Gamma^n\frac{\Delta x_i}{\gamma} + \phi_i^n\left(1 - \frac{\Delta x_i}{\gamma}\right). \tag{3.58}$$

By replacing γ in the boundary condition interpolation in equation 3.56, equations 3.57 and 3.58 reduce to standard, second order embedded boundary conditions using ghost nodes. It should also be noted that the values of either right or left boundary conditions, ϕ_{i+1} or ϕ_{i-1} are not replaced in the solution; only their flux terms are affected.

There are some stability issues with the final form of equations 3.57 and 3.58. The first, is the $\lim_{\gamma\rightarrow 0}\frac{\Delta}{\gamma} = \infty$ causes solution instability when $\gamma/\Delta x \leq 0.05$. By keeping equations 3.57 and 3.58 in their given form for $\gamma/\Delta x \geq 0.05$, and replacing the interpolation of the embedded boundary condition in equation 3.56 with $\phi_i = \phi_\Gamma$, this stability constraint is removed by adding a simple Dirichlet boundary condition to the point collocated on Γ.

The second stability concern is how to treat ϕ_Γ^n and ϕ_Γ^{n+1}. This is done by noting in equation 3.57 that $\phi_\Gamma^n = \phi_\Gamma^{n+1}$. This was found to be consistent with analytical solutions,

and using a dt of the order used for the smallest scales of ϕ, will give second order results (see section 4.1).

The third, and final, stability constraint has to do with implementation in N dimensions. When a FV cell is cut only the fluxes in the direction that will cross Γ are used to determine the form of the evolution equation for that cell. For example, in the cells shown In figure 3.13a the CHT boundary condition would be applied for the $\phi_{i+1,j}$, and the fluxes in y would be set equal at each face of the FV cell at $\{i, j-1\}$ and $\{i, j+1\}$. In figure 3.13b the boundary lies across both the FV cell faces that connect $\phi_{i,j}$ to $\phi_{i+1,j}$ and $\phi_{i,j-1}$. The CHT boundary conditions would then be applied at both of those points. Canceling out the fluxes near Γ that do not apply directly to a CHT boundary for that cell is justified by the physical assumptions that: near the interface a flux is not orthogonal to $\mathbf{n}_\Gamma$ and will not conduct heat across that interface,

$$\mathbf{F} \times \mathbf{n}_\Gamma = 0 \quad \text{if} \quad \mathbf{F} \parallel \mathbf{n}_\Gamma, \tag{3.59}$$

constraining the near interface physics to CHT, second isotherms near Γ will be parallel to it from the absence of source terms and local discontinuities,

$$\boldsymbol{\nabla}\phi \parallel \mathbf{n}_\Gamma << \boldsymbol{\nabla}\phi \perp \mathbf{n}_\Gamma, \tag{3.60}$$

and thirdly, the simple numerical constraint that there is no sub-grid scale model being used for cut cells, other than the CHT condition from section 2.4.

Essentially, the CHTIB decouples the fluid and solid domains by leveraging the the FVM. The resulting form transfers information using high order interpolation methods, which pass through the CHT boundary conditions. In this way, either the solid or the fluid domain can only indirectly effect the other and only in a way that is prescribed in equations 3.52-3.53.

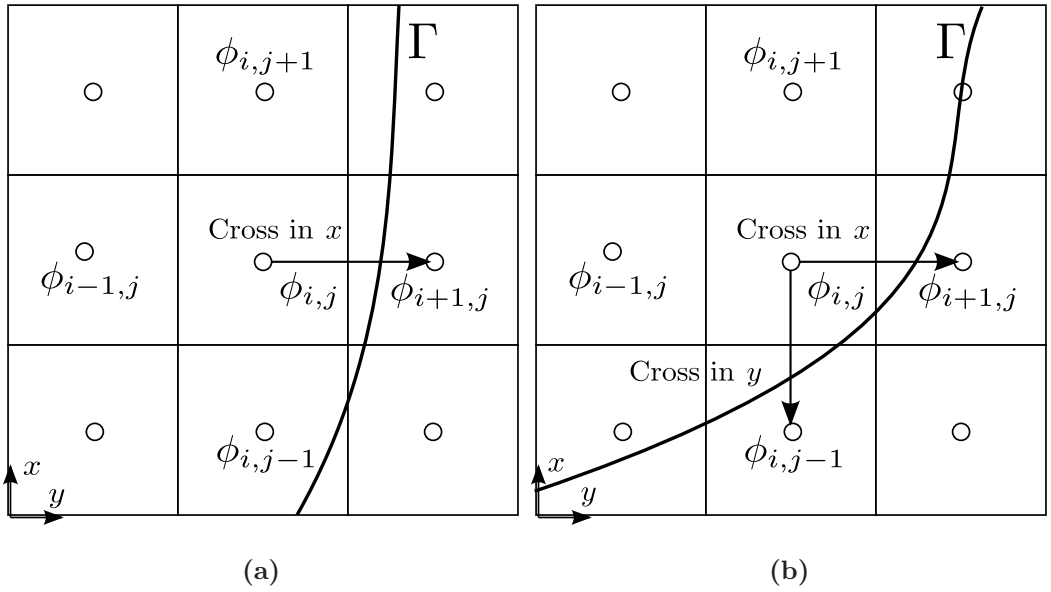

Figure 3.13: a.) Two dimensional schematic showing how Γ would forced the CHT boundary conditions to be applied at $\phi_{i+t,j}$. b.) Two dimensional schematic showing how Γ would forced the CHT boundary conditions to be applied at $\phi_{i+t,j}$ and $\phi_{i,j-1}$.

3.4.5 Ablation Condition

3.5 Thermal Ablation

In order to discretize equation 2.14 the same interpolation stencils and second order discretizations used in equation 3.54 are used again adding in the melting temperature, ϕ_m,

$$|\mathbf{v}_\Gamma|\mathbf{n}_\Gamma = \frac{1}{2L_s\rho_s\gamma}\left[\kappa_s\left(3\phi_\Gamma - 4\tilde{\phi}_{s1} + \tilde{\phi}_{s2}\right) - \kappa_f\left(-3\phi_\Gamma + 4\tilde{\phi}_{f1} - \tilde{\phi}_{f2}\right)\right] \quad \text{if} \quad \phi_\Gamma \geq \phi_m. \tag{3.61}$$

This time, though, they are not, or are not guaranteed to be, orthogonal to the mesh. This behavior is seen in figure 4.6b. The interpolated values in figure 4.6b, and equation 3.61, are found via trilinear interpolation, which has been shown to keep second order accuracy on structured grids. The surface velocity, $\mathbf{v}_\Gamma$, is used for the boundary condition in the momentum IB and it is applied to the level set field, G, at Γ, which evolves the boundary in time. The FMM is used to keep G a signed distance function, and to conserve the mass of the ablated body.

The addition of v_Γ adds an additional CFL condition,

$$\begin{aligned} CFL_{\text{abl}} = \max\Bigg\{ \mathrm{CFL}_{\mathbf{n}_x} &= \left|\frac{\Delta t}{\Delta x}\left(\mathbf{n}_x \cdot \mathrm{v}_{\mathbf{\Gamma}}\right)\right|, \\ \mathrm{CFL}_{\mathbf{n}_y} &= \left|\frac{\Delta t}{\Delta x}\left(\mathbf{n}_y \cdot \mathrm{v}_{\mathbf{\Gamma}}\right)\right|, \\ \mathrm{CFL}_{\mathbf{n}_z} &= \left|\frac{\Delta t}{\Delta x}\left(\mathbf{n}_z \cdot \mathrm{v}_{\mathbf{\Gamma}}\right)\right| \Bigg\}, \end{aligned} \tag{3.62}$$

where $\max(\cdot)$ returns the maximum values of the inputs, to the time evolution scheme in sections 3.1 and 3.2 which is associated with the level set field. Like CFL constrains on momentum and scalar transport, a particle located on Γ cannot pass more than one computational node in Δt, and ideally progresses through computational cells in multiple time steps. Increasing the CFL constraint above the one proposed in equation 3.62 was shown to cause inconsistency in mass conservation and oscillations in the momentum and

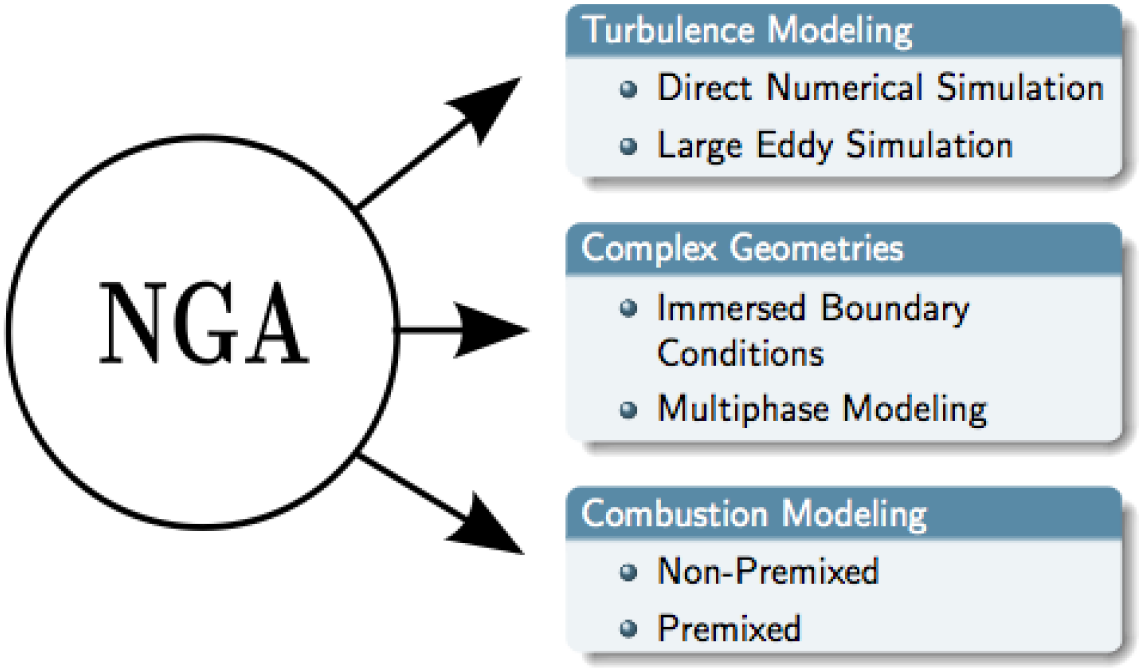

Figure 3.14: A flow chart showing the various capabilities of NGA, from [9].

scalar solutions near Γ (see section 4.2.1).

3.5.1 NGA-ARTS Flow Solver

The flow solver used in this current study is named the Next Generation Advanced Reactive Turbulent Simulator [9], NGA-ARTS, or just NGA, for short. It has been developed based on the flow solver written by Charles David Pierce in 2001 [84] through 2004 [57] for progressive variable scalar simulation of combustion at Stanford University. NGA is a FV-based flow solver with the capability of simulating both LES and DNS for low Mach number flows, with variable density as shown in figure 3.14. It also features a range of modules and methods to solve turbulent reacting flows with non-grid conforming boundary conditions, which have been supplemented by this research. All the FV schemes in NGA are discretely conservative for mass, momentum, and kinetic energy with the ability to increase

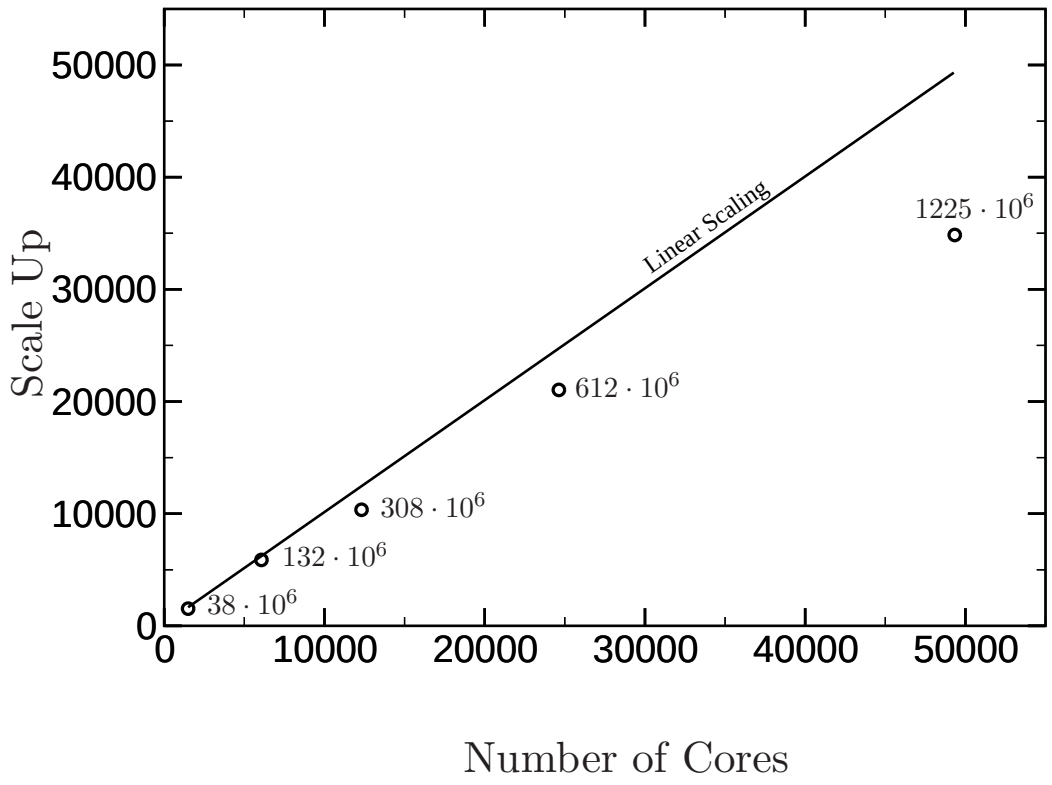

Figure 3.15: Data taken from [9] with NGA run on Kraken at the National Institute of Computer Science, University of Tennessee. The numbers next to the data points represent the number of computational nodes used for each simulation.

the order of the accuracy at the initiation of a simulation.

NGA uses MPI subroutines giving it the capability of scaling well to 50000 cores for simulations that lend themselves to good load balancing (see figure 3.15). This scaling does not hold true for much of this work as the geometries are inherently non-symmetric and certain areas of boundaries will take longer to exit their solution subroutines adding some inevitable idle time in cores that do not have a portion of the IB. This was found to be no more than a 5%-25% increase than running non-ablating IB simulations on similar geometries.

Chapter 4

VALIDATION STUDIES

4.1 Thermal IB Validation

4.1.1 An Isothermal Cylinder in Crossflow Resolution Study

The first validation was carried out for an isothermal cylinder in a cross flow to determine the level of solid/fluid decoupling inherent in the CHT algorithm from section 3.4.4 and to bolster the results presented in chapter 6. Numerical resolution tests were performed to determine the rate of mass loss and Nusselt number, Nu, (the ratio of convective and diffusive heat flux),

$$Nu = \frac{\left[\frac{\partial \phi_\Gamma - \widetilde{\phi}_{\gamma_{Nu}}}{\partial \gamma_{Nu}}\right]_\Gamma}{\frac{\phi_\gamma - \phi_\infty}{D}} = -\left(\frac{\partial \phi}{\partial \gamma_{Nu}}\right)_\Gamma \mathbf{n}_\Gamma \rightarrow \overline{Nu} = -\frac{1}{S}\oint_S \left(\frac{\partial \phi}{\partial \gamma_{Nu}}\right)_\Gamma \mathbf{n}_\Gamma dS, \tag{4.1}$$

convergence for the ablation algorithm set out in section 3.5. In equation 4.1 γ_{Nu} will be determined as twice the minimum near surface computational node spacing, seen in figure 4.2, where S is the surface area of the cylinder in figure 4.1. Doubling the smallest grid spacing is necessary to ensure that only nodes in either the fluid or solid are used to interpolate the stencil for normal derivative in equation 4.1. For sections 4.1.1 through 4.2.1

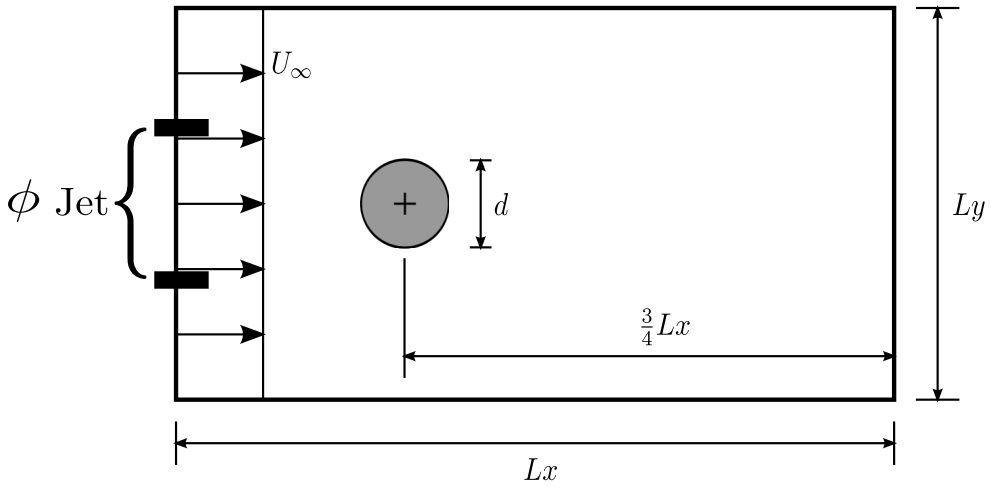

Figure 4.1: The experimental set up for the cylinder in crossflow numerical experiment.

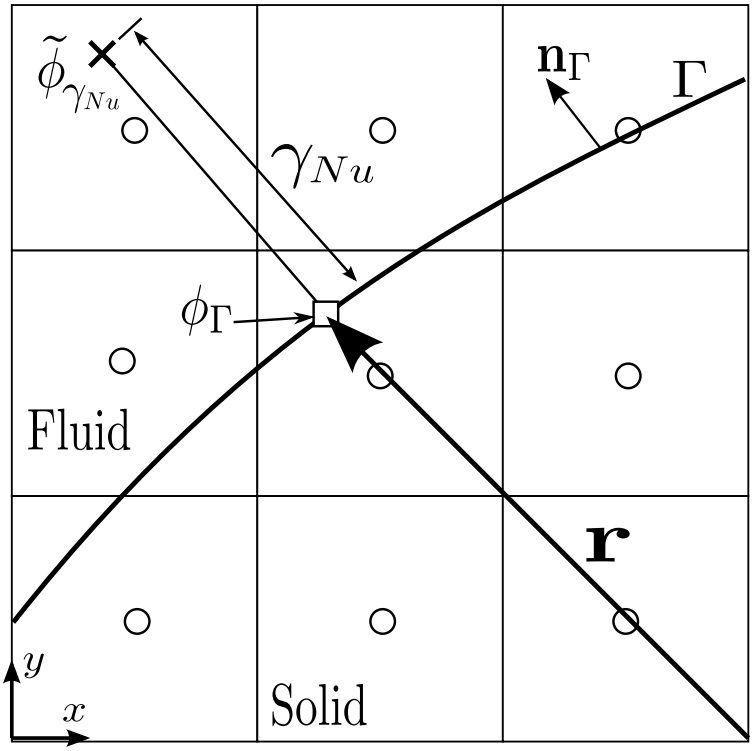

Figure 4.2: The experimental set up for nusselt number interpolation at Γ, and r is the vector from the center of mass of the body in cross flow to the surface.

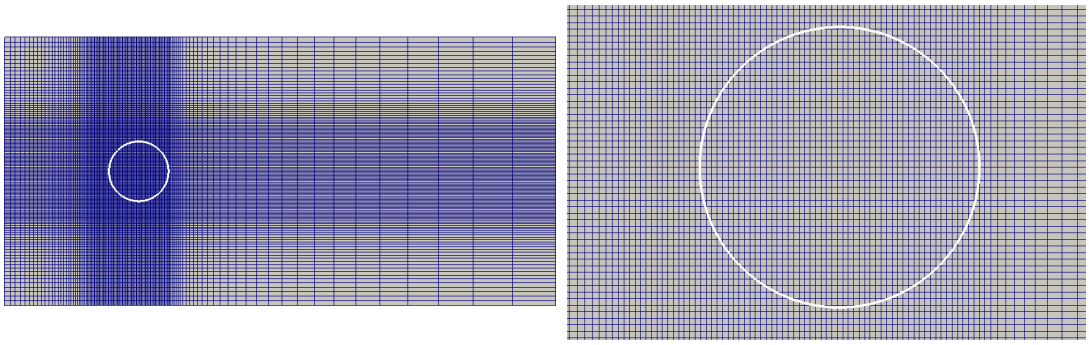

(a) **(b)**

Figure 4.3: a.) The fully stretched grid for a cylinder in crossflow (with the IB shown in white). b.) A close up of the uniform grid near the cylinder in Crossflow.

geometric stretching of the grid was done (as is shown in figure 4.3) which gives uniform spacing within $1.5D$ (where D is the cylinder diameter) of the cylinder and better solution of the wake for higher Reynolds numbers. The classic $\overline{Nu}$-Re correlation from Churchill et al. 1977 [13],

$$\overline{Nu} = 0.3 + \frac{0.62 Re^{\frac{1}{2}} Pr^{\frac{1}{3}}}{\left[1 + (0.4/Pr)^{\frac{2}{3}}\right]^{\frac{1}{4}}}, \tag{4.2}$$

is one set of the physical and numerical experiments used to evaluate the Nusselt number for various Reynolds numbers around the cylinder in figure 4.3a. A comprehensive collection of $\overline{Nu}$-Re correlations can be found in [106]. This is shown in figure 4.4 and table 4.1 along with other numerical and experimental data. Table 4.1 and figure 4.4 both show excellent data reproduction of previous studies. The Nusselt number is also evaluated as a function of the angle, θ, around the cylinder in figure 4.5. Again, locally there is an excellent agreement between the current study and previous studies shown in figure 4.5. The evaluation of differences between the data in the literature over numerous vortex shedding cycles of the larger Reynolds numbers can be explained by either longer or shorter averages taken from each set of data, their experimental accuracies and precision, which are typically

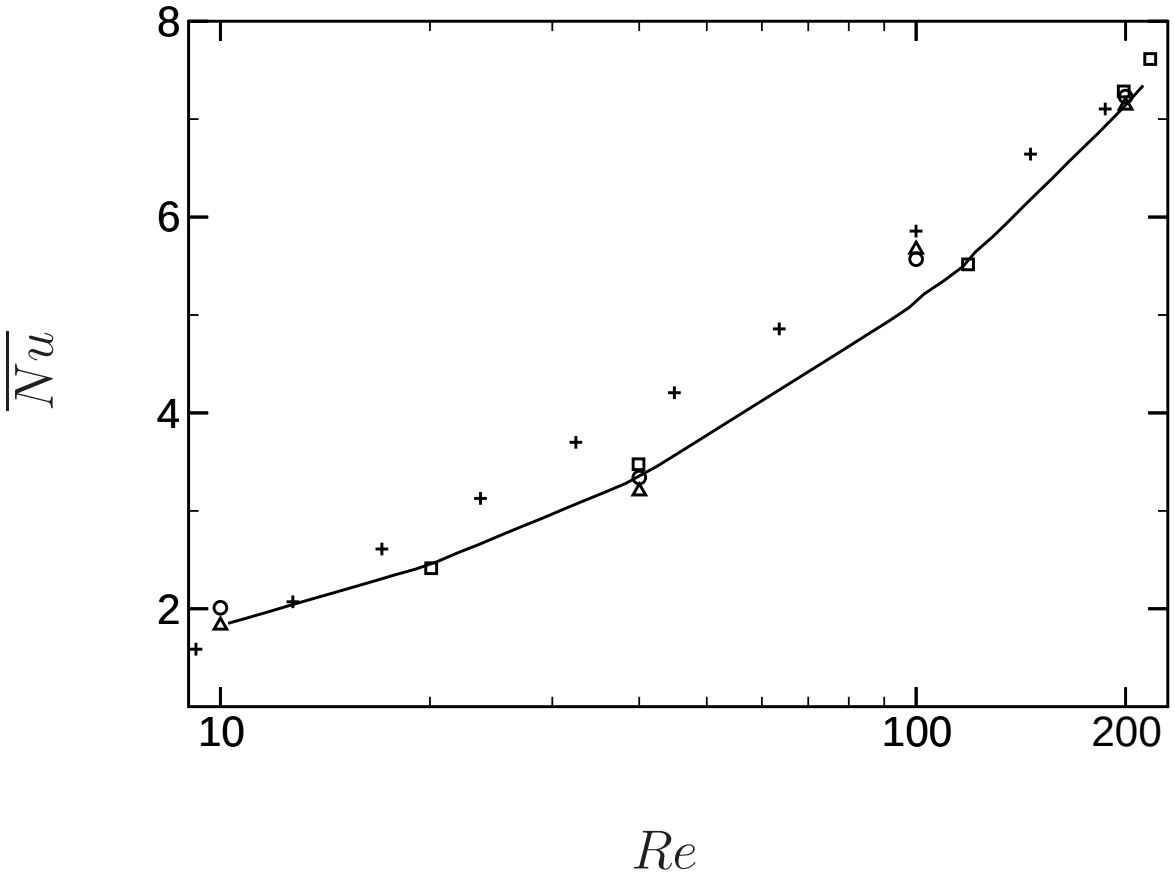

Figure 4.4: A plot of the time averaged Nusselt number, $\overline{Nu}$, versus Re for the present study ($\circ\,\circ\,\circ$),**[10]** $(+\,+\,+)$, **[11]** ($\square\square\square$), **[12]** ($\triangle\,\triangle\,\triangle$), **[13]** (——).

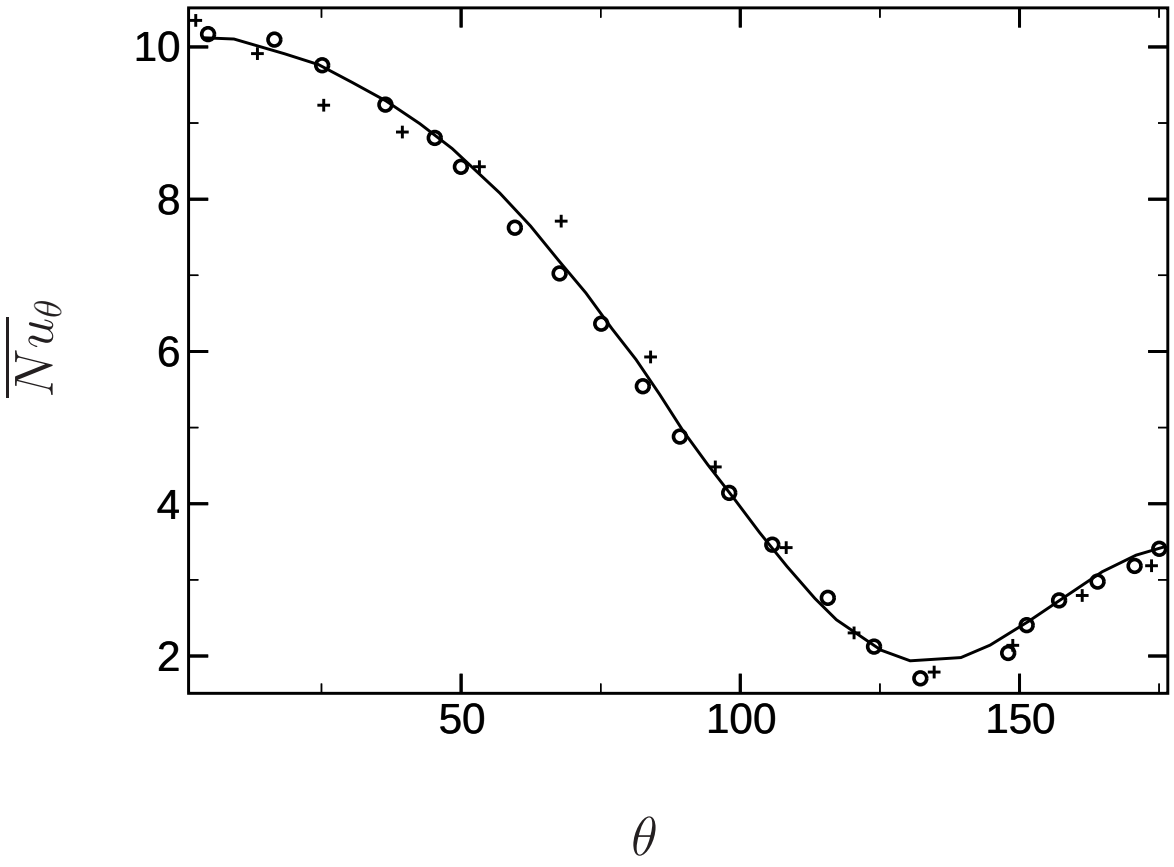

Figure 4.5: A plot of the time averaged, $\overline{Nu}_\theta$, versus the angle around the cylinder showing the present study ($\circ\,\circ\,\circ$), [14] ($+\,+\,+$), and [12] (——).

Table 4.1: $\overline{Nu}$ and Re for isothermal cylinders at various grid resolutions, and from previous studies. The columns showing grid resolutions are from the present study and are the resolution for $1.5D$ around the cylinder, (see figure 4.3).

	$\overline{Nu}$					
				Nodes		
d Re	[107]	[12]	[11]	64^2	128^2	256^2
10	1.86	1.83	—	2.06	2.01	2.01
40	3.28	3.20	3.47	3.38	3.37	3.34
100	—	5.67	5.51	5.64	5.60	5.57
200	—	7.14	7.28	7.33	7.23	7.23

not mentioned in the various analyses.

4.1.2 Co-annular Cylinder Resolution Study

A second validation was performed with one of the few CHT analytical solutions. The velocity and temperature fields for two co-annular cylinders (see figure 4.6a) are given by

$$u_\theta = 0 \quad \text{and} \quad u_r(r) = \begin{cases} 0 & \text{for } R_i < r < R_m \\ -\dfrac{R_o R_m^2 U_\infty}{R_o^2 - R_m^2}\dfrac{1}{r} + \dfrac{R_o U_\infty}{R_o^2 - R_m^2} r & \text{for } R_m < r < R_o \end{cases} \tag{4.3}$$

in cylindrical coordinates, and

$$\phi_r(r) = \begin{cases} \phi_{in} + \dfrac{\phi_{out} - \phi_{in}}{\log_{10}\left(\frac{R_m}{R_i}\right) + \left(\frac{\kappa_s}{\kappa_f}\right)\log_{10}\left(\frac{R_o}{R_m}\right)} \log_{10}\left(\dfrac{r}{R_i}\right) & \text{for } R_i < r < R_m \\ \phi_{out} - \dfrac{\phi_{out} - \phi_{in}}{\left(\frac{\kappa_f}{\kappa_s}\right)\log_{10}\left(\frac{R_m}{R_i}\right) + \log_{10}\left(\frac{R_o}{R_m}\right)} \log_{10}\left(\dfrac{R_o}{r}\right) & \text{for } R_m < r < R_o \end{cases} \tag{4.4}$$

respectively, where the dimensions are given in figure 4.6a and $Re = 50$. The figures 4.7 a,b,c, and d, show the $L_2 = \sum |\phi_{exact} - \phi| / |\phi_{exact}|$ and $L_\infty = \max|\phi_{exact} - \phi|$ norms

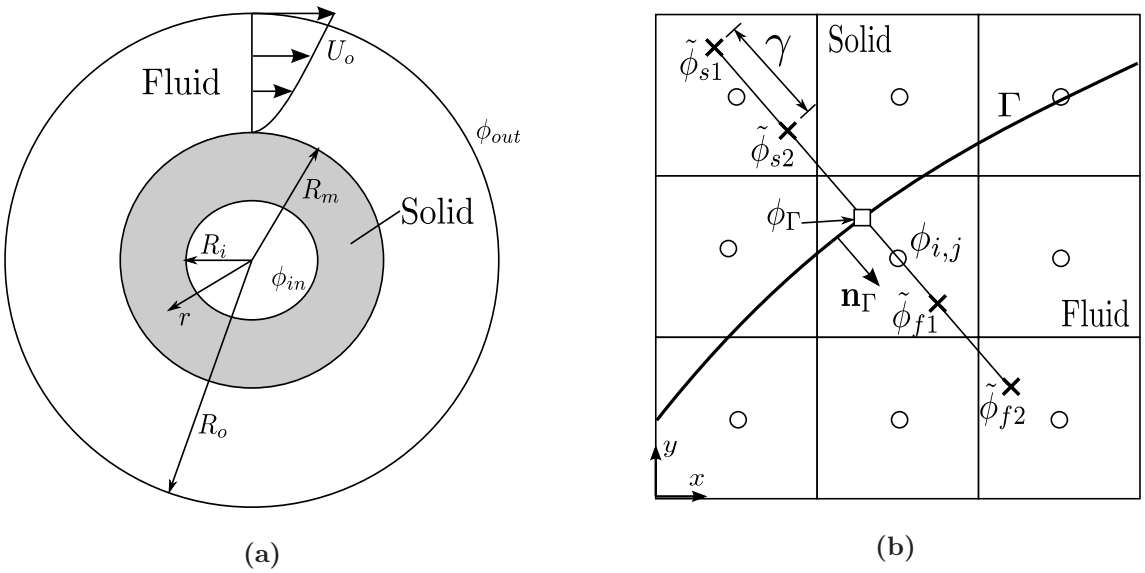

Figure 4.6: a.) The schematic of the validation study domain. b.) The stencil used to calculate the ablation velocity.

after reaching the convergence criteria of $L_2^{n+1} - L_2^n| \leq 1 \cdot 10^{-9}$ ($max\,(\text{iterations}) \approx 20000$ iterations at $dt = 1 \cdot 10^{-4}$), and at steady state. The time series shown in figure 4.8 gives a good indication that even in the transient flow regime the CHT equations are still holding the temporally evolving temperature profiles to the sharp boundary at the discontinuity of κ. Even with $\kappa_s >> \kappa_f$, as shown in figure 4.8c the initial discontinuity of the time series is nearly square and the solution remains stable, even in the points close to the interface. During the development of the CHT algorithm defined in section 3.4.4, experiments were run purely explicitly and it was noted that as the ratio κ_s/κ_f was increased, so was the temporal stiffness of the time evolution equation, making large κ rations slow and unwieldy. The adition of the CHT boundary conditions to an implicit solver has mitigated the issues of small dt for large κ_s/κ_f.

Both the plots in figures 4.8b and 4.8d, the final steady state result lays directly over the analytical solution given in equation 4.4, showing very little deviation at any point including interfacial points. Two different approaches were used to find the final steady

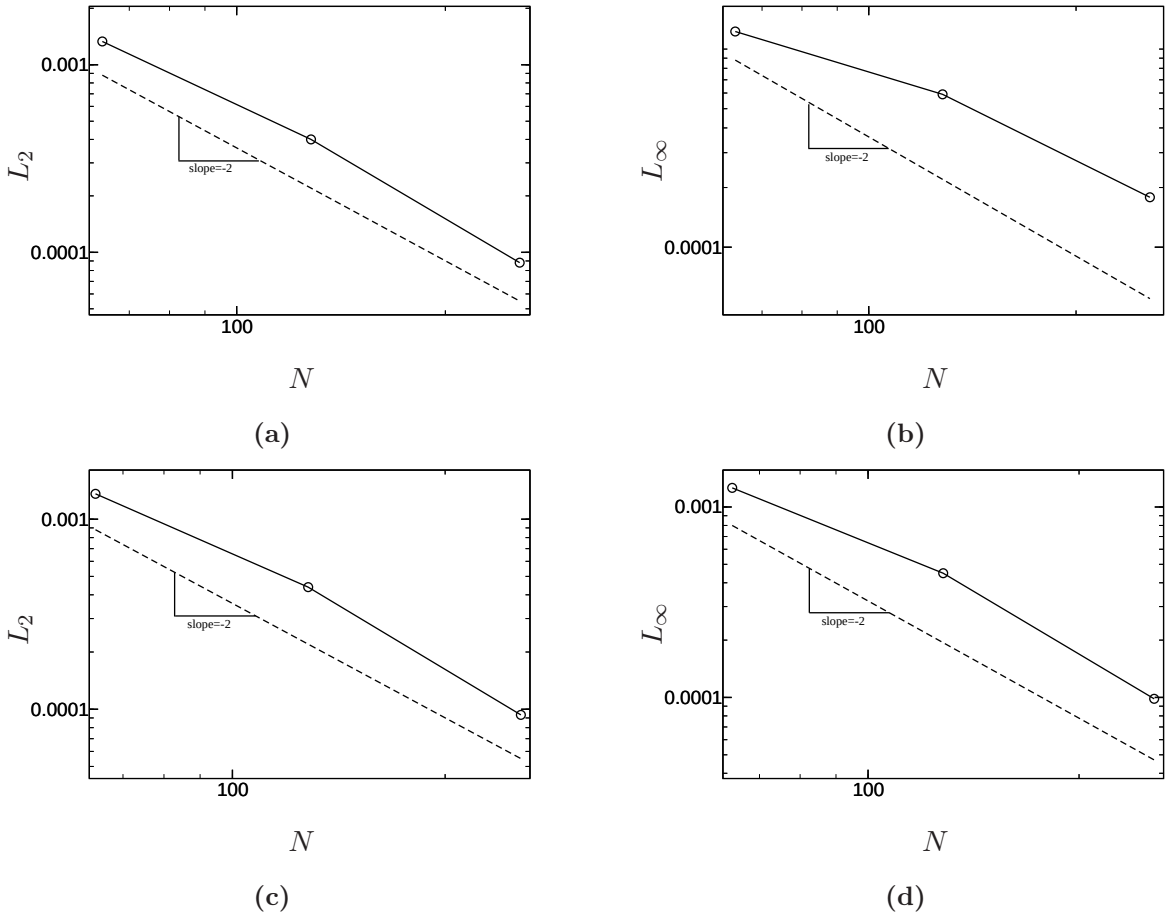

Figure 4.7: a.) The L_2 error norm for temperature and b.) the L_∞ error norm for temperature both for $\kappa_s/\kappa_f = 9$. c.) The L_2 error norm for temperature, and d.) The L_∞ error norm for temperature, both for $\kappa_s/\kappa_f = 900$. All four plots show second order convergence of error, $(- - -)$ is a line with LOG-LOG slope of -2 and $(\cdots)$ are the error norms, they are both plotted against the number of nodes, $N = N_x = N_y$ in the simulation.

state of the system, which were:

1. Initiating the temperature fields to equation 4.4 and waiting until the error norms converged.

2. Letting the fields pass through transience to the steady state solution in equation 4.4.

Both simulation types produced indistinguishable error plots (figure 4.7), that were second order convergent for L_∞, and L_2.

4.2 Ablation Algorithm Validation

4.2.1 Ablation Cylinder Resolution Study

As previously mentioned, there exists a lack of analytical and experimental solutions within the solution capabilities of current CFD algorithms. To this end the ablation algorithm is validated by running a very well resolved, ablating, cylinder in cross flow. The numerical experiment uses a refined grid of $N_x = N_y = 512$, in a $1.5D$ box around the cylinder is used as a benchmark to check the interface and mass loss conversion rate. The actual domain size is much larger than the near cylinder domain size and grid spacing. The largest value of the Reynolds number, $Re = 200$, from section 4.1.1 is used in this validation study for the initial flow before the onset of vortex shedding. To check both the shape and mass loss convergence of the ablating cylinder shown in figure 4.9a the normal of the $N_x = N_y = 512$ is projected onto the the surface of the $N_x = N_y = 64, 128, 256$ cases, as shown in figure 4.10. The radii from the centroid of the ablated cylinders are used to construct both the $L_2 = |R_\Gamma - R_{\text{exact}}| / R_{\text{exact}}$ and $L_\infty = \max |R_\Gamma - R_{\text{exact}}|$. The resulting convergence is shown in figure 4.11 and both show second order convergence.

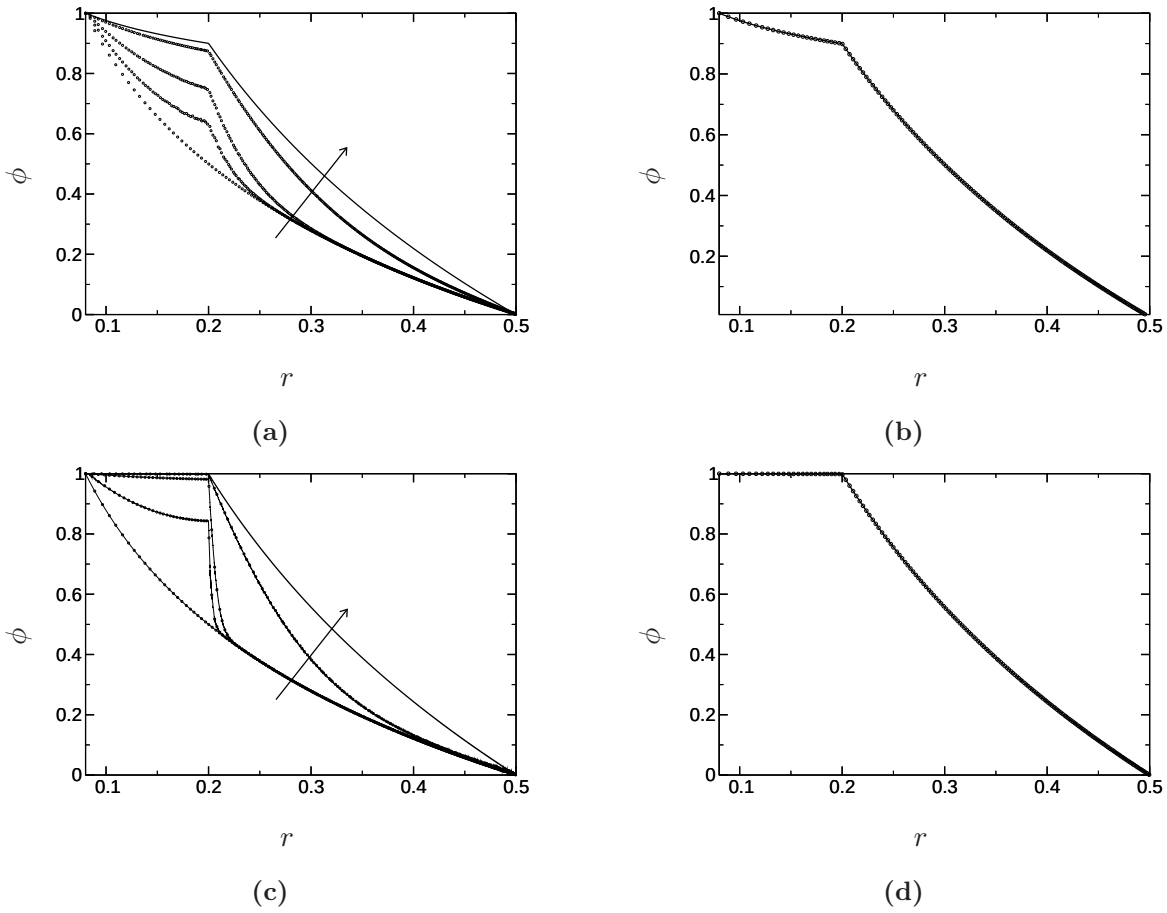

Figure 4.8: a.) The time series for the temperature profile plotted with the analytical solution, b.) and the steady state temperature profile plotted against the analytical solution for$\kappa_s/\kappa_f = 9$. c.) The time series for the temperature profile plotted with the analytical solution, d.) and the steady state temperature profile plotted against the analytical solution for$\kappa_s/\kappa_f = 900$, lines have been added to the time series to help distinguish each time step. $(---)$ is the analytical solution $(\circ\circ\circ)$are the temperature profiles increasing with time in direction of the arrow. All plots shown are from the $N_x = 256$, $N_y = 256$ simulations with every two hundredth point removed from the plot to make it easier to see individual points.

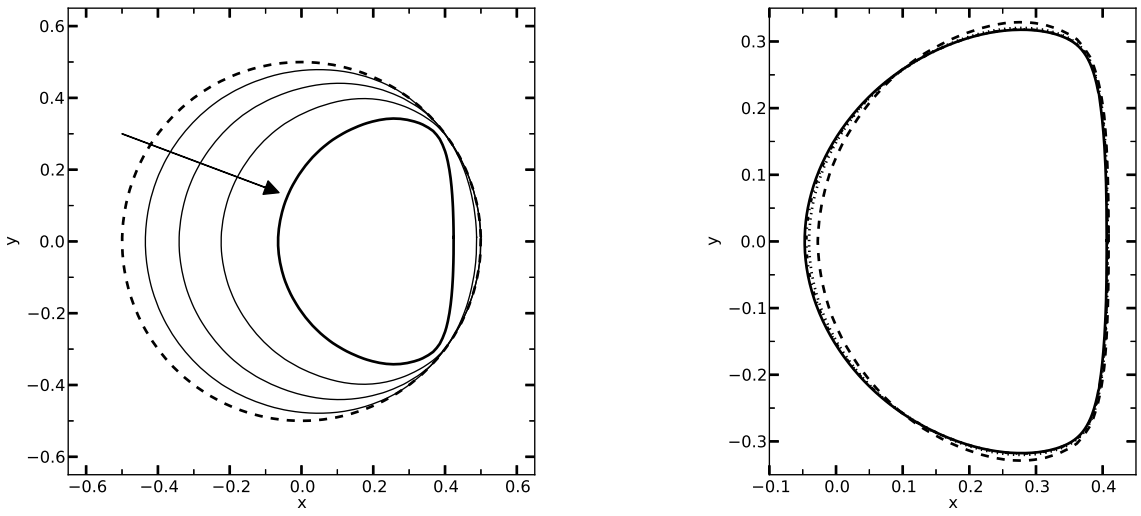

(a) **(b)**

Figure 4.9: The melting cylinder interface for Re=200 and Ste=1 for, a.) the receding cylinder at various times for $N_x = N_y = 512$ where the arrow denotes melting progression and $(- - -)$ is the initial state, and b.) 75% mass loss of $N_x = N_y$ =64 $(- - -)$,128 $(\cdots)$, 256 $(- \cdot -)$, 512 (——).

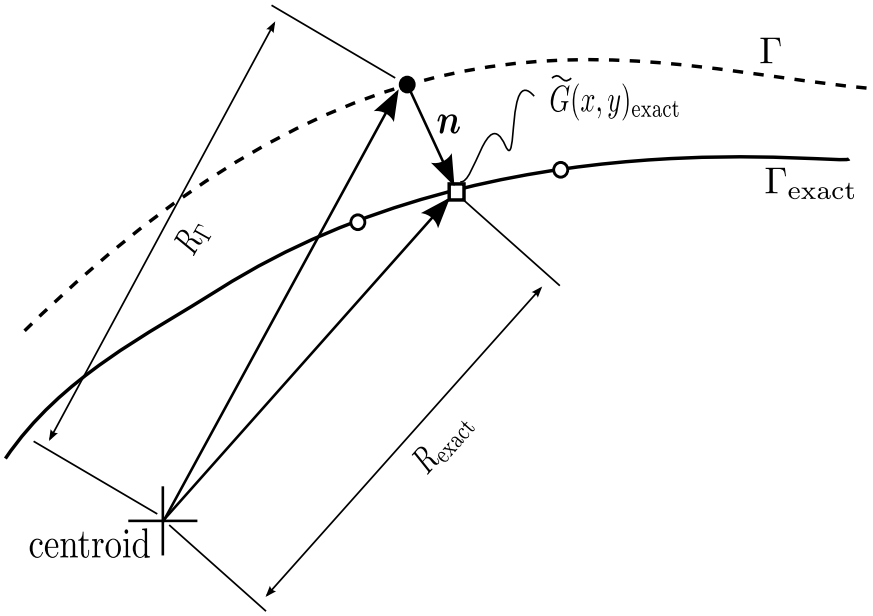

Figure 4.10: Error evaluation of for the various shapes produced by the different resolution cylinder ablation numerical experiments. R_{exact} is the radius, from the centroid of the $N_x = N_y = 512$ ablated cylinder at 75% mass loss, and R_Γ is the radius of the experimental study surface from the same centroid.

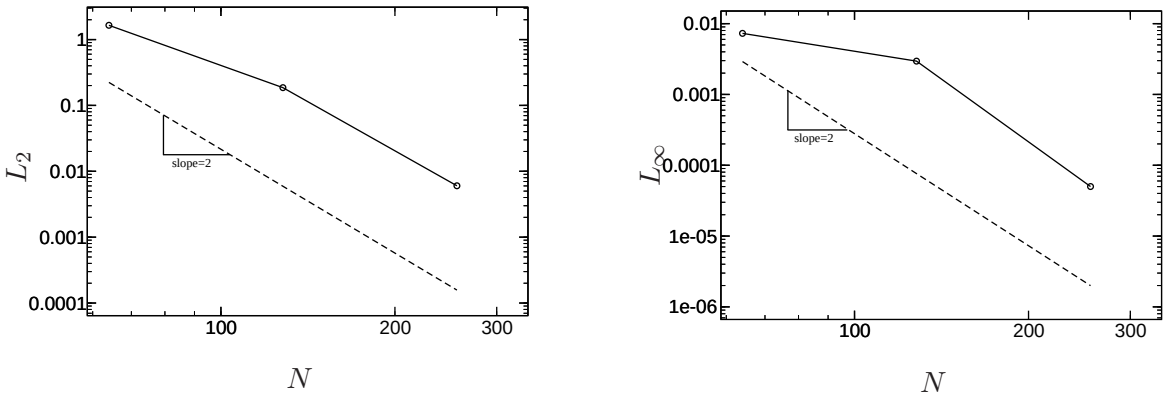

Figure 4.11: The L_2, a.), and L_∞, b.), error norms calculated for ablating cylinders by using the radii from figure 4.10

4.2.2 Gallium Melted by a Convective Flow

There are few physical experiments which are suitable for the application of DNS necessary to validate the ablation algorithm. Even a very simple geometry, at moderate flow velocity and a small characteristic length, as in Ameen et al. 1990 [108], give Reynolds numbers in the range of $5000 - 10000$. For studies where a cylinder is in cross-flow the critical Re at which cylinders are no longer representable by two dimensional geometries is $Re = 250$, [109]. Simulation of Reynolds numbers of that order would require computationally restrictive grid resolutions such as in [110] and [111], and would not provide a basis of the common physics that would be found at smaller Reynolds numbers. This restrains the validation experiments, for ablation, to ones where Re is small, and the geometry allows for an adequately small grid resolution, while still being two dimensional. This criteria is met by a physical experiment, performed by Gau et al. 1983 [15], where a thin slab of gallium is headed from one side and cooled from the other; with adiabatic boundaries on the top and bottom. This geometry is shown in figure 4.12. The experimental data were then compared to a body fitted grid numerical experiment by Jana et al. 2007 [2] with the parameters and properties given in table 4.2. The FV equations from chapter 3 for momentum and scalar transport are normalized with the Boussinesq buoyancy approximation shown in appendix C.

The fit of the present study is a closer match to the numerical experiment than to the experimental procedure used in [15] and specifically refined for Gallium in [1]. The differences between the numerical and physical experiment are due to environmental factors of the physical experiment and a low resolution, both in time and space, of the wall position results from [1]. There could also be three dimensional flow phenomena not captured in the 2D numerical experiment, but present in the physical experiment. As well as the experimental procedure from [15].

The numerical experiment from [2] also shows a slight discrepancy between the

Table 4.2: The dimensionless parameters, taken from [1], [2] and [3], and properties, taken from [1], [4], [5], and [6] used in the gallium melting experiment in section 4.2.2.

Property	Value	Units	Parameter	value
ρ_f	6093	$\left[\frac{Kg}{m^3}\right]$	Ste	0.044
μ_f	$1.81 \cdot 10^{-3}$	$\left[\frac{kf}{s \cdot m}\right]$	Pr	0.0216
κ_f	32.4	$\left[\frac{W}{m \cdot K}\right]$	Ra	$7 \cdot 10^5$
α_f	$2.39 \cdot 10^{-6}$	$\left[\frac{m^2}{s}\right]$	Re	3000
c_{pf}	2225	$\left[\frac{J}{Kg \cdot K}\right]$	—	—
β_f	$5 \cdot 10^{-6}$	$\left[\frac{1}{m}\right]$	—	—
L_s	$8.016 \cdot 10^4$	$\left[\frac{J}{kg}\right]$	—	—
ρ_s	5910	$\left[\frac{Kg}{m^3}\right]$	—	—
κ_s	20	$\left[\frac{W}{m \cdot K}\right]$	—	—
α_s	$1.93 \cdot 10^{-6}$	$\left[\frac{m^2}{s}\right]$	—	—
c_{ps}	1751.5	$\left[\frac{J}{Kg \cdot K}\right]$	—	—
ϕ_H	311.0	$[K]$	—	—
ϕ_C	301.3	$[K]$	—	—
ϕ_m	302.78	$[K]$	—	—
G_y	9.81	$\left[\frac{m}{s^2}\right]$	—	—
L_y	0.0889	$[m]$	—	—

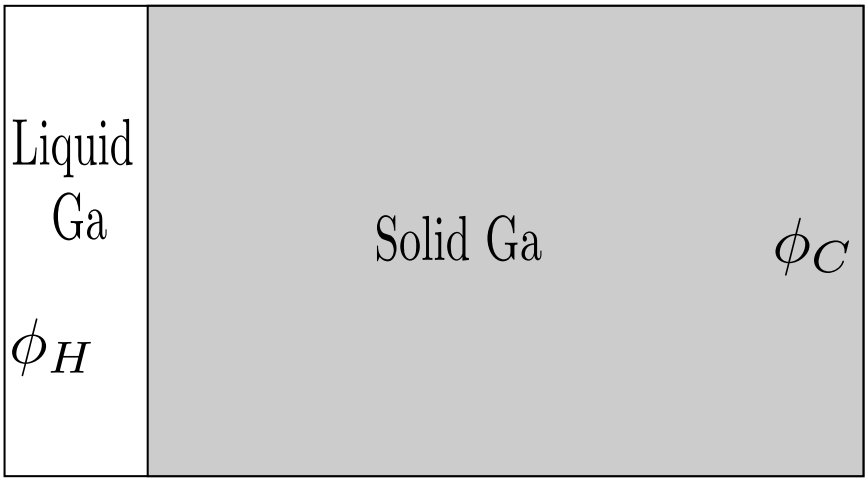

Figure 4.12: The experimental set up for the numerical experiment to simulate data from [15], [1], and [2]

present results and the numerical experiment. This difference can almost certainly be linked to the grid stretching algorithm as the solution is not perfectly grid-independent ([112] and [6]). Though the order of accuracy cannot be measured in this instance the maximum error between both the data sets used in the comparisons is under $\pm 5\%$, even after 30 hours of simulation time. While a direct comparison cannot be made, the relatively minute error shows that the ablation algorithm from section 3.5 is adequately reproducing the proper physics.

The difference between the experimental results from [15] and the present study shown in figure 4.13 was tentatively explained in [6]. This discrepancy was attributed to the measurement of the interface in the physical experiment performed in [15]. When the interface was measured the heating was stopped, and the liquid was poured out. Then the simulation was re-started with the convection velocity now at zero. To simulate this a numerical experiment has been run stalling the velocity (reducing it by 5 orders of magnitude) at the corresponding times to when Gau et. al 1986 and 1983, [15] and [1], stopped their experiment to measure the interface. The results are shown (in figure 4.14. The resulting interface profile is an excellent match to the experimental data and resolves the conflict

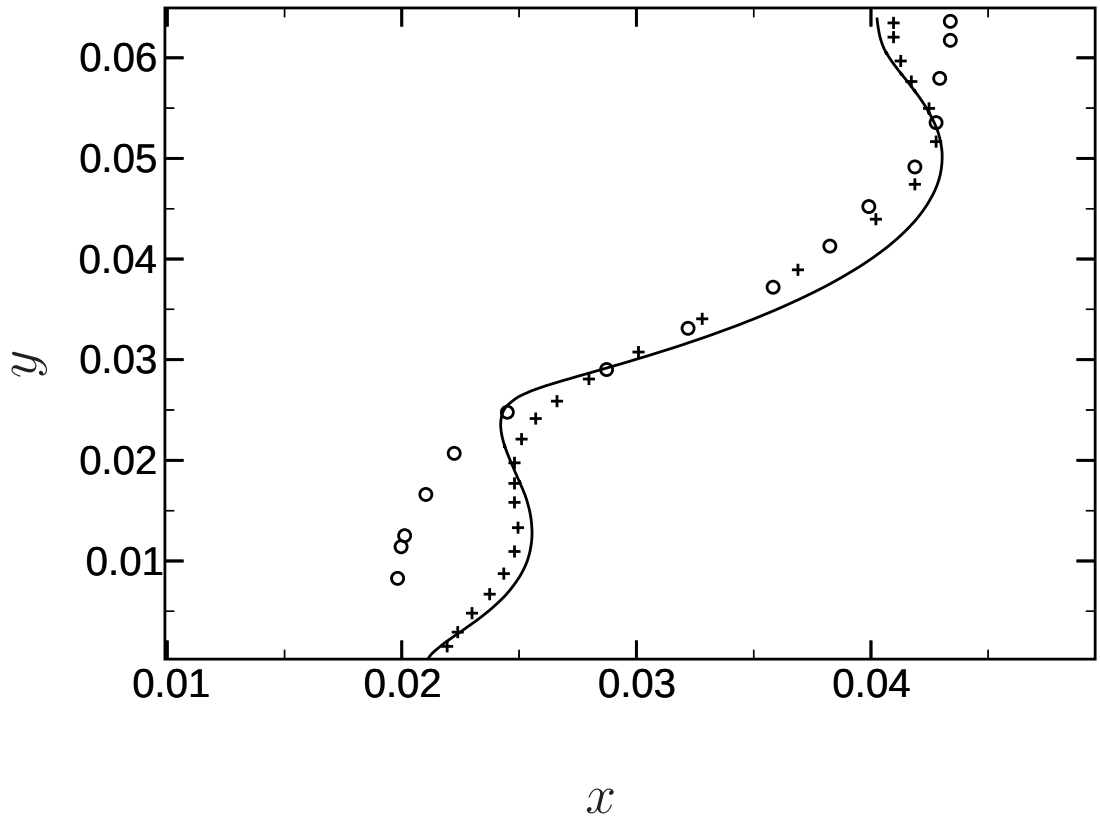

Figure 4.13: Wall positions at 600 seconds for the present simulation (——), [15] (∘ ∘ ∘), and [2] (+ + +).

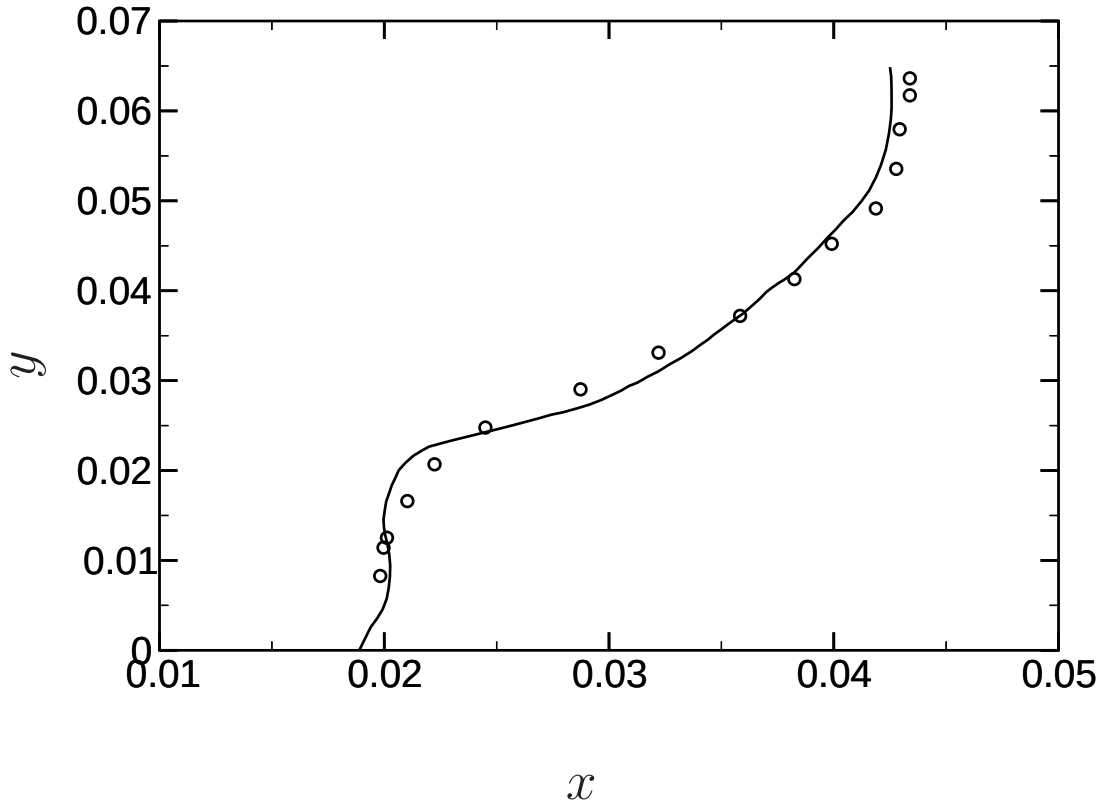

Figure 4.14: Wall positions at 600 seconds for the present study with velocity stalling (——), and [1] (○ ○ ○).

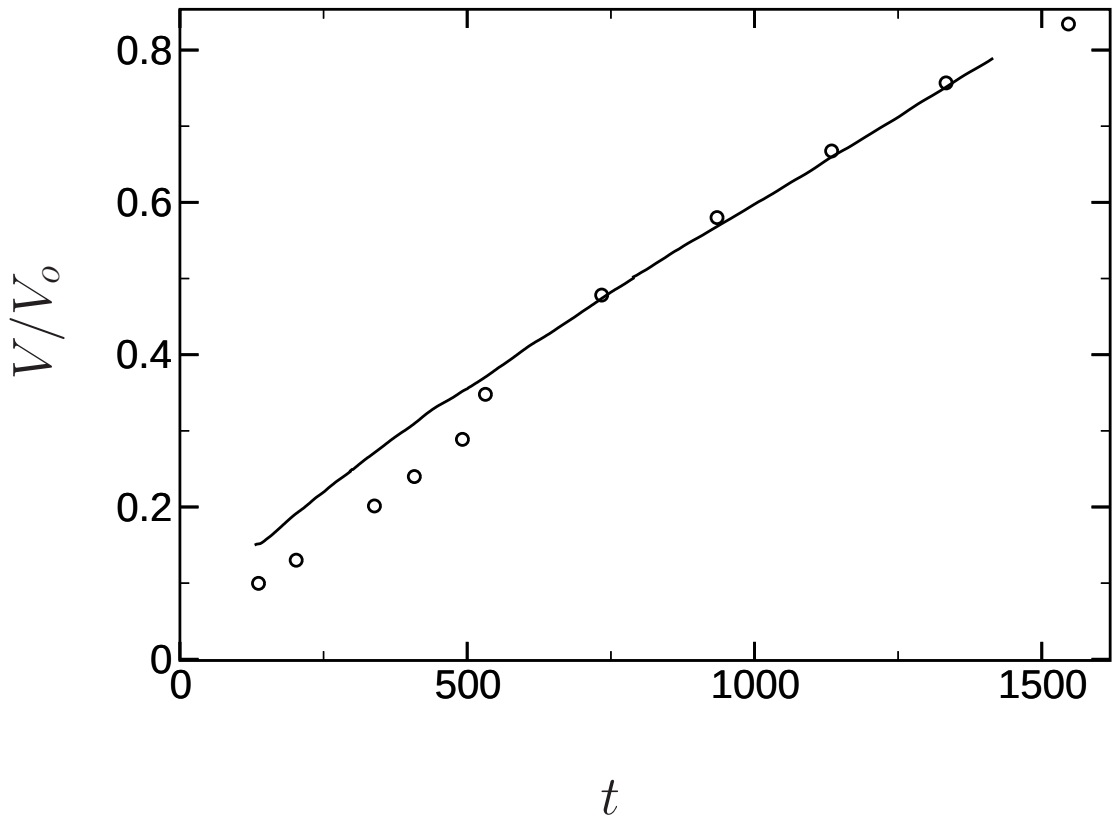

Figure 4.15: The liquid fraction, V/V_o of the present study (——), and [1] (o o o).

between the experimental interface and numerical experiment interface.

The third validation of the ablation algorithm is done by comparing the solid mass loss (as in the amount of the solid melted), through the volume fraction (current over initial volume V/V_o), which is compared with results from [1]. Again, a direct comparison is not possible with the resolution of the data available but the mass loss from the present study is within $\pm 5\%$ of the experimental data at any given time. The discrepancy can be explained by the pour-out experimental method previously mentioned, variation in the experimental ambient temperature, and measurements.

The strong correlation between the interfaces shown in figure 4.13-4.14 provide results that show both the thermal and momentum IB yield results that show a strong correlation between the physics of the experimental studies from [15] and [1]. Along with

the strong correlation of the mass loss results shown in figure 4.15 this shows that the CHTIB and ablation algorithms are effectively reproducing the physical experiment, within acceptable error bounds. These results, along with the results from section 4.2.1, provide sufficient confidence that the ablation algorithm is also satisfactorily mass conserving.

Chapter 5

ISOTHERMAL EXPANDING TURBULENT CHANNEL

5.1 Turbulence in Wall Bounded Flows

5.1.1 The General Dynamics of Turbulence

Before reviewing the results produced from the expanding channel system, a brief review of wall bounded flow dynamics is necessary as well as a brief definition of turbulence. Turbulent flow is described as a flow with a chaotic velocity field comprised of a steady, average flow field with an underlying fluctuating or random and chaotic velocity field. Some flows, specifically some complex two dimensional ones such as Rayleigh-Bérnard convection (see appendix C), may *look* turbulent but do not contain a fluctuating velocity field, only an average one. In the absence of the fluctuating velocity component, the flow is, by definition, laminar. One of the more commonly studied types of flows, and the specific kind of flow of interest to this work, are turbulent wall-bounded flows i.e. channels, boundary layers, and blunt objects in cross flow. DNS of geometries much more complicated than these are

usually not possible becauses of the phenomena occurring near the boundaries in turbulent wall-bounded flow. The energy exchange between the core flow and boundaries, cause many issues in the DNS of even very simple flows [28]. One of the most frequently studied of these wall bounded flows are turbulent, periodic, channels which are used in the turbulent sections of this work. Channels are simple, canonical flows to both study and simulate, making them a typical benchmark for new numerical algorithms or simulation techniques.

Turbulent channel flow, periodic in two directions (see figure 5.7), is typically characterized by a qualitative, "know-it-when-you-see-it" association of large and small self-similar "whorls" (defined by Richardson 1920 [113]), which is a structured dynamics of vortices, and eddies (visualized with Q from [114] and [115] and explained in section 5.3.1). These are typically clustered near the walls as in figure 5.11. While an in-depth description of eddies and vortices follows in section 5.3.1, it is sufficient to say here that they are coherent structures, with a wide range of scales, that are the energy containing, and dissipating, turbulent structures. Here the scales refer to the different size structures where fluctuating quantities exist extending from the smallest scaling parameter, typically defined by energy dissipation and viscosity, and the largest geometric scale of the flow [116]. A more quantitative requirement for the establishment of turbulent flow is shown in figures 5.8a and 5.8b, which are valid over a wide range of $Re_{u_\tau} = 100 \sim 600$ and $Re_{L_y/2} = 2000 \sim 12000$ based on channel half-width and the mean velocity [30]. Outside of the range of $Re_{u_\tau} = 100 \sim 600$ the kinematic and energy statistics, while still looking very similar to those in figure 5.8 begin to have maxima and minima that move much closer to the wall [117] and have higher magnitudes of fluctuation, [118], than seen in the current study.

The dynamics inside periodic channels can be separated into four semi-distinct areas that show consistent averages, and fluctuations in kinematic and energy statistics. The different layers occur at various separations of scales in a turbulent flow. The separate

layers in a wall bounded flow, then, are near the wall, $y^+ < 5$, the viscous sublayer, at $5 \leq y^+ \leq 50$ is the buffer layer, $50 < y^+ < 450$ is the logarithmic layer, and $450 < y^+$ is the core flow or outer region. These are not hard and fast regions and they will fluctuate with the normal cycles found in turbulent flow but they are typically used as reference points when explaining the structure of a turbulent flow, and its general structure. The need to distinguish different layers in a wall bounded flow come from the anisotropic and inhomogeneous nature of wall bounded flow which segregates regions with distinct scaling of the energy containing eddies.

The layers of a wall-bounded turbulent flow are broad representations of different ranges of pertinent momentum and energy scales inside a turbulent flow. This makes turbulence a multiscale phenomenon with energy residing in different size eddies, or vortices, whose energy cannot be dissipated until the limiting small scale has the energy from larger scales transferred to it. In turbulent flow this was first described by Kolmorgorov in 1941 [119]. The description sets up an energy hierarchy between large and small structures inside turbulent flows. With the larger structures at the integral scale, $\mathscr{I}$,

$$\ell_{\mathscr{I}} \sim \frac{L_y}{2} \quad \mathrm{u}_{\mathscr{I}} \sim U_c \quad t_{\mathscr{I}} = \frac{\ell_{\mathscr{I}}}{\mathrm{u}_{\mathscr{I}}}, \tag{5.1}$$

or the largest length of physical relevance, carrying more energy that is transferred to the smaller and smaller scales as the larger structures are broken up by the chaotic velocity field, mean shear or high mean velocity near the core. The kinetic energy in the largest structures, at the integral scale, is transferred down to the smallest scale, the Kolmorgorov micro-scales,

$$\ell_{\mathrm{K}} \sim \left(\frac{\nu^3}{\varepsilon}\right)^{\frac{1}{4}} \quad \mathrm{v}_{\mathrm{K}} \sim (\nu\varepsilon)^{\frac{1}{4}} \quad t_{\mathrm{K}} \sim \left(\frac{\nu}{\varepsilon}\right)^{\frac{1}{4}}, \tag{5.2}$$

at which time the energy at the micro-scale is dissipated through molecular, or viscous dissipation, shown in figure 5.1 as a procession of eddy break up [120], or energy cascade. Equation 5.2 is linked to equation 5.1 through,

$$\frac{\ell_{\mathscr{I}}}{\ell_{\mathrm{K}}} \sim Re_{\mathscr{I}}^{\frac{3}{4}} \quad \frac{t_{\mathscr{I}}}{t_{\mathrm{K}}} = Re_{\mathscr{I}}^{\frac{1}{2}} \quad \frac{\mathrm{u}_{\mathscr{I}}}{\mathrm{v}_{\mathrm{K}}} = Re_{\mathscr{I}}^{\frac{1}{2}}, \tag{5.3}$$

and the centerline Reynolds number, $Re_{U_c} = U_c \frac{L_y}{2}/\nu$. Using a channel as an example the largest length scale would be $= L_y/2$ with $\overline{u}_L y/2$ and the smallest ℓ and u_τ. Equations 5.1 and 5.2 comes from the rate of energy transfer, Π, from the largest to the smallest scales.

$$\Pi \sim \frac{u^2}{\ell} \sim \nu S_{ij} S_{ij} \sim \nu \left(\frac{\mathrm{v}^2}{\ell_\mathrm{K}} \right) \tag{5.4}$$

A more in-depth look at equation 5.2 shows that the viscosity does not directly dissipate energy; rather, it describes the scale at which energy is no longer dissipated through turbulent motion.

Recent work has shown that the energy cascade model set forward by Kolmorgorov and Richardson is actually more granular than first thought. While it was understood that the energy cascade is global, it is also fractal in nature occurring at every size of scale down to the micro-scales, at every level of a wall bounded flow. This implies that the majority of the TKE produced at any distance from the wall would have energy containing eddies at least as large as the distance from the wall to the micro-scale where the energy is dissipated. Meaning that most of the energy at any given distance from the wall will also be dissipated at that distance as well [121].

5.1.1.1 Viscous Sublayer and Near Wall Region

The viscous sublayer (also know as the near-wall region), and below, is the area of the largest average shear in the flow and is considered to be shear-dominated (inertial effects can be neglected). Most structures are of the Kolmorgorov scale or smaller (viscous scale). The smallest scales are associated with the 'mopping up' of energy coming down the energy cascade in figure 5.1. Most of the dissipation of turbulent energy is done in the upper layers leaving $\approx 5\%$ to be dissipated in the near wall region where the kinetic energy is dissipated as heat generated at scales smaller, and equal to, the Kolmorgorov scale (excluding any sort of rigorous thermodynamic considerations).

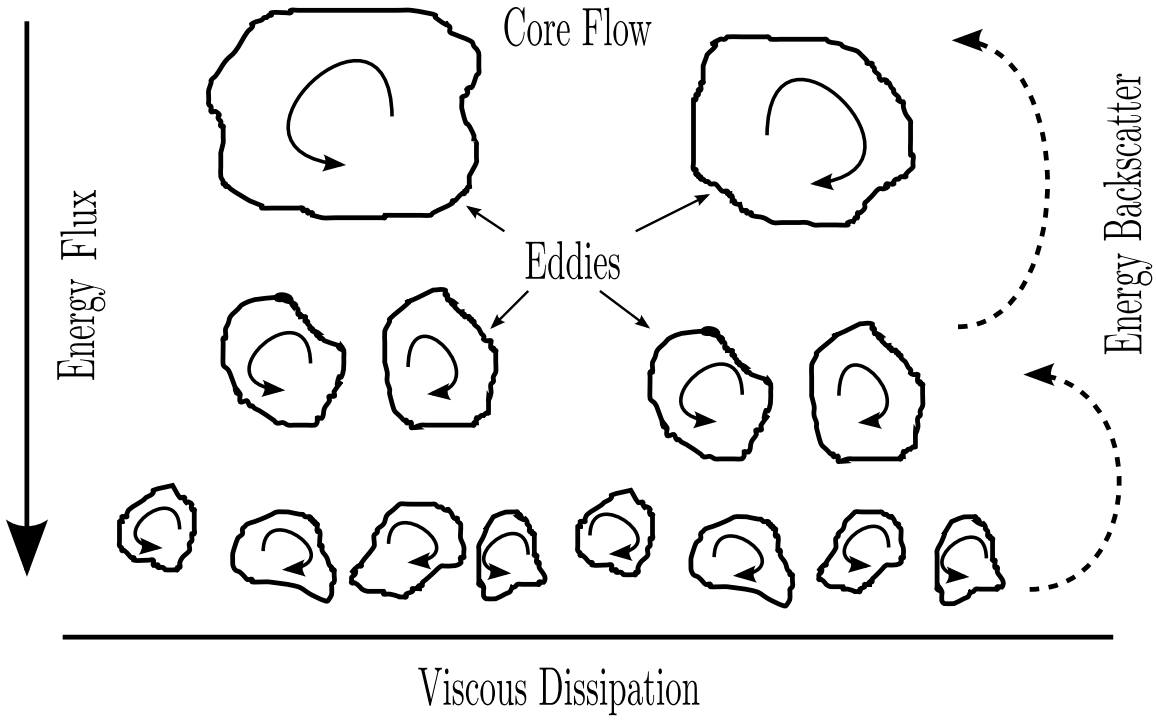

Figure 5.1: A schematic of the Kolmorgorov energy cascade taken from Frisch 1995 [16].

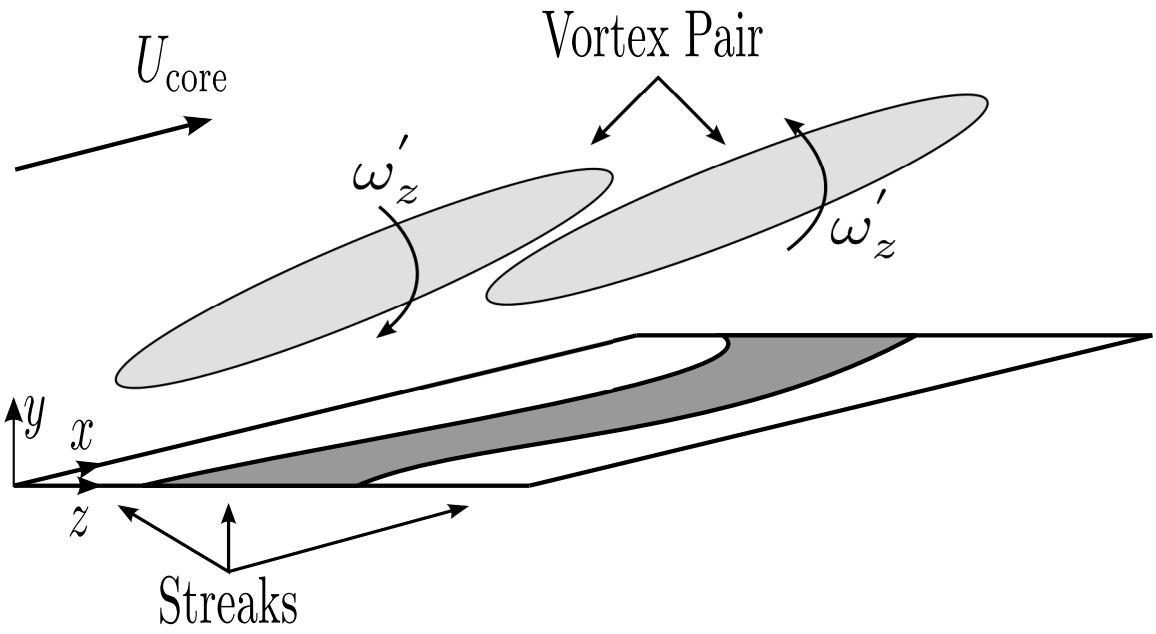

Figure 5.2: The general structure of high and low velocity streaks with its flanking vortices. Note here that the structure of the streaks is three dimensional but the projection of the velocity is shown below the vortices.

5.1.1.2 The Buffer Layer

The buffer layer in wall bounded flows is typically. The area of the greatest turbulent intensity (see figure 5.8) and is a layer in turbulent flows where both the viscous and inertial effects need to be accounted for. It is also considered to be in the "near wall" region but is not a part of the viscous sublayer. The general structure of the velocity field in the buffer region is of high and low velocity, streamwise (u) streaks superimposed on the mean shear. They were first identified, experimentally, by Klebanoff *et al.* 1962 [122], and linked to turbulent cycles by Kline *et al.* 1967 [123], with their behavior qualitatively described by Kim *et al.* 1971 [124]. These streaks of high and low streamwise velocity are directly related to the $u^{'}$ as the average velocity is uniform, and consistently scale linearly with $y^{+} \sim u^{+}$. Both streaks and average velocity uniformity are shown, extensively, in both experimental, [125] and numerical studies, [126], [127], and [128]. The streaks are generated along with quasi-streamwise vortices, defined by their coherence in time and their ability to pump high speed flow the wall and slow speed fluid away from the wall. The velocity footprint on the isoplanes, cut parallel to the streamwise flow, located at $y^{+} \approx 20$ and $y^{+} \approx 5$ can be seen in figures 5.3 and 5.4 showing the high and low velocity streaks of $u^{'}$ at different heights. A cross section of the set of streaks is also shown in figure 5.6b. It is also fairly well understood that there are associated pairs of flanking vortices linked to each set of streaks, [129], as shown in figure 5.6a. This is not necessarily always the case (though it is so on average): sometimes only one vortex is paired with a streak, sometimes there are several [130], but this seems to be part of the general dynamics of the streak-vorticity structure, [131]. Although the streaks can be seen in the near wall region, the vortices accompanying them mostly reside in the upper layers, specifically the logarithmic and buffer layers.

The importance of the streak and vortex structures and their relationship to the onset of shear turbulence is well defined, though this process is not fully understood beyond a cause and effect type relationship. The general structure of the streak-vortex, though

Figure 5.3: High and low $u^{'}$ streaks at $y^{+} \approx 20$ with the lighter values showing larger $u^{'}$

Figure 5.4: High and low $u^{'}$ streaks at $y^{+} \approx 5$ with the lighter values showing larger $u^{'}$

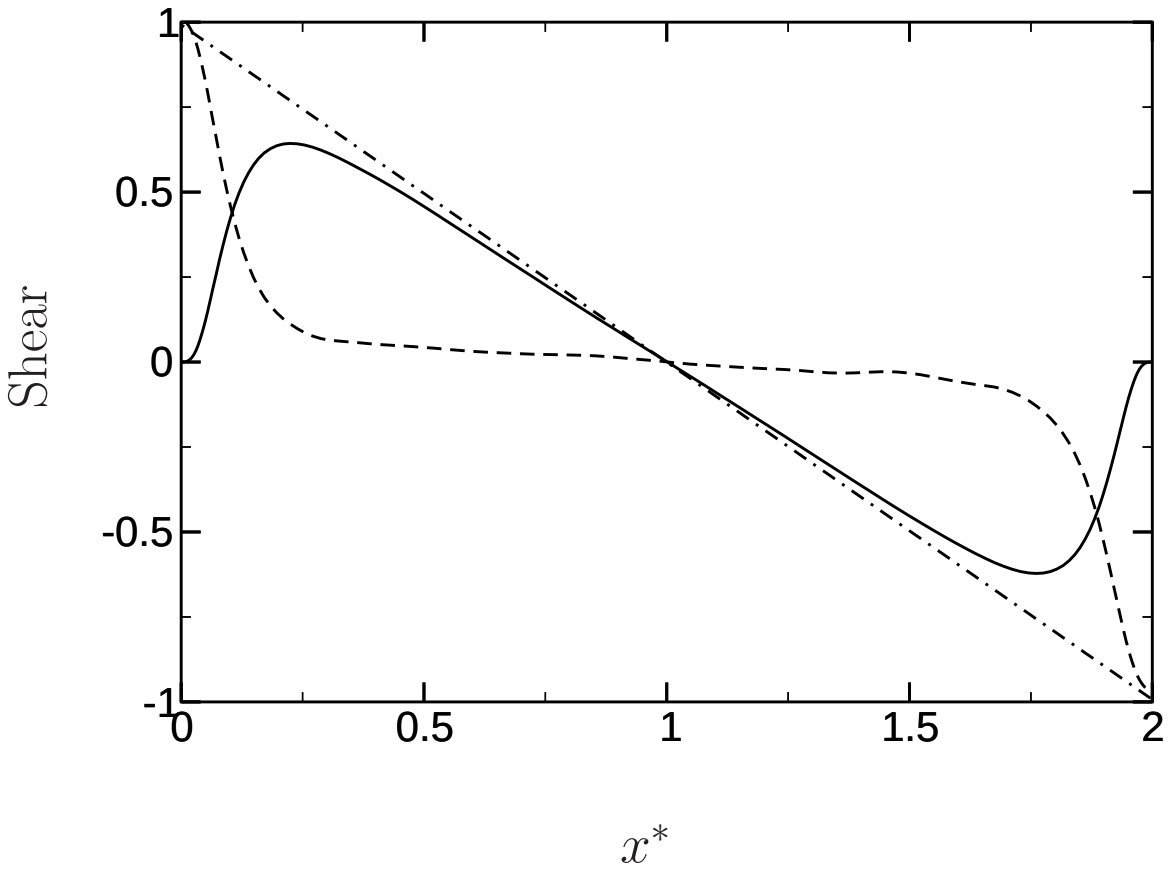

Figure 5.5: The average shear, $(- - -)\ d\overline{u}/dy$**, reynolds shear stress,** $(——)-u'v'$ **and the total shear stress,**$(- \cdot -)\ d\overline{u}/dy - u'v'$

relatively straight forward in the minimal boxes described by [130], look chaotic globally, until statistics are used to find the underlying organization. The streaks are arrayed in an irregular, alternating, sinuous structure, averagely spaced in the streamwise direction at $x^+ \approx 1000$ and in the spanwise direction at $z^+ \approx 100$ [132]. The quasi-steamwise vortices associated with each streak are angled away from the wall but stay in the near wall region for a distance of $x^+ \approx 400$. As the vortices lift off and move into the core of the flow they break up and become disorganized and the vorticity field begins to look more like homogenous turbulence [133], [134].

Establishing a relationship between the vortices is the next logical step in the pro-

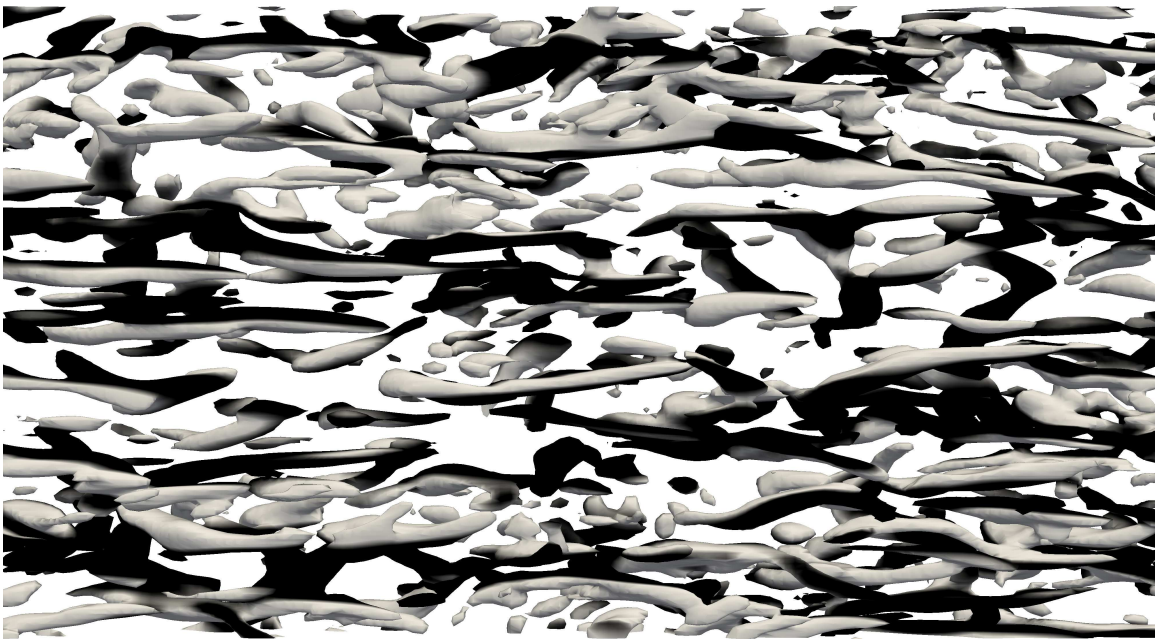

(a)

(b)

Figure 5.6: a.) $u^{'}$ **streaks superimposed over vortices shown with** $Q = 150$**, and the lighter values showing larger** $u^{'}$**. The view is from above perpendicular to the** y **axis b.)** $u^{'}$ **Streaks shown at a cross section at** $L_y/2$ **with the lighter values showing larger** $u^{'}$**.**

gression of their coherent description. It was first assumed that the vortices were generated by the spatial instability of the streaks [135], while the streaks were caused by the transport of the mean of the velocity gradient near the wall by the circulation of the vortices. This has been established as the cyclical relationship of near wall turbulence by both analytical [136],[137] and numerical [138], [139] analyses. This start is good but it does not define a beginning, or main initiator of the turbulent cycle. Jiménez *et al.* 1999 [140] described this cycle and showed that a disruption of the streaks, for $y^+ \approx 10 - 60$, will cause the vortices to eventually weaken or die away. The same study also shows that although the vortices pull energy from the core of the flow, and that they generate the steaks weakening the vortices only weakly disrupts the coherence of the turbulent flow. The final finding of the 1999 Jiménez study showed that when energy was cut off from the core flow to the buffer layer, it remained turbulent with kinematic and energy statistics changing little from a normal wall-bounded flow. This result showed that the buffer layer is autonomous from the rest of the flow and the turbulence inside is self-sustaining.

5.1.1.3 The Logarithmic and Outer Layers

The logarithmic layer begins above the buffer layer and marks the beginning of the region where the velocity scales directly with the distance from the wall and the importance of viscosity is eclipsed by inertial forces. This makes the logarithmic layer the transition between scaling associated with the Kolmorgorov length scales to the integral length scales. Assuming that the only important scaling parameter was, in fact, the distance from the wall, y, Townsend 1980 [141] states that the velocity will follow,

$$\overline{u}^+ = \frac{1}{k_o}\ln\left(y^+\right) + A, \tag{5.5}$$

where the $k_o \approx 0.3 - 0.4$ is Kármán's constant, and is approximately universal [142], and A depends on the near wall region of the flow being considered. Equation 5.5 is the "log-law of the wall" and comes form the self similar solution of the near wall velocity where the

mean shear, $d\overline{u}/dy$, is assumed to be equal to the first term of a high order asymptotic expansion, $\int \left(\partial\overline{u^+}/\dot{\mathrm{y}}^+\right) dy^+ = \int 1/k_o y^+ dy^+$ [143] and [144]. This is only valid in the overlap region where the dynamics scale linearly with y and the energy containing eddies are largely inertial, and inviscid.

This can also be another seemingly misleading portion of the description of wall bounded turbulent flow. Though equation 5.5 is called the "log-law of the wall" it is not representative of the logarithmic layer. The layer is considered logarithmic only when all scales are proportional to y [134]. This will not occur without Re of at least 2000 as in Del Alamo *et al.* 2004 [145] which would be an order of magnitude greater than the channels simulated in this work. This means that because Re_{u_τ} is only 125 there is no appreciable logarithmic layer in this study. The log-law of the wall is indicative of the upper portion of the buffer layer where the inertial scales are prevalent, and where equation 5.5 is no longer valid. Close to the wall, the viscous scales are the prevalent energy containing and dissipating scale, seen in figure 5.10 for the IC of the expanding channel. This overlap of energetic and dissipative scales is arguably one of the most important properties of a wall-bounded flow. Though it is geometrically negligible when compared to the core flow, a majority of the velocity loss across all the layers resides in the near wall and buffer layer region [144]. This causes the near wall region to possess the maximum of the average shear from which the turbulent velocity fluctuations arise.

The purpose of simulating a low Re, which is turbulent but not a full wall-bounded flow, is to assess the initial effect that wall perturbations will have on the viscous and buffer layers alone, thereby reducing the dynamic and structure variability. This assumption is valid as the logarithmic layer is present it is decoupled from the rest of the flow shown by Lozano-Durán et. al 2014 [146]. The buffer layer is also decoupled from the rest of the flow, as Jiménez *et. al* 1999 [140] showed that when energy was not supplied by core flow the buffer layer still produced autonomous cycles of turbulent sweeps and ejections (the

down and upwash from vortices which produce the buffer layer streaks). The computational limitations are also a factor in the simulation of very large Re channels even in 2006 Hoyas and Jiménez [147] note that the simulation of a channel at $Re_{u_\tau} = 2000$ produced 25TB of data, while showing the presence of a logarithmic layer.

The outer and core flow will not be discussed in detail in this work outside of their relationship to the near wall region. That relationship is minimal, and because the mean velocity of the outer region breaks up the vortices and energy carrying eddies. The logarithmic layer is of less importance than the near wall regions to the establishment of physical models and theory of the more chaotic and turbulent regions in a wall bounded flow.

5.2 Expanding Channel Experimental Set Up

To better study the effects of non-equilibrium on turbulent flow and its coherent structures, a well studied flow at a statistical steady state is perturbed. For most of the work presented here, the boundary conditions for momentum and scalar transport, because of the possibility of asymmetry and their dynamic nature, are incapable of sustaining statistical equilibrium in turbulent flows. The flow used here is a channel flow that has reached sustained turbulent equilibrium. The channel is non-dimensionalized by the skin friction velocity, $u_\tau = \mu \partial u / \partial y$, and the channel half width, $L_y/2$ giving the non-dimensional groups in equation 5.8. Substituting the dimensionless groups into equations 2.1-2.2 give the dimensionless, incompressible, low Mach number, forms,

$$\boldsymbol{\nabla} \cdot \mathbf{u} = 0 \tag{5.6}$$

and,

$$\partial_t (\mathbf{u}) + \boldsymbol{\nabla} \cdot (\mathbf{u} \otimes \mathbf{u}) = -\nabla P + \frac{1}{Re} \boldsymbol{\nabla} \cdot \boldsymbol{\nabla} \mathbf{u} \tag{5.7}$$

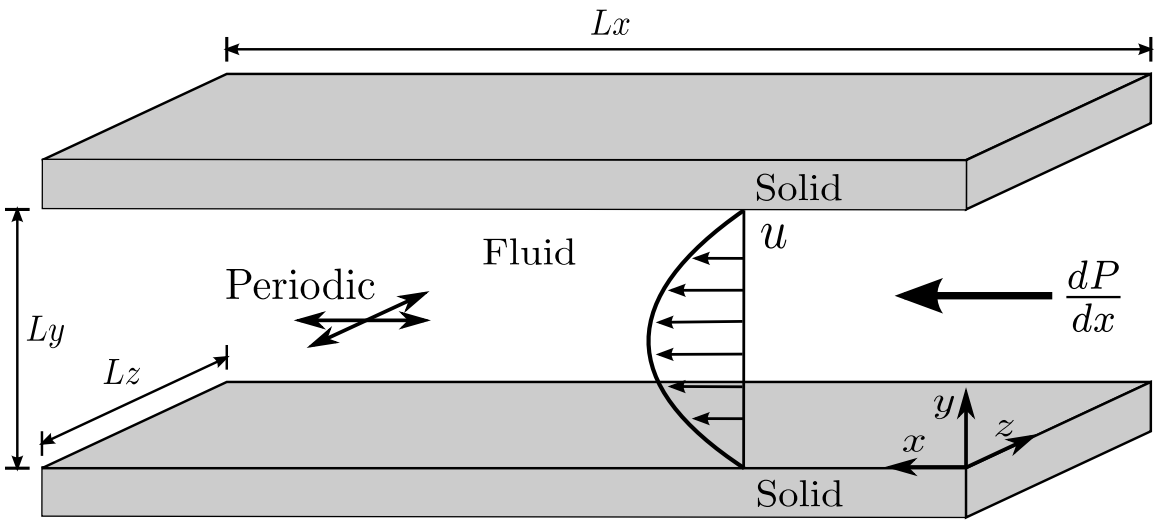

Figure 5.7: The dimensions of the IC channel showing periodicity in x and z. L_x,L_y and L_z are large enough to allow the formation of multiple large turbulent structures shown by Jiménez et al. [17].

respectively. The dimensionless groups used in equations 5.6-5.7 are

$$\mathbf{u}^* = \mathbf{u}\left[\frac{1}{u_\tau}\right] \qquad \mathbf{x}^* = \mathbf{x}\left[\frac{1}{L_y/2}\right] \qquad t^* = t\left[\frac{u_\tau}{L_y/2}\right] \qquad P^* = P\left[\frac{1}{\rho_f u_\tau^2}\right] \qquad Re = \frac{u_\tau L_y}{2\nu} \tag{5.8}$$

omitting the $*$ in the final transport equations. The channel dimensions are $L_x = 10$, $L_y = 2$, $L_z = 5$, the pressure gradient, $dP/dx = 1$, is constant, and periodicity is held in the x and z directions, as is shown in figure 5.7. The initial conditions in the channel are at a statistical steady state for $Re_{u_\tau} = 125$, as shown in figure 5.8 for the root mean square (*rms*) velocities and TKE budget, concurrent with the statistics in, [29] and [148], and the budgets in [149] and [28], respectively.

A "statistical steady state or statistical equilibrium" (used interchangeably) are when equilibrium is reached between the production of kinetic energy, from the driving force of the flow, and the dissipation of turbulent energy at the wall (figure 5.8b) and the total shear, $-\overline{u'v'} + (1/Re_{u_\tau})\partial\overline{u}/\partial y$ is linear in the wall normal direction (see figure 5.5), [150]. Production and dissipation of turbulent kinetic energy are two terms in the turbulent

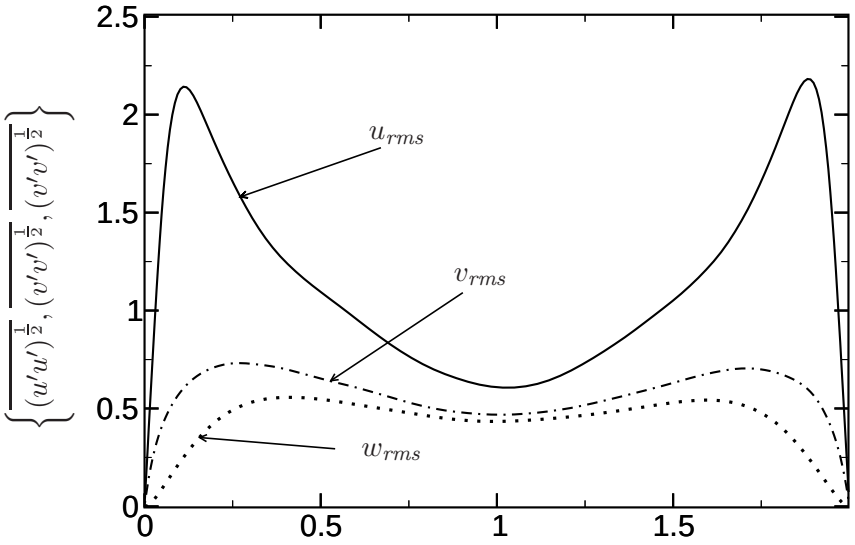

(a)

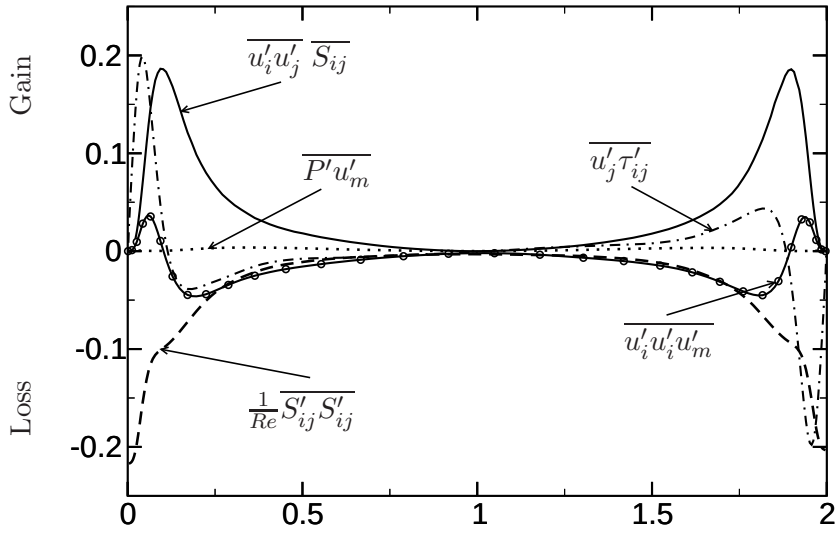

(b)

Figure 5.8: a.) Time averaged *rms* velocities, $\overline{(u'u')^{\frac{1}{2}}}$, $\overline{(v'v')^{\frac{1}{2}}}$, $\overline{(w'w')^{\frac{1}{2}}}$, and b.) the TKE budget, equation 5.10, for the expanding channel.

kinetic energy equation, or budget in two dimensions is

$$\frac{\partial k}{\partial t} = \frac{\partial}{\partial x_m}\left[-\overline{P' u'_m} + \overline{u'_j \tau'_{ij}} - \frac{1}{2}\overline{u'_i u'_i u'_m}\right] - \overline{u'_i u'_j}\ \overline{S_{ij}} - \frac{1}{Re}\overline{S'_{ij} S'_{ij}}, \tag{5.9}$$

where $k = \frac{1}{2}\overline{u'_i u'_i}$ is the mean fluctuating turbulent kinetic energy, $\overline{\tau'_{ij}}$ is the mean fluctuating viscous stresses, $S'_{ij} = \frac{1}{2}(\partial u'_i/\partial x_j + \partial u'_j/\partial x_i)$ is the symmetric portion of the strain rate tensor, and apostrophes designate fluctuating quantities. The fluctuating quantities in equation 5.9 come from a standard Reynolds decomposition of a variable into the fluctuating and average terms, $\mathbf{u} = \overline{\mathbf{u}} + \mathbf{u}'$. The various terms on the RHS of equation 5.9 are also know as

$$\begin{aligned}
-\overline{P' u'_m} \quad &\rightarrow \quad \text{pressure transport} \\
\overline{u'_j \tau'_{ij}} = \nu \overline{u'_j S'_{ij}} \quad &\rightarrow \quad \text{viscous diffusion} \\
-\overline{u'_i u'_i u'_m} \quad &\rightarrow \quad \text{turbulent convection} \\
-\overline{u'_i u'_j}\ \overline{S_{ij}} = \mathcal{P} \quad &\rightarrow \quad \text{generation or turbulent production term} \\
\nu \overline{S'_{ij} S'_{ij}} = \varepsilon \quad &\rightarrow \quad \text{turbulent dissipation}
\end{aligned} \tag{5.10}$$

and these will be used to discuss the finding in the following sections using Einstein notation to keep the definitions more notationally compact and straightforward.

The terms $\mathcal{P}$ and ε are two of the important terms in turbulent modeling where the "turbulent" in front of both will be omitted here. For instance the $k - \varepsilon$ turbulence model specifically uses the average dissipation to account for energy dissipation in simple flows. LES and RANS are more complex closure models, but they too depend on the average dissipation rate, or the Reynolds-stresses or both, and that is a priori data. Even with intensive modeling and filtering procedures (the latter for LES) without a prior knowledge of the flow and its statistical behavior from DNS or physical experiments the results from turbulent models can be thrown off by even slightly unsteady or non-equilibrium physics, and flow behavior, which is why DNS is used in this work.

The channel was then perturbed, by expansion, as shown in figure 5.9, at a rate that is a function the skin friction velocity of the, $\mathbf{v}_\Gamma(u_\tau)$, and only in the wall normal

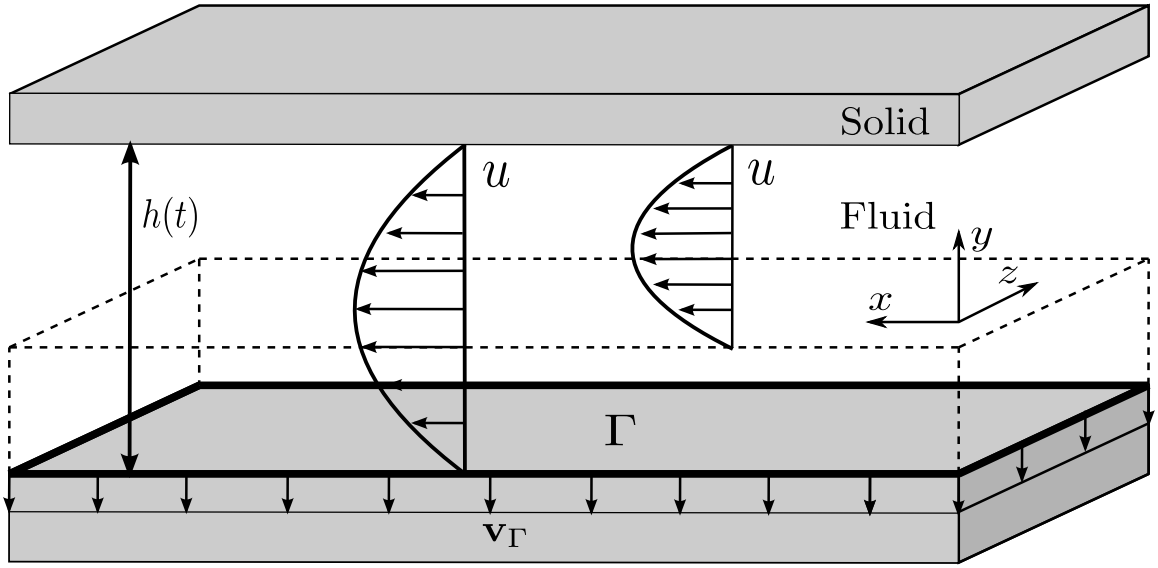

Figure 5.9: The expanding channel with the $(- - -)$ showing the channel expansion.

direction; $\mathrm{v}_\Gamma \sim u_\tau \rightarrow \mathrm{v}_\Gamma = Au_\tau \hat{\boldsymbol{\jmath}}$ where $A = \{4, 2, 1, 0.5, 0.2, 0.1, 0.01\}$. The velocity boundary fractions were chosen to give a good representation of all possible scales and physics that may be present, i.e. $\mathrm{v}_\Gamma \sim 0.2 \sim (\nu/\varepsilon)^{\frac{1}{4}}$ is the Kolmogorov velocity micro-scale and a $\mathrm{v}_\Gamma \sim u_\tau$ is on the scale with the skin friction velocity. The initial wall conditions are also shown in figure 5.10 on both the IB and non-IB side of the channel (as are all IC in this section) for the average longitudinal velocity. The slight deviation from linearity in the viscous sublayer portion of figure 5.10b is due to the fact that figure 5.10 shows only the initial velocity field and is a snapshot (not averaged in time but averaged in space), and a small deviation in $\overline{u}^+$ from $\overline{u}^+ = y^+$ is expected.

As the boundary moves the grid resolution in the exposed cavity is kept at $\Delta y^+_{\min} = 0.3$, consistent with $Re_{u_\tau} = 125$, and below the spacing of $\Delta y^+ \leq 6.25$ from [29]. This grid spacing, $\Delta y^+_{\min} = 0.3$, is also below the the Kolmogorov scale of $\Delta y^+ \sim 2$ calculated from $\partial_t \overline{\varepsilon}$ in [151] and [152], near the wall. With the values of $\mathrm{v}_\Gamma \geq (\nu\varepsilon)^{\frac{1}{4}}$ the dissipation was seen to decrease, reducing the Kolmogorov micro-scale, leading to a decrease in the necessary

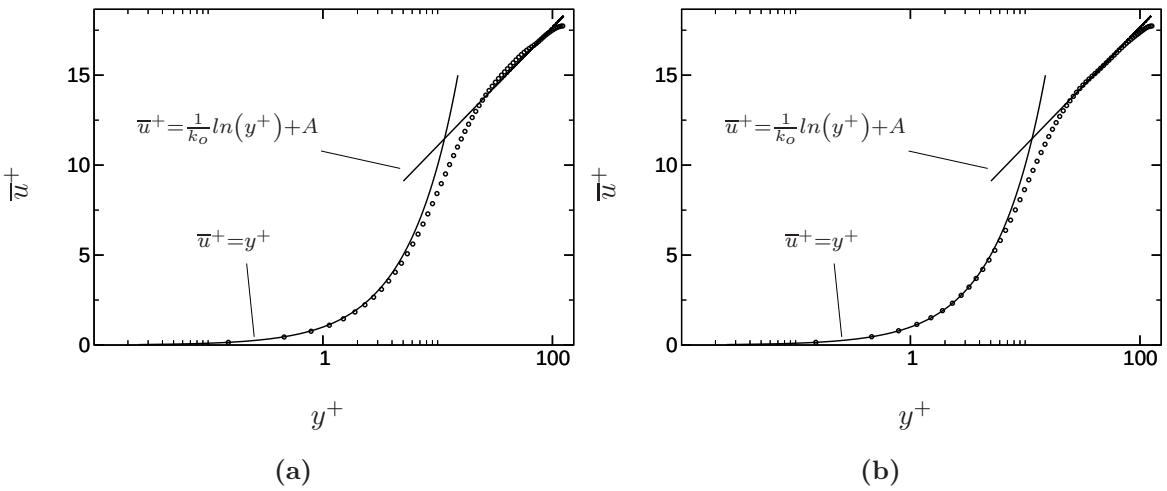

Figure 5.10: a.) The normal, no-slip channel side, near wall velocity. b.) The IB side near wall velocity. For both plots $\{—\}$ is $\overline{u}^+ = y^+$ for $y^+ \leq 5$ and is $\overline{u}^+ = \frac{1}{k_o}\ln(y^+) + A$ for $y^+ > 5$, $A \approx 4.5$ and $k_o \approx 0.35$ is Kármán's constant, and $\{\circ\circ\circ\}$ is u^+ from the simulation.

resolution in the exposed cavity.

At the full expansion of the channel the new half-width will be $L_y/2 = 1.125$, and keeping the viscosity at $\nu = 0.008$ gives the new Reynolds number, $Re_{u_\tau} = 149$. As $Re_{final} > Re_{initial}$, the spatial resolution must also satisfy the larger, final Re. Using $Re_{u_\tau} = 149$ gives $\Delta y^+_{\min} = 0.35$, which is still well below both the Kolmogorov scaling and the necessary minimum resolution near the wall shown in [151] and [152], mentioned previously.

The results from this study are used to determine the non-linear, non-equilibrium, and unsteady flow effects on typical standards of turbulence study: including the TKE budget; and the development of coherent structures; and their reaction to an applied, constant wall velocity. Data from section 5.3.1 will then be used to help elucidate the physics of the ablative channel in section 6.1.

5.3 Results

5.3.1 Flow Topology and Coherent Structures

Vortex identification is a much-studied field but one in which much of the work can be influenced by the researcher's assigned thresholds, or identification criteria, to identify a space where vortex may have formed. This can be difficult because a vortex is a phenomenon that does not have a precise definition, only a set of principles that it must adhere too [153]:

(I) The vorticity, $\boldsymbol{\omega}$, in a vortex must be strong enough to move fluid perpendicular to the main core flow.

(II) The vortex should last longer than local turnover tim.,

(III) They should be chaotic and unpredictable.

Some other caveats can be added to I-III. The first is that it can be expected that if a vortex has been identified it would have increasing $\boldsymbol{\omega}$ as the center of the vortex is reached form the outer surface of the vortex. Second, the maximum pressure of a vortex occurs on the outside of the vortex but there does not necessarily need to be a minimum of pressure inside the vortex [115].

Mathematically, vortex envelopes (places where ideally a vortex should be) are shown in this work with the Q criteria equation 5.11. Other metrics can be used to show vortex structure in complex flow, such as vorticity or pressure isosurfaces but they suffer from drawbacks. Isosurfaces of vorticity are more readily used in unbounded flows because near a no-slip boundary the shear tends to be much larger than the local vortical motion near the wall [154]. This makes it difficult to set an isosurface threshold to see vortices near a boundary and those in the flow as well. Pressure isosurfaces yield much better global vortex envelope eduction, as opposed to vorticity isosurfaces, but they tend to "smear out"

in areas populated by multiple vortices because the pressure isosurface used to define the edge of a vortex can be affected by the pressure of surrounding vortices as seen in [154] and [155]. For these reasons Q will be used as the only vortex eduction criteria as it encompasses both pressure and vorticity (again, see equation 5.11) into a much more sophisticated vortex eduction scheme.

The initial velocity conditions are shown in figure 5.11 with coherent structures shown for the isosurfaces of the Q criteria and these are

$$Q = \frac{1}{2}\left(\Omega_{ij}\Omega_{ij} - S_{ij}S_{ij}\right) = \frac{1}{4}\left(\boldsymbol{\omega}^2 - 2S_{ij}S_{ij}\right) = \frac{1}{2\rho}\boldsymbol{\nabla}\cdot\boldsymbol{\nabla}P, \tag{5.11}$$

where

$$S_{ij} = \frac{1}{2}\left(\frac{\partial u_i}{\partial x_j} + \frac{\partial u_j}{\partial x_i}\right) \quad \text{and} \quad \Omega_{ij} = \frac{1}{2}\left(\frac{\partial u_i}{\partial x_j} - \frac{\partial u_j}{\partial x_i}\right) \tag{5.12}$$

Q is the second invariant of the velocity gradient tensor $\boldsymbol{\nabla}\mathbf{u}$ and the balance between strain and rotation rate in the flow, Ω_{ij} is the rotation rate, and S_{ij} is the strain rate. Alternately, the rotation rate and strain rate tensors in Q are also the anti-symmetric and symmetric parts of $\boldsymbol{\nabla}\mathbf{u}$. Thus, $Q > 0$ is a measure of the areas of the flow where the strain rate is smaller than the rotation rate, [156], making them a quantitative visual representation of a vortex envelop. As well as showing Q, the lighter contours in all of the figures in this section denote higher velocities, and black represents $\mathbf{u} = 0$.

In figures 5.15 through 5.18 it is apparent that the figures showing $\mathrm{v}_\Gamma \geq 0.5u_\tau$ have a lack of semi-streamwise vorticities in the cavity left by the receding wall, and that $u_{\text{cavity}} << \overline{u}_{\text{core}}$. While $0.1u_\tau \geq \mathrm{v}_\Gamma \leq 0.5u_\tau$ show more pronounced vortex activity in the space left by the wall, while the approximate range, $0.1u_\tau \leq \mathrm{v}_\Gamma$, does not vary from, qualitatively, the ICs in figure 5.11 i.e. it looks like the Q from a turbulent channel without a receding wall. Initially, at the 10% level the shear free layer is small and not evident until wall units are used to scale the y axis, where it is then seen, up to the edge of the buffer layer. As the wall cavity increases in size from 25%, 50%, 75% to 100% the different structure of the flows become more evident, seen in figures 5.12 to 5.18.

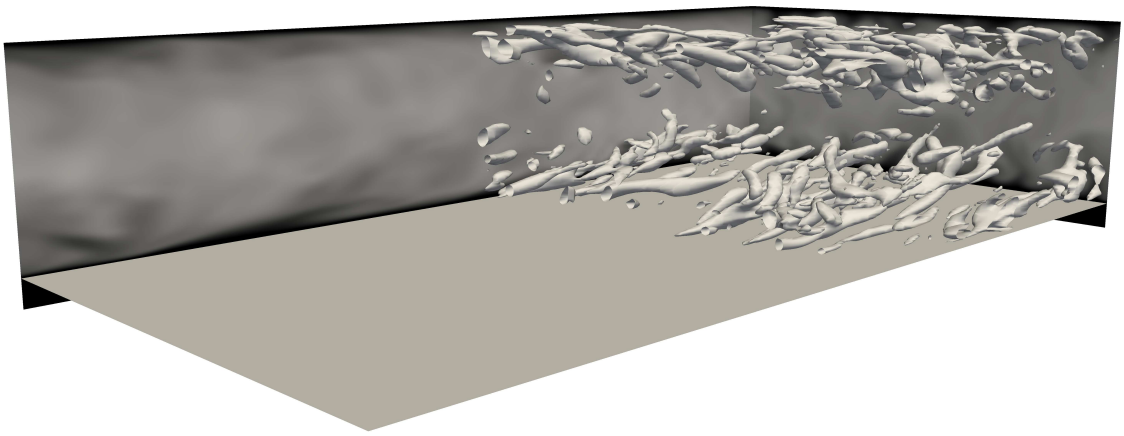

(a)

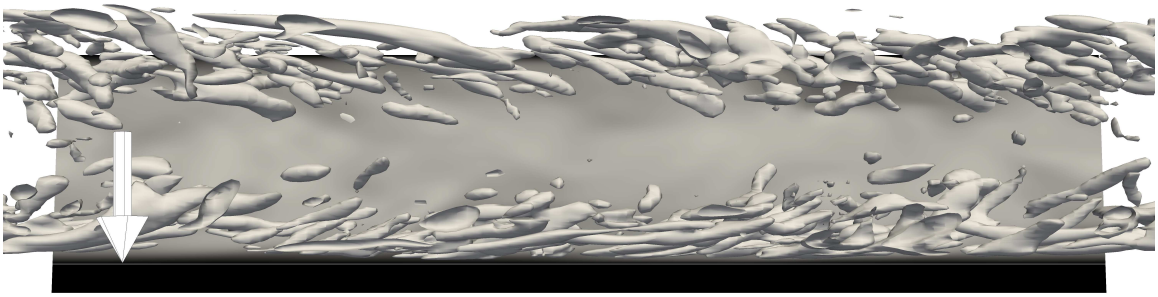

(b)

Figure 5.11: a.) The initial velocity field shown with half the coherent structures removed to show the lower IB wall, and b.) a side view showing the Poisson of the IB wall and coherent structures; $Q = 150$ with the large, lower left corner, arrow pointing to the position of the IB wall and contours showing $3 \leq u^* \geq 20$.

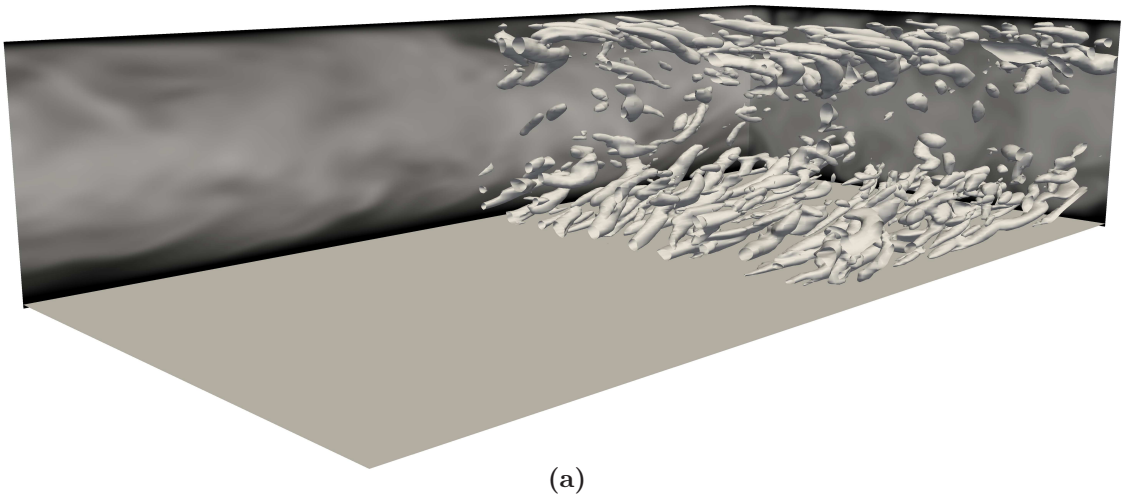

(a)

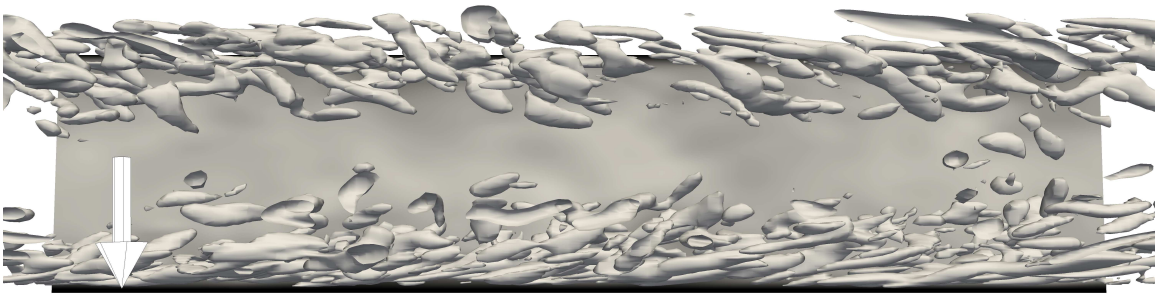

(b)

Figure 5.12: Expanding channel coherent structures for $\mathbf{v}_{\Gamma.} = 0.01u_\tau$ and $Q = 150$

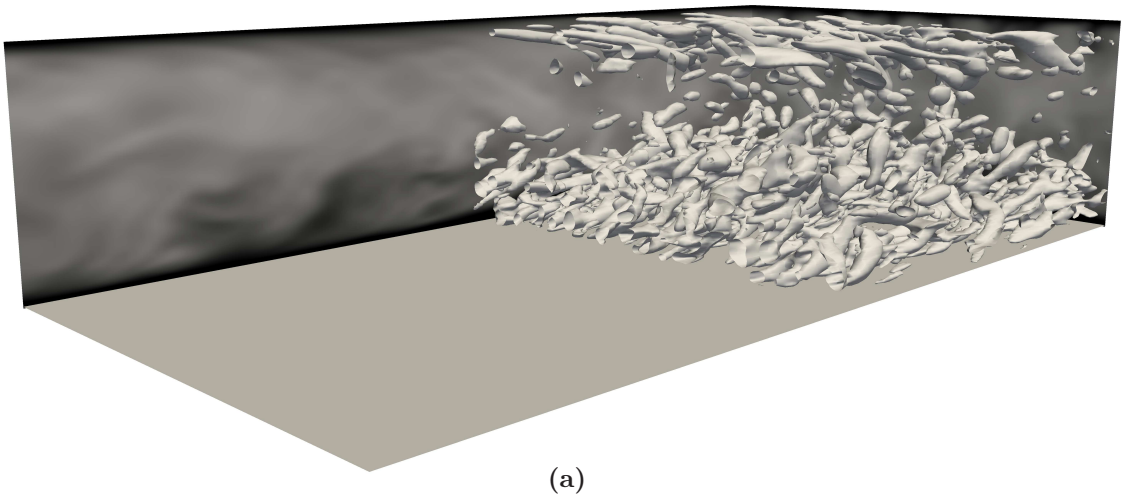

(a)

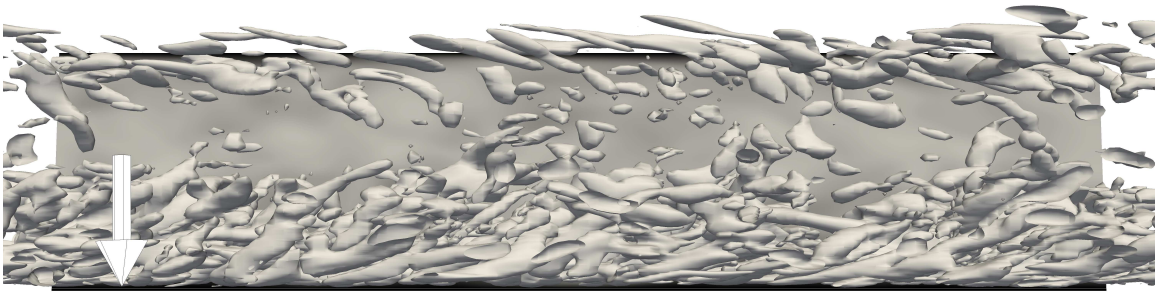

(b)

Figure 5.13: Expanding channel coherent structures for $\mathbf{v}_\Gamma = 0.1u_\tau$ and $Q = 150$

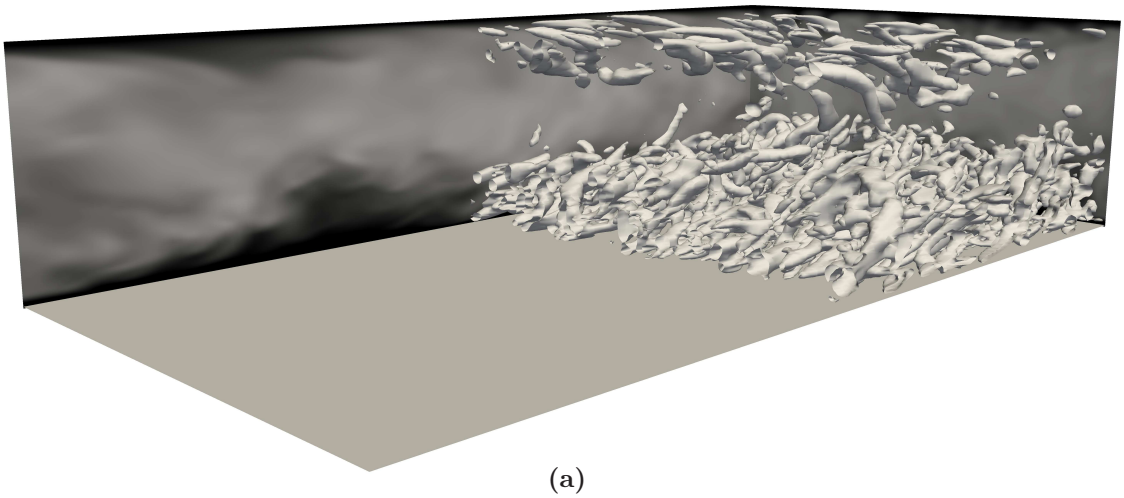

(a)

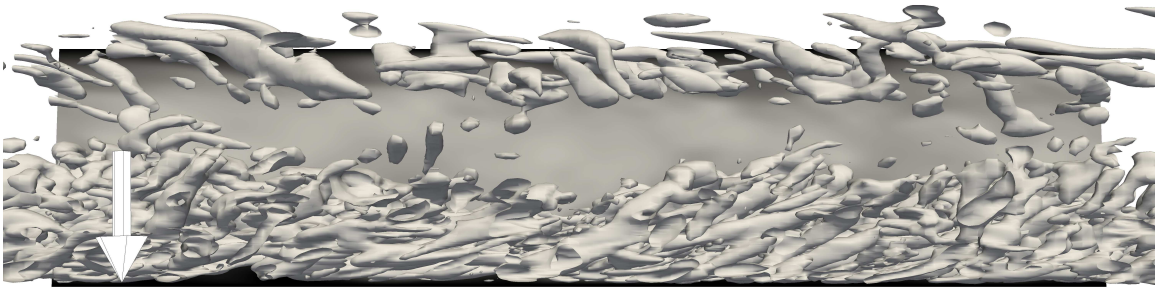

(b)

Figure 5.14: Expanding channel coherent structures for $\mathbf{v}_\Gamma = 0.2u_\tau$ and $Q = 150$

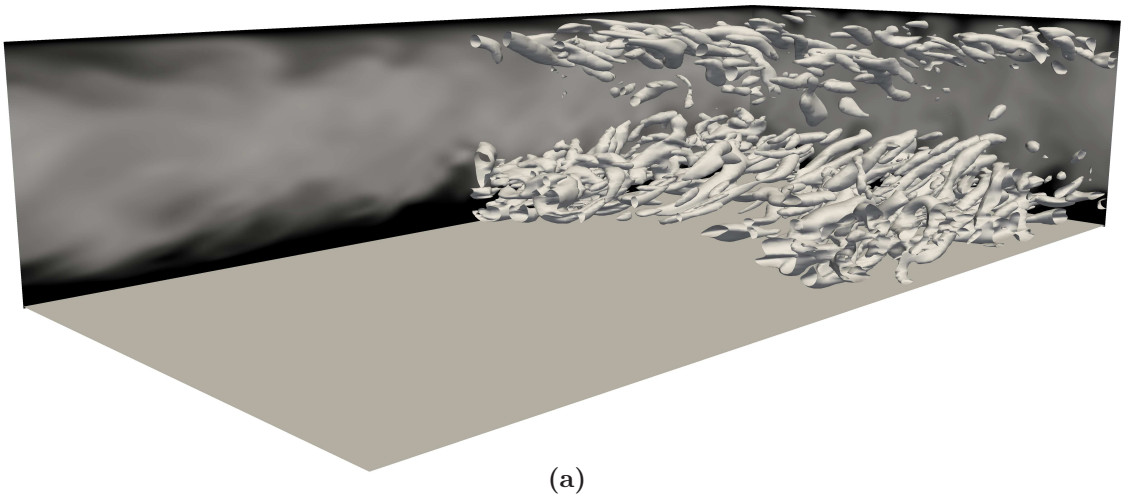

(a)

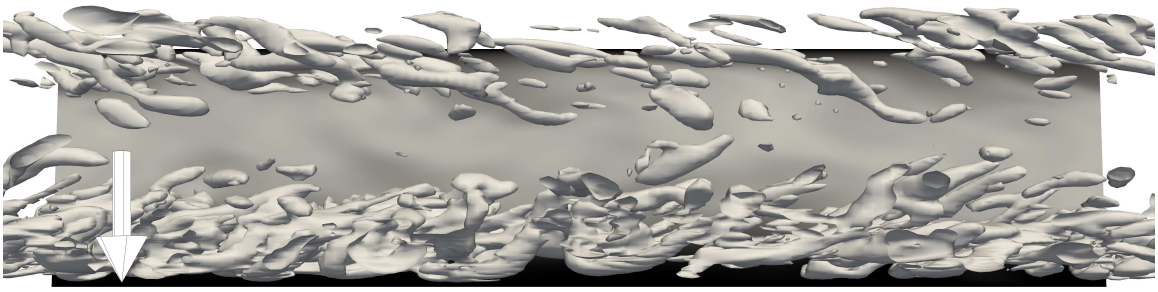

(b)

Figure 5.15: Expanding channel coherent structures for $\mathbf{v}_\Gamma = 0.5u_\tau$ and $Q = 150$

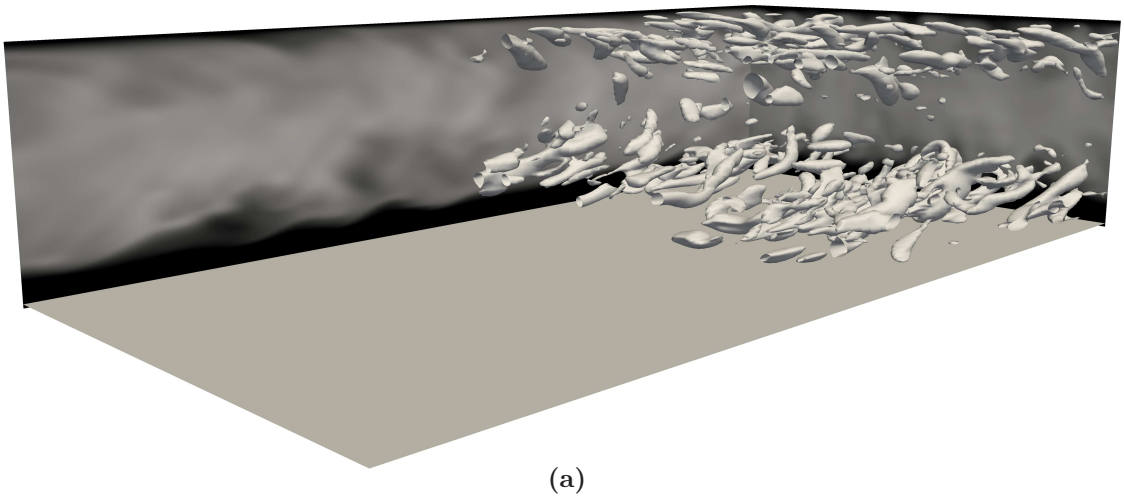

(a)

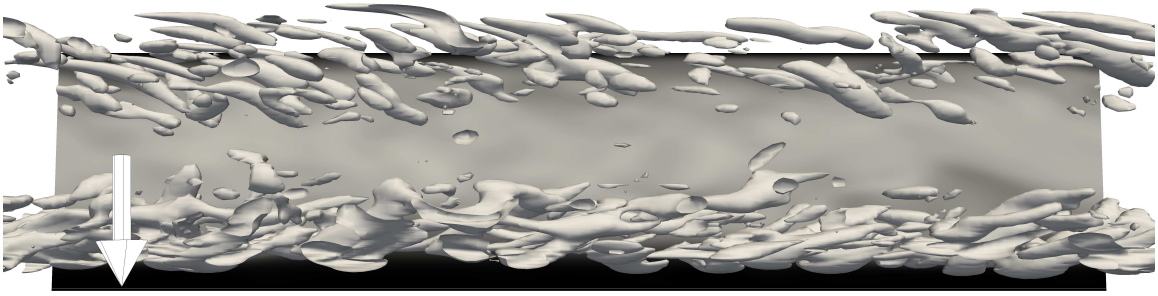

(b)

Figure 5.16: Expanding channel coherent structures for $\mathbf{v}_\Gamma = u_\tau$ and $Q = 150$

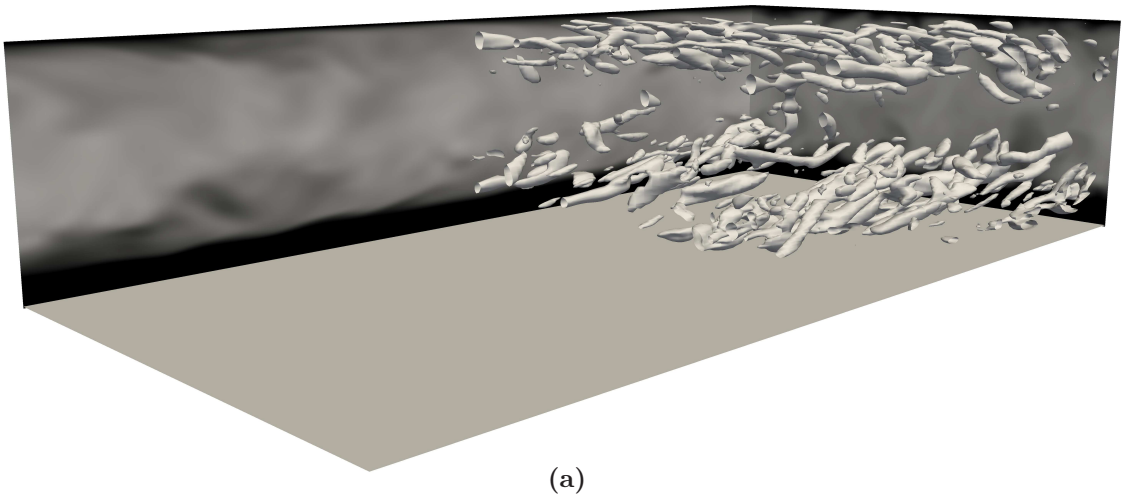

(a)

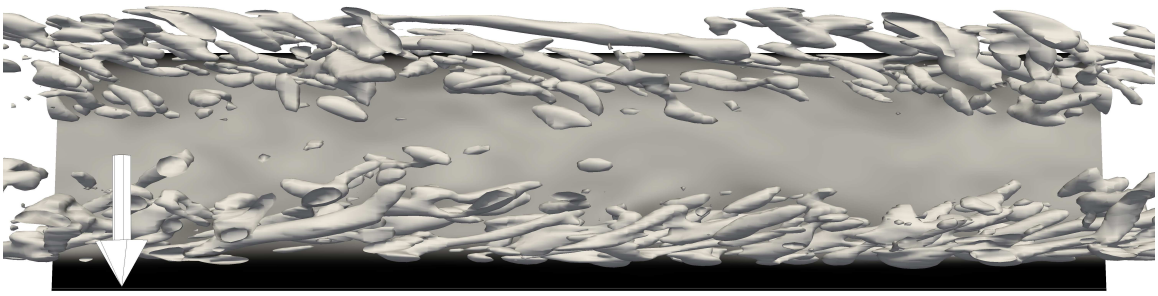

(b)

Figure 5.17: Expanding channel coherent structures for $\mathbf{v}_\Gamma = 2u_\tau$ and $Q = 150$

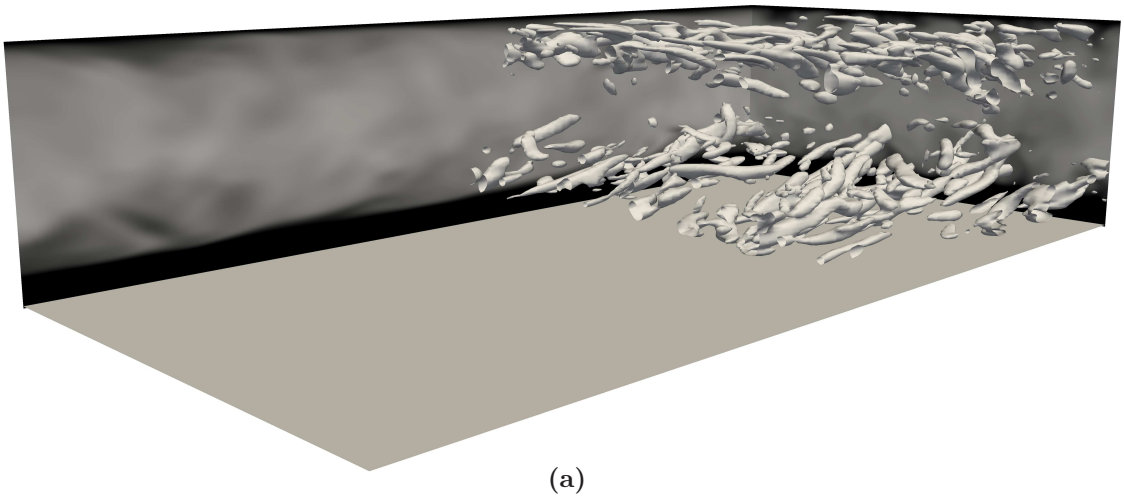

(a)

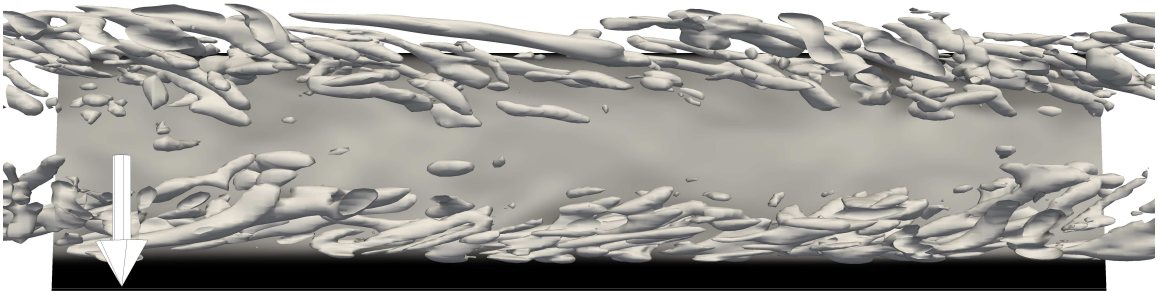

(b)

Figure 5.18: Expanding channel coherent structures for $\mathbf{v}_\Gamma = 4u_\tau$ and $Q = 150$

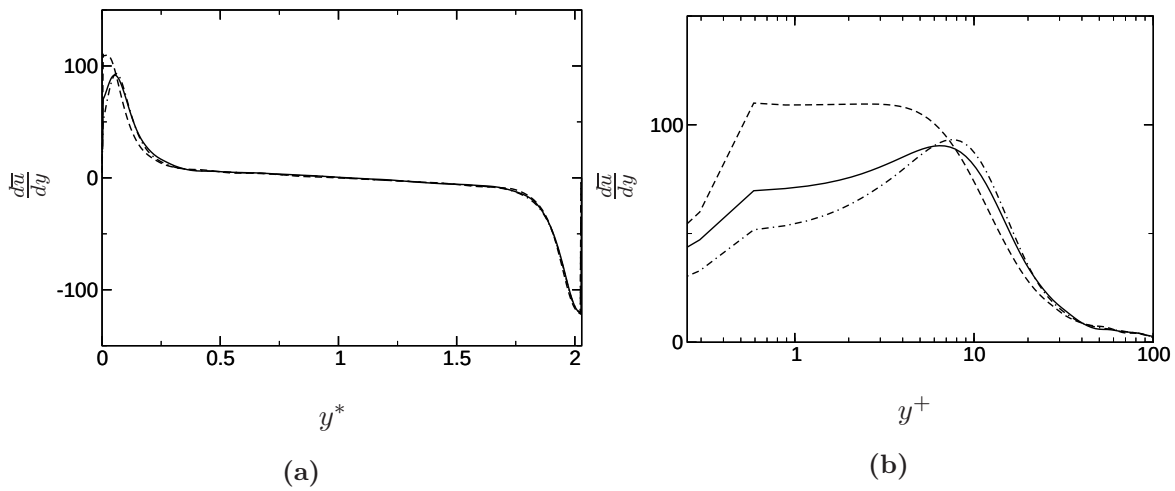

Figure 5.19: $(- - -)$ $\mathbf{v_\Gamma} = 0.01$, $(\text{——})\mathbf{v_\Gamma} = 0.1$, $(- \cdot -)$ $\mathbf{v_\Gamma} = 0.2$ **a.) Expanding channel** $\frac{d\overline{u}}{dy}$ **data for** 10% **expansion. b.) Expanding channel** $\frac{d\overline{u}}{dy}$ **data for** 10% **expansion for the IB half of the channel, in wall units.**

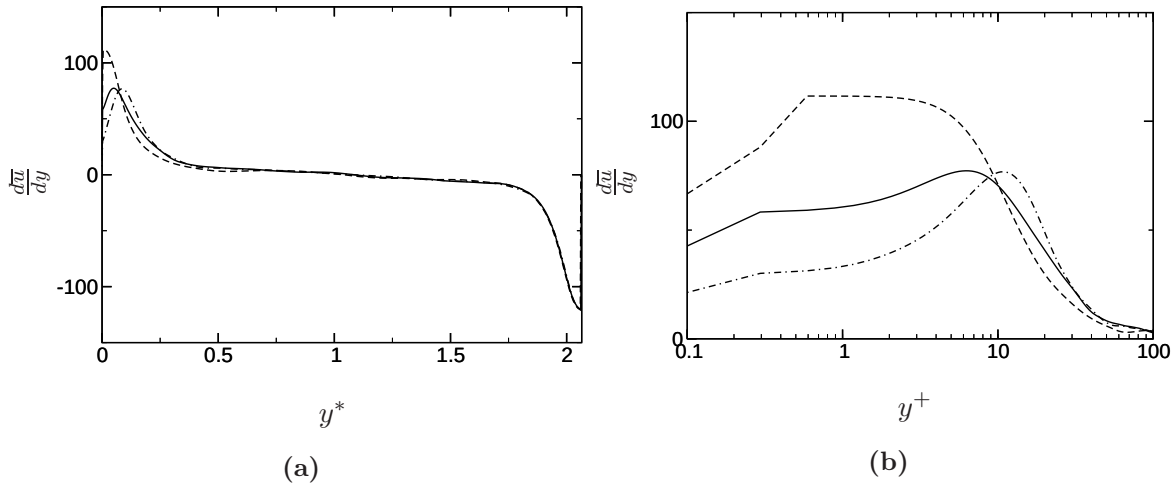

Figure 5.20: $(- - -)$ $\mathbf{v_\Gamma} = 0.01$, $(\text{——})\mathbf{v_\Gamma} = 0.1$, $(- \cdot -)$ $\mathbf{v_\Gamma} = 0.2$ **a.) Expanding channel** $\frac{d\overline{u}}{dy}$ **data for** 25% **expansion. b.) Expanding channel** $\frac{d\overline{u}}{dy}$ **data for** 25% **expansion for the IB half of the channel, in wall units.**

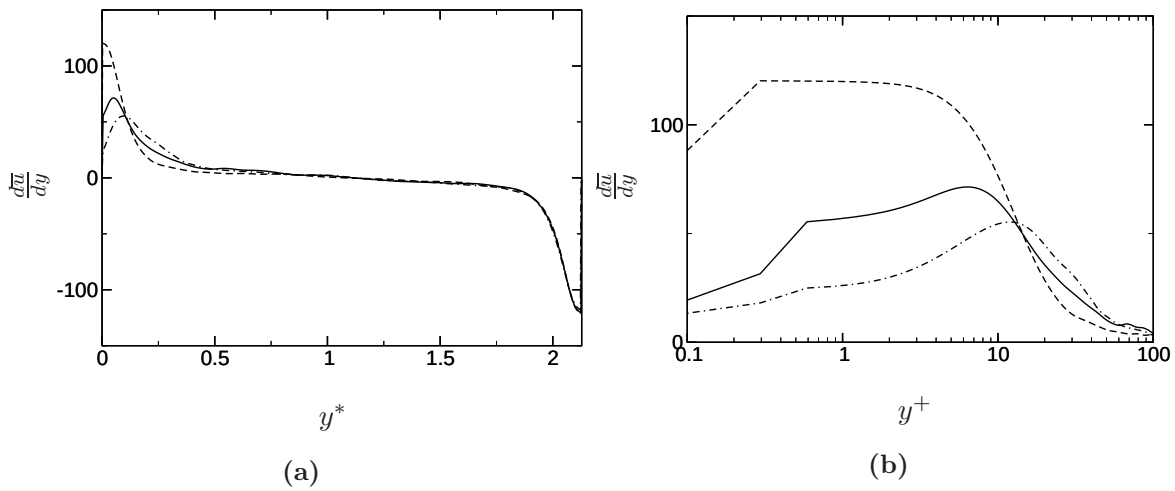

Figure 5.21: $(- - -)$ $\mathbf{v_\Gamma} = 0.01$, $(\text{——})\mathbf{v_\Gamma} = 0.1$, $(- \cdot -)$ $\mathbf{v_\Gamma} = 0.2$ **a.) Expanding channel** $\frac{d\overline{u}}{dy}$ **data for** 50% **expansion. b.) Expanding channel** $\frac{d\overline{u}}{dy}$ **data for** 50% **expansion for the IB half of the channel, in wall units.**

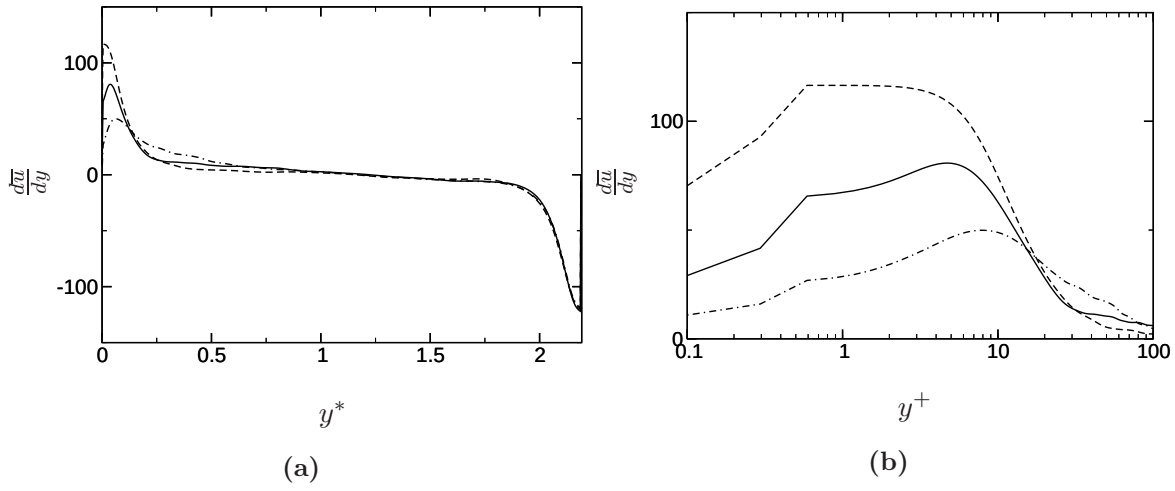

Figure 5.22: $(- - -)$ $\mathbf{v_\Gamma} = 0.01$, $(\text{——})\mathbf{v_\Gamma} = 0.1$, $(- \cdot -)$ $\mathbf{v_\Gamma} = 0.2$ **a.) Expanding channel** $\frac{d\overline{u}}{dy}$ **data for** 75% **expansion. b.) Expanding channel** $\frac{d\overline{u}}{dy}$ **data for** 75% **expansion for the IB half of the channel, in wall units.**

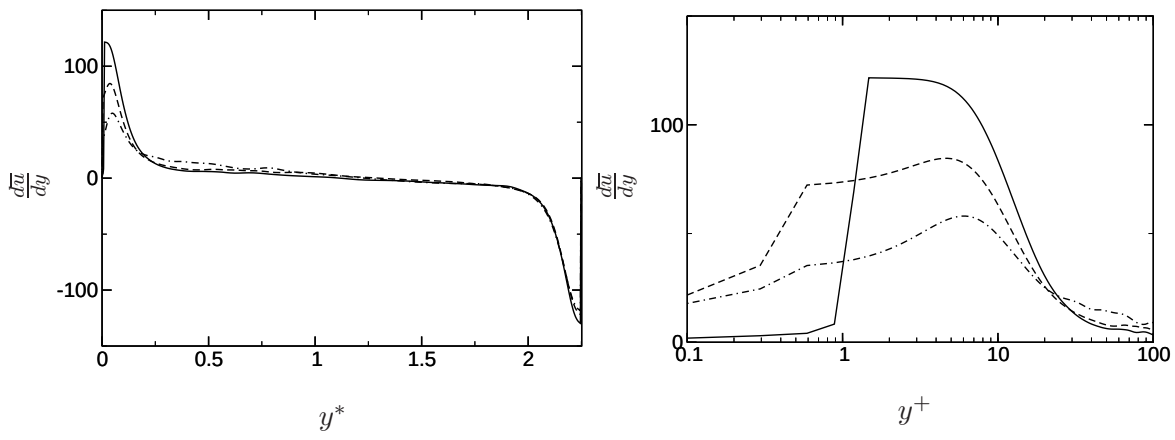

Figure 5.23: $(- - -)$ $\mathbf{v_\Gamma} = 0.01$, $(\text{——})\mathbf{v_\Gamma} = 0.1$, $(- \cdot -)$ $\mathbf{v_\Gamma} = 0.2$ **a.) Expanding channel $\frac{d\overline{u}}{dy}$ data for 100% expansion. b.) Expanding channel $\frac{d\overline{u}}{dy}$ data for 100% expansion for the IB half of the channel, in wall units.**

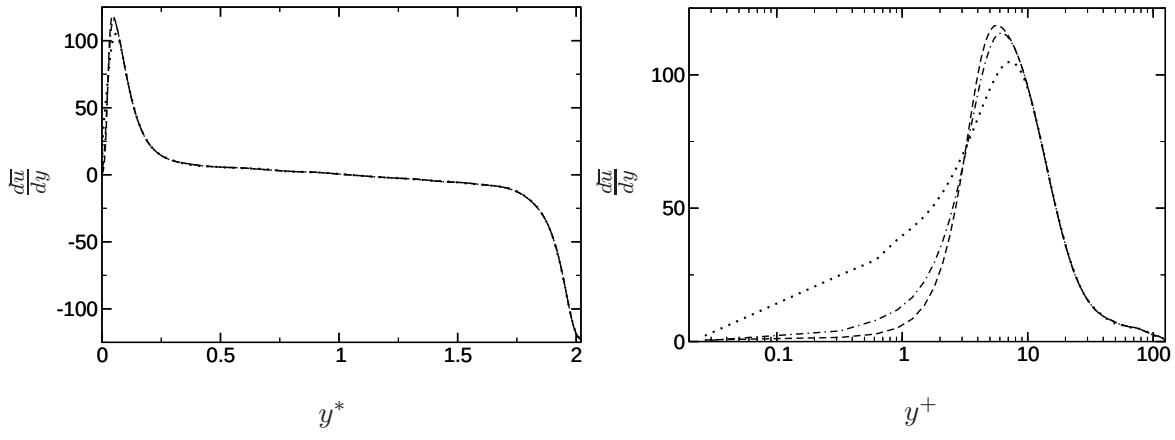

Figure 5.24: $(- - -)$ $\mathbf{v_\Gamma} = 4$, $(- \cdot -)$ $\mathbf{v_\Gamma} = 2$, $(\text{——})\mathbf{v_\Gamma} = 1$, $(\cdots)$ $\mathbf{v_\Gamma} = 0.5$ **a.) Expanding channel $\frac{d\overline{u}}{dy}$ data for 10% expansion. b.) Expanding channel $\frac{d\overline{u}}{dy}$ data for 10% expansion for the IB half of the channel, in wall units.**

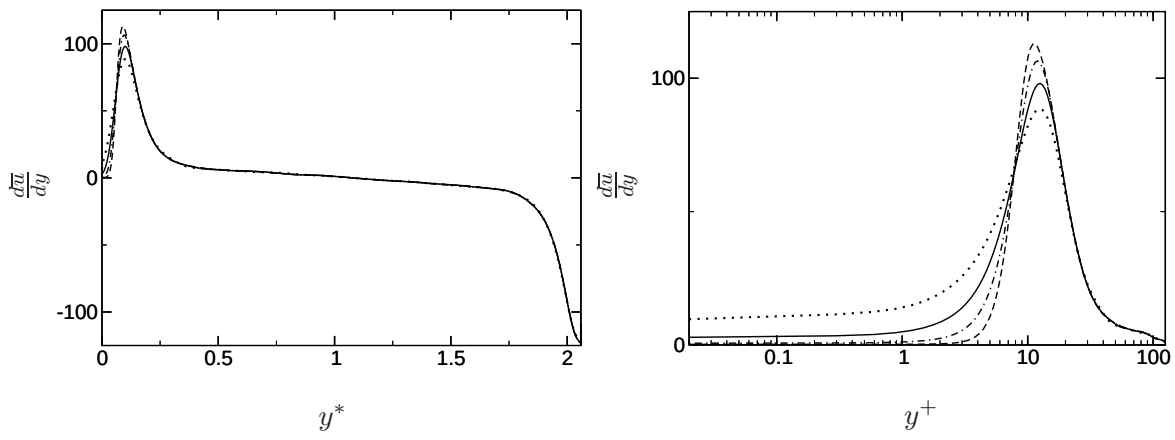

(a) **(b)**

Figure 5.25: $(- - -)\,\mathbf{v}_\Gamma = 4$, $(- \cdot -)\,\mathbf{v}_\Gamma = 2$, $(\text{——})\mathbf{v}_\Gamma = 1$, $(\cdots)\,\mathbf{v}_\Gamma = 0.5$ **a.) Expanding channel $\frac{d\overline{u}}{dy}$ data for 25% expansion. b.) Expanding channel $\frac{d\overline{u}}{dy}$ data for 25% expansion for the IB half of the channel, in wall units.**

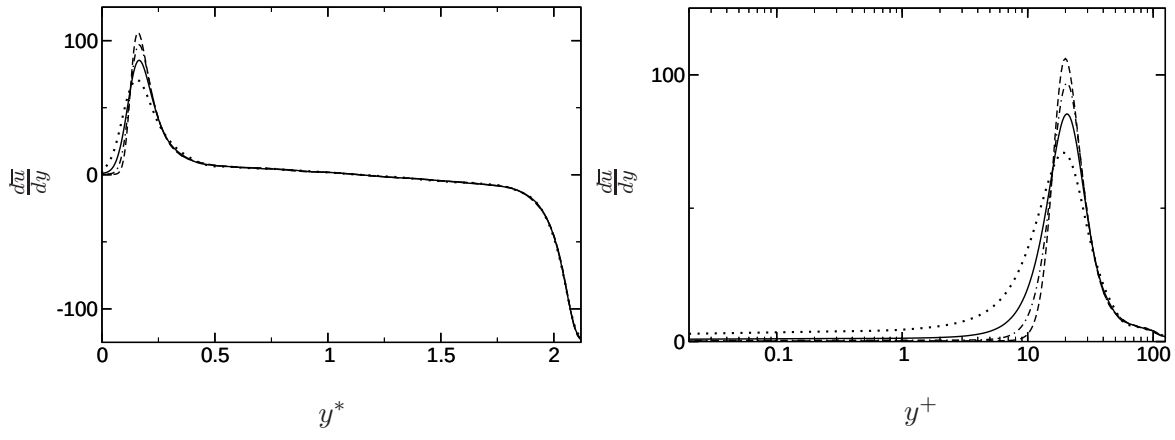

(a) **(b)**

Figure 5.26: $(- - -)\,\mathbf{v}_\Gamma = 4$, $(- \cdot -)\,\mathbf{v}_\Gamma = 2$, $(\text{——})\mathbf{v}_\Gamma = 1$, $(\cdots)\,\mathbf{v}_\Gamma = 0.5$ **a.) Expanding channel $\frac{d\overline{u}}{dy}$ data for 50% expansion. b.) Expanding channel $\frac{d\overline{u}}{dy}$ data for 50% expansion for the IB half of the channel, in wall units.**

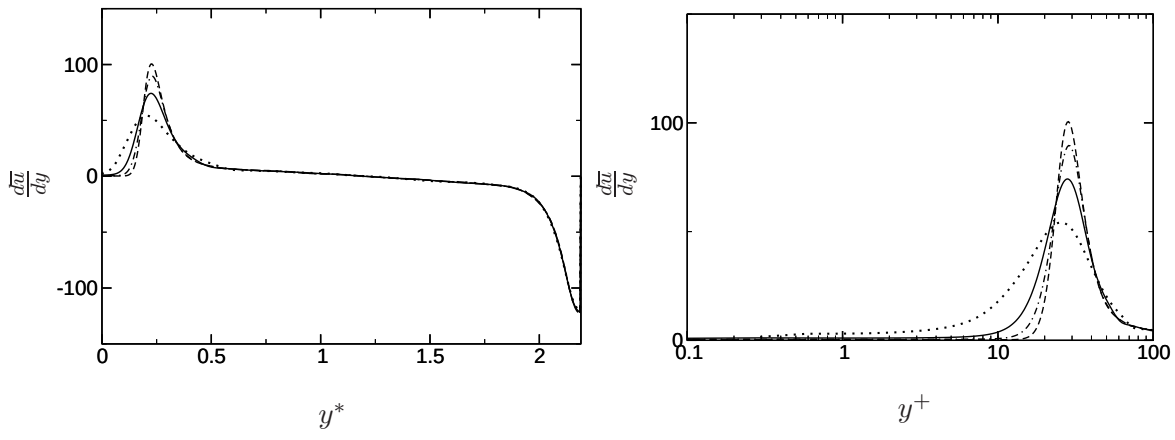

(a) **(b)**

Figure 5.27: $(- - -)\,\mathbf{v_\Gamma} = 4$, $(- \cdot -)\,\mathbf{v_\Gamma} = 2$, $(\text{——})\mathbf{v_\Gamma} = 1$, $(\cdots)\,\mathbf{v_\Gamma} = 0.5$ **a.) Expanding channel $\frac{d\overline{u}}{dy}$ data for 75% expansion. b.) Expanding channel $\frac{d\overline{u}}{dy}$ data for 75% expansion for the IB half of the channel, in wall units.**

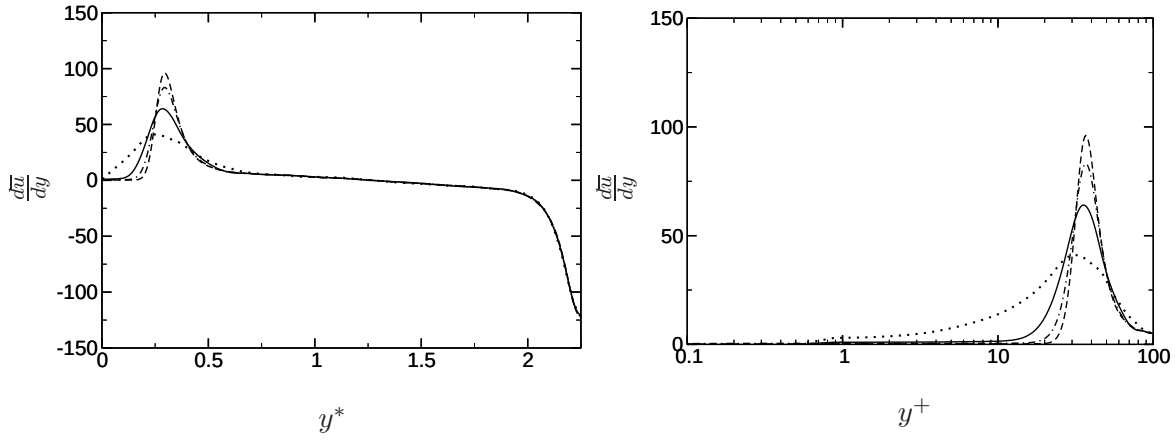

(a) **(b)**

Figure 5.28: $(- - -)\,\mathbf{v_\Gamma} = 4$, $(- \cdot -)\,\mathbf{v_\Gamma} = 2$, $(\text{——})\mathbf{v_\Gamma} = 1$, $(\cdots)\,\mathbf{v_\Gamma} = 0.5$ **a.) Expanding channel $\frac{d\overline{u}}{dy}$ data for 100% expansion. b.) Expanding channel $\frac{d\overline{u}}{dy}$ data for 100% expansion for the IB half of the channel, in wall units.**

For velocities faster than $\mathbf{v}_\Gamma \geq 0.5u_\tau$ the lack of coherent structures can be explained by the lack of shear, and Reynolds stresses in these areas making them laminar, (see the average shear series of figures figure 5.24-5.28). Without rotation and strain (see equation 5.11) there cannot be vortices, a rather un-interesting, but valid, explanation for the faster recession regimes. The slower recession regimes, $\mathbf{v}_\Gamma \geq 0.5u_\tau$, appear to be much more intriguing. Specifically, for $\mathbf{v}_\Gamma = 0.5u_\tau$ through $\mathbf{v}_\Gamma = 0.1u_\tau$ wherein the dissipation drops to zero before the wall production term in the cavity is still non-zero. The excess production of TKE is not dissipated, and it can only be transferred back to the core at rate defined by energy cascade ε. The last velocity $\mathbf{v}_\Gamma = 0.01u_\tau$ shows comparable ε, $\mathcal{P}$, and the fluctuating terms, to the IC of the channel. This is not physically significant other than that it shows that there is a lower end of wall motion that does not cause any distinct change in the channel flow structures, or equilibrium. This is born out in the average shear stress series of figures 5.19-5.23 where $d\overline{u}/dy \neq 0$ at the wall, even though it is moving at a constant velocity.

Comparing the qualitative data of the streak formation is done with figures 5.29a-5.29b. The snapshots are taken at $L_x/2$ for $\mathbf{v}_\Gamma = 0.1$ to $\mathbf{v}_\Gamma = 0.5$, at 75% channel expansion. For all three velocities, the streaks appear to be attenuated or elongated where only two are shown. This is not seen in figures 5.30a and 5.30b, for $\mathbf{v}_\Gamma = 1$ and $\mathbf{v}_\Gamma = 2$ respectively, where the streaks are either adjacent to the dynamic wall or directly above the shear free layer. The autocorrelation function,

$$R_{11} = \frac{u^{'}(x,y,z)\, u^{'}(x,y,z+\Delta z)}{u^{'}(x,y,z)^2}, \tag{5.13}$$

in the spanwise direction, shown in figures 5.32-5.34 for various wall distances y^*, of the fluctuating velocities at the same expansion what is seen qualitatively in figure 5.29. The streaks are now 20% taller, figure 5.31, than the streaks seen in figure 5.6b. This effect begins to tail off at $\mathbf{v}_\Gamma = 0.1$, figure 5.30b, and is much more pronounced in figure5.30a for $\mathbf{v}_\Gamma = 0.5$.

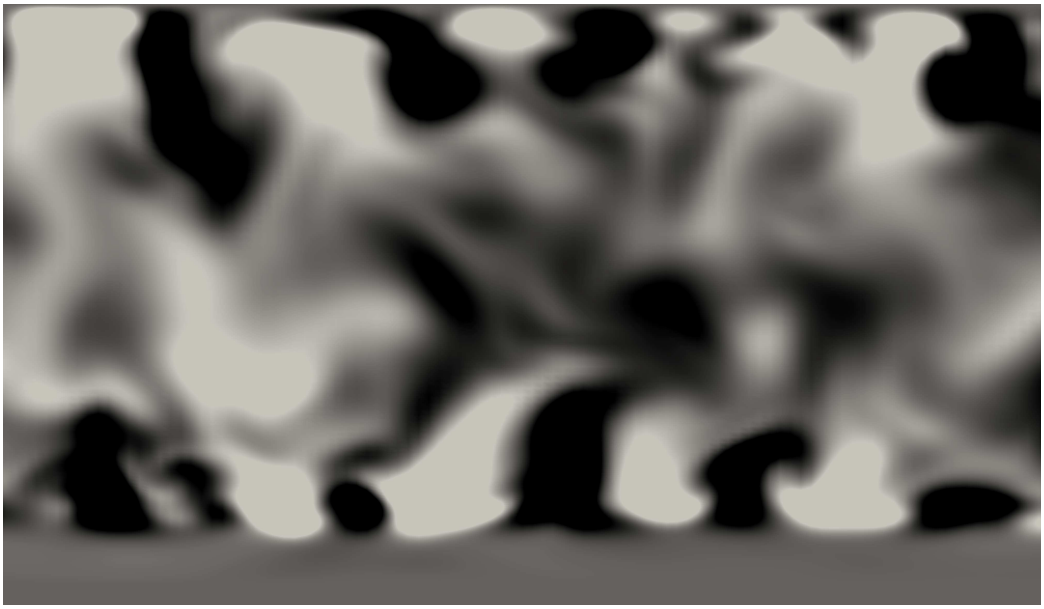

(a)

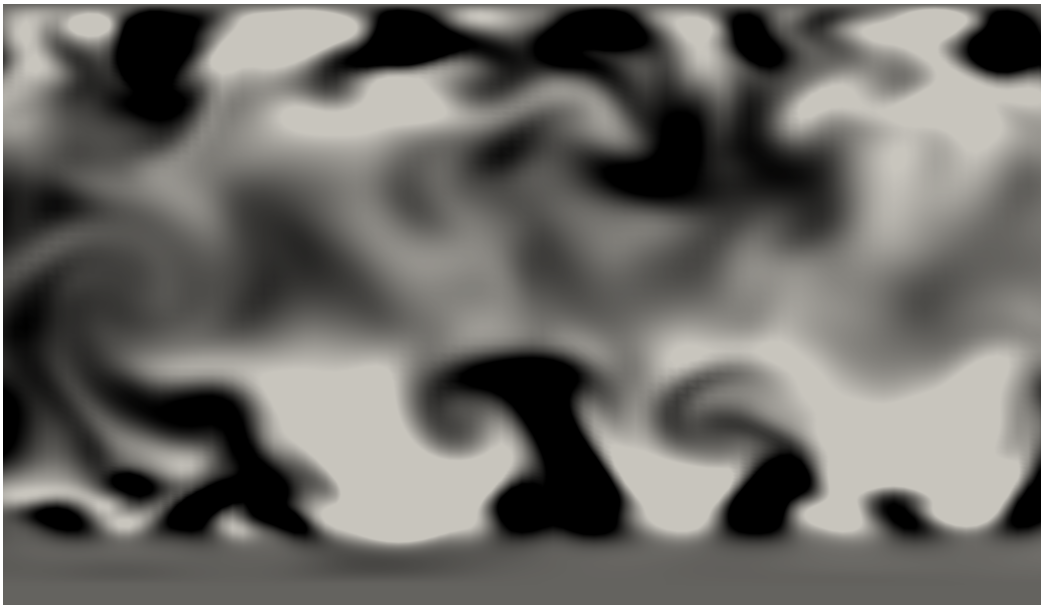

(b)

Figure 5.29: a.) $u^{'}$ **Streaks shown at a cross section at** $L_y/2$ **with the lighter values showing larger** $u^{'}$**, for** $\mathbf{v}_\Gamma = 2$ **at a channel expansion of** 75% **b.)** $u^{'}$ **Streaks shown at a cross section at** $L_y/2$ **with the lighter values showing larger** $u^{'}$**, for** $\mathbf{v}_\Gamma = 1$ **at a channel expansion of** 75%

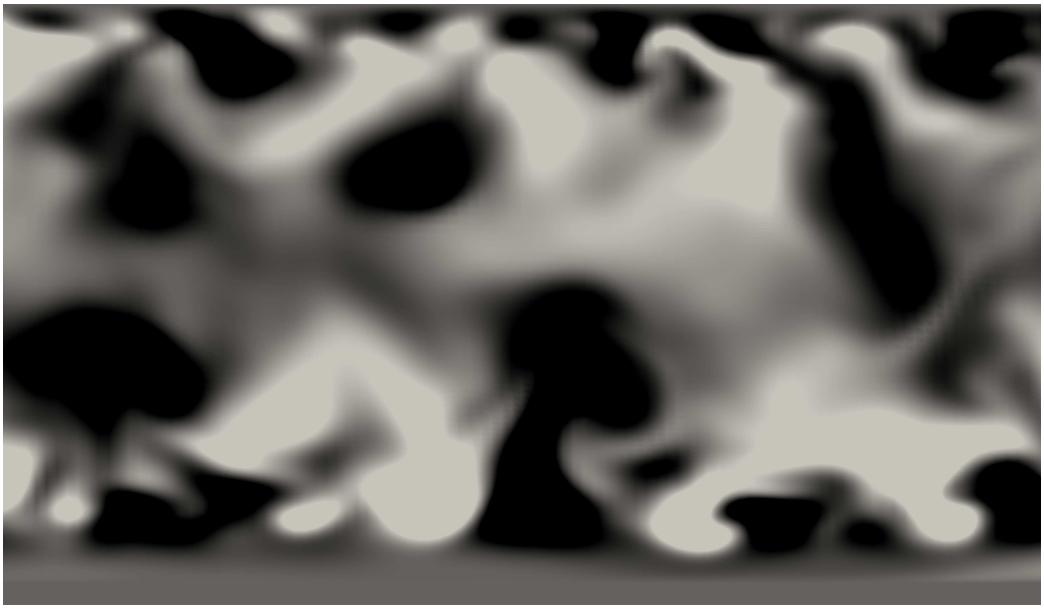

(a)

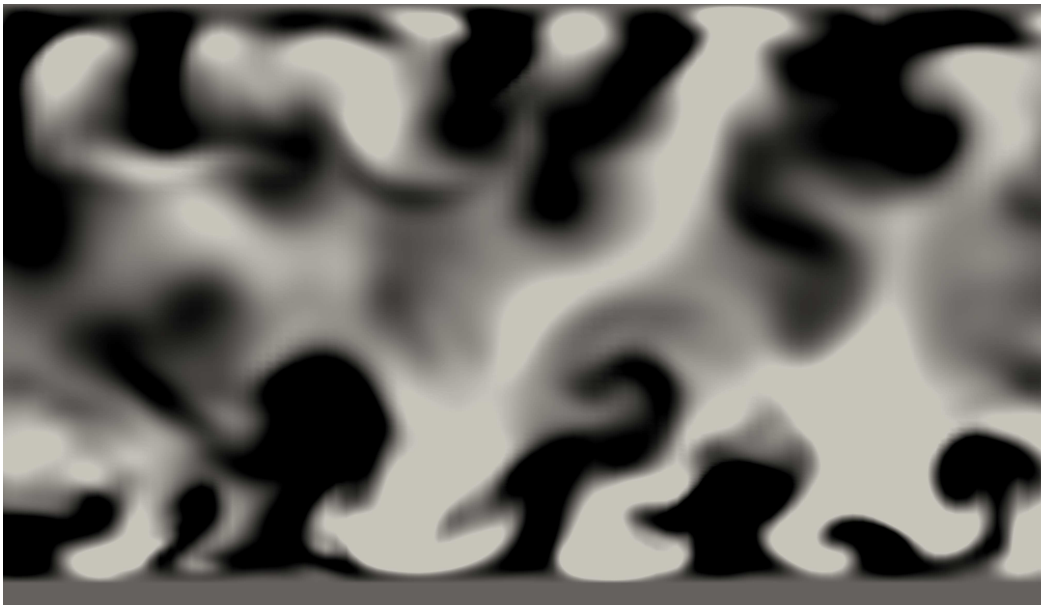

(b)

Figure 5.30: a.) $u^{'}$ **Streaks at a cross section at** $L_y/2$ **with the lighter values showing larger** $u^{'}$**, for** $\mathbf{v}_\Gamma = 0.5$ **at a channel expansion of** 75% **b.)** $u^{'}$ **Streaks at a cross section at** $L_y/2$ **with the lighter values showing larger** $u^{'}$**, for** $\mathbf{v}_\Gamma = 0.1$ **at a channel expansion of** 75%

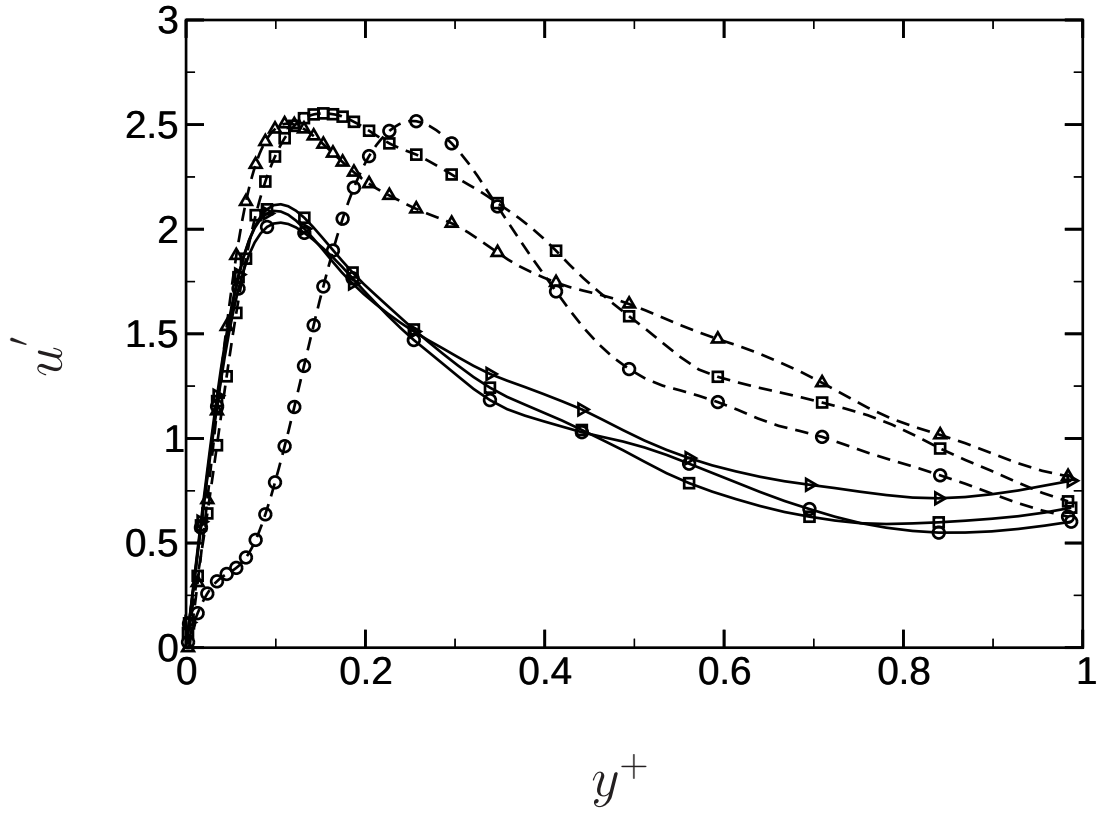

Figure 5.31: Overlays of u_{rms} velocities from the IB side of the channel $(- - -)$, and the non-IB side of the channel (——)of $\mathbf{v}_\Gamma = 0.1$ ($\triangle\,\triangle\,\triangle$), $\mathbf{v}_\Gamma = 0.2$ ($\square\square\square$)and $\mathbf{v}_\Gamma = 0.5$ ($\circ\,\circ\,\circ$), where the x axis has been rescaled so that $L_{y75\%}/2 = 1$.

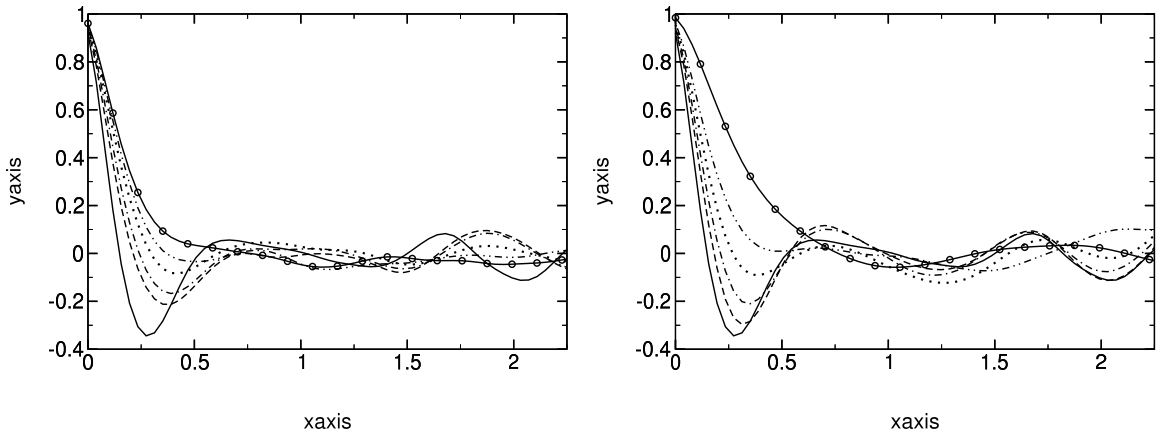

(a) **(b)**

Figure 5.32: The spanwise, z, autocorrelation function, R_{11} of $\mathbf{v}_\Gamma = 0.1$, of $u^{'}$ at various heights a.) $y = 6.05 \cdot 10^{-3}$ (——), $y = 5.32 \cdot 10^{-2}$ $(- - -)$, $y = 7.68 \cdot 10^{-2}$ $(- \cdot -)$, $y = 0.12$ $(\cdot \cdot \cdot)$, $y = 0.19$ $(- \cdot \cdot -)$, $y = 0.26$ $(\circ \circ \circ)$, **and b.)** $y = 2.17$ (——), $y = 2.13$ $(- - -)$, $y = 2.10$ $(- \cdot -)$, $y = 2.05$ $(\cdot \cdot \cdot)$, $y = 1.96$ $(- \cdot \cdot -)$, $y = 1.15$ $(\circ \circ \circ)$, **for a channel expansion of $L_{y75\%}$, and the receding wall and the initial position is at $y = 0$.**

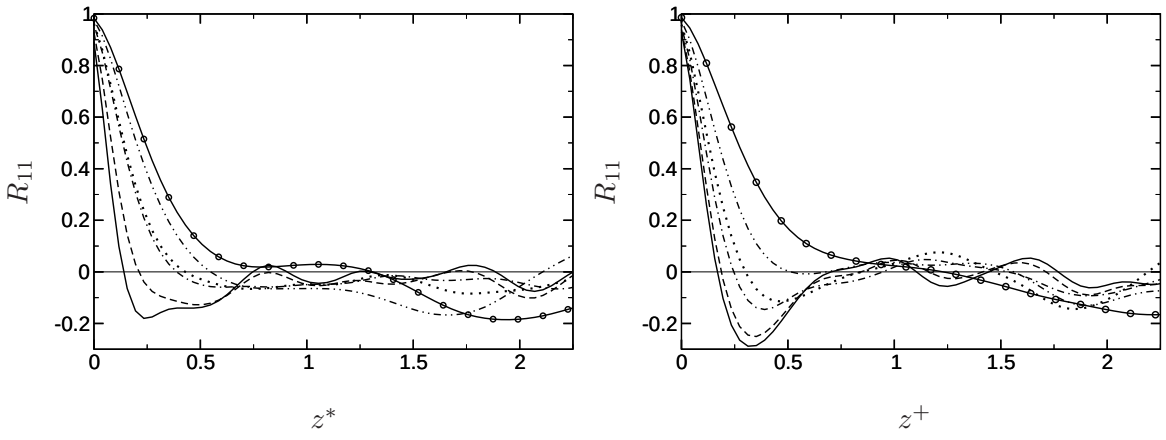

(a) **(b)**

Figure 5.33: The spanwise, z, autocorrelation function, R_{11} of $\mathbf{v}_\Gamma = 0.2$, of $u^{'}$ at various heights a.), $y = 7.44 \cdot 10^{-3}$ (——), $y = 5.46 \cdot 10^{-2}$ $(- - -)$, $y = 0.30$ $(- \cdot -)$, $y = 0.41$ $(\cdot \cdot \cdot)$, $y = 0.84$ $(- \cdot \cdot -)$, $y = 1.06$ $(\circ \circ \circ)$, and b.) $y = 2.17$ (——), $y = 2.15$ $(- - -)$, $y = 2.13$ $(- \cdot -)$, $y = 2.10$ $(\cdot \cdot \cdot)$, $y = 1.73$ $(- \cdot \cdot -)$, $y = 1.15$ $(\circ \circ \circ)$, for a channel expansion of $L_{y75\%}$, and the receding wall and the initial position is at $y = 0$.

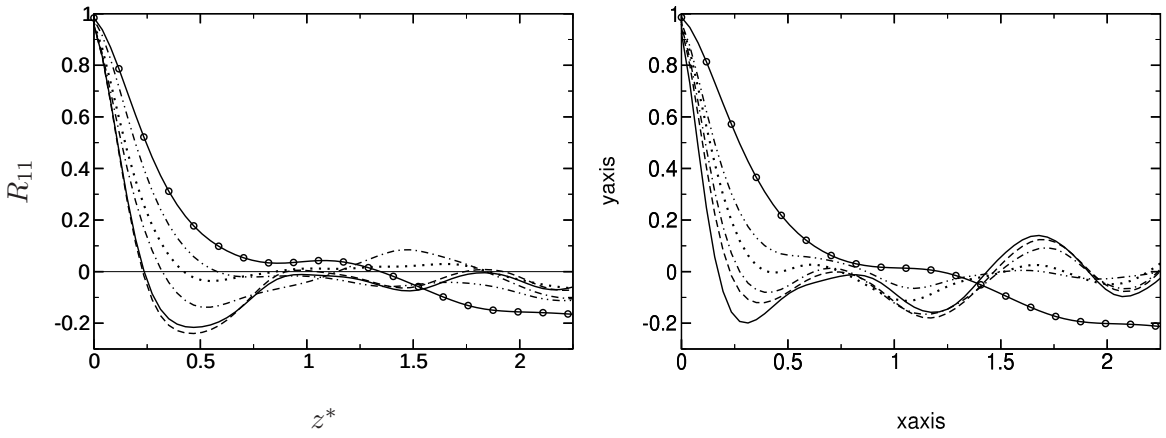

Figure 5.34: The spanwise, z, autocorrelation function, R_{11} of $\mathbf{v}_\Gamma = 0.2$, of u' at various heights a.), $y = 7.44 \cdot 10^{-3}$ **(——),** $y = 5.46 \cdot 10^{-2}$ $(- - -)$, $y = 0.30$ $(- \cdot -)$, $y = 0.41$ $(\cdot \cdot \cdot)$, $y = 0.84$ $(- \cdot \cdot -)$, $y = 1.06$ $(\circ \circ \circ)$, **and b.)** $y = 2.17$ **(——),** $y = 2.15$ $(- - -)$, $y = 2.13$ $(- \cdot -)$, $y = 2.10$ $(\cdot \cdot \cdot)$, $y = 2.0$ $(- \cdot \cdot -)$, $y = 1.15$ $(\circ \circ \circ)$, **for a channel expansion of** $L_{y75\%}$, **and the receding wall is at** $y = 0$.

Jiménez 1999 [157] showed that disruption of the streaks can significantly damp turbulent intensities near the wall. Figures 5.30-5.34 have shown that wall movement can increase the size of the steaks, the size of the intensities, and the amount of streamwise vortices even though the wall shear is reduced (figures 5.19-5.23). For a range of wall velocities between $\mathbf{v}_\Gamma = 0.5 - 0.1$ the wall seems to leave a more turbulent wake as it moves away from the wall than $0.1 \leq \mathbf{v}_\Gamma$ and $\mathbf{v}_\Gamma \geq 0.5$. To make sure this is not an artifact of the IBM, or of the ICs, the $\mathbf{v}_\Gamma$ is set to $\approx \infty$. Essentially, this removes the wall immediately from the flow domain leaving the channel to run though a transient state, shown in figures 5.35-5.37 and then is allowed to reach a statistical equilibrium. The interesting part of this experiment is that the lower wall, where $\mathbf{v}_\Gamma \to \infty$ stays essentially coherent as seen in figure 5.40 where the streaks are not dissipated (figures 5.35-5.37 where neither are the streamwise vortices). The total time until the channel is fully at turbulent statistical equilibrium is $t^* = 3.5 - 4$, and the velocity of the center of the most turbulent area can be measured by checking the rate of motion by the maximum of both u_{rms} and $d\overline{u}/dy$, as shown in figure 5.40, which shows a range of $-0.2 \leq \mathbf{v}_\Gamma \geq 0.4$ encompassing the small scale velocity, $\mathrm{v_K} \approx 0.23$ for a channel with $Re_{u_\tau} = 125$ from equation 5.2.

By $t^* \approx 4$ the channel with $\mathbf{v}_\Gamma = \infty$ has settled back down to $d\overline{u}/dy - u^{'}v^{'} = constant$ and has reached a statistical steady state (see figure 5.39 and 5.40). The plot in figure 5.38 only shows data until $t^* \approx 0.3$ because at that time the turbulent leading front has completely moved into the space left by the evacuated wall as shown in figure 5.40 and figures 5.35-5.37.

The time for the $\mathbf{v}_\Gamma \to \infty$ channel to relax to a statistical steady state matches the result from leaving the expanding channels at $\mathbf{v}_\Gamma = 0.1$, $\mathbf{v}_\Gamma = 0.2$, and $\mathbf{v}_\Gamma = 0.5$ to reach a statistical steady sate after they have reached $L_{y100\%}$, $t^* \approx 3.5$ which is also true for the faster wall velocities. This shows that the presence of the wall moving at a particular velocity close to the Kolmorgorov small scale velocity will leave a disturbed wake with

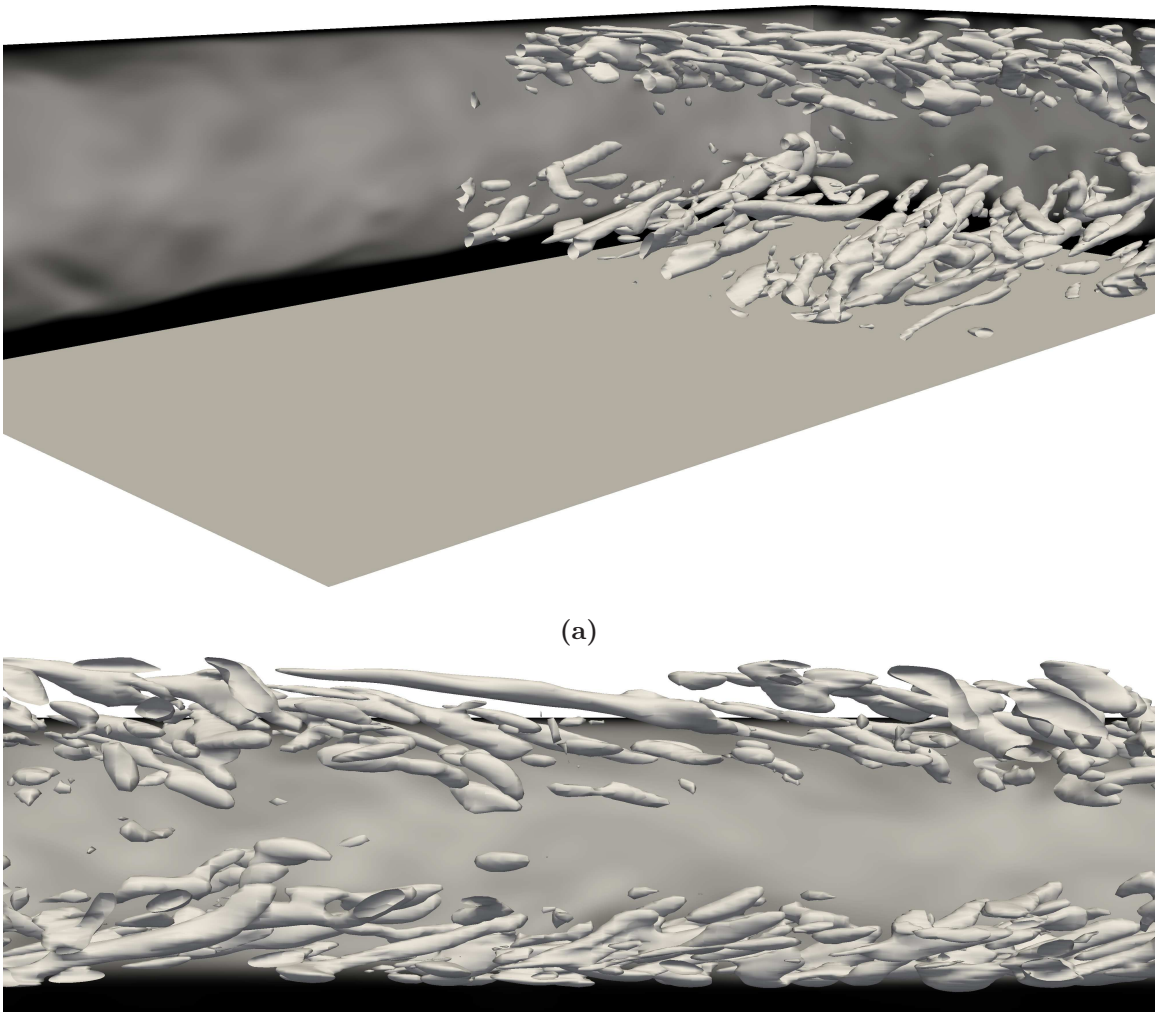

(a)

(b)

Figure 5.35: The $\mathbf{v}_\Gamma = \infty$ channel coherent structures with $Q = 150$ iso-surfaces at 33% of the time until a statistical steady state is reached.

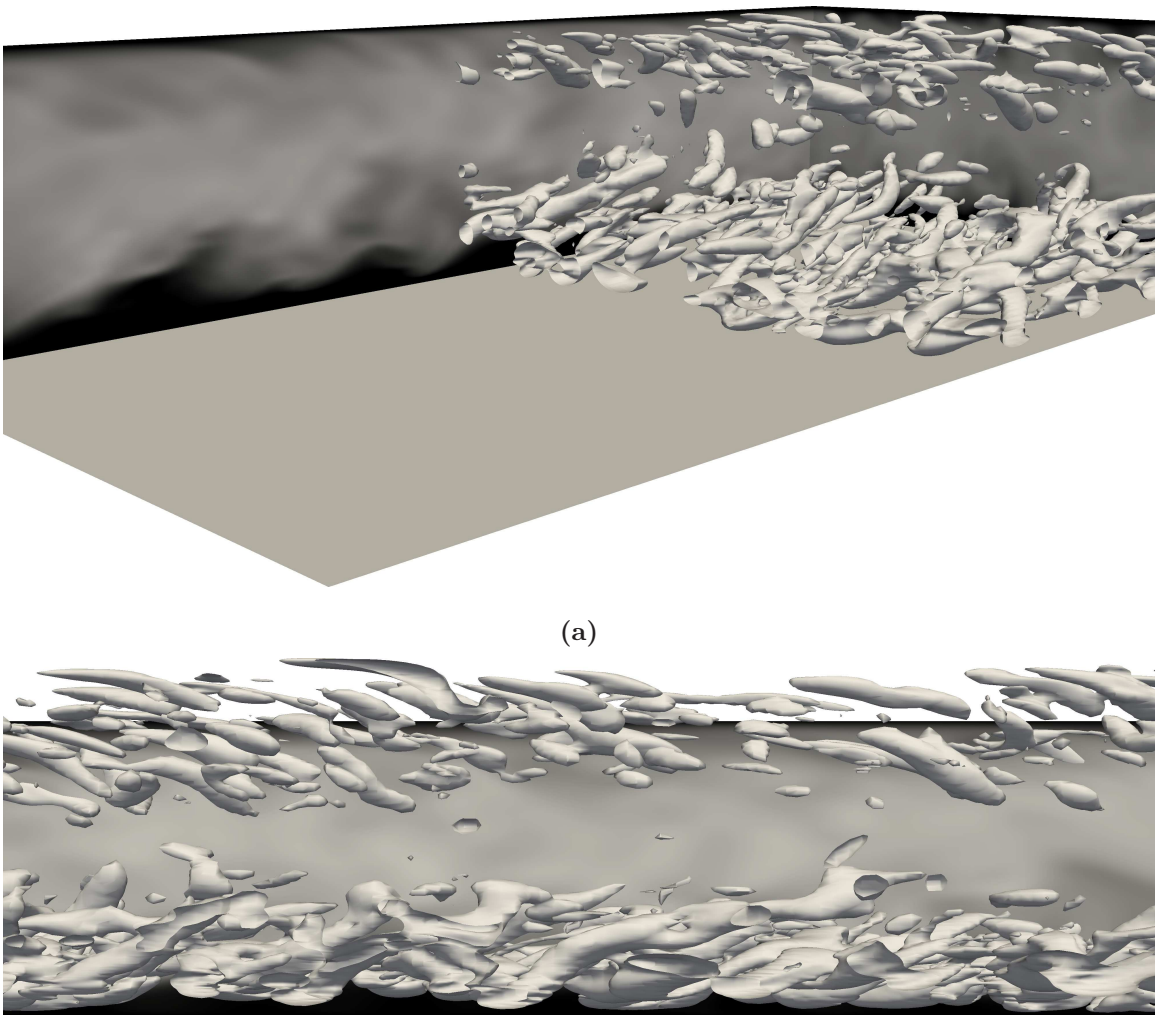

(a)

(b)

Figure 5.36: The $\mathbf{v_\Gamma = \infty}$ channel coherent structures with $Q = 150$ iso-surfaces at 66% of the time until a statistical steady state is reached.

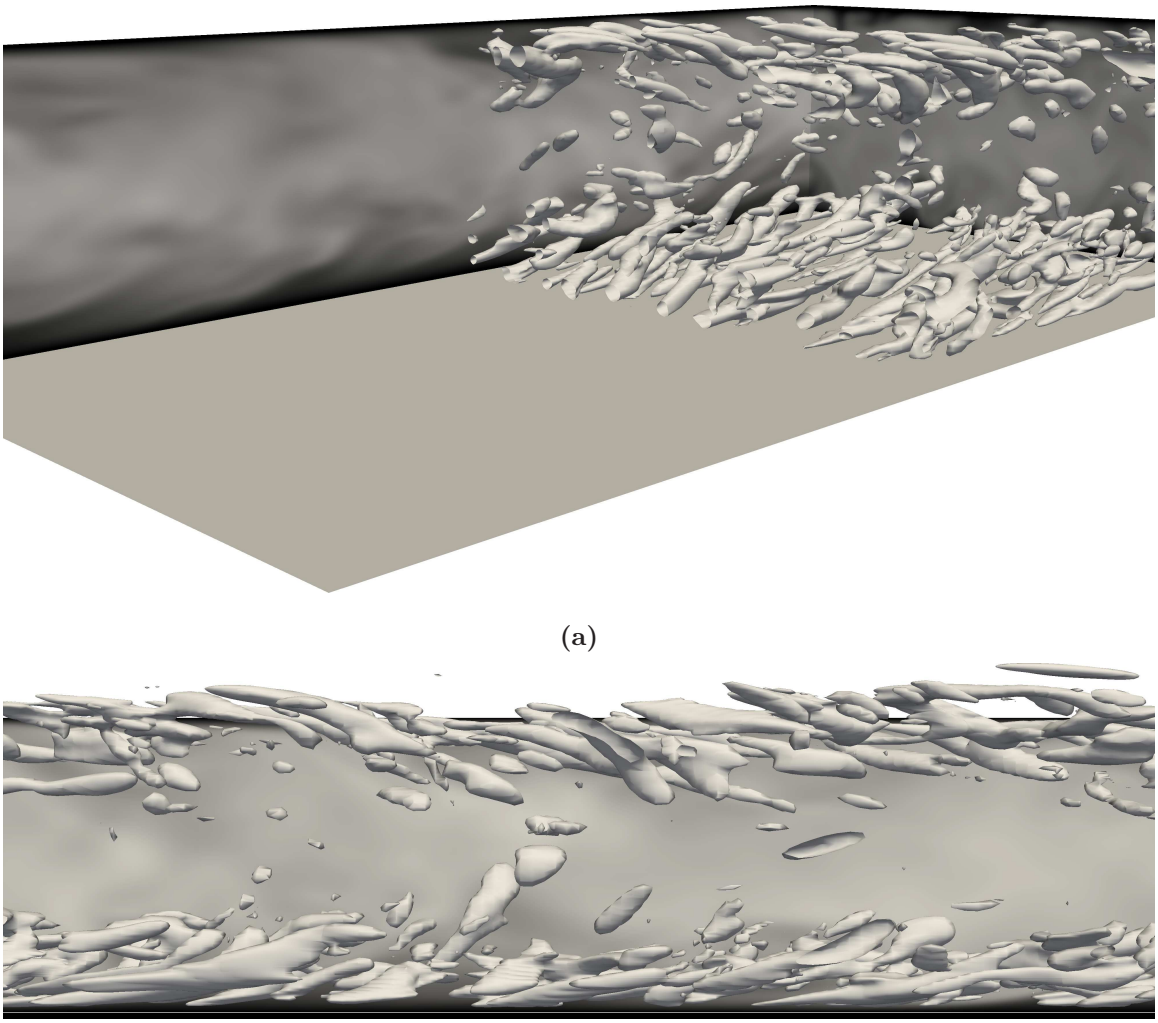

(a)

(b)

Figure 5.37: The $\mathbf{v}_\Gamma = \infty$ channel coherent structures with $Q = 150$ iso-surfaces at 100% of the time until a statistical steady state is reached.

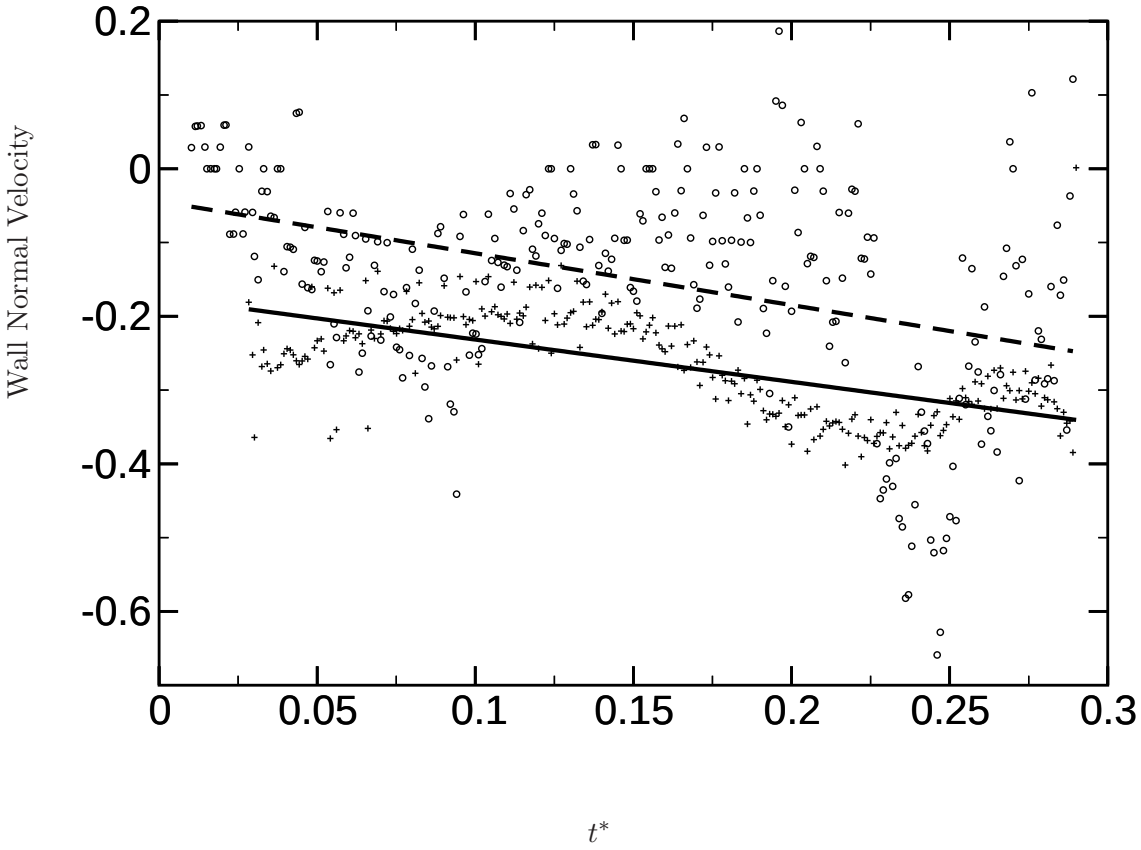

Figure 5.38: The $(\circ\circ\circ)$are the wall normal velocity of the inflection point of of u'_{rms} and $(+++)$are the velocity of the inflection point of $d\overline{u}/dy$ as they both move into the cavity left by the wall with $\mathbf{v_\Gamma = \infty}$, where $(---)$ and (——)are their averages, respectively.

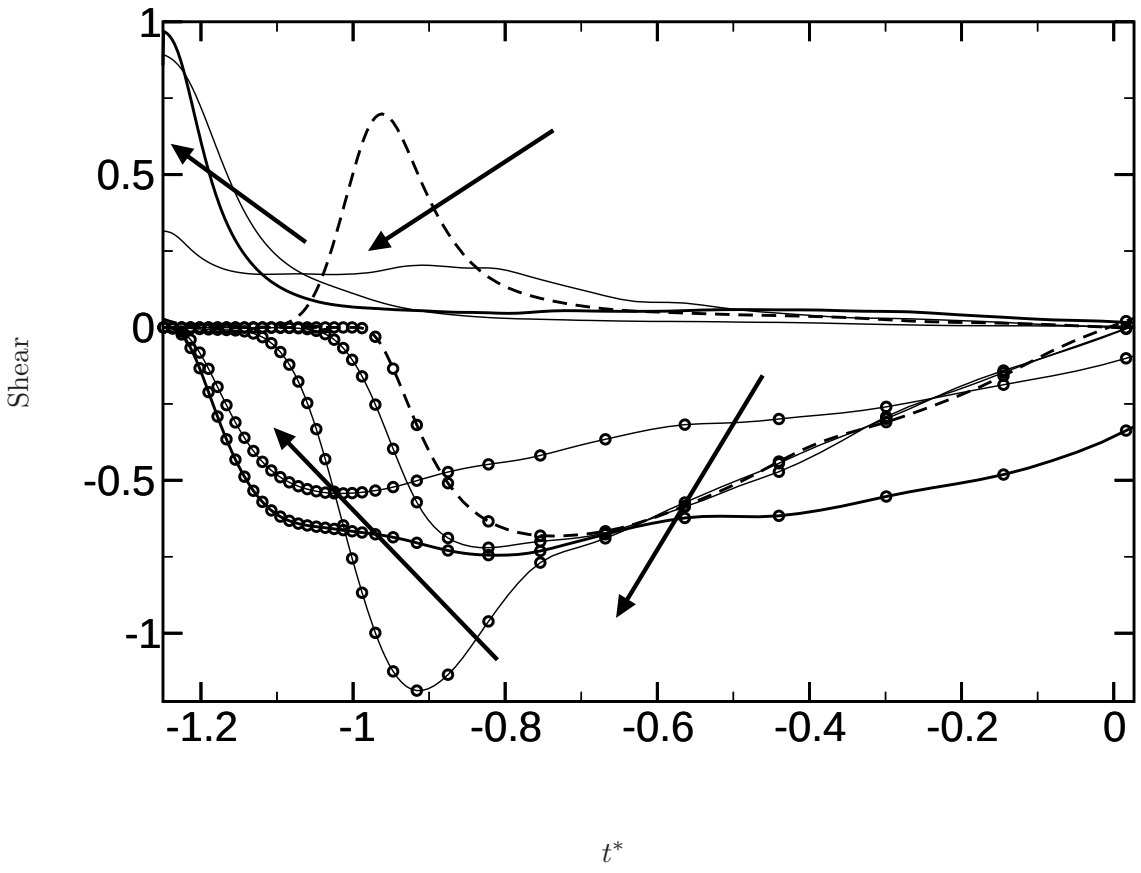

Figure 5.39: The time progression of the average shear, $(- - -)\ d\overline{u}/dy$, and the reynolds shear stress $-u^{'}v^{'}$, $(\circ\circ\circ)$, where $(- - -)$ represents the final position, (——)is the initial position and arrows show the direction of progression.

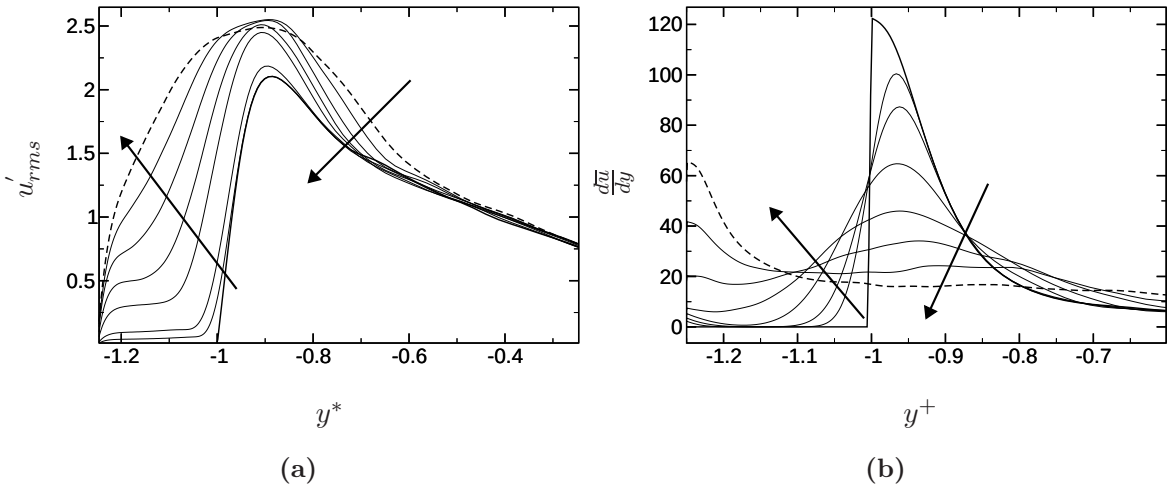

Figure 5.40: The time progression of the a.) u'_{rms} and b.) $\frac{d\overline{u}}{dy}$ for the channel where $\mathbf{v}_\Gamma = \infty$, where $(- - -)$ represents the final position, (——)is the initial position, and arrows show the direction of progression.

stronger turbulent intensity and larger coherent structures. As this was not seen with the data from the channel with $\mathbf{v}_\Gamma \to \infty$ it can be assumed at this low Re the presence of the wall is causing this effect.

5.3.2 Turbulent Production and Dissipation

Based on the results in section 5.3.1, it would be assumed that the faster wall velocities ($\mathbf{v}_\Gamma = 1, 2, 4$) do not see an increase in production or dissipation on the dynamic wall boundary side of their flow as that portion of the flow is laminar. This is in fact true, as shown in the figure series 5.46-5.50 where there is a decrease in both production and dissipation for all channel widths for $\mathbf{v}_\Gamma = 1, 2, 4$, expected with the drop of mean shear shown in figures 5.24-5.28 and there is no production or dissipation until $L_{y50\%}$ when both production and dissipation start to increase slightly. Less dynamic wall effects can also be seen for the slowest wall velocity, $\mathbf{v}_\Gamma = 0.01$ where there is no change throughout recession of either the production or dissipation from that of a channel without a moving wall, figures

5.41-5.45. Again, going with what was seen in section 5.3.1 only the wall velocities of $\mathbf{v}_\Gamma = 0.1, 0.2, 0.5$ will be scrutinized in this study.

The dissipation and production of $\mathbf{v}_\Gamma = 0.1$, 0.2, 0.5 do not change much, initially (figure 5.41 and 5.46), but as the channel expands there is a large increase in production. For $\mathbf{v}_\Gamma = 0.5$, by $L_{y75\%}$, the production has nearly doubled as shown in figures 5.41-5.50. The dissipation in turn correspondingly decreases for $\mathbf{v}_\Gamma = 0.1$, 0.2, 0.5 by $L_{y75\%}$, also shown in figures 5.41-5.50. The increase of production and decrease in dissipation accounts for the resulting turbulent structures seen in figures 5.13-5.15. The larger area of production seen in 5.41-5.50 is expected from the taller streaks mentioned in section 5.3.1 and shown in the u'_{rms} velocities seen in figure 5.31, but the larger streaks seen for $\mathbf{v}_\Gamma = 0.5$ do not produce a larger area of turbulent production when compared to the $\mathbf{v}_\Gamma = 0.2$. This is explained by the larger area the covered by the turbulent intensity shown in figure 5.31 for $\mathbf{v}_\Gamma = 0.2$ when compared to $\mathbf{v}_\Gamma = 0.5$.

The channel $\mathbf{v}_\Gamma = \infty$ channel was also checked in this study but it did not yield results any more elucidating than found in the previous section. The flow was shown to stay relatively coherent, in terms of dissipation and production, with a decrease in dissipation in the cavity and an increase in production consistent with figure 5.39-5.40.

5.3.3 Summary

The findings in section 5.3 show that for velocities of the order of u_τ, the dynamic wall has little to no effect on the flow until it begins to move into the cavity left by the wall after full recession has occurred, $L_{y100\%}$. For all of the standard turbulent measures (production, dissipation, mean shear, and turbulent intensity) the wall velocities of the order of u_τ change very little until the turbulent area above the wall where they begins to act similar to the channel expanded with $\mathbf{v}_\Gamma = \infty$. For the needs of this study, especially in chapter 6, these velocities,($\mathbf{v}_\Gamma = 1$, 2 4), as well as the slowest velocity, $\mathbf{v}_\Gamma = 0.01$, were not studied in depth.

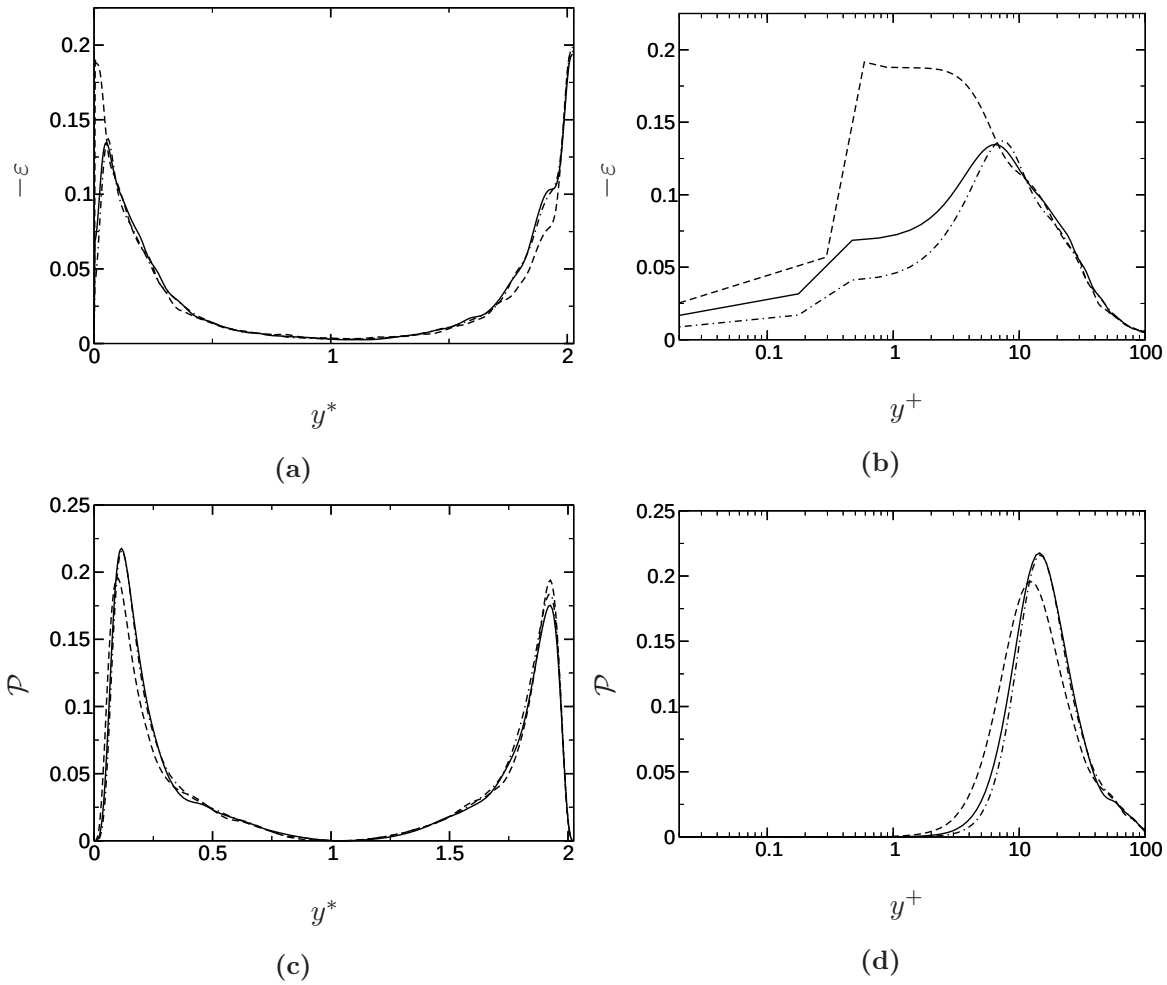

Figure 5.41: $(- - -)$ $\mathbf{v}_\Gamma = 0.01$, $(\text{——})\mathbf{v}_\Gamma = 0.1$, $(- \cdot -)$ $\mathbf{v}_\Gamma = 0.2$ **a.) Expanding channel ε and $\mathcal{P}$ data for 10% expansion. b.) Expanding channel ε and $\mathcal{P}$ data for 10% expansion for the IB half of the channel, in wall units.**

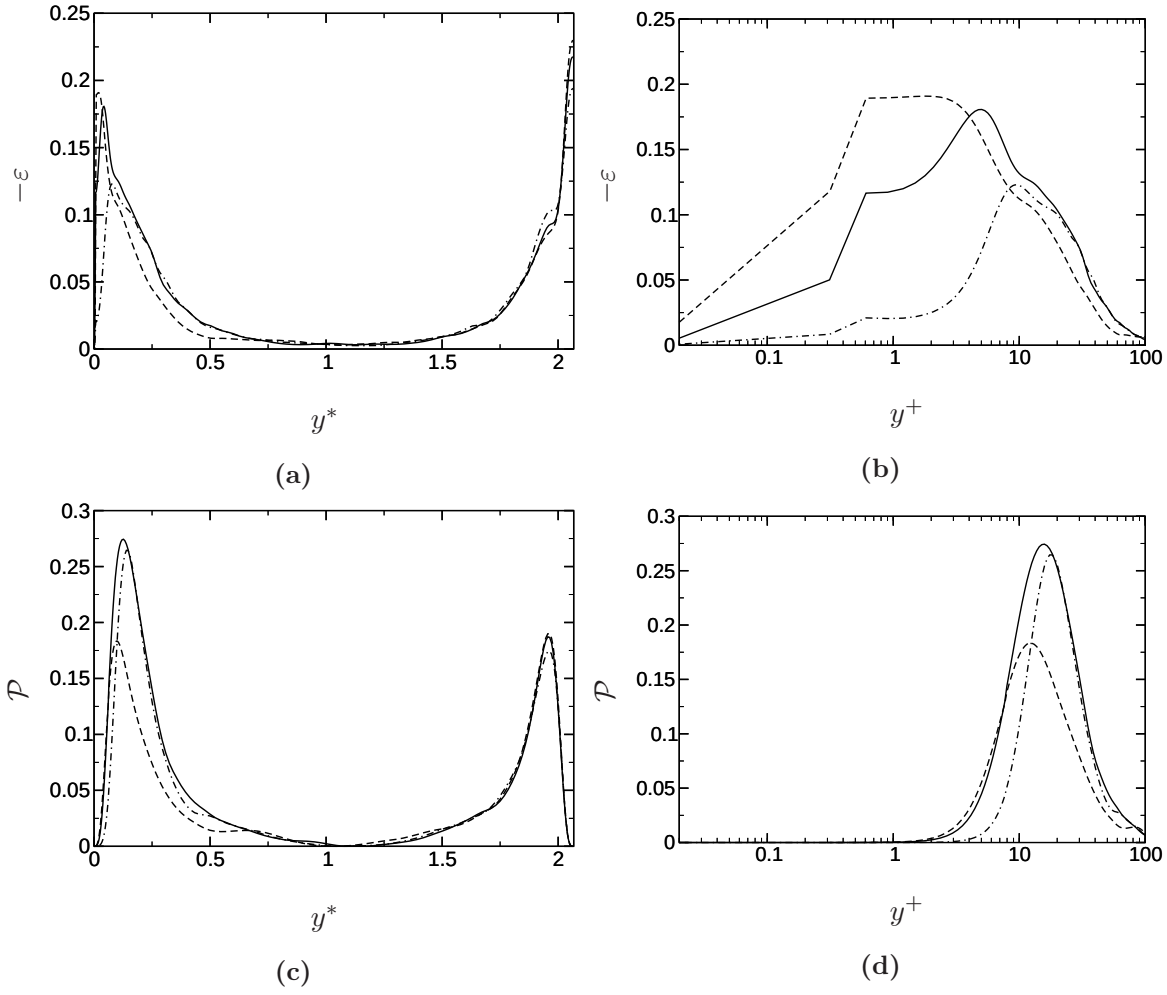

Figure 5.42: $(- - -)$ $\mathbf{v}_\Gamma = 0.01$, $(\text{——})\mathbf{v}_\Gamma = 0.1$, $(- \cdot -)$ $\mathbf{v}_\Gamma = 0.2$ **a.) Expanding channel ε and $\mathcal{P}$ data for 25% expansion. b.) Expanding channel ε and $\mathcal{P}$ data for 25% expansion for the IB half of the channel, in wall units.**

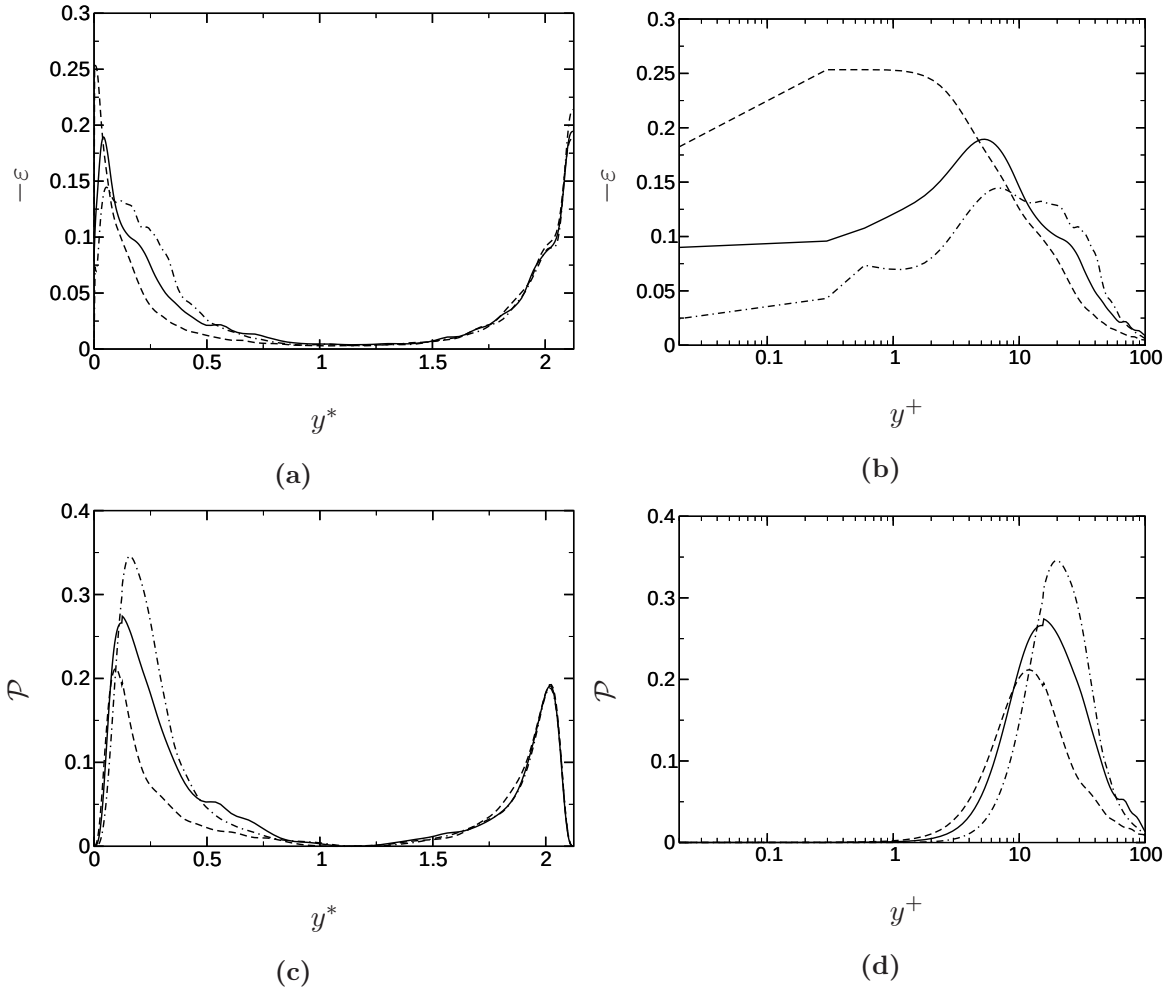

Figure 5.43: $(- - -)$ $\mathbf{v}_\Gamma = 0.01$, $(\text{——})\mathbf{v}_\Gamma = 0.1$, $(- \cdot -)$ $\mathbf{v}_\Gamma = 0.2$ **a.) Expanding channel ε and $\mathcal{P}$ data for 50% expansion. b.) Expanding channel ε and $\mathcal{P}$ data for 50% expansion for the IB half of the channel, in wall units.**

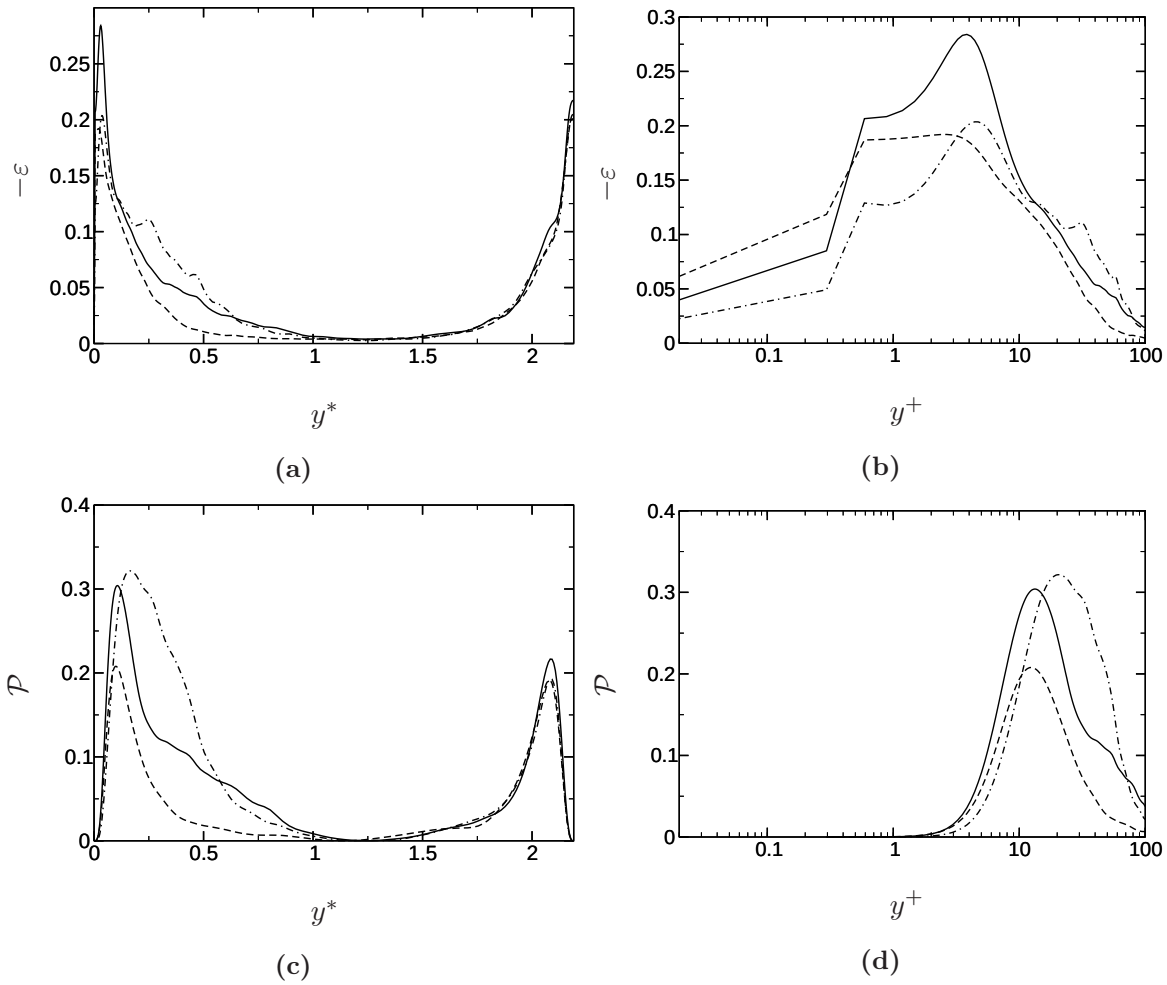

Figure 5.44: $(- - -)\,\mathbf{v}_\Gamma = 0.01$, $(\text{——})\mathbf{v}_\Gamma = 0.1$, $(- \cdot -)\,\mathbf{v}_\Gamma = 0.2$ **a.) Expanding channel ε and $\mathcal{P}$ data for 75% expansion. b.) Expanding channel ε and $\mathcal{P}$ data for 75% expansion for the IB half of the channel, in wall units.**

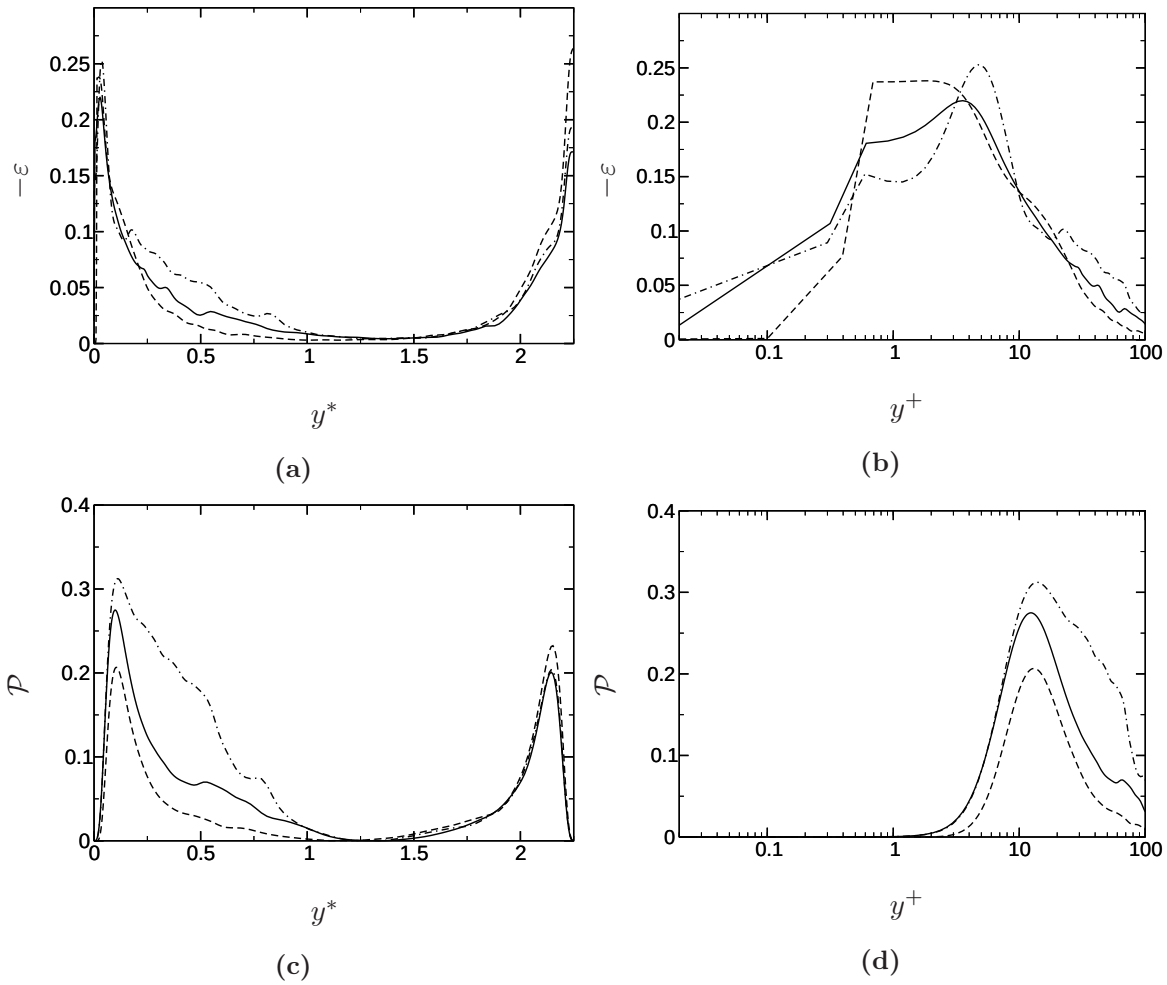

Figure 5.45: $(- - -)\,\mathbf{v}_\Gamma = 0.01$, $(\text{——})\mathbf{v}_\Gamma = 0.1$, $(- \cdot -)\,\mathbf{v}_\Gamma = 0.2$ **a.) Expanding channel ε and $\mathcal{P}$ data for 100% expansion. b.) Expanding channel ε and $\mathcal{P}$ data for 100% expansion for the IB half of the channel, in wall units.**

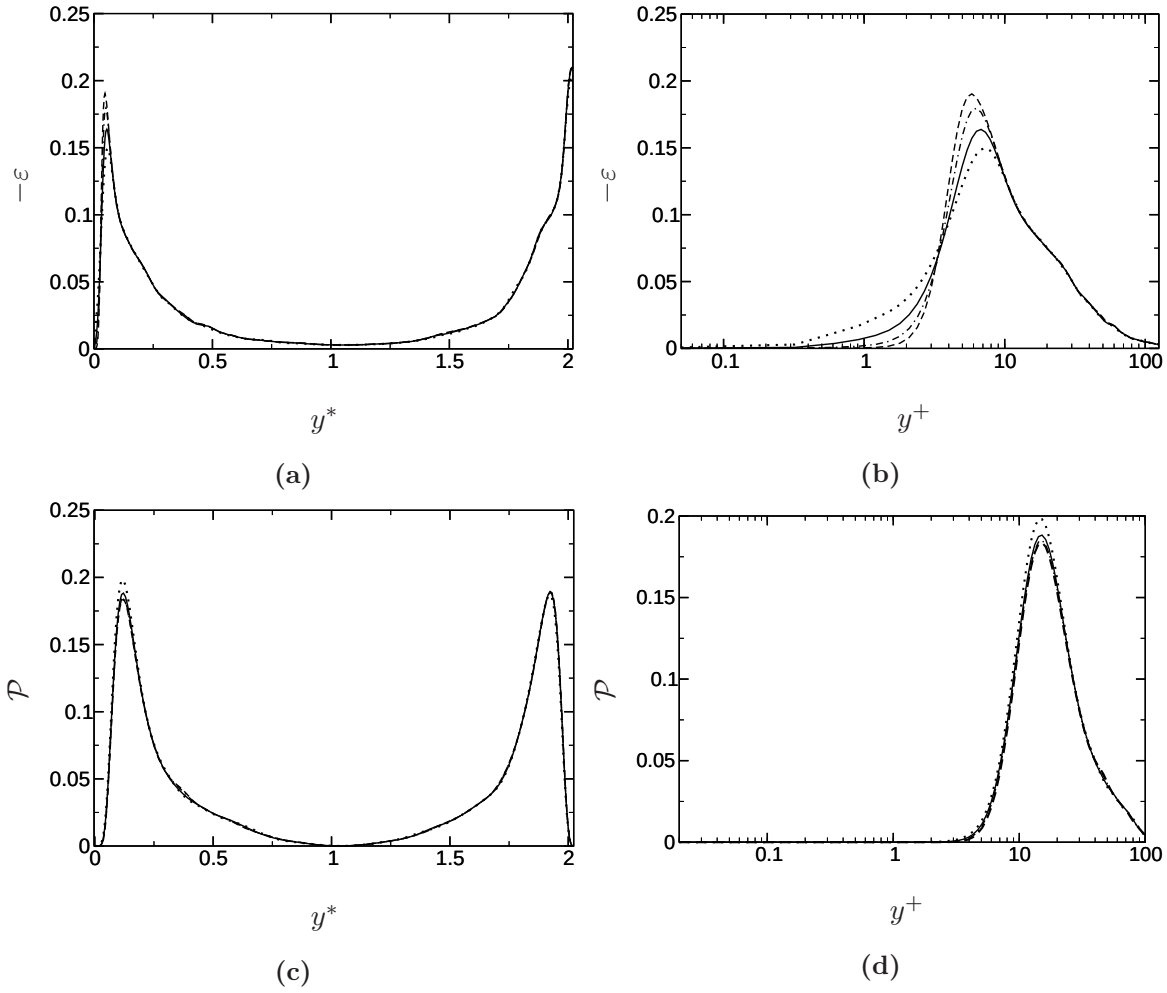

Figure 5.46: $(- - -)\,\mathbf{v}_\Gamma = 4$, $(- \cdot -)\,\mathbf{v}_\Gamma = 2$, $(\text{——})\mathbf{v}_\Gamma = 1$, $(\cdots)\,\mathbf{v}_\Gamma = 0.5$ **a.) Expanding channel ε and $\mathcal{P}$ data for 10% expansion. b.) Expanding channel ε and $\mathcal{P}$ data for 10% expansion for the IB half of the channel, in wall units.**

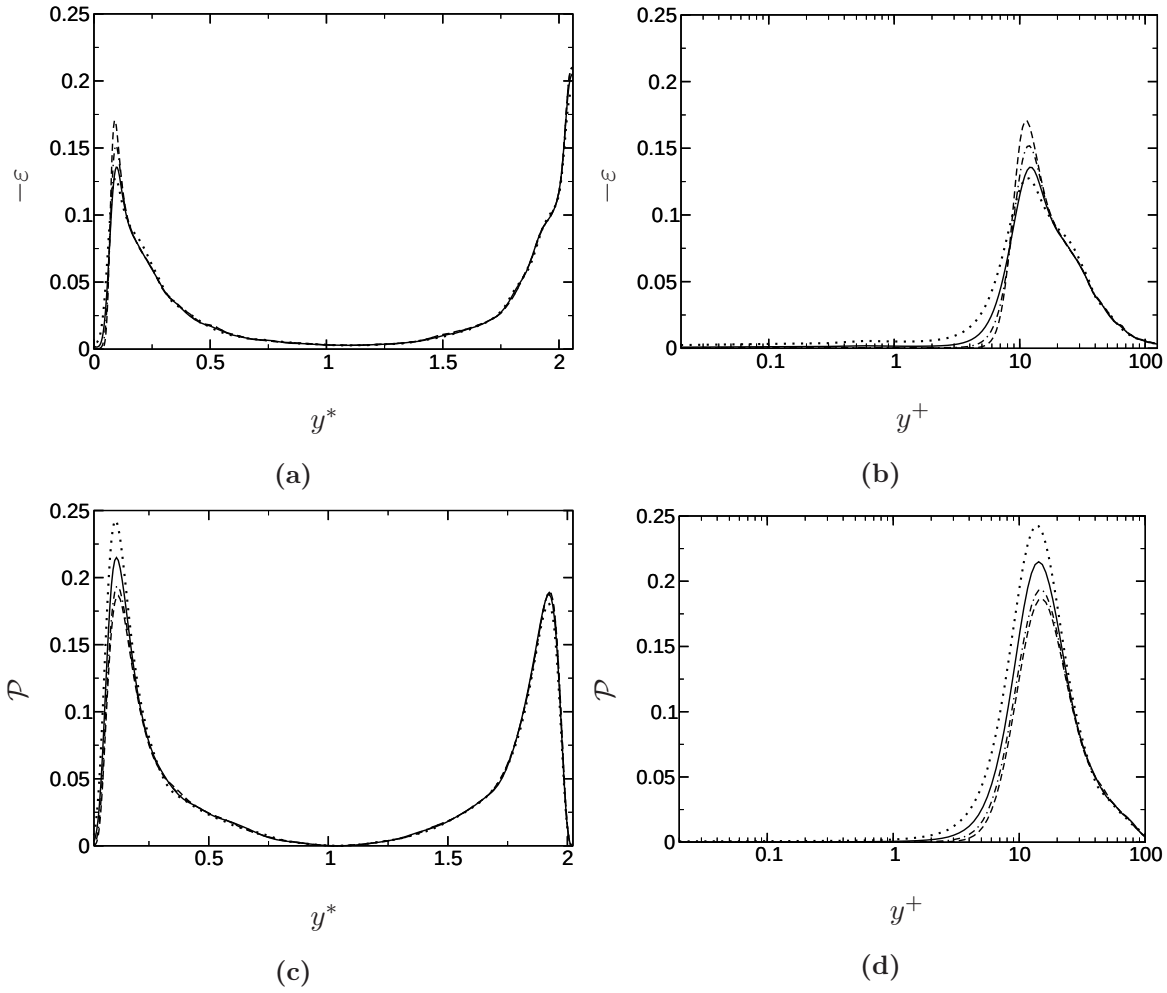

Figure 5.47: $(- - -)\,\mathbf{v}_\Gamma = 4$, $(- \cdot -)\,\mathbf{v}_\Gamma = 2$, $(\text{——})\mathbf{v}_\Gamma = 1$, $(\cdots)\,\mathbf{v}_\Gamma = 0.5$ **a.) Expanding channel ε and $\mathcal{P}$ data for 25% expansion. b.) Expanding channel ε and $\mathcal{P}$ data for 25% expansion for the IB half of the channel, in wall units.**

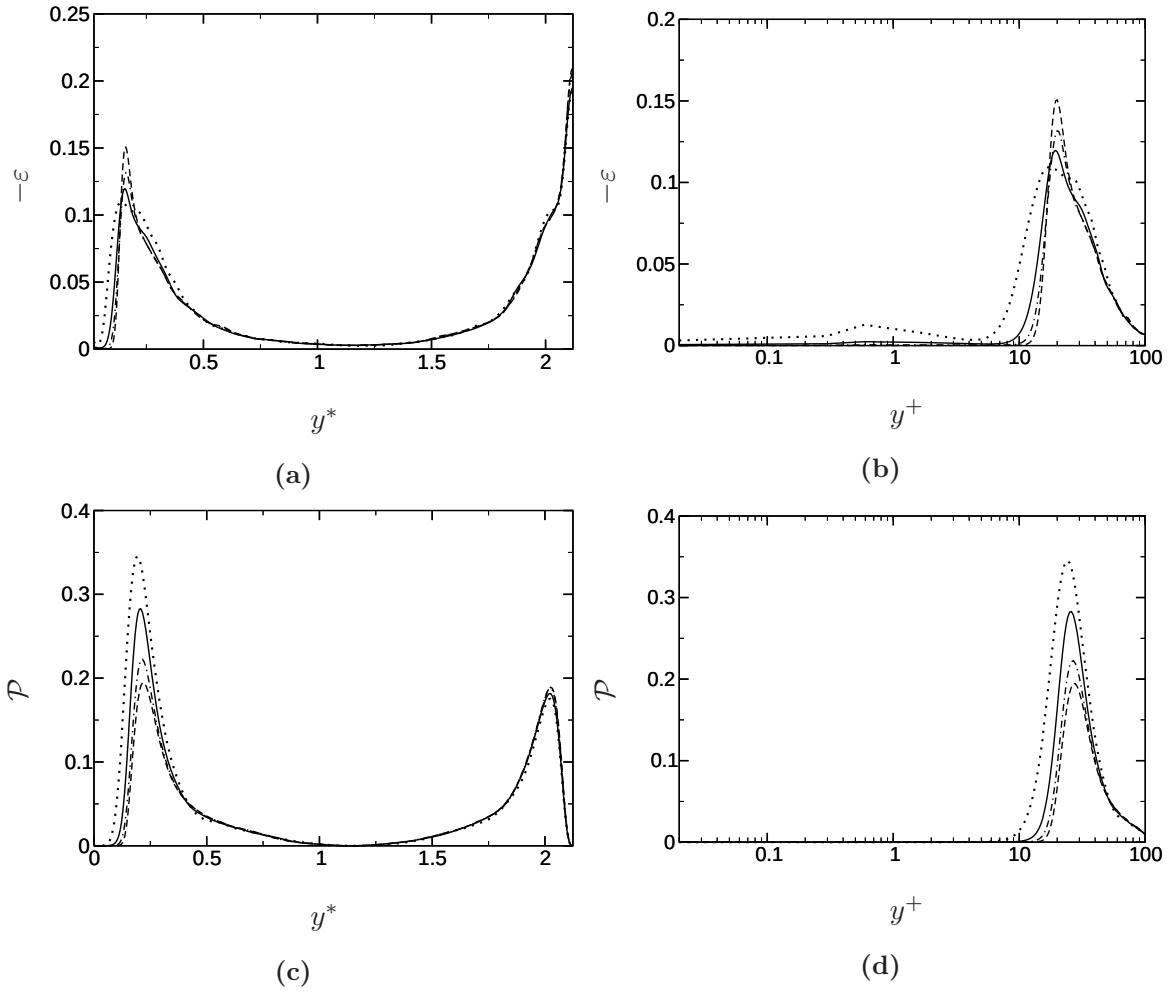

Figure 5.48: $(- - -)\,\mathbf{v}_\Gamma = 4$, $(- \cdot -)\,\mathbf{v}_\Gamma = 2$, $(\text{——})\mathbf{v}_\Gamma = 1$, $(\cdots)\,\mathbf{v}_\Gamma = 0.5$ **a.) Expanding channel ε and $\mathcal{P}$ data for 50% expansion. b.) Expanding channel ε and $\mathcal{P}$ data for 50% expansion for the IB half of the channel, in wall units.**

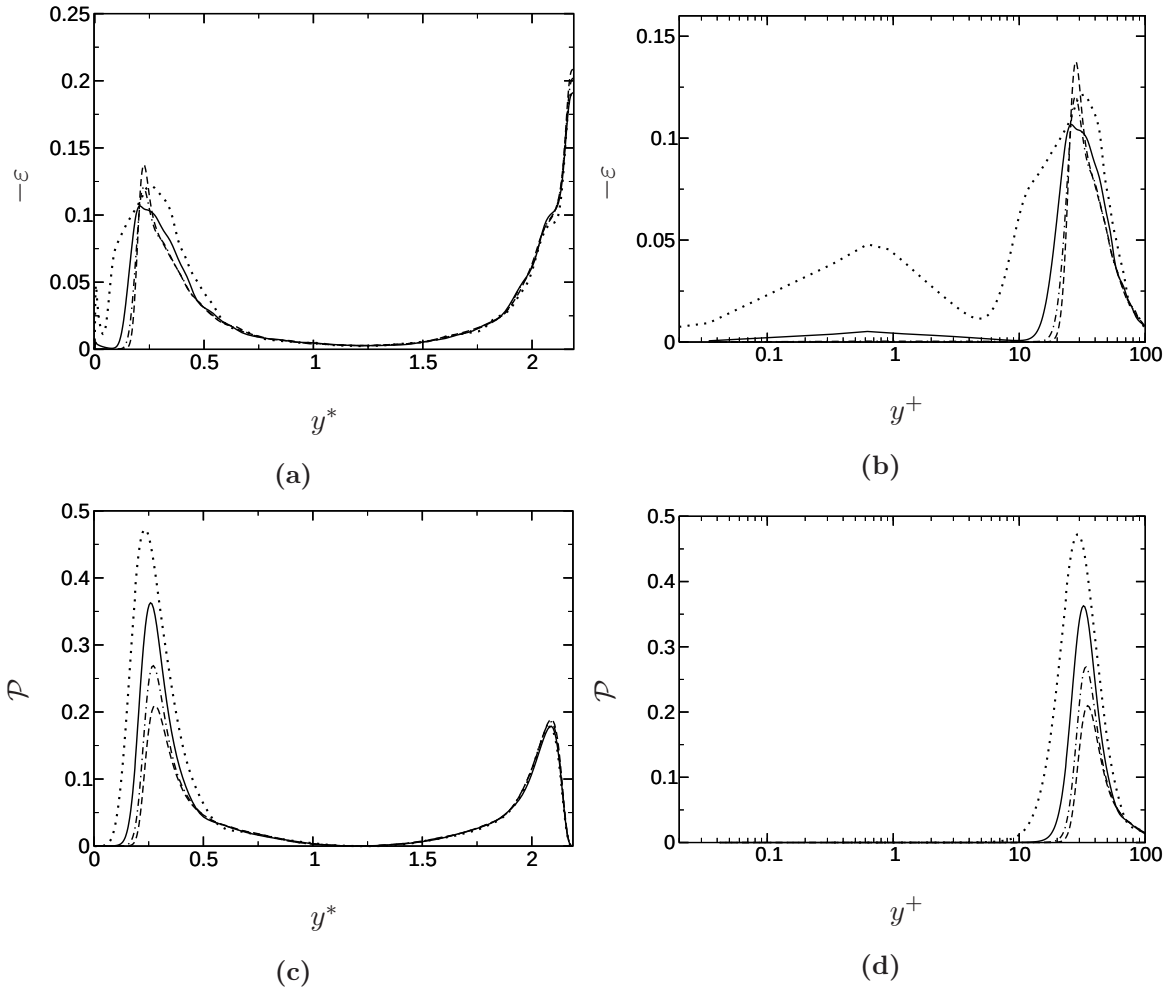

Figure 5.49: $(- - -)\,\mathbf{v}_\Gamma = 4$, $(- \cdot -)\,\mathbf{v}_\Gamma = 2$, $(\text{——})\mathbf{v}_\Gamma = 1$, $(\cdots)\,\mathbf{v}_\Gamma = 0.5$ **a.) Expanding channel ε and $\mathcal{P}$ data for 75% expansion. b.) Expanding channel ε and $\mathcal{P}$ data for 75% expansion for the IB half of the channel, in wall units.**

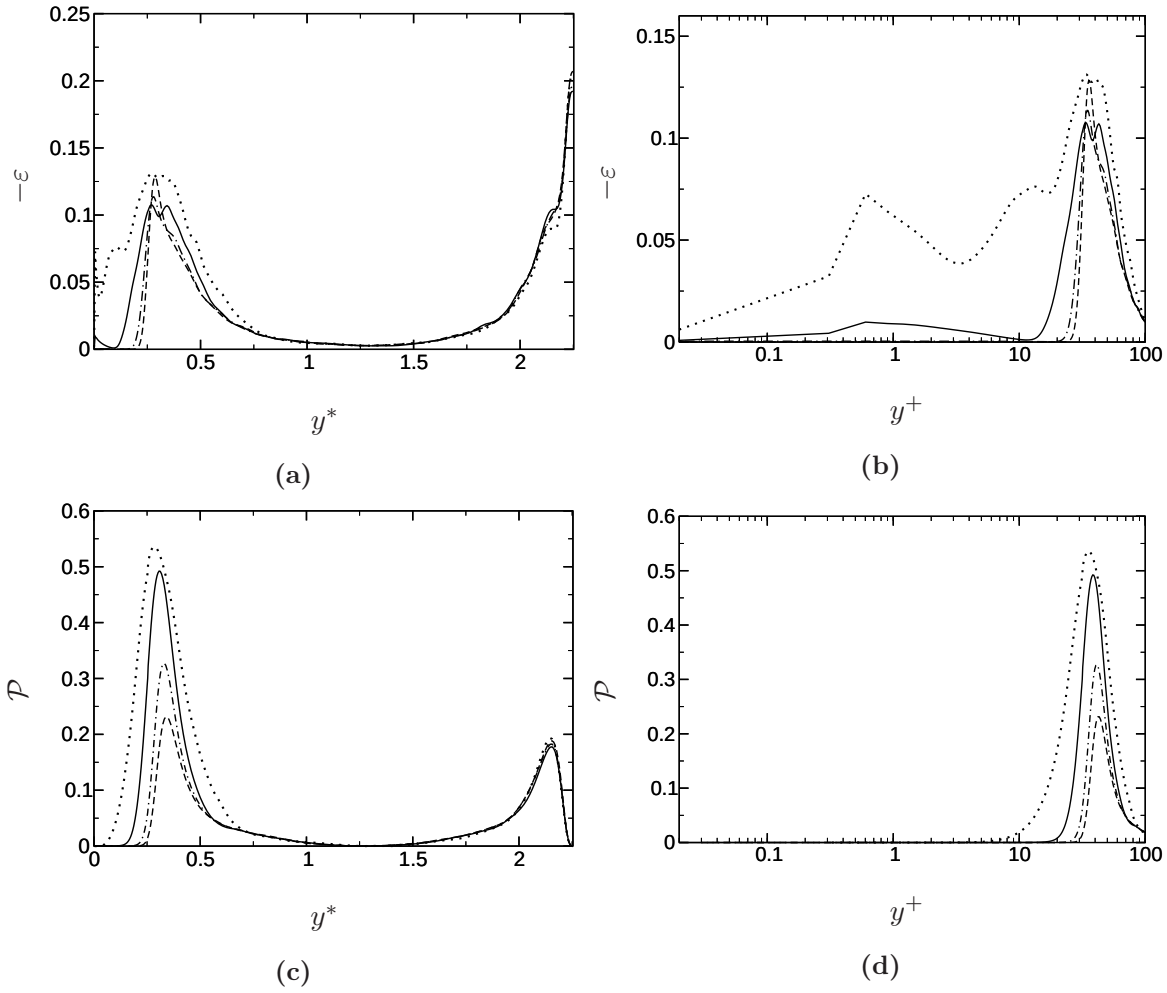

Figure 5.50: $(- - -)\,\mathbf{v}_\Gamma = 4$, $(- \cdot -)\,\mathbf{v}_\Gamma = 2$, $(\text{——})\mathbf{v}_\Gamma = 1$, $(\cdots)\,\mathbf{v}_\Gamma = 0.5$ **a.) Expanding channel ε and $\mathcal{P}$ data for 100% expansion. b.) Expanding channel ε and $\mathcal{P}$ data for 100% expansion for the IB half of the channel, in wall units.**

They were used to develop a regime where the wall recession velocity has an effect on the statistical steady state nature of the turbulence. Comprehensive studies of these velocities will be done in later works.

The wall velocities around the micro-scale velocity, $v_K \approx 0.23$, ($\mathbf{v}_\Gamma$ = 0.1, 0.2, 0.5) prove to be much more significant than their faster and slower counterparts on the coherent structures and non-equilibrium flow effects. At ($\mathbf{v}_\Gamma$ = 0.1, 0.2, 0.5) there is a noticeable increase in semi-streamwise vortices shown with Q in figures 5.13-5.15. There is also a decrease in dissipation in the wake of the receding wall. This is caused by a thin shear free layer (figures 5.19-5.28) which also causes an increases the turbulent production. The increase in production generates a wake of attenuated streak structures which are 20% larger and much wider than streaks seen in typical channel with $Re_{u_\tau} = 125$.

The importance of these findings is that in the wake of v_K order wall velocities the turbulent intensities increase and coherent structures grow larger. This is directly related to the mixing of the passive scalar in that turbulent wake. The increase in semi-streamwise vortices and the fluctuating velocities greatly increase mixing in the absence of gravity [158], [159], [160], and [161]. For future studies on ablation by the transport of a passive scalar this is notable.

Chapter 6

TURBULENT ABLATING CHANNEL

Laplacian The dynamics of an ablative wall in a heated, turbulent channel are assessed at different Stefan numbers while keeping all other parameters constant. As the channel expands due to material removal the pressure gradient is kept constant and all dynamic measurements are made after a short ablation period while keeping the Reynolds number consistent from the beginning of ablation to the end. The changing geometry of the wall is also assessed to determine if it has any noticeable effect on the turbulent structures and intensities.

6.1 Experimental Setup

The channel set up for ablative flow is the same channel as was shown in section 5.2 except that it is less resolved, $N_x = N_z = 64$ and $N_y = 128$. The reasons for this is touched upon in section 3.4.3. The scarified surface that produces a pressure Laplacian that requires numerous iterations, precludes FFTs, and non-symmetric relaxation can be seen in figures

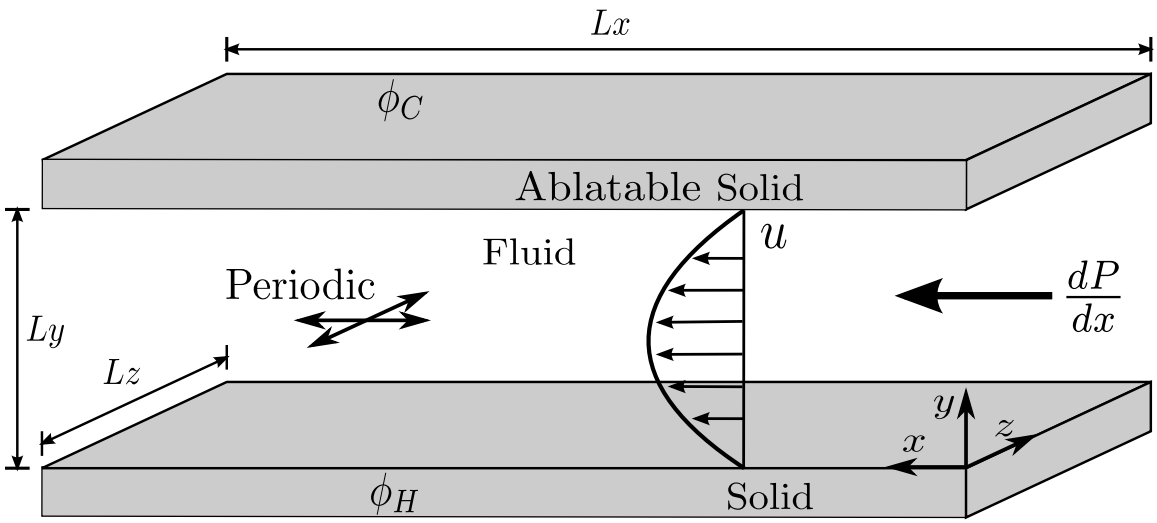

Figure 6.1: The dimensions of the IC channel showing periodicity in x and z. Lx,Ly, Lz the hot, ϕ_H and ϕ_C boundaries, and the abatable surface. The dimensions are all equivalent to figure 5.7.

6.3-6.5 for higher Stefan number, Ste, simulations. Owing to the coarse mesh, this condition causes non-physical solutions. As such, the simulations were only run until 50% of the abatable material was removed and most of the analyses are done in the linear regions shown in figures 6.24b at $V/V_o = 30\%$. Other than the difference in node numbers the geometry of the experiment is ostensibly the same as that in chapter 5 (see figure 6.1). The channel is heated from one side and is let run with no ablation until it reaches a thermal and dynamic statistical steady state. When ablation is started, as in section 3.5 the critical melting/ablation temperature, ϕ_m, is set just below the average surface temperature at steady state using an approach similar to [162] and [163]. The dimensions are the same, as well as the momentum parameters (see equations 5.8 and 6.1 and section 5.2). The additional dimensionless parameters used in the simulation are,

$$\begin{aligned} \phi^* &= \frac{\phi - \phi_C}{\phi_H - \phi_C} & \mathbf{u}^* &= \mathbf{u}\left[\frac{1}{u_\tau}\right] & \boldsymbol{x}^* &= \boldsymbol{x}\left[\frac{1}{Ly/2}\right] & t^* &= t\left[\frac{u_\tau}{Ly/2}\right] \\ Re &= \frac{u_\tau Ly/2}{\nu} & Pr &= \frac{\alpha_f}{\nu} & P^* &= P\left[\frac{1}{\rho_f u_\tau^2}\right] \end{aligned} \tag{6.1}$$

where $Pr = 1$, $\alpha_s/\alpha_f = 10$, $Re = 125$, $\rho_s = \rho_f$, $cp_s = cp_f$, and they are used to non-dimensionalized equations 2.2,

$$\partial_t \mathbf{u}^* + \boldsymbol{\nabla}^* \cdot (\mathbf{u}^* \otimes \mathbf{u}^*) = -\boldsymbol{\nabla}^* \cdot \mathbb{I} P^* + \frac{1}{Re_{u_\tau}} \boldsymbol{\nabla}^* \cdot \boldsymbol{\nabla}^* \mathbf{u}^* \tag{6.2}$$

2.1,

$$\nabla \cdot \mathbf{u}^* = 0 \tag{6.3}$$

2.4,

$$\partial_t \phi^* + \boldsymbol{\nabla}^* \cdot (\mathbf{u}^* \phi^*) = \frac{1}{Re_{u_\tau} Pr} \boldsymbol{\nabla}^* \cdot \boldsymbol{\nabla}^* \phi^* \tag{6.4}$$

2.4,

$$\partial_t \phi^* = \frac{\alpha_s}{\alpha_f} \frac{1}{Re_{u_\tau} Pr} \boldsymbol{\nabla}^* \cdot \boldsymbol{\nabla}^* \phi^* \tag{6.5}$$

2.10

$$\phi_s^* = \phi_f^*, \tag{6.6}$$

2.11

$$\frac{\alpha_s \rho_s cp_s}{\alpha_f \rho_f cp_f} \boldsymbol{\nabla}^* \phi_s^* \cdot \mathbf{n} = \boldsymbol{\nabla}^* \phi_f^* \cdot \mathbf{n} \tag{6.7}$$

and 2.14,

$$\mathbf{v}_\Gamma^* = \frac{Ste}{L_s Pr Re_{u_\tau}} \left[\frac{\alpha_s}{\alpha_f} \frac{\partial \phi^*}{\partial \mathbf{n}_{\Gamma s}^*} - \frac{\rho_f cp_f}{\rho_s cp_s} \frac{\partial \phi^*}{\partial \mathbf{n}_{\Gamma f}^*} \right] \quad \text{if} \quad \phi_\Gamma^* \geq \phi_m^*. \tag{6.8}$$

In the future the $(\cdot)^*$ will be omitted when referencing equations 6.2-6.8.

6.2 Results

6.2.1 Flow Topology and Dynamics

As the channel ablates and the solid mass in the wall normal direction decreases, the peaks and valleys can be readily seen in figures 6.3-6.8 to be increasing in height and depth as the *Ste* increases for the given volume removal. Figures 6.3-6.8 also show that as the *Ste* is reduced the ablatable surface flattens and does not have such noticeable peaks and

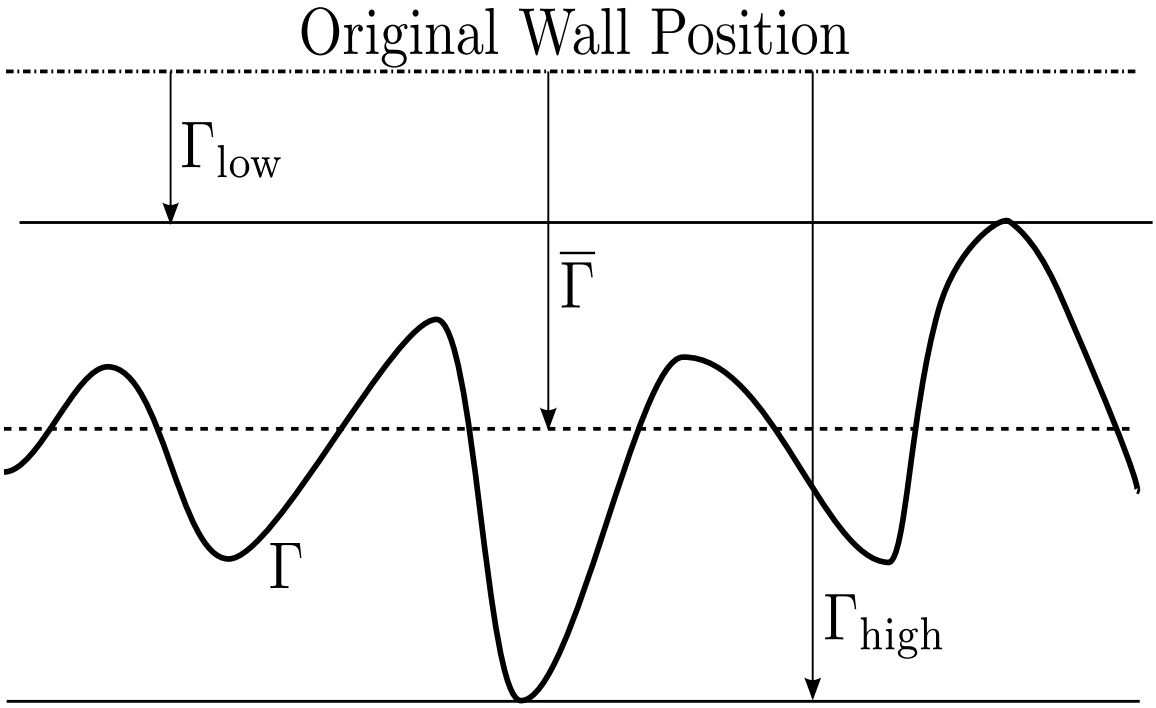

Figure 6.2: The surface heights and average height, $\overline{\Gamma}$, used in surface topology and flow dynamics calculations.

valleys, as in figures 6.7 and 6.8 specifically. It shows that at $V/V_o = 30\%$ there is little to no deviation of the surface height from Γ_{low} to Γ_{high} for $Ste = 0.1$ and $Ste = 0.01$ when compared to the larger Stefan numbers. This phenomenon does not only occur at $V/V_o = 30\%$ but also occurs in the entire run up to $V/V_o = 30\%$ as seen in figures 6.30-6.26 where the variation of wall height is smaller than ℓ_{K}, from equation 5.2, for Re_{u_τ}.

Unlike in section 5.3.1, a cursory analysis of the semi-streamwise vortices in figures 6.3-6.8 show that they are not more abundant on the dynamic boundary side of the channel when compared to the stationary side. This would seem to be at odds with the results shown in chapter 5 where wall velocities, encompassing v_K, of $0.1 \geq \mathbf{v}_\Gamma \leq 0.5$ were shown to cause a distinct increase in the turbulent production, the height of the streaks, and a reduction in both dissipation and mean shear at the wall.

The lack of turbulent intensity increase is investigated with figures 6.9-6.14. Unlike

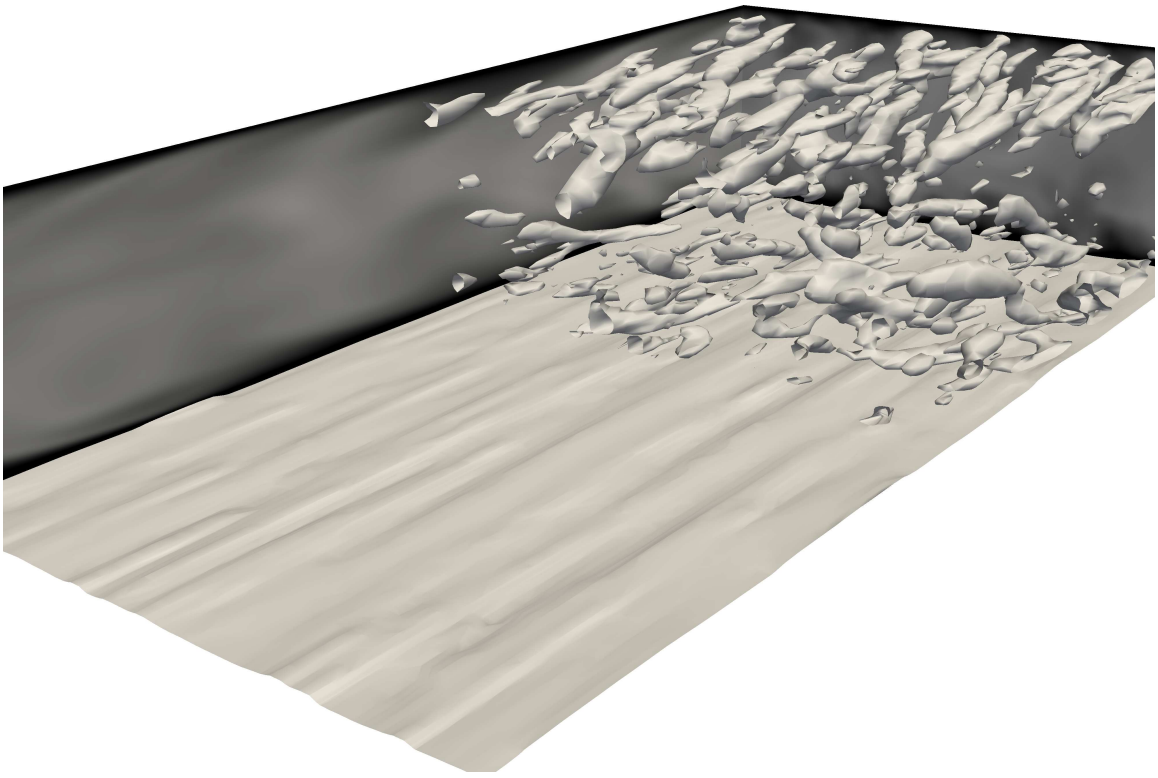

(a)

(b)

Figure 6.3: An ablating channel, at 30% solid volume loss, with $Ste = 2$, isosurfaces of $Q = 50$, and $u^{'}$ contours shown.

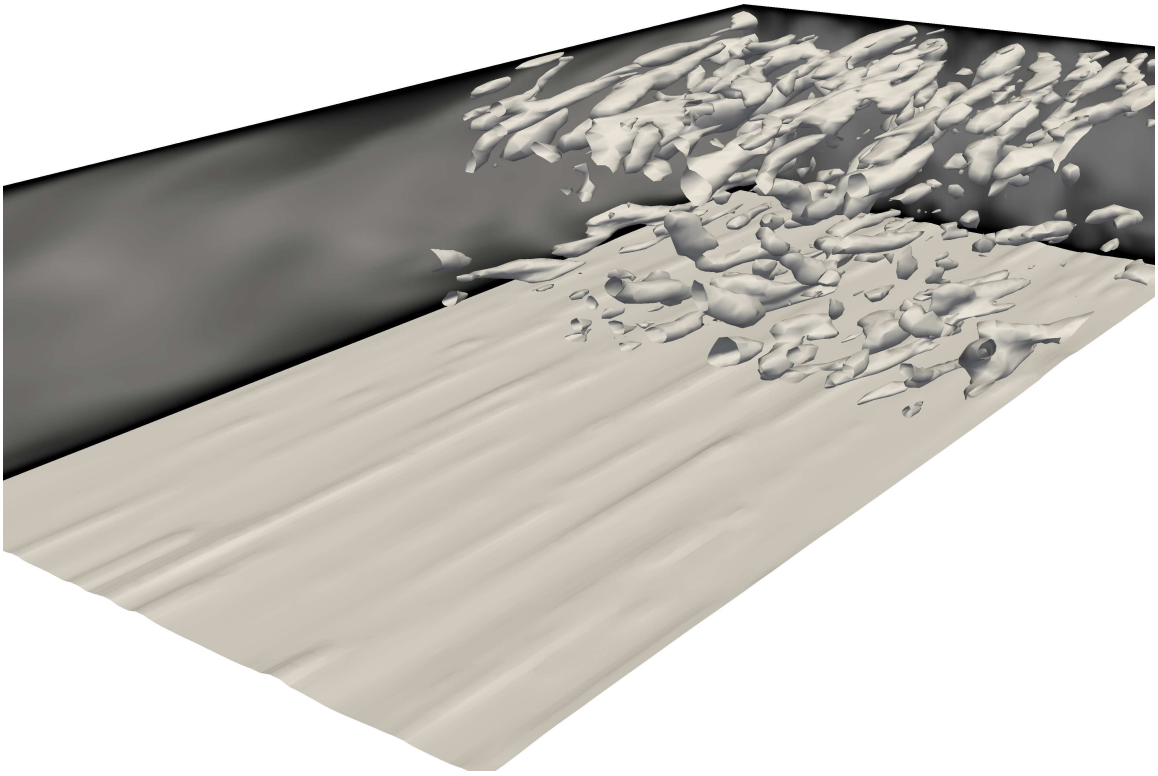

(a)

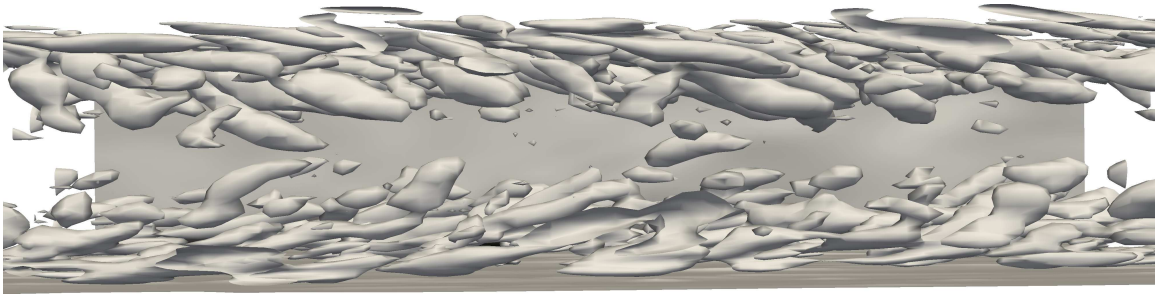

(b)

Figure 6.4: An ablating channel, at 30% solid volume loss, with $Ste = 1$, isosurfaces of $Q = 50$, and $u^{'}$ contours shown.

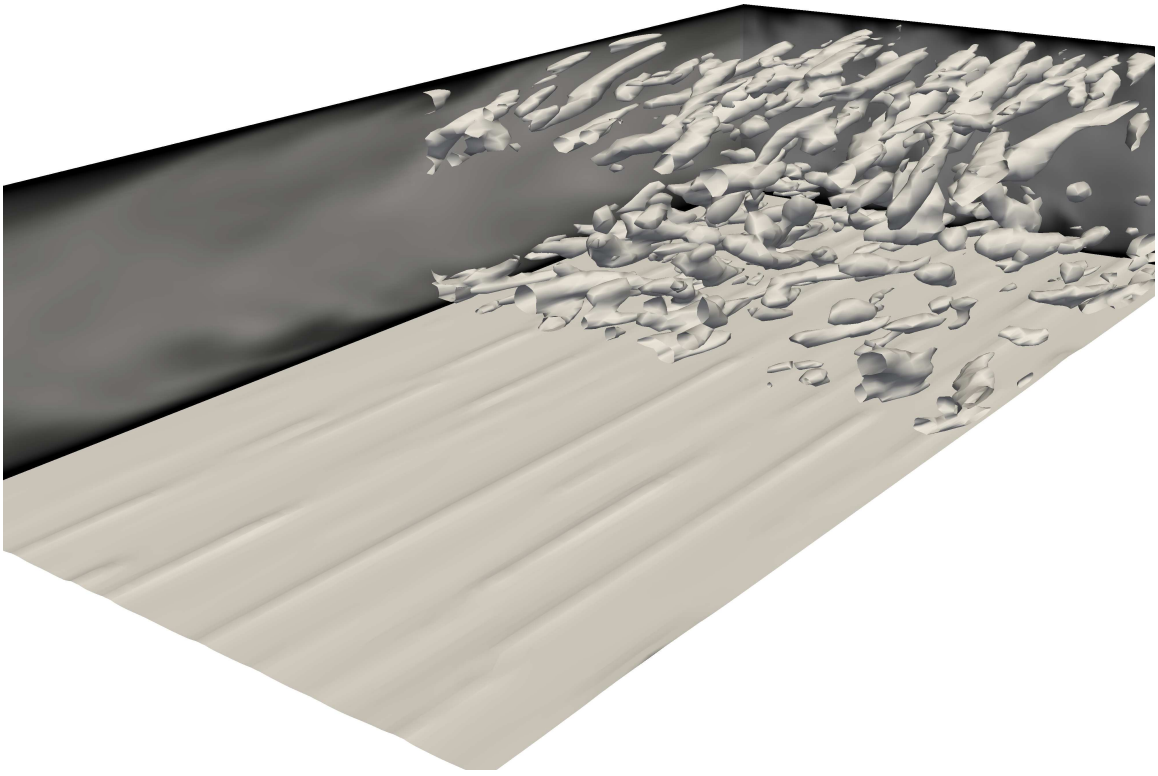

(a)

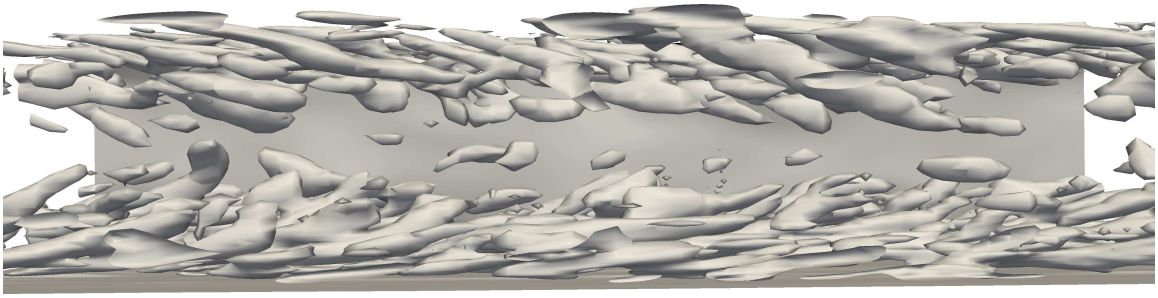

(b)

Figure 6.5: An ablating channel, at 30% solid volume loss, with $Ste = 0.5$, iso-surfaces of $Q = 50$, and $u^{'}$ contours shown.

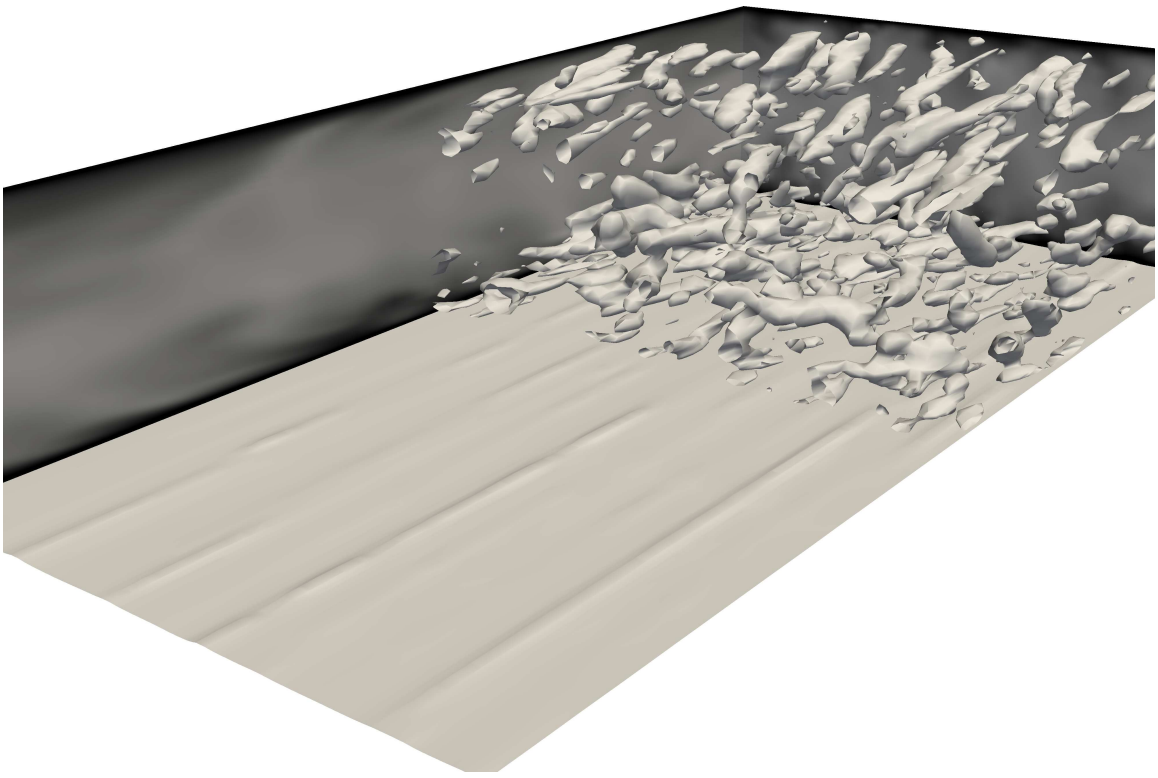

(a)

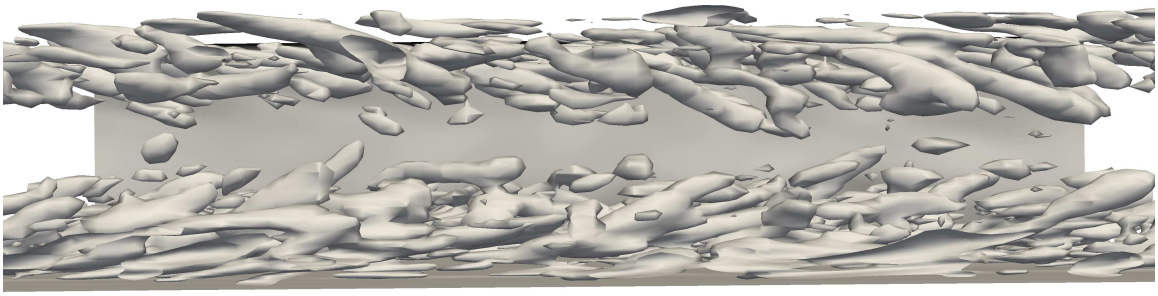

(b)

Figure 6.6: An ablating channel, at 30% solid volume loss, with $Ste = 0.25$, isosurfaces of $Q = 50$, and u' contours shown.

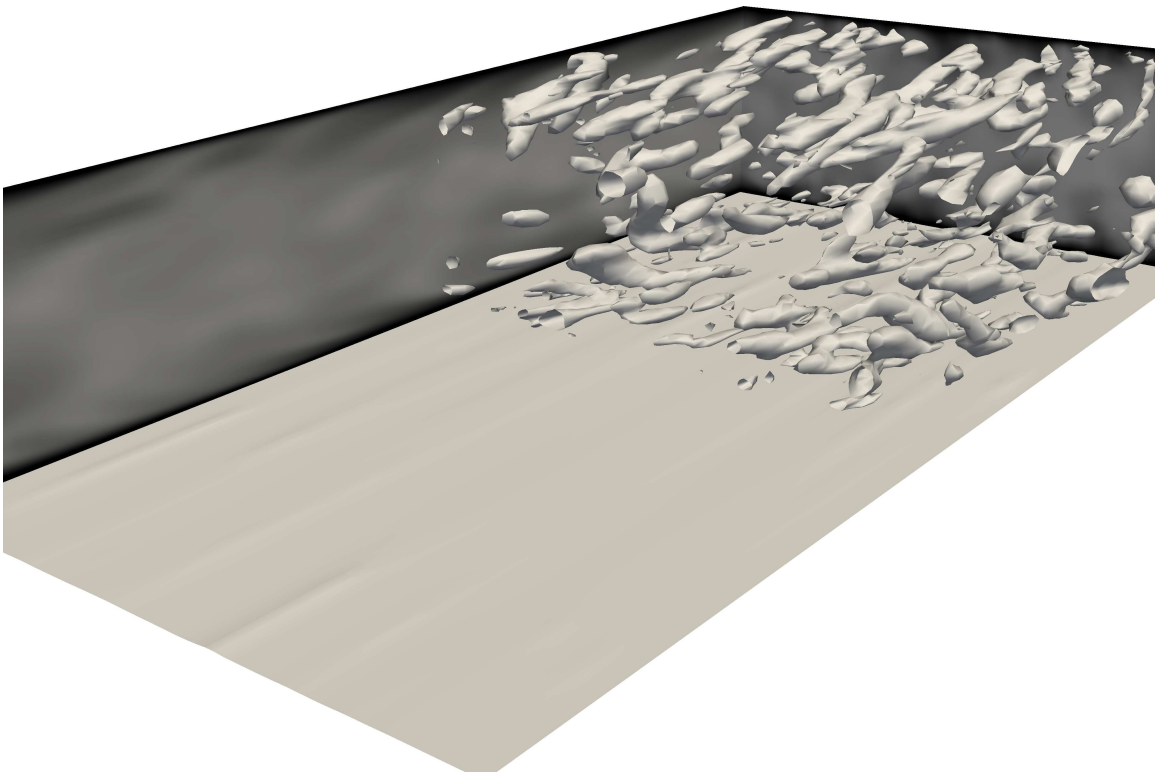

(a)

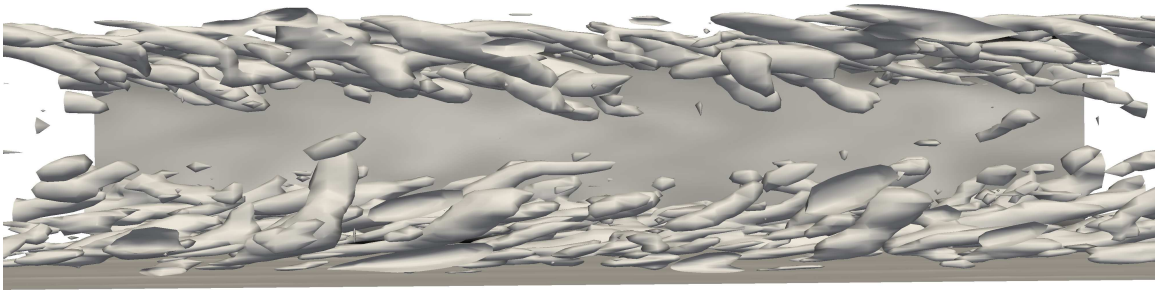

(b)

Figure 6.7: An ablating channel, at 30% solid volume loss, with $Ste = 0.1$, iso-surfaces of $Q = 50$, and $u^{'}$ contours shown.

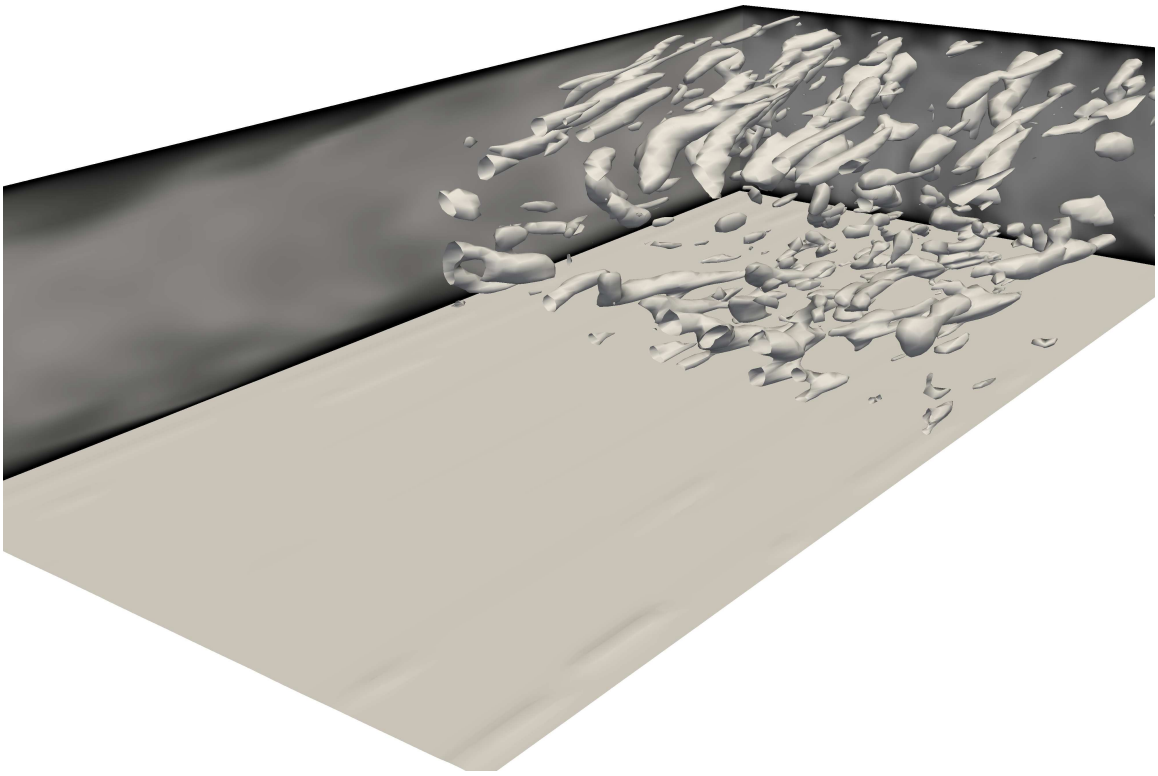

(a)

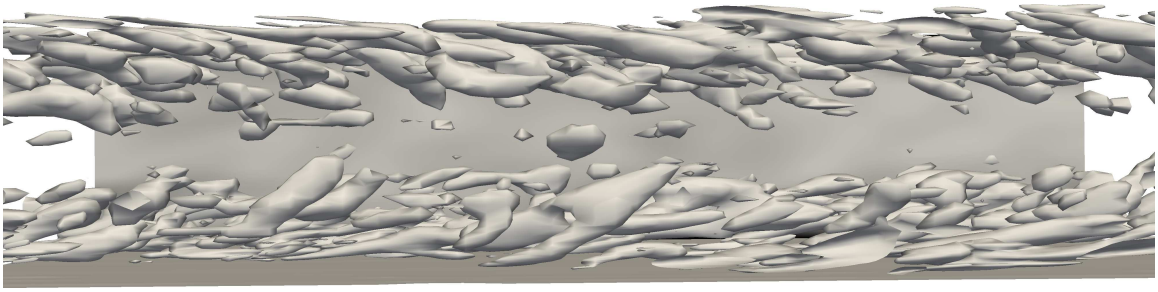

(b)

Figure 6.8: An ablating channel, at 30% solid volume loss, with $Ste = 0.01$, isosurfaces of $Q = 50$, and $u^{'}$ contours shown.

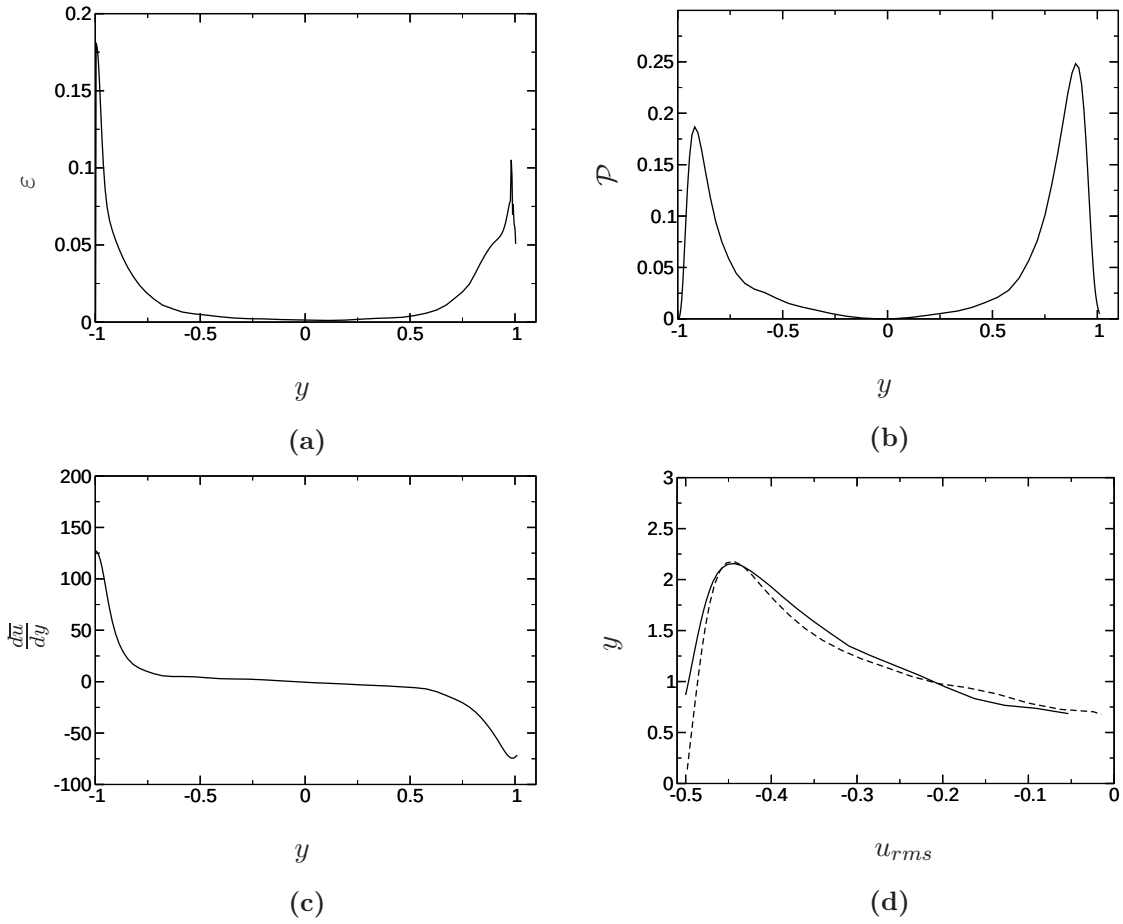

Figure 6.9: a.) The production b.) dissipation c.) mean shear and d.) u_{rms} **(ablating side (——)and, non-ablating side** $(- - -)$ **) for** $Ste = 2$ **at** $V/V_o = 30\%$**.**

section 5.3.1 there is also no substantial increase in production and decrease in dissipation. For all of the Ste tested there is a small increase in production and a small decrease in dissipation, but not as marked as that shown in figures 5.19-5.28. While the change in production and dissipation are uniform across Ste. There is a decrease in $d\overline{u}/dy$ by nearly half for $Ste \geq 1$ while the mean shear for $Ste < 1$ stays near the expected value of $d\overline{u}/dy = 125$; consistent for a $Re_{u_\tau} = 125$ channel (see figures 6.9c-6.14c). There is also no increase in the overall size or in the intensity of the streaks, as shown in figures 6.9d-6.14d, concurrent with that shown in figures 5.32-5.34.

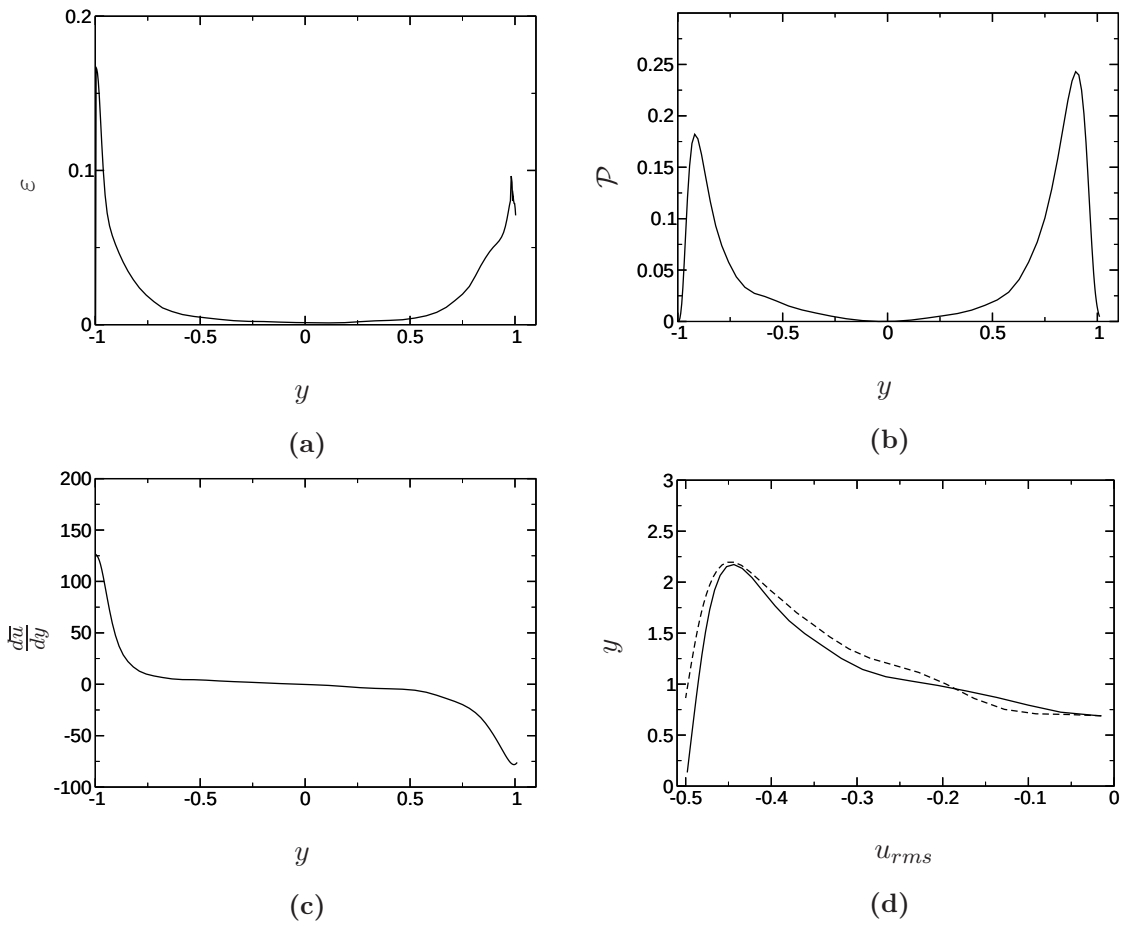

Figure 6.10: a.) The production b.) dissipation c.) mean shear and d.) u_{rms} (ablating side (——)and, non-ablating side $(- - -)$) for $Ste = 1$ at $V/V_o = 30\%$.

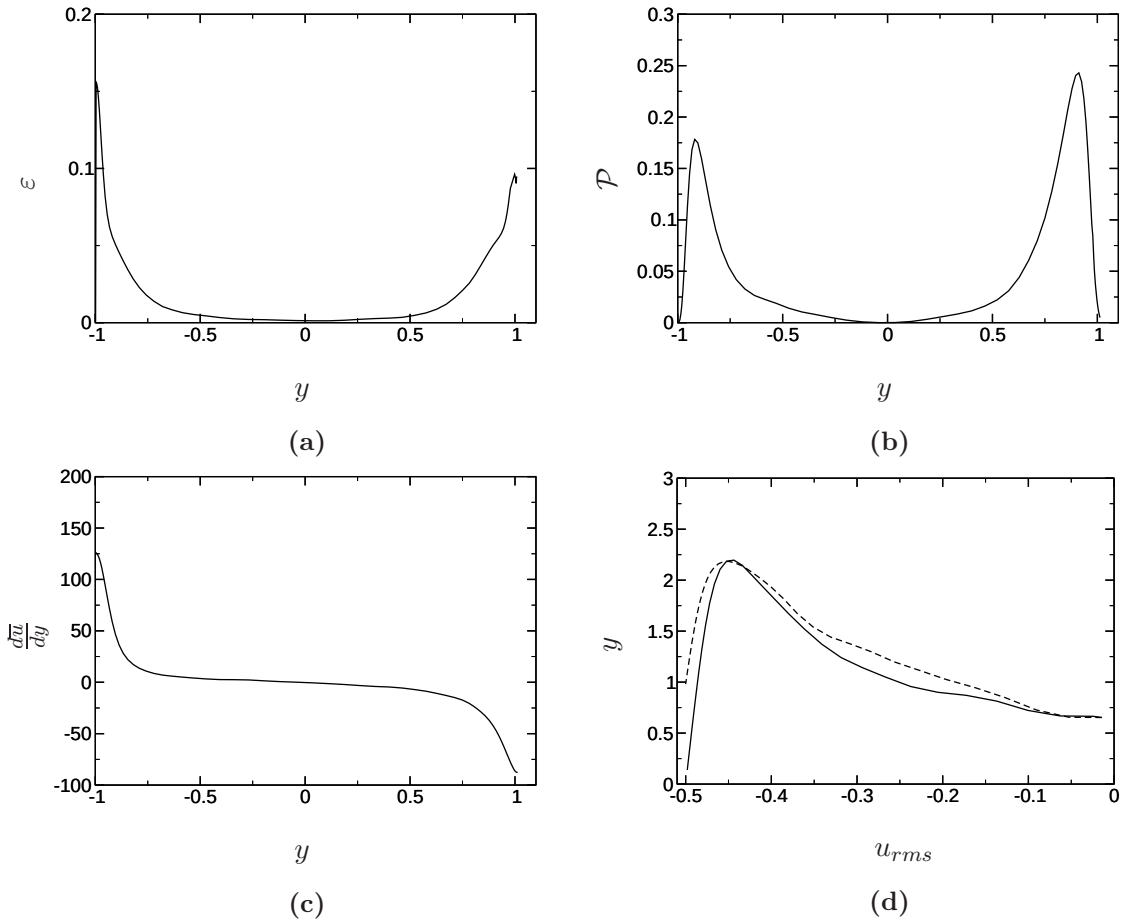

Figure 6.11: a.) The production b.) dissipation c.) mean shear and d.) u_{rms} (ablating side (——)and, non-ablating side $(- - -)$) for $Ste = 0.5$ at $V/V_o = 30\%$.

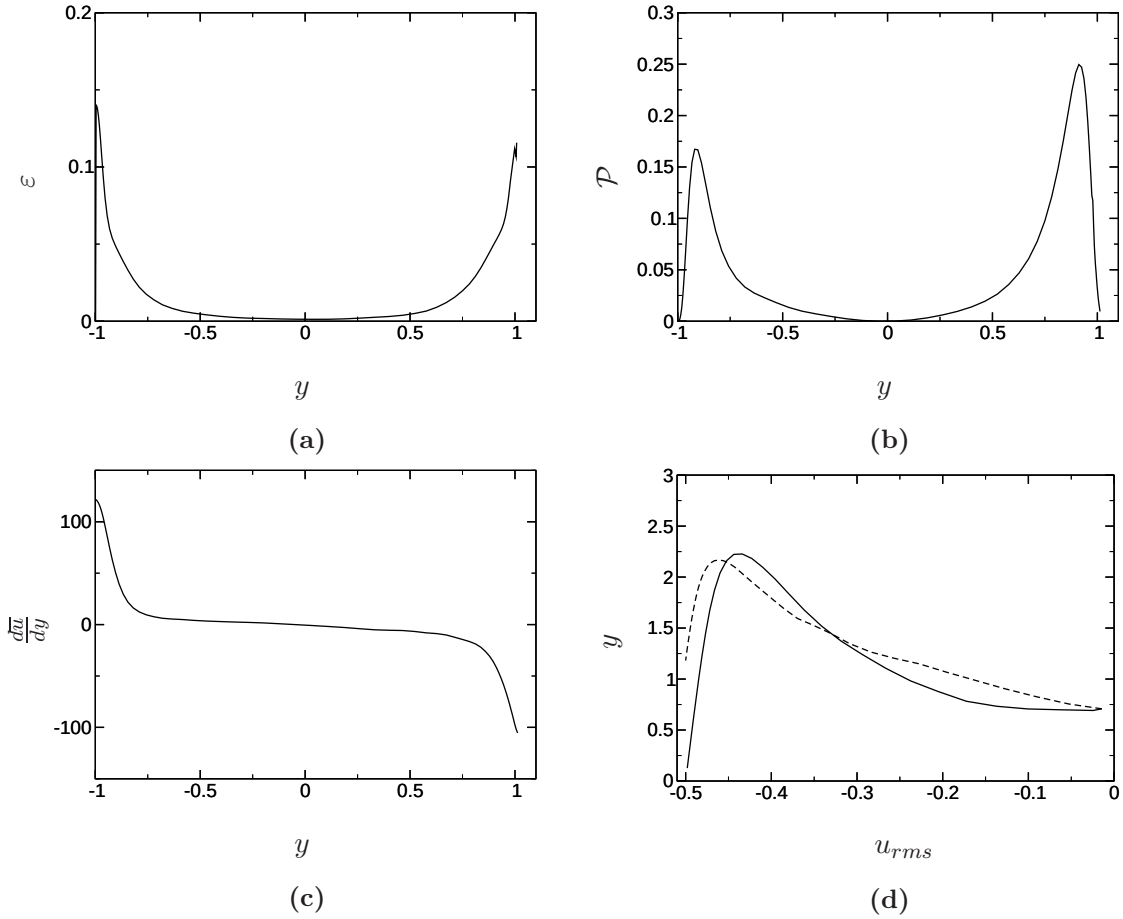

Figure 6.12: a.) The production b.) dissipation c.) mean shear and d.) u_{rms} (ablating side (——)and, non-ablating side $(- - -)$) for $Ste = 0.25$ at $V/V_o = 30\%$.

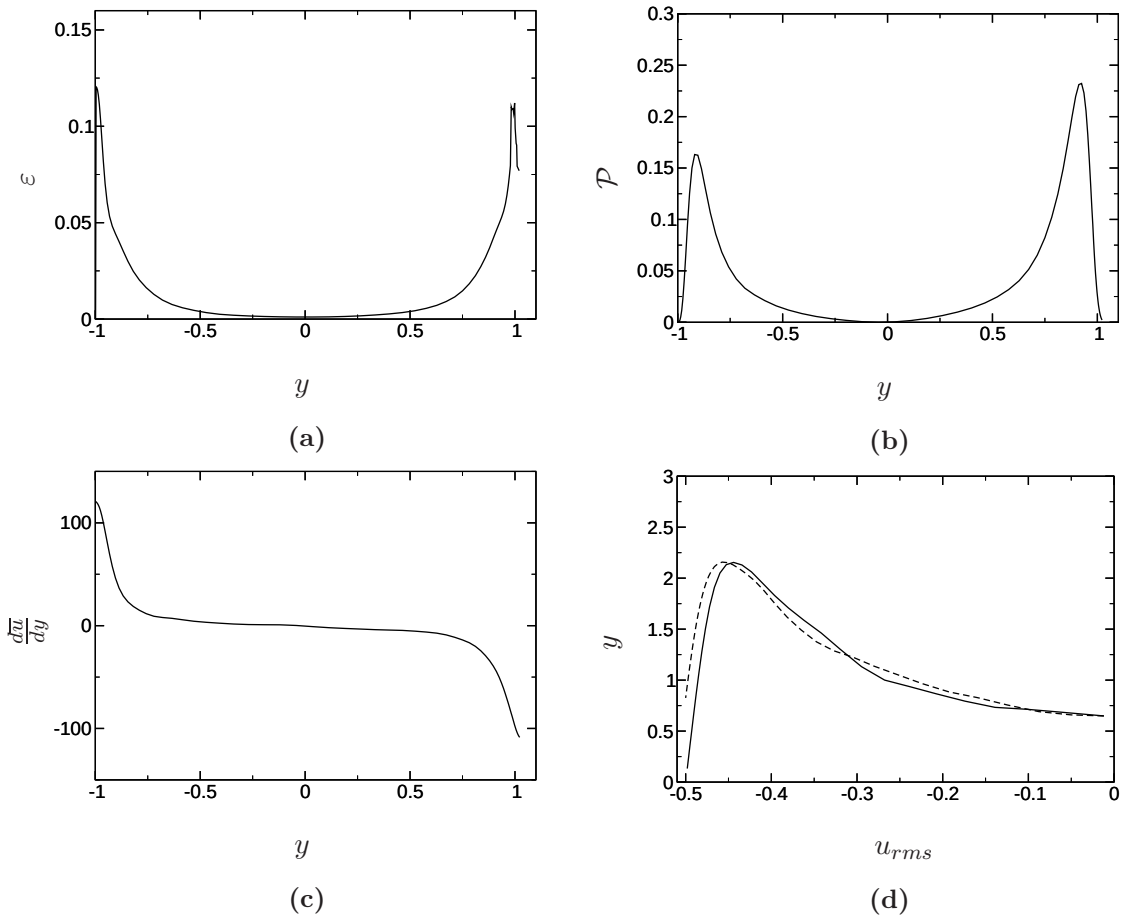

Figure 6.13: a.) The production b.) dissipation c.) mean shear and d.) u_{rms} (ablating side (——)and, non-ablating side $(- - -)$) for $Ste = 0.1$ at $V/V_o = 30\%$.

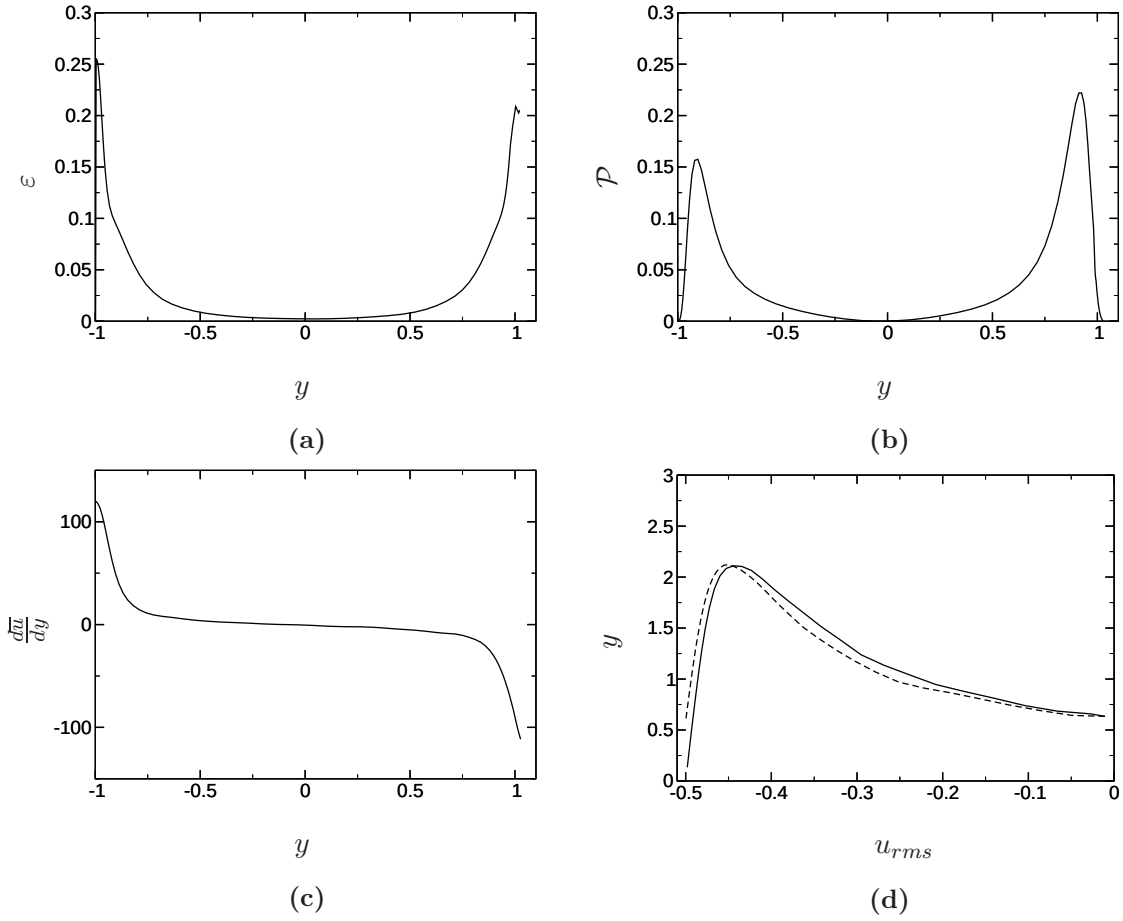

Figure 6.14: a.) The production b.) dissipation c.) mean shear and d.) u_{rms} **(ablating side (——)and, non-ablating side** $(- - -)$ **) for** $Ste = 0.01$ **at** $V/V_o = 30\%$**.**

The streak spacing is also of importance. The initial theory of this work was to assume the streaks, and their vortices, would convect higher ϕ to the ablative surface. This would cause the streak-vortex pairing to act like the side of an end-mill bit and auger out a cavity like the rounded size of a cylinder. The streaks would then tend to sit in the cavity and they would not wander back and forth across the channel as they typically do [164]. These sorts of channels are apparent in figures 6.5-6.6 on the ablated surface, particularly in figures 6.5a and 6.6a. This can be seen qualitatively by comparing the high and low velocity streaks just above the ablated surface and the height of the surface as is done in figures 6.15 and 6.16 for $Ste = 0.5$ and $Ste = 0.25$ where the valleys in the ablated wall correspond almost directly to the high speed velocity streaks near the wall.

The autocorrelation function is again used to determine the size of the structure where adjacent velocities correlate and their placement above the ablated surface. The algorithm starts by checking the first node in the channel in one slice of the nodes in the z-plane, at each particular height, specific to the different Ste numbers. The fluctuating velocity, $u'_{i,j,k}(y_{\text{check}})$ is compared to the nodes on either side of it in the same x-plane until they no longer correlate, giving the width, Ψ_{CS}, of the area of coherence. After each side of the coherent structure is found the center is located and the distance to the wall, ϖ_{CS}, and Γ_{high} are found. The "checking height", y_{check}s are referenced from Γ_{low}. The next point is tested to make sure it was not in the previous Ψ_{CS} and until a point outside Ψ_{CS} from the previous coherent structure is found to avoid doubly counting coherent structures on the y_{check}. This procedure is outlined in figure 6.17, and is done for all z planes. The search procedure is conducted at multiple y_{check}, above Γ_{low}, throughout the buffer and near wall layers. The resulting data are not in a very useful form. To make it more informative, a probability density function (PDF) is taken of the data using the discretization of $\delta_{\Gamma} = (\Gamma_{\text{high}} - \Gamma_{\text{low}})/5$ as the separate probability bins to pull Ψ_{CS} data from. This is used to find the probability of different sized coherent structure to be above wall cavities of different depths. The results are given in figures 6.18-6.19.

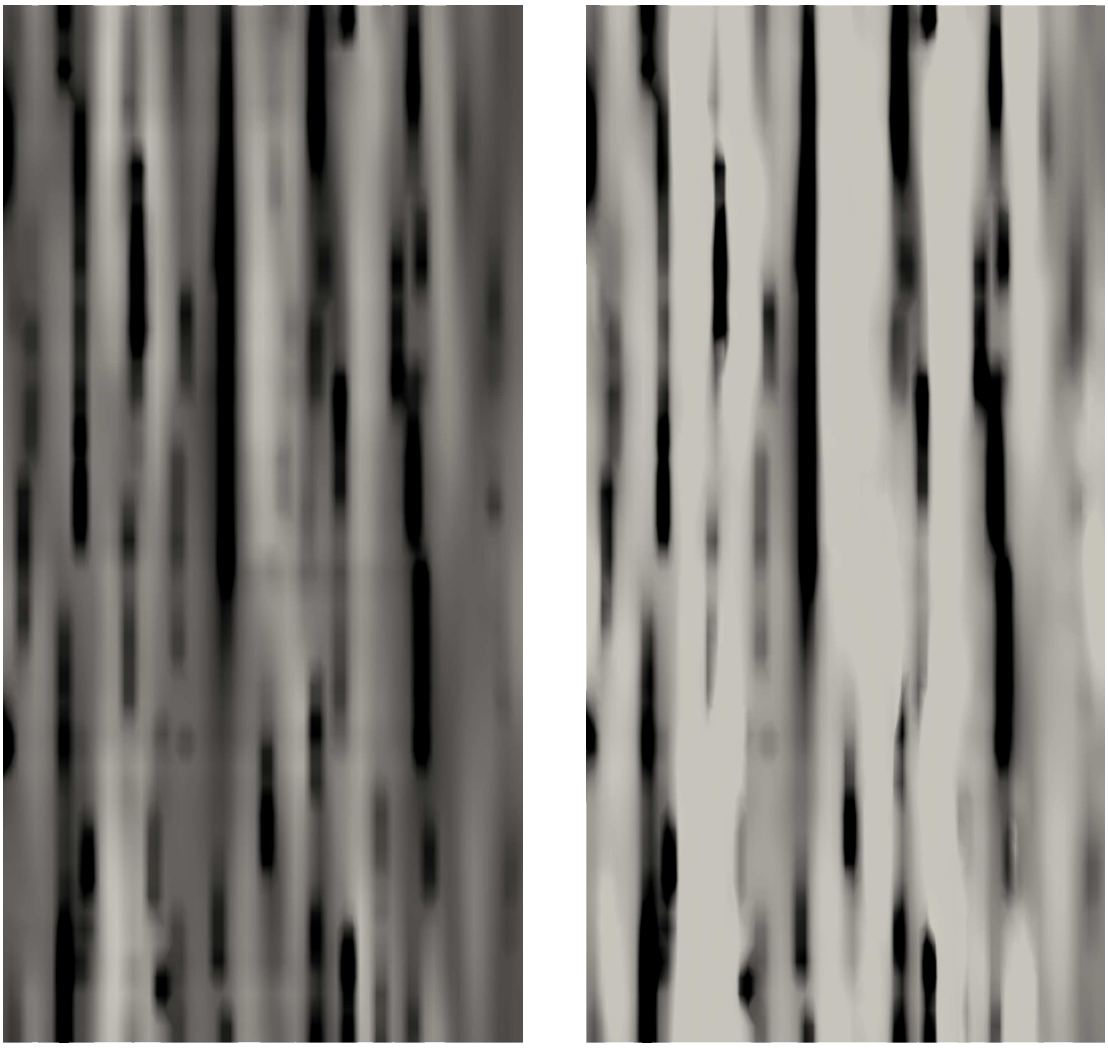

(a) (b)

Figure 6.15: For $Ste = 0.5$ a.) an elevation plot of the wall where lighter areas have been ablated more than the darker areas, and b.) a surface plot just above the ablated surface of $u^{'}$.

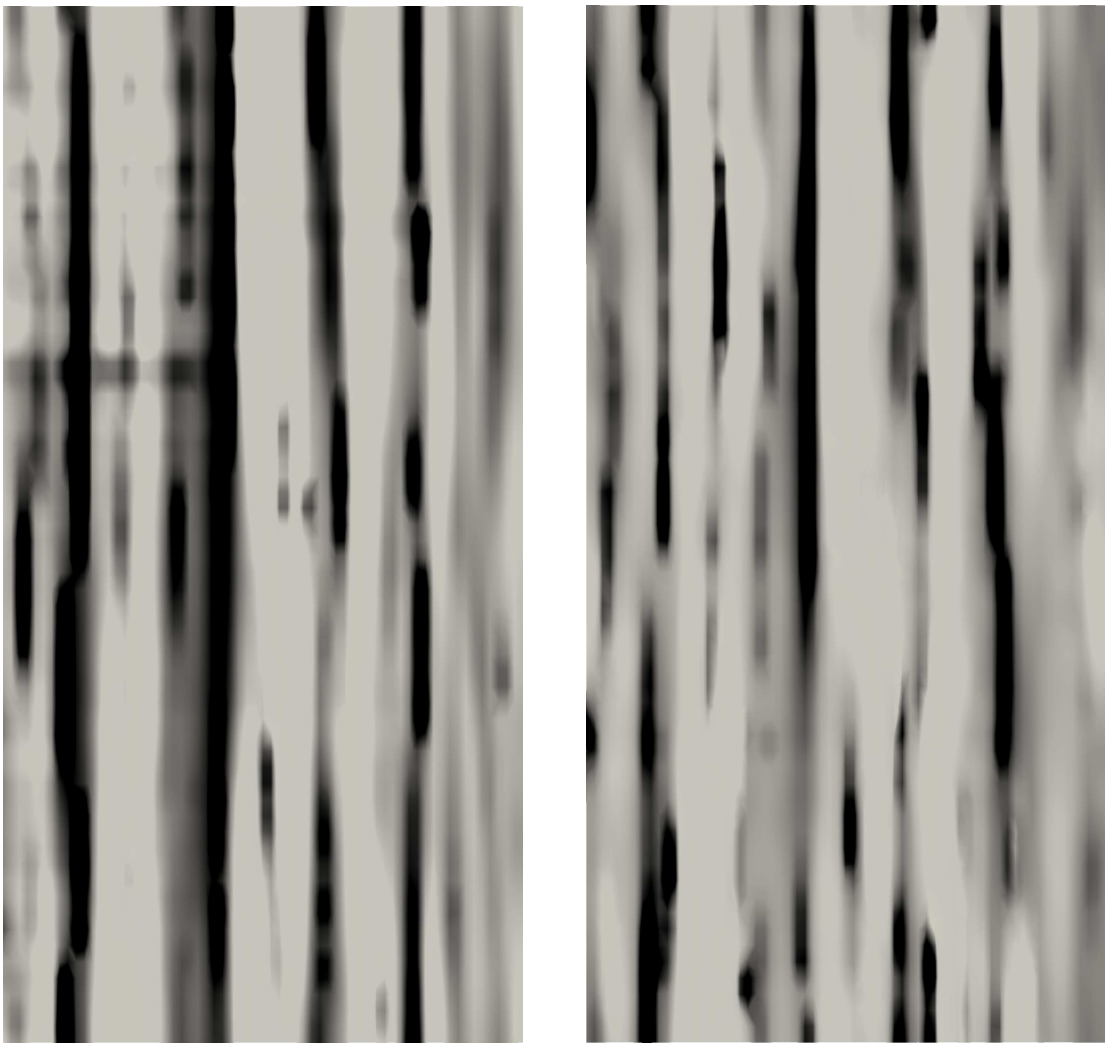

(a) (b)

Figure 6.16: For $Ste = 0.25$ a.) an elevation plot of the wall where lighter areas have been ablated more than the darker areas, and b.) a surface plot just above the ablated surface of $u^{'}$.

Table 6.1: A table condensing information from figures 6.18-6.23 showing the frequency of coherent structures in each bin. Node data for $5\delta_\Gamma$ has been omitted as it is zero for all Ste tested.

Ste	2	1	0.5	0.25	0.1	0.01
δ_Γ	$4.83 \cdot 10^{-3}$	$3.55 \cdot 10^{-3}$	$3.22 \cdot 10^{-3}$	$3.83 \cdot 10^{-3}$	$3.06 \cdot 10^{-3}$	$2.88 \cdot 10^{-3}$
$y_{\text{check 1}}$	$8.69 \cdot 10^{-3}$	$8.69 \cdot 10^{-3}$	$6.30 \cdot 10^{-3}$	$6.30 \cdot 10^{-3}$	$6.30 \cdot 10^{-3}$	$1.54 \cdot 10^{-3}$
CS freq. δ_Γ	105	150	575	348	839	1615
CS freq. $2\delta_\Gamma$	124	833	1696	1242	1340	567
CS freq. $3\delta_\Gamma$	1223	449	8	5	45	0
CS freq. $4\delta_\Gamma$	965	44	0	0	0	0
$y_{\text{check 2}}$	$4.56 \cdot 10^{-3}$	$4.56 \cdot 10^{-3}$	$3.83 \cdot 10^{-2}$	$3.83 \cdot 10^{-2}$	$3.83 \cdot 10^{-2}$	$2.65 \cdot 10^{-3}$
CS freq.δ_Γ	103	130	578	409	734	1577
CS freq. $2\delta_\Gamma$	227	1017	1626	1326	1339	527
CS freq. $3\delta_\Gamma$	736	521	4	10	0	0
CS freq. $4\delta_\Gamma$	560	23	0	0	0	0
$y_{\text{check 3}}$	0.188	0.188	0.162	0.162	0.162	$8.84 \cdot 10^{-2}$
CS freq. δ_Γ	103	143	0439	499	746	1452
CS freq. $2\delta_\Gamma$	601	1244	1577	1507	1249	411
CS freq. $3\delta_\Gamma$	731	647	28	21	7	0
CS freq. $4\delta_\Gamma$	571	11	0	0	0	0
$y_{\text{check 4}}$	0.372	0.372	0.327	0.327	0.286	0.37
CS freq. δ_Γ	83	411	498	504	661	1784
CS freq. $2\delta_\Gamma$	345	1310	1577	1560	1471	293
CS freq. $3\delta_\Gamma$	814	490	28	15	1	0
CS freq. $4\delta_\Gamma$	464	7	0	0	0	0

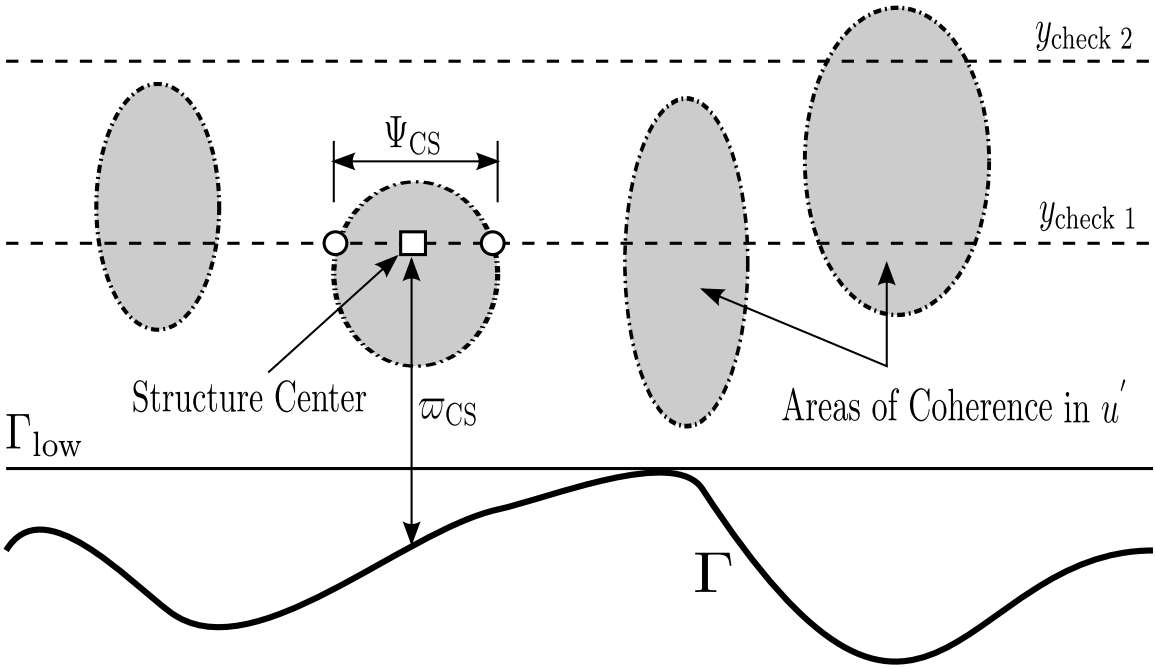

Figure 6.17: A schematic of how the search algorithm and the auto correlation function find ϖ_{CS} and Ψ_{CS} for a particular structure

The coherent structures, namely the streaks, and their position over the troughs, or areas where more material has been removed from the wall, can be corroborated with figures 6.18-6.23. The data suggest for $Ste \geq 0.25$ coherent structures with a width of $0.5 \geq \Psi_{CS} \leq 1$ have an 80% probability of occurring over the areas where the most ablation has occurred. This is also shown in table 6.1 where the frequency of structures is much higher in the lower δ_Γ bands which corresponds to a band taken closer to Γ_{high}. As opposed to the simulations with $Ste < 0.25$, which have coherent structures spread out all across the surface. The reason for this is that there is almost no variation in the surface height from simulations with $Ste < 0.25$ (see figure 6.30 and figure 6.31).

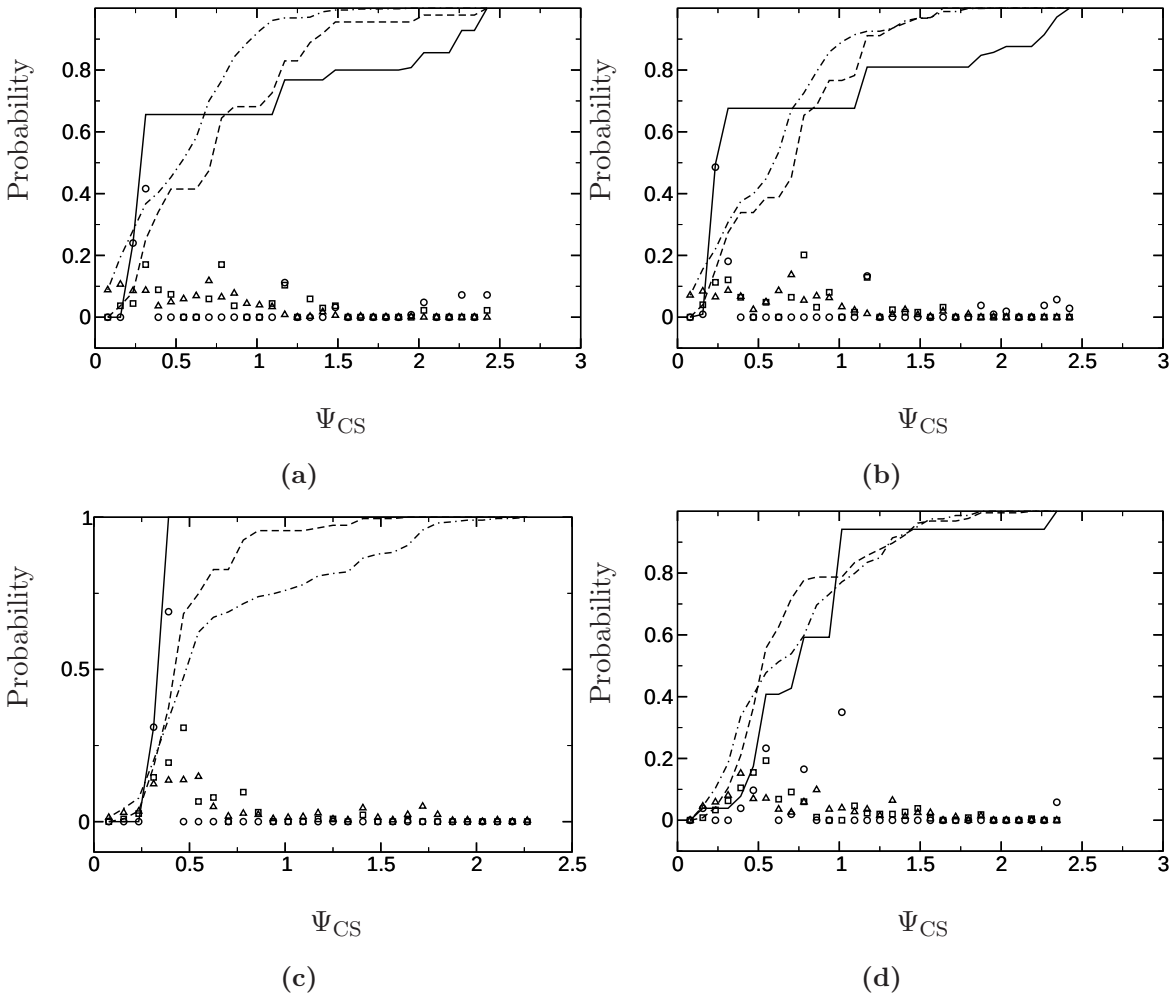

Figure 6.18: PDFs at $(\Gamma_{\mathbf{low}} - \varpi_{\mathbf{CS}}) - \delta_\Gamma$, $(\circ\,\circ\,\circ)$, $(\Gamma_{\mathbf{low}} - \varpi_{\mathbf{CS}}) - 2\delta_\Gamma$,$(\square\square\square)$, $(\Gamma_{\mathbf{low}} - \varpi_{\mathbf{CS}}) - 3\delta_\Gamma$,$(\triangle\,\triangle\,\triangle)$, **and PDF sums,** (——), $(-\,-\,-)$, $(-\,\cdot\,-)$, **respectively, for, a.)** $y_{\mathbf{check}} = 8.69 \cdot 10^{-3}$ **b.)** $y_{\mathbf{check}} = 4.56 \cdot 10^{-2}$ **c.)** $y_{\mathbf{check}} = 0.188$ **d.)** $y_{\mathbf{check}} = 0.372$ **where** $\delta_\Gamma = 4.83 \cdot 10^{-3}$, $(\Gamma_{\mathbf{high}} - \Gamma_{\mathbf{low}}) = 7.41 \cdot 10^{-2}$, **and** $Ste = 2$.

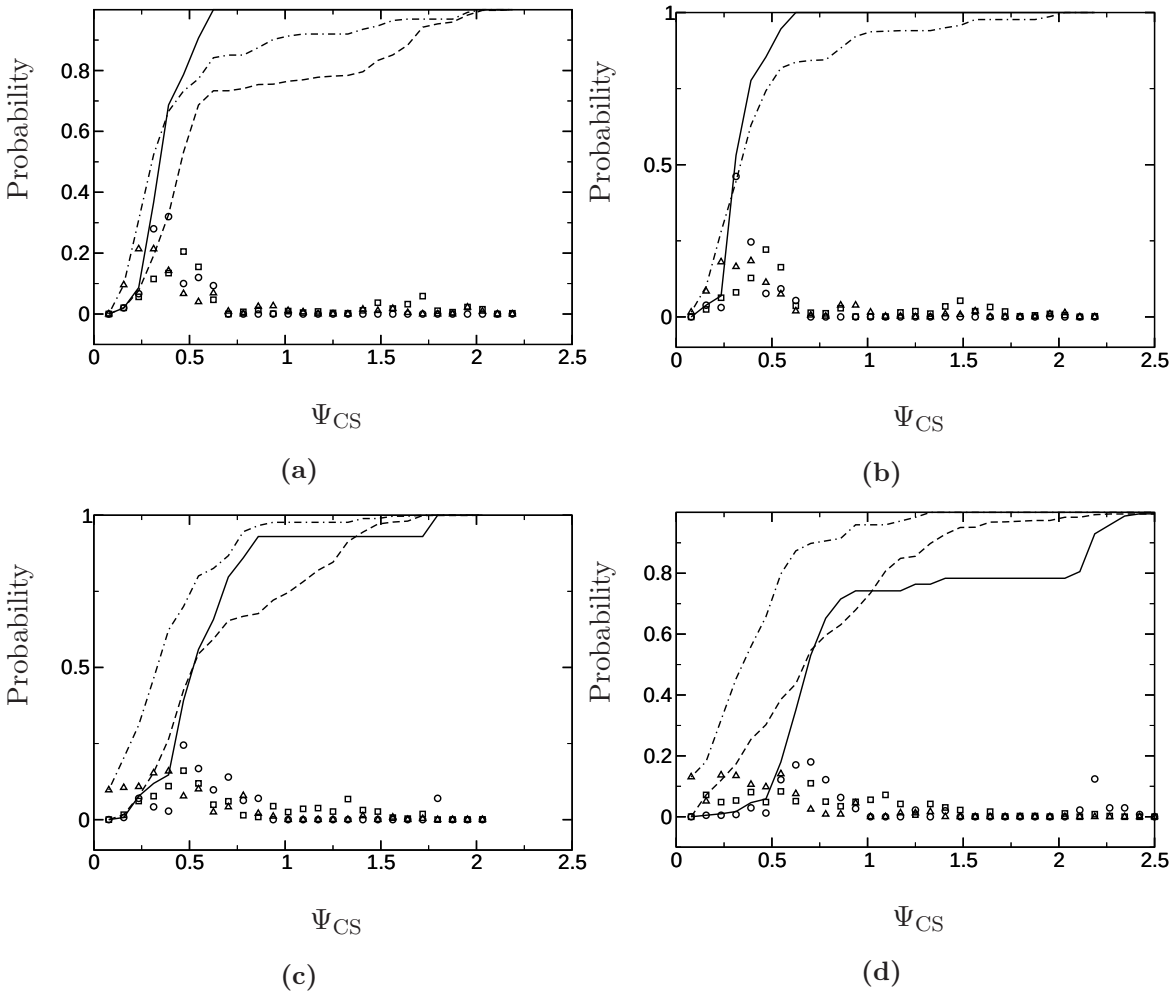

Figure 6.19: PDFs at $(\Gamma_{\mathbf{low}} - \varpi_{\mathbf{CS}}) - \delta_\Gamma$, $(\circ\,\circ\,\circ)$, $(\Gamma_{\mathbf{low}} - \varpi_{\mathbf{CS}}) - 2\delta_\Gamma$,$(\square\square\square)$, $(\Gamma_{\mathbf{low}} - \varpi_{\mathbf{CS}}) - 3\delta_\Gamma$,$(\triangle\,\triangle\,\triangle)$, **and PDF sums,** (——), $(-\,-\,-)$, $(-\,\cdot\,-)$, **respectively, for, a.)** $y_{\mathbf{check}} = 8.69 \cdot 10^{-3}$ **b.)** $y_{\mathbf{check}} = 4.56 \cdot 10^{-2}$ **c.)** $y_{\mathbf{check}} = 0.188$ **d.)** $y_{\mathbf{check}} = 0.372$ **where** $\delta_\Gamma = 3.55 \cdot 10^{-3}$, $(\Gamma_{\mathbf{high}} - \Gamma_{\mathbf{low}}) = 5.68 \cdot 10^{-2}$, **and** $Ste = 1$.

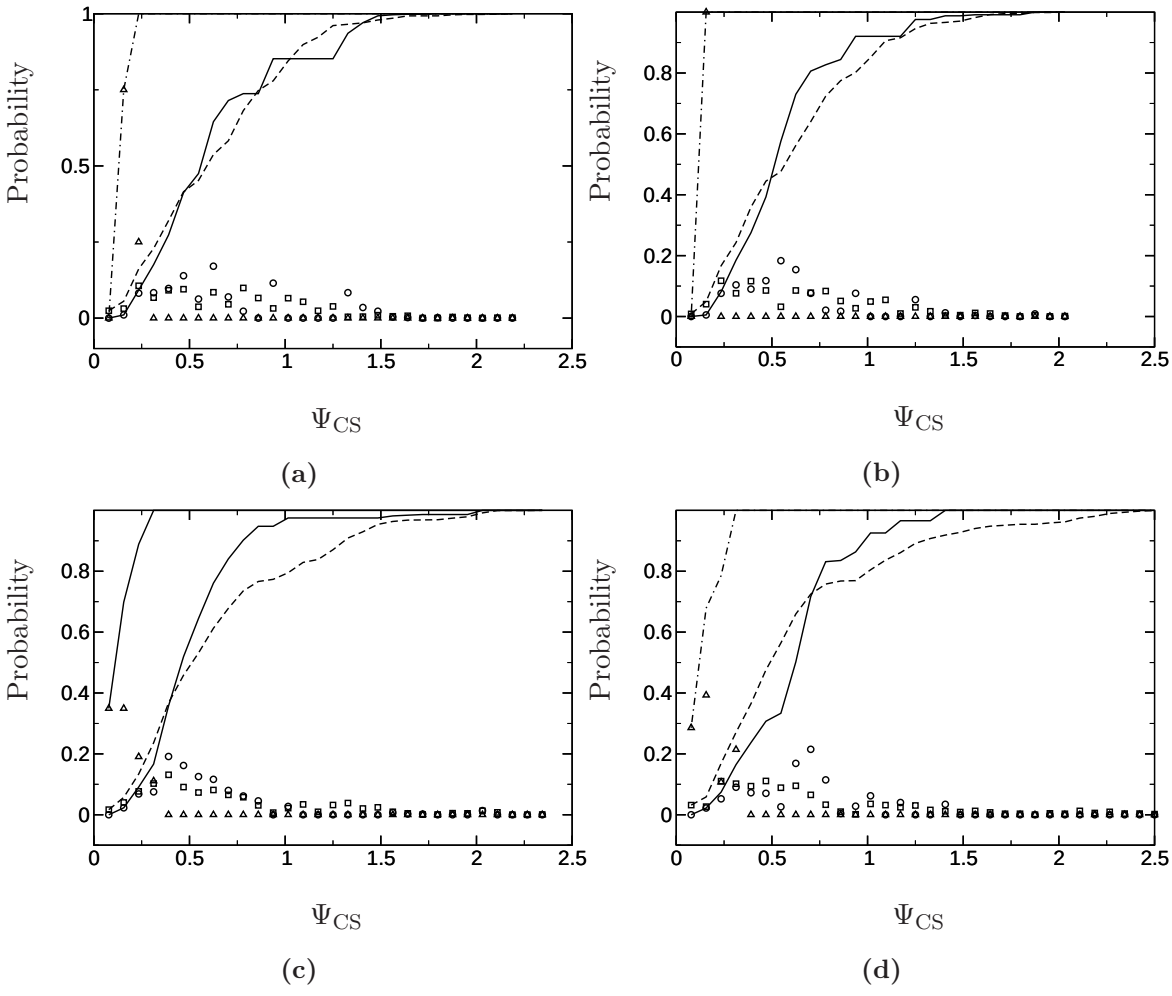

Figure 6.20: PDFs at $(\Gamma_{\mathbf{low}} - \varpi_{\mathbf{CS}}) - \delta_\Gamma$, $(\circ\,\circ\,\circ)$, $(\Gamma_{\mathbf{low}} - \varpi_{\mathbf{CS}}) - 2\delta_\Gamma$,$(\square\square\square)$, $(\Gamma_{\mathbf{low}} - \varpi_{\mathbf{CS}}) - 3\delta_\Gamma$,$(\triangle\,\triangle\,\triangle)$, **and PDF sums,** (——), $(- - -)$, $(- \cdot -)$, **respectively, for, a.)** $y_{\mathbf{check}} = 6.30 \cdot 10^{-3}$ **b.)** $y_{\mathbf{check}} = 3.81 \cdot 10^{-2}$ **c.)** $y_{\mathbf{check}} = 0.162$ **d.)** $y_{\mathbf{check}} = 0.372$ **where** $\delta_\Gamma = 3.22 \cdot 10^{-3}$, $(\Gamma_{\mathbf{high}} - \Gamma_{\mathbf{low}}) = 5.68 \cdot 10^{-2}$, **and** $Ste = 0.5$.

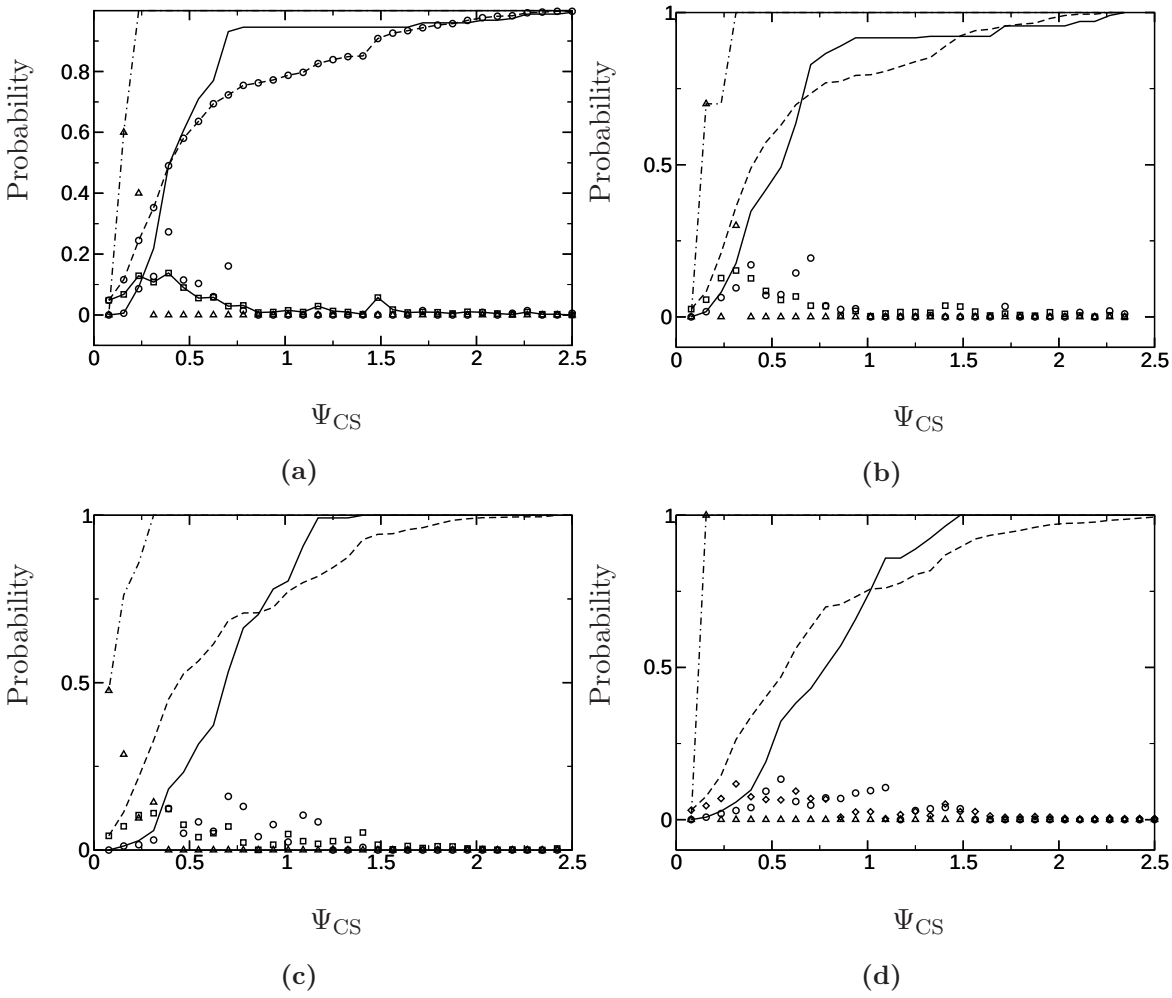

Figure 6.21: PDFs at $(\Gamma_{\mathbf{low}} - \varpi_{\mathbf{CS}}) - \delta_\Gamma$, $(\circ\,\circ\,\circ)$, $(\Gamma_{\mathbf{low}} - \varpi_{\mathbf{CS}}) - 2\delta_\Gamma$,$(\square\square\square)$, $(\Gamma_{\mathbf{low}} - \varpi_{\mathbf{CS}}) - 3\delta_\Gamma$,$(\triangle\,\triangle\,\triangle)$, **and PDF sums,** (——), $(- - -)$, $(- \cdot -)$, **respectively, for, a.)** $y_{\mathbf{check}} = 6.30 \cdot 10^{-3}$ **b.)** $y_{\mathbf{check}} = 3.81 \cdot 10^{-2}$ **c.)** $y_{\mathbf{check}} = 0.162$ **d.)** $y_{\mathbf{check}} = 0.372$ **where** $\delta_\Gamma = 3.19 \cdot 10^{-3}$, $(\Gamma_{\mathbf{high}} - \Gamma_{\mathbf{low}}) = 5.10 \cdot 10^{-2}$, **and** $Ste = 0.25$.

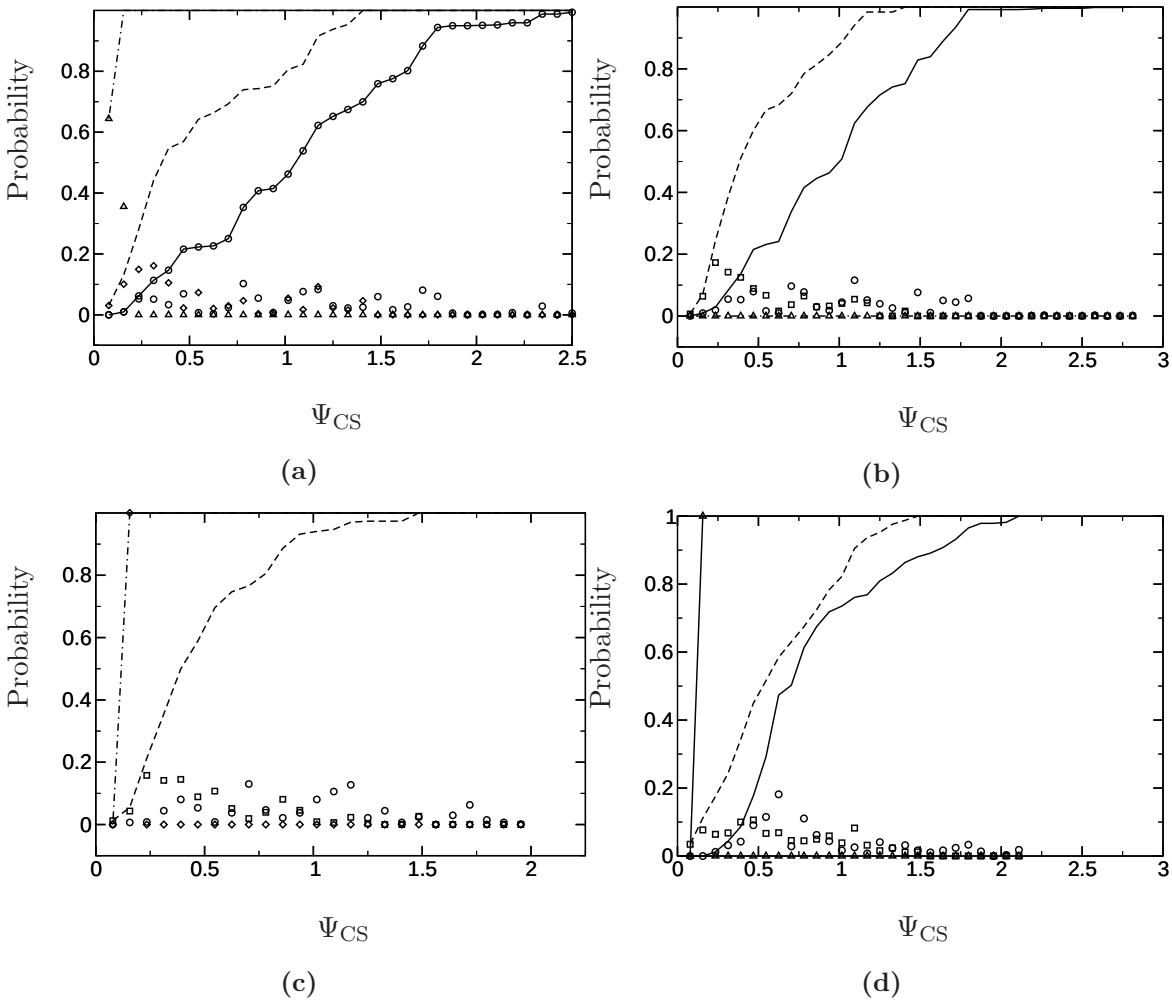

Figure 6.22: PDFs at $(\Gamma_{\mathbf{low}} - \varpi_{\mathbf{CS}}) - \delta_\Gamma$, $(\circ\,\circ\,\circ)$, $(\Gamma_{\mathbf{low}} - \varpi_{\mathbf{CS}}) - 2\delta_\Gamma$,$(\square\square\square)$, $(\Gamma_{\mathbf{low}} - \varpi_{\mathbf{CS}}) - 3\delta_\Gamma$,$(\triangle\,\triangle\,\triangle)$, **and PDF sums,** (——), $(-\,-\,-)$, $(-\,\cdot\,-)$, **respectively, for, a.)** $y_{\mathbf{check}} = 6.30 \cdot 10^{-3}$ **b.)** $y_{\mathbf{check}} = 3.83 \cdot 10^{-2}$ **c.)** $y_{\mathbf{check}} = 8.84 \cdot 10^{-2}$ **d.)** $y_{\mathbf{check}} = 0.28$ **where** $\delta_\Gamma = 3.05 \cdot 10^{-3}$, $(\Gamma_{\mathbf{high}} - \Gamma_{\mathbf{low}}) = 4.88 \cdot 10^{-2}$, **and** $Ste = 0.1$

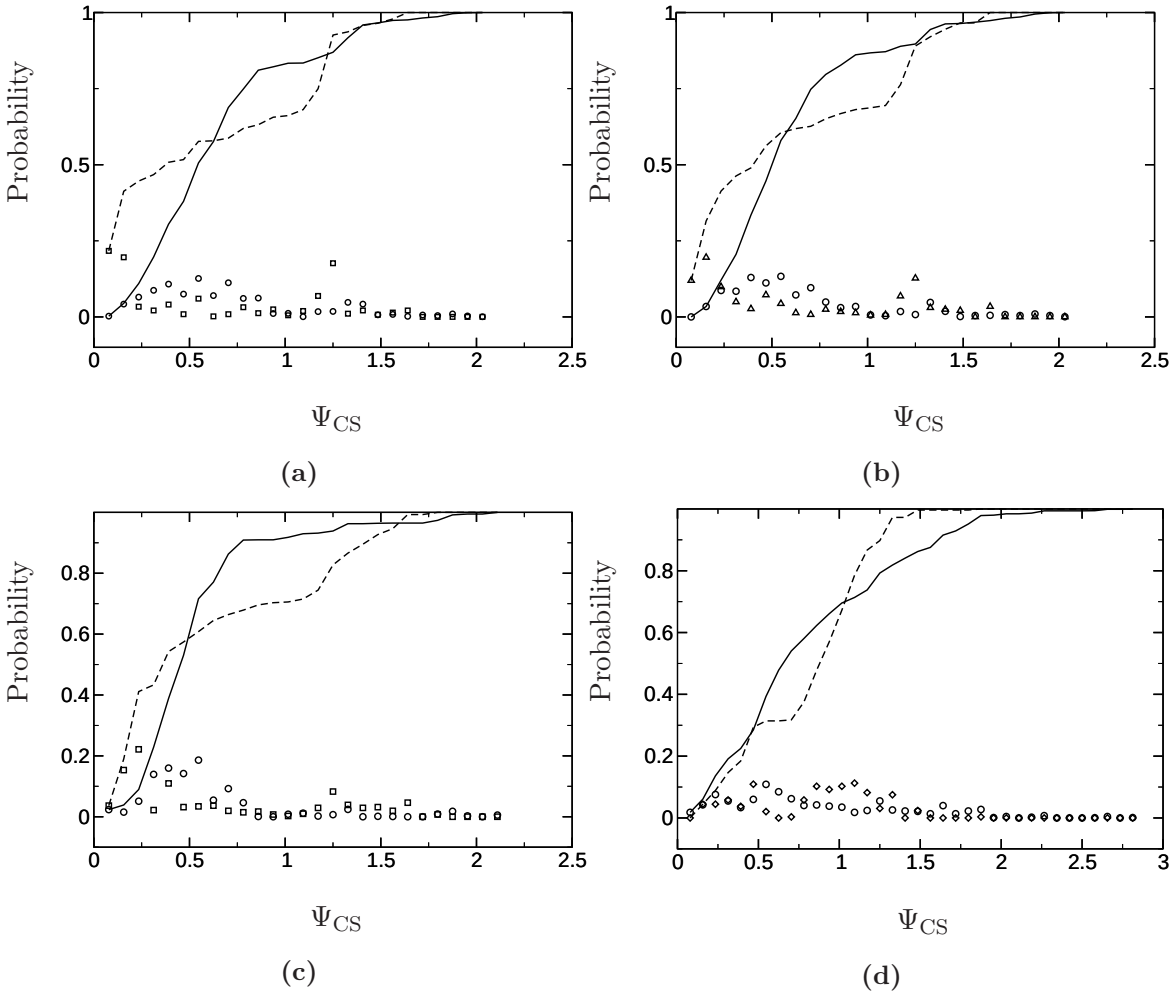

Figure 6.23: PDFs at $(\Gamma_{\mathbf{low}} - \varpi_{\mathbf{CS}}) - \delta_\Gamma$, $(\circ\,\circ\,\circ)$, $(\Gamma_{\mathbf{low}} - \varpi_{\mathbf{CS}}) - 2\delta_\Gamma$,$(\square\square\square)$, $(\Gamma_{\mathbf{low}} - \varpi_{\mathbf{CS}}) - 3\delta_\Gamma$,$(\triangle\,\triangle\,\triangle)$, **and PDF sums,** (——), $(-\,-\,-)$, $(-\,\cdot\,-)$, **respectively, for, a.)** $y_{\mathbf{check}} = 1.54 \cdot 10^{-3}$ **b.)** $y_{\mathbf{check}} = 2.65 \cdot 10^{-2}$ **c.)** $y_{\mathbf{check}} = 8.84 \cdot 10^{-2}$ **d.)** $y_{\mathbf{check}} = 0.372$ **where** $\delta_\Gamma = 2.88 \cdot 10^{-3}$, $(\Gamma_{\mathbf{high}} - \Gamma_{\mathbf{low}}) = 4.62 \cdot 10^{-2}$, **and** $Ste = 0.01$

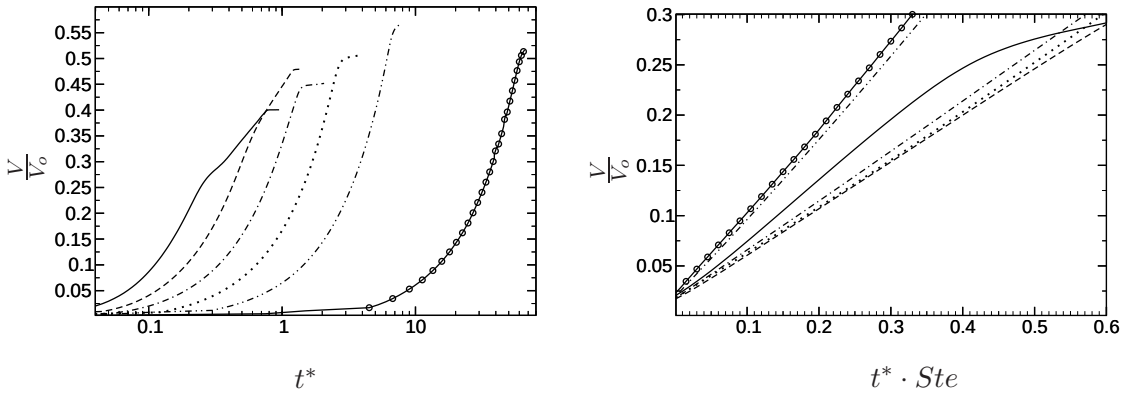

Figure 6.24: a.) The raw data in a semi-log plot for volume loss, V/V_o, for $Ste = 2$ (——), $Ste = 1$ $(- - -)$, $Ste = 0.5$ $(- \cdot -)$, $Ste = 0.25$ $(\cdots)$, $Ste = 0.1$ $(- \cdot\cdot -)$, $Ste = 0.1$ $(\circ\circ\circ)$. b.) The scaled data for volume loss, V/V_o, $Ste = 2$ (——), $Ste = 1$ $(- - -)$, $Ste = 0.5$ $(- \cdot -)$, $Ste = 0.25$ $(\cdots)$, $Ste = 0.1$ $(- \cdot\cdot -)$, $Ste = 0.1$ $(\circ\circ\circ)$.

6.2.1.1 Surface Topology and Volume/Mass Loss

The volume loss rates of all the tested Stefan numbers follow a similar patter. Initially there is a noisy period when the simulation starts and there is minimal solid volume lost. Subsequently, the evolutions are linear with correlation coefficients of $R = 0.9999$, until they abruptly plateau which is shown in the raw data semi-log plot in figure 6.24a. Clipping the initial noisy period of all the volume loss rates and normalizing the time by Ste gives figure 6.24b. This results in two groups, assuming that the values for $Ste = 2$ are more correlated with the lower group than the upper group consisting of $Ste = 0.1$ and $Ste = 0.01$. This supports what was observed in figures 6.7-6.8 where the lowest two tested Stefan numbers appear to have no surface structures and do indeed have very small geometric fluctuations in height, figures 6.30-6.31.

The general shape of the average surface velocity over time is consistent among the

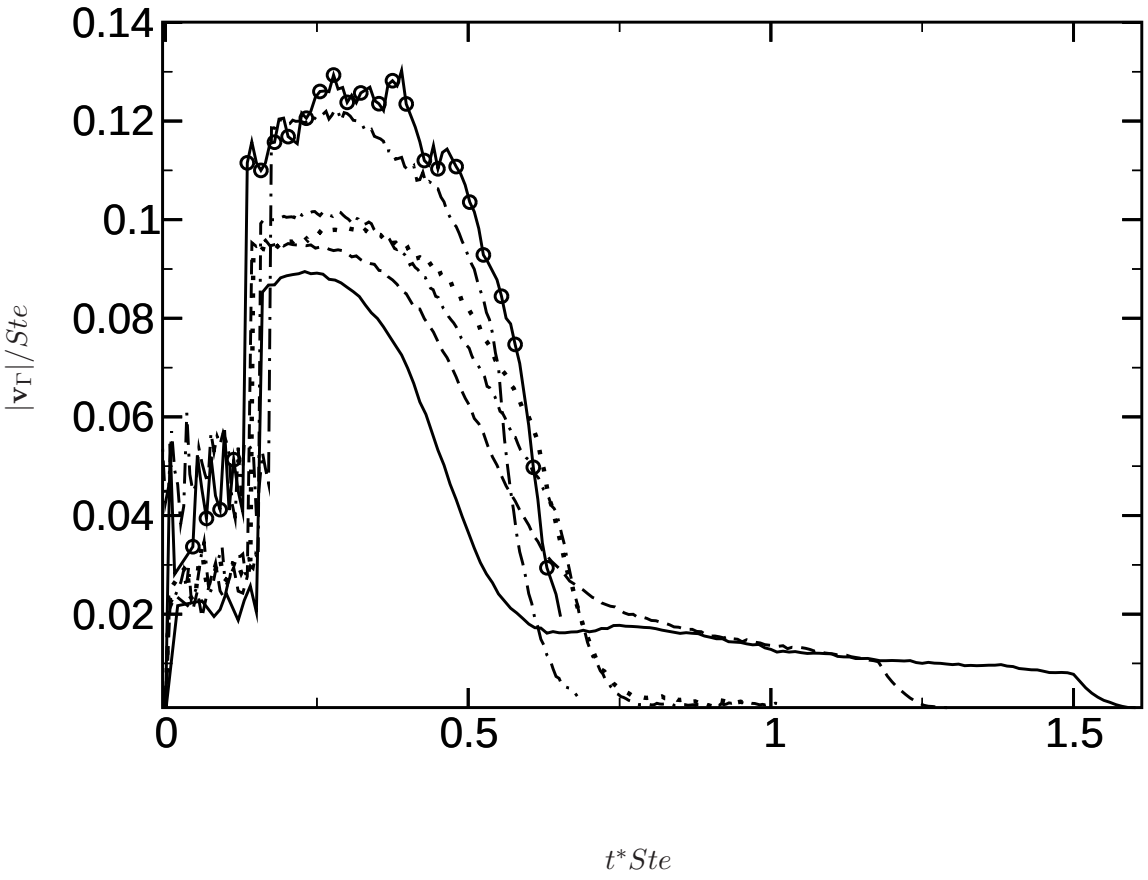

Figure 6.25: The scaled surface velocity for for $Ste = 2$ (——), $Ste = 1$ $(- - -)$, $Ste = 0.5$ $(- \cdot -)$, $Ste = 0.25$ $(\cdot \cdot \cdot)$, $Ste = 0.1$ $(- \cdot \cdot -)$, $Ste = 0.1$ $(\circ\,\circ\,\circ)$.

tested Ste. From section 6.2.1.1 and figure 6.24 this would be expected. The initial surface velocity is noisy and then jumps to a near constant value then drops slowly to zero (see figures 6.26-6.31). Interestingly the surface velocity also scales in time with Ste as shown in figure 6.25. The only difference between the mass loss scaling and the velocity scaling is that the velocity needs to be multiplied by the reciprocal of Ste which follows from equation 6.8. The scaling is not perfect: there are two definite groups made up of $Ste \geq 0.25$ and $Ste \leq 0.1$ just as in figure 6.24b.

The average wall height does not scale like either $\mathbf{v}_\Gamma$ or V/V_o does but for all the Stefan numbers it does approach a value of $\Gamma_{\text{high}} \approx 0.06$ for $Ste \geq 0.25$. For $Ste \leq 0.1$ there

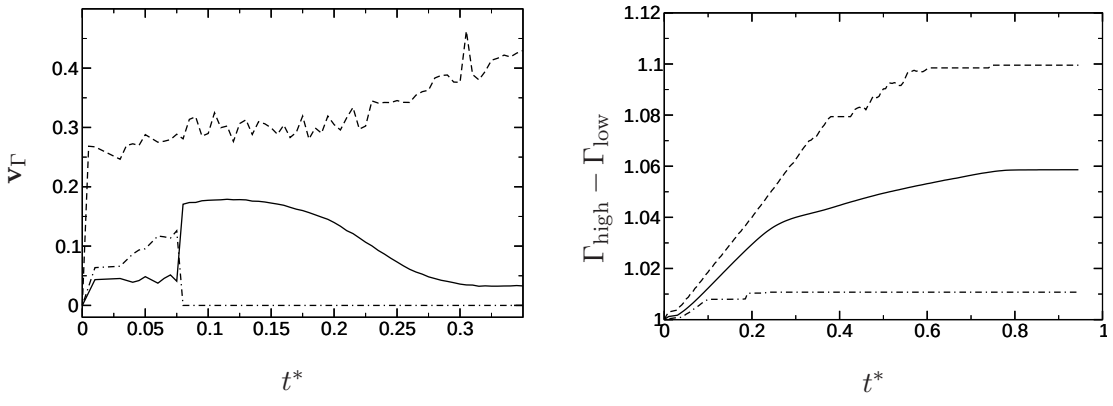

Figure 6.26: a.) The average surface velocity, $\overline{\mathrm{v}_\Gamma}$ and (——), the maximum surface velocity $\max(\mathrm{v}_\Gamma)$ and $(- - -)$,and the minimum surface velocity, $\max(\mathrm{v}_\Gamma)$ and $(- \cdot -)$. b.) The average surface height, $\overline{\Gamma}$ and (——), the maximum surface height $\Gamma_{\mathbf{high}}$ and $(- - -)$, and the minimum surface height, $\Gamma_{\mathbf{high}}$ and $(- \cdot -)$. Both a.) and b.) are for $Ste = 2$.

is little variation in the wall height as can be seen in figures 6.26b-6.31b where there is very little difference between the average wall height and the maximum wall height.

6.3 Summary

The results in this section show that despite the presence of an average wall velocity consistent with v_K and the numerical experiment in chapter 5 there is little effect on the turbulent intensities and production of the flow for all the tested Stefan numbers. Aside from a slight increase in production and decrease in dissipation there is nothing on the same order as shown in chapter 5. The turbulent intensities and the streak size were also not altered as the channel ablated, for all tested Stefan numbers. The explanation derived from the work in the previous chapter can tentatively attribute this behavior to a non-zero mean shear at the ablating wall at all times. The thin shear free layer found for constant wall velocities

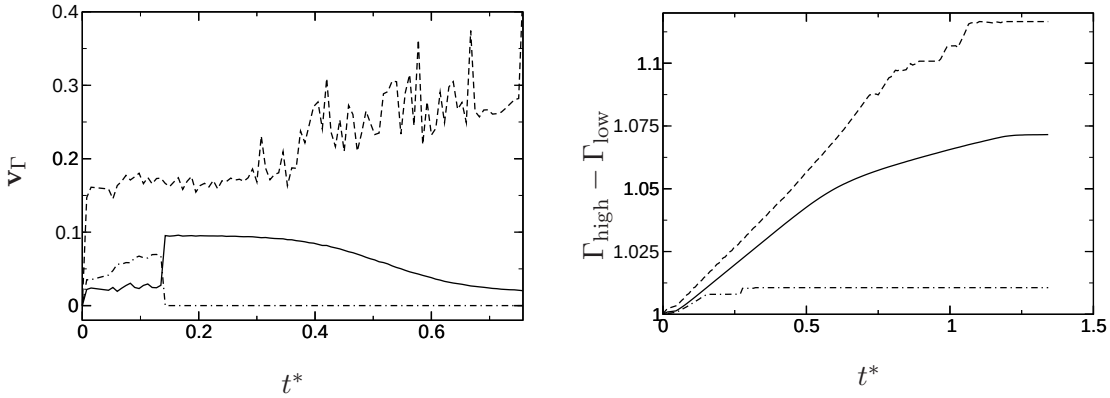

(a) (b)

Figure 6.27: a.) The average surface velocity, $\overline{\mathbf{v}_\Gamma}$ and (——), the maximum surface velocity $\max(\mathbf{v}_\Gamma)$ and $(- - -)$,and the minimum surface velocity, $\max(\mathbf{v}_\Gamma)$ and $(- \cdot -)$. b.) The average surface height, $\overline{\Gamma}$ and (——), the maximum surface height $\Gamma_{\mathbf{high}}$ and $(- - -)$, and the minimum surface height, $\Gamma_{\mathbf{high}}$ and $(- \cdot -)$. Both a.) and b.) are for $Ste = 1$.

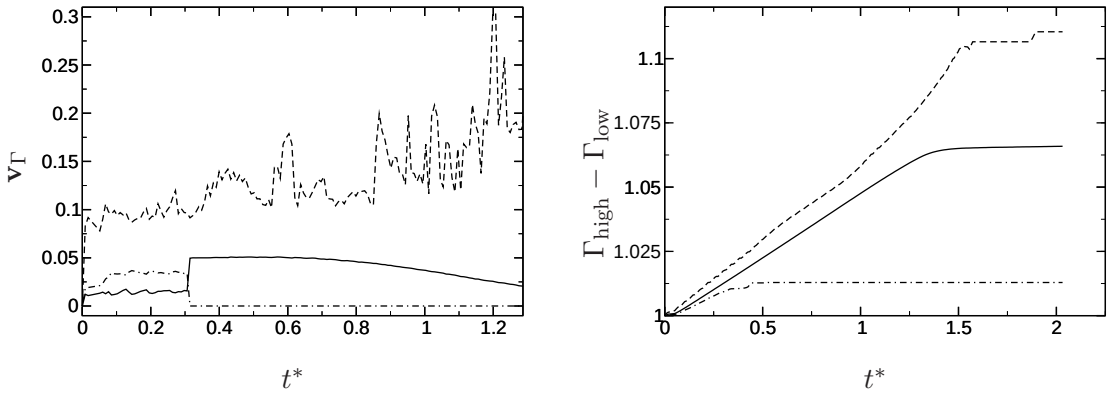

(a) (b)

Figure 6.28: a.) The average surface velocity, $\overline{\mathbf{v}_\Gamma}$ and (——), the maximum surface velocity $\max(\mathbf{v}_\Gamma)$ and $(- - -)$,and the minimum surface velocity, $\max(\mathbf{v}_\Gamma)$ and $(- \cdot -)$. b.) The average surface height, $\overline{\Gamma}$ and (——), the maximum surface height $\Gamma_{\mathbf{high}}$ and $(- - -)$, and the minimum surface height, $\Gamma_{\mathbf{high}}$ and $(- \cdot -)$. Both a.) and b.) are for $Ste = 0.5$.

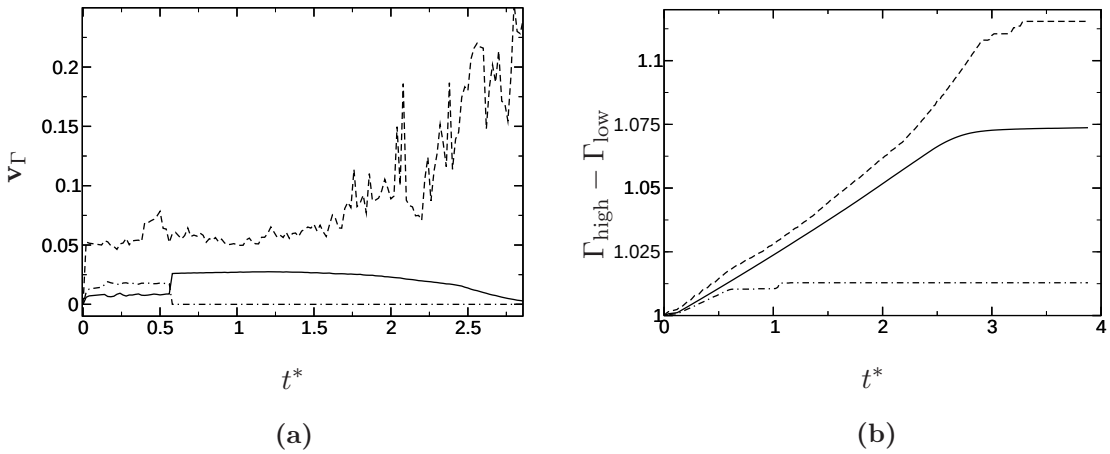

(a) (b)

Figure 6.29: a.) The average surface velocity, $\overline{v_\Gamma}$ and (——), the maximum surface velocity max (v_Γ) and $(- - -)$,and the minimum surface velocity, max (v_Γ) and $(- \cdot -)$. b.) The average surface height, $\overline{\Gamma}$ and (——), the maximum surface height Γ_{high} and $(- - -)$, and the minimum surface height, Γ_{high} and $(- \cdot -)$. Both a.) and b.) are for $Ste = 0.25$.

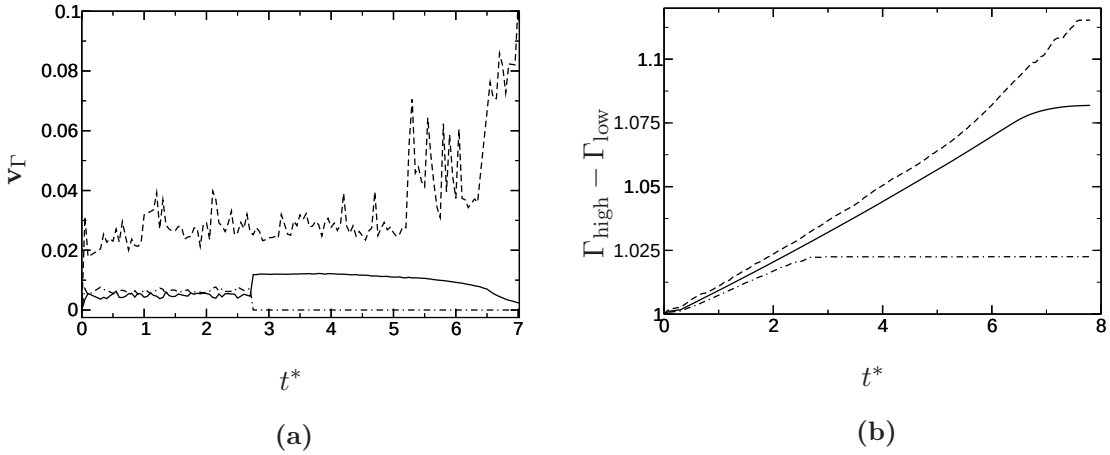

(a) (b)

Figure 6.30: a.) The average surface velocity, $\overline{v_\Gamma}$ and (——), the maximum surface velocity max (v_Γ) and $(- - -)$,and the minimum surface velocity, max (v_Γ) and $(- \cdot -)$. b.) The average surface height, $\overline{\Gamma}$ and (——), the maximum surface height Γ_{high} and $(- - -)$, and the minimum surface height, Γ_{high} and $(- \cdot -)$. Both a.) and b.) are for $Ste = 0.1$.

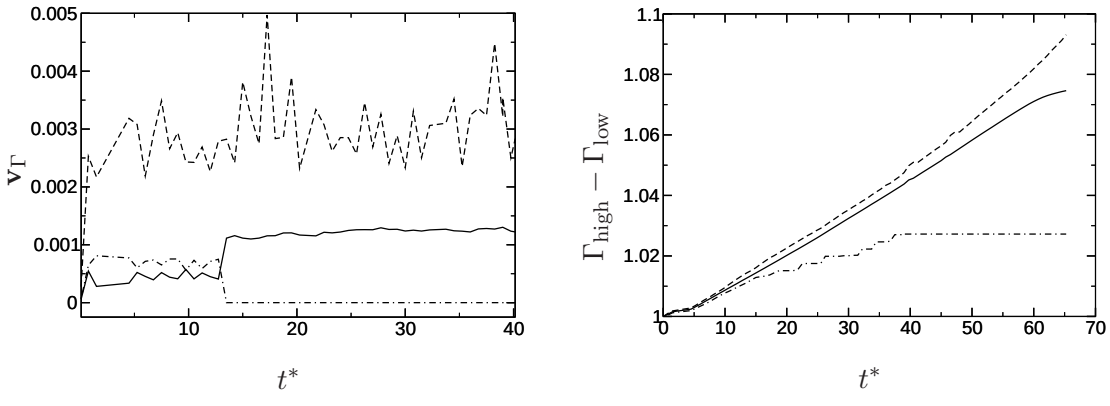

(a) **(b)**

Figure 6.31: a.) The average surface velocity, $\overline{\mathbf{v}_\Gamma}$ and (——), the maximum surface velocity $\max(\mathbf{v}_\Gamma)$ and $(- - -)$,and the minimum surface velocity, $\max(\mathbf{v}_\Gamma)$ and $(- \cdot -)$. b.) The average surface height, $\overline{\Gamma}$ and (——), the maximum surface height $\Gamma_{\mathbf{high}}$ and $(- - -)$, and the minimum surface height, $\Gamma_{\mathbf{high}}$ and $(- \cdot -)$. Both a.) and b.) are for $Ste = 0.01$.

was not seen here. There was a reduction of mean shear for the cases where the average ablation velocity as close to v_K although it never dropped to zero. Without the reduction of shear at the wall there cannot be a subsequent drop in near wall dissipation, which is the theorized cause of the turbulent wake seen for the constant wall velocities $0.1 \geq \mathbf{v}_\Gamma \leq 0.5$. This is still only a theory and will need to be addressed in future work.

While the streaks did not increase in size or intensity, they did effect the surface geometry of the ablating wall, which in turn affected the streaks. The PDFs in figures 6.18-6.23, table 6.1, and the images in figures 6.15 and 6.16 show that as the channel surface was removed it was done so in a very specific manner. The high-velocity streaks settled over the areas where the most material had been removed. This kept the streaks in semi-constant positions over these areas of greater material removal consistently throughout the simulations. This did not seem to dampen the streaks as the mean shear stayed high, and the turbulent intensities were at appropriate levels for a channel with $Re_{u_\tau} = 125$.

Although, for the larger Stefan numbers this correlation between deep troughs and the streaks was not as prevalent because the surface produced by $Ste = 2$ and $Ste = 1$ was much less uniform than that produced by the lower Ste.

The scaling of both V/V_o and $\mathbf{v}_\Gamma$ with the Stefan number was expected from its relationship to the normal velocity, and through that the mass loss, in equation 6.8. The plateauing of the surface velocity and the surface depth is due to the balancing of the energy input from the hot side of the channel and the cold side of the channel. Once that equilibrium is reached the surface will no longer ablate or will do so very slowly.

Chapter 7

CONCLUDING REMARKS AND FUTURE WORK

7.1 Concluding Remarks

The purpose of this study was to develop a structured finite volume flow solver capable of simulating complex non-grid conforming boundary conditions for both momentum and energy (EIBM). The flow solver, NGA-ARTS, was used as the base code for the addition of the EIBM because it already had the capability of simulating multi-physics flows with finite chemistry and a robust momentum IBM, which had been shown in previous works to be second order accurate. The EIBM was broken down into CHT and ablative scalar boundary conditions where both were shown to correlate well with previous experimental and numerical results and to be second order convergent, as well as accurate.

The isothermal expanding channel showed distinctly different regimes of both local and global equilibrium for different wall velocities. The wall velocities of the order of the Kolmorgorov microscale velocity produce a distinct turbulent wake behind them. This

wake was caused by the stretching of the coherent streak structures by $10\% - 20\%$ over their opposite wall, and equilibrium values. The stretching caused the dynamic side of the channel to see an increase in both semi-streamwise vortices and turbulent intensity. The wall velocities an order of magnitude greater than the microscale velocities, showed results comparable to a turbulent channel where the lower wall is removed and the cavity was left to become part of the turbulent channel, while the slowest velocity was shown to stay in equilibrium throughout expansion. These three different regimes of differing equilibrium will require new, unsteady, representations of production and dissipation if they are to be modeled with LES or RANS.

The turbulent ablating channel did not correlate to the isothermal channel as well as was assumed in the initial hypothesis of this study. There was little increase in the turbulent intensity or production which is associated with the isothermal expanding channel. There was also no increase in the amount of semi-streamwise vortices associated with the tested Stefan. However the effect on the coherent structures as a whole was not zero. It was shown that the streaks both statistically and visually stayed over the deeper eroded channels and did not move throughout the numerical experiment. This begs the question, are the streaks causing the channeling, or are the streaks settling in the channels because the channels are there? As the streaks are the mechanism in which core fluid is transported normal to the wall the answer is probably the former.

The ablating channel also showed two regimes of mass-loss and surface velocity defining different regions scalable with the Stefan number. Along with the small loss of equilibrium at these lower wall velocities, up to the Kolmorgorov micro-scale velocity, it can be assumed with a decent probability that modeling of these sorts of flows should be straight forward.

7.2 Future Work

This study produced a massive database of results. The isothermal channel alone produced 1TB of data. This data will need to be parsed and studied in detail for other relationships between the dynamic boundary conditions and non-equilibrium, namely vorticity and the energy distribution at different scales. The resulting analysis should be sufficient to find the domains in which the EIBM is effective, and where it is not, for more complex flows at higher velocities and discrepancies between the fluid and solid parameters. Proceeding in this manner, different erosion conditions can be added based on either chemical composition, such as TPS, or mechanical erosion of material, such as sediment. The code itself will also need to be optimized. At the moment the computational cost is high when the surfaces are complex and simulated in three dimensions. This is due to a large amount of MPI communication during the definition of the surface geometry.

The research goals for the future of this study are summarized below.

- Optimization of the EIBM's computer code
- Add oxidization, pyrolysis, and other chemically based ablation models
- Investigate the feasibility of applying a mechanical ablation model, such as that used for sediment erosion
- Expand the scope and application of the EIBM to more complex flows, and to flows with higher Reynolds numbers
- Assess the resultant database from this work in more detail i.e. energy and vorticity, and their relationship to the coherent structures
- Break down the database results and to use them to define regimes of equilibrium and non-equilibrium flow for future modeling applications (LES)

Appendix A

A.1 Generic Numerical Boundary Conditions

A.1.1 General Transport Equation

A generic time evolution equation for of a general transport equation (GTE), in one dimension, is give as

$$\partial_t \boldsymbol{\phi} = f\left(\boldsymbol{\phi}^{n+\frac{1}{2}}\right) \tag{A.1}$$

where $\boldsymbol{\Phi} = \boldsymbol{\phi}^{n+\frac{1}{2}} = \left(\boldsymbol{\phi}^{n+1} + \boldsymbol{\phi}^{n}\right)/2$ is the time average of $\boldsymbol{\phi}$ between the time steps n and $n+1$. For generality $\boldsymbol{\phi}$ is a vector but can be substituted out for a scalar quantity. The time discretization of equation A.1 is,

$$\frac{\boldsymbol{\phi}^{n+1} - \phi^{n}}{\Delta t} = f\left(\boldsymbol{\Phi}\right). \tag{A.2}$$

The implicit solution of equation A.2 is found using an iterative Newton-Raphson method. The advantage of this method over other implicit or semi-implicit methods (such as the Crank-Nicholson method) is that using midpoint time advancement within an iterative solver greatly increases non-linear stability. With non-linear stability being of a greater necessity for complex turbulent and chemically reactive, coupled flows. Expanding equation A.2 about the time step n, and iterating over the Newton-Raphson index k, and rearranging gives the form of the time evolution equation. If $\boldsymbol{\phi}^{k,n+1}$ gives the fully discretized form of

equation A.1 is

$$\left[1-\frac{1}{2}\Delta t\frac{\partial f}{\partial \boldsymbol{\phi}}\right]\left(\boldsymbol{\phi}_{im}^{k+1,n+1}-\boldsymbol{\phi}_{im}^{k,n+1}\right)=\boldsymbol{\phi}_{im}^{k=0,n}-\boldsymbol{\phi}_{im}^{k,n+1}+\Delta t f\left(\boldsymbol{\Phi}\right), \tag{A.3}$$

where the mid-point form is $\boldsymbol{\Phi}=\left(\boldsymbol{\phi}_{im}^{k,n+1}+\boldsymbol{\phi}_{im}^{k=0,n}\right)/2$ (see appendix B). The Jacobian, $\partial f/\partial\boldsymbol{\phi}$, in equation A.3, reduces to the operators for a trapezoidal method for linear PDEs, and the initial guess, $\boldsymbol{\phi}^{k=0,n}$ is the initial time before iteration. Equation A.3 is also known as the Delta or the Residual form of the time evolution equation. It is a scheme which is closely related to the implicit Beam-Warming, [165] and [166], method in that it minimizes the residual, $\mathbf{Res}_i=\left(\boldsymbol{\phi}_{im}^{k+1,n+1}-\boldsymbol{\phi}_{im}^{k,n+1}\right)$.

The mid-point function in the Right Hand Side (RHS) of A.3 is discretized in a typical FV flux formulation using a staggered grid like that given in figures A.1 and A.2,

$$\begin{aligned} f\left(\boldsymbol{\Phi}\right)=&\boldsymbol{\nabla}\cdot\left(\boldsymbol{\nabla}\alpha\boldsymbol{\Phi}\right)= \\ &\boldsymbol{\nabla}\cdot\mathbf{F}=\left(\frac{\boldsymbol{\Phi}_{i_m+1}-\boldsymbol{\Phi}_{i_m}}{x_{i_m+1}-x_{i_m}}\tilde{\alpha}_{i+1}-\frac{\boldsymbol{\Phi}_{i_m}-\boldsymbol{\Phi}_{i_m-1}}{x_{i_m}-x_{i_m-1}}\tilde{\alpha}_i\right)\frac{1}{x_{i+1}-x_i}. \end{aligned} \tag{A.4}$$

The tilde in equation A.4 refers to a variable interpolated from it's standard position to the face of the C.V, $\mathbf{F}$ is the diffusive flux, and the furthest right hand side is the full discretization of $f\left(\boldsymbol{\Phi}\right)$. The Left Hand Side (LHS) of equation A.3 is discretized and put in a typical form for of the implicit side of finite difference discretizations,

$$a_i\boldsymbol{\phi}_{i_m-1}^{k+1,n+1}+b_i\boldsymbol{\phi}_{i_m}^{k+1,n+1}+c_i\boldsymbol{\phi}_{i_m+1}^{k+1,n+1}=RHS. \tag{A.5}$$

The coefficients from equation A.5 are given in equations A.6-A.8,

$$a_i=-\frac{\Delta t}{2}\left(\frac{\tilde{\alpha}_i}{x_{i_m}-x_{i_m-1}}\right)\frac{1}{x_{i+1}-x_i}, \tag{A.6}$$

$$b_i=1+\frac{\Delta t}{2}\left(\frac{\tilde{\alpha}_{i+1}}{x_{i_m+1}-x_{i_m}}+\frac{\tilde{\alpha}_i}{x_{i_m}-x_{i_m-1}}\right)\frac{1}{x_{i+1}-x_i}, \tag{A.7}$$

$$c_i=-\frac{\Delta t}{2}\left(\frac{\tilde{\alpha}_{i+1}}{x_{i_m+1}-x_{i_m}}\right)\frac{1}{x_{i+1}-x_i}, \tag{A.8}$$

and they are the same as the coefficients in equation A.4, again, for linear PDEs.

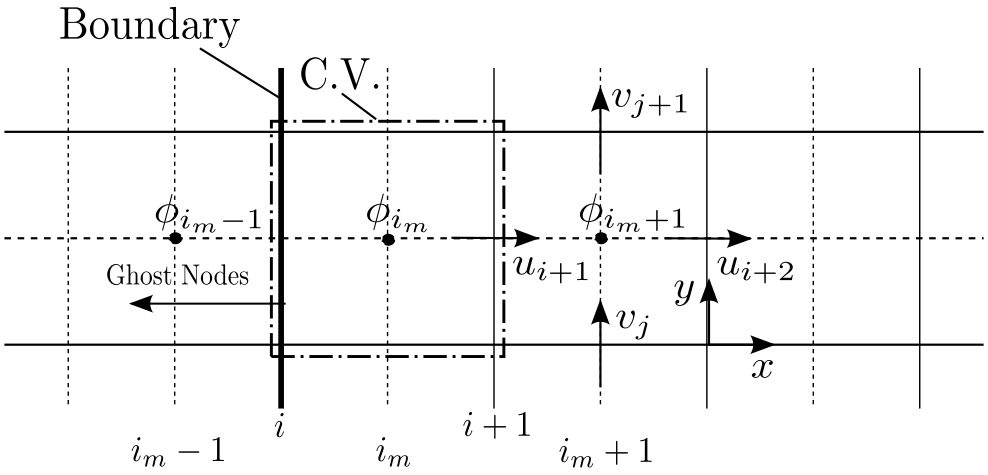

Figure A.1: A computational cell showing the mesh staggering and the domain boundary coming from the left.

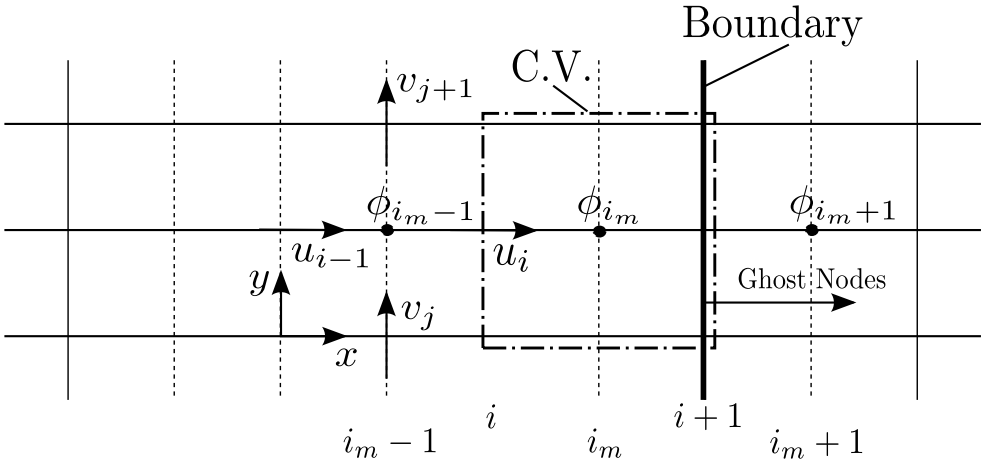

Figure A.2: A computational cell showing the mesh staggering and the domain boundary coming from the right.

A.1.2 Dirichlet Boundary Conditions

To embed Dirichlet boundary conditions into the FV scheme the values at the boundary, $\boldsymbol{\phi} = \boldsymbol{\phi}_o$, are interloped from the ghost nodes at $\boldsymbol{\phi}_{i_m-1}$ and $\boldsymbol{\phi}_{i_m+1}$ (see figures A.2 and A.1) so that the value of $\boldsymbol{\phi}$ at i is $\boldsymbol{\phi}_o$. This keeps the difference scheme $O\left(\Delta x^2\right)$ at the boundary. If the boundary conditions are not implemented as below, because of the staggered grid, the gradient of the midpoint quantities would have to be calculated with $O\left(\Delta x^1\right)$ backward differences at the face of the cells at the boundary. For the two cases given in figures A.1 and A.2 the boundary conditions will be $\boldsymbol{\phi}_{ol}$, and $\boldsymbol{\phi}_{or}$, respectively. This procedure is used only when the PDE solved with equation A.3 is linear, the non-linear version will have a much more complicated Jacobian, $\partial f/\partial\phi$, and will addressed in a later section.

The interpolation, for the explicit RHS, for figure A.1, is given as,

$$\boldsymbol{\phi}_{ol} = \frac{\boldsymbol{\phi}_{i_m} - \boldsymbol{\phi}_{i_m-1}}{x_{i_m} - x_{i_m-1}}\left(x_i - x_{i_m-1}\right) + \boldsymbol{\phi}_{i_m-1} \quad \rightarrow \quad \boldsymbol{\phi}_{i_m-1} = 2\boldsymbol{\phi}_{ol} - \boldsymbol{\phi}_{i_m}. \tag{A.9}$$

If the boundary condition at x_i is applied implicitly, and is time independent, then equation A.9 is valid for all time; $\boldsymbol{\phi}_{ol}^{k,n} = \boldsymbol{\phi}_{ol}^{k,n+1} = \boldsymbol{\phi}_{ol}^{k+1,n+1}$. For the right hand boundary, figure A.2, the analogous right hand boundary equation interpolation to equation A.9 is,

$$\boldsymbol{\phi}_{or} = \frac{\boldsymbol{\phi}_{i_m+1} - \boldsymbol{\phi}_{i_m}}{x_{i_m+1} - x_{i_m}}\left(x_{i+1} - x_{i_m}\right) + \boldsymbol{\phi}_{i_m+1} \quad \rightarrow \quad \boldsymbol{\phi}_{i_m+1} = 2\boldsymbol{\phi}_{or} - \boldsymbol{\phi}_{i_m}, \tag{A.10}$$

where here too, $\boldsymbol{\phi}_{or}^{k,n} = \boldsymbol{\phi}_{or}^{k,n+1} = \boldsymbol{\phi}_{or}^{k+1,n+1}$. The correct boundary conditions will need to be in the mid-point form. For example, substituting $\boldsymbol{\phi}^{k=0,n}$ and $\boldsymbol{\phi}^{k+1,n+1}$ into equation A.9, then adding the resulting equations, and dividing by two gives,

$$\frac{1}{2}\left(\boldsymbol{\phi}_{i_m-1}^{k,n+1} + \boldsymbol{\phi}_{i_m-1}^{k=0,n}\right) = \frac{1}{2}\left[4\boldsymbol{\phi}_{ol} - \left(\boldsymbol{\phi}_{i_m}^{k,n+1} + \boldsymbol{\phi}_{i_m}^{k=0,n}\right)\right] \quad \rightarrow \quad \boldsymbol{\Phi}_{i_m-1} = 2\boldsymbol{\phi}_{ol} - \boldsymbol{\Phi}_{i_m}. \tag{A.11}$$

Then, converting $\boldsymbol{\phi}$ to the mid-point form in equation A.10,

$$\frac{1}{2}\left(\boldsymbol{\phi}_{i_m+1}^{k,n+1} + \boldsymbol{\phi}_{i_m+1}^{k=0,n}\right) = \frac{1}{2}\left[4\boldsymbol{\phi}_{or} - \left(\boldsymbol{\phi}_{i_m}^{k,n+1} + \boldsymbol{\phi}_{i_m}^{k=0,n}\right)\right] \quad \rightarrow \quad \boldsymbol{\Phi}_{i_m+1} = 2\boldsymbol{\phi}_{or} - \boldsymbol{\Phi}_{i_m}. \tag{A.12}$$

Substituting the interpolations, equations A.11 and A.12 for the ghost nodes in equation A.4 and figures A.1 and A.2 gives the boundary conditions for the left hand boundary,

$$f\left(\mathbf{\Phi}\left(x=0\right)\right)=\boldsymbol{\nabla}\cdot\mathbf{F}=\left(\frac{\mathbf{\Phi}_{i_m+1}-\mathbf{\Phi}_{i_m}}{x_{i_m+1}-x_{i_m}}\tilde{\alpha}_{i+1}-2\frac{\mathbf{\Phi}_{i_m}-\phi_{ol}}{x_{i_m}-x_{i_m-1}}\tilde{\alpha}_i\right)\frac{1}{x_{i+1}-x_i}, \tag{A.13}$$

and right hand boundary,

$$f\left(\mathbf{\Phi}\left(x=Lx\right)\right)=\boldsymbol{\nabla}\cdot\mathbf{F}=\left(2\frac{\phi_{or}-\mathbf{\Phi}_{i_m}}{x_{i_m+1}-x_{i_m}}\tilde{\alpha}_{i+1}-\frac{\mathbf{\Phi}_{i_m}-\mathbf{\Phi}_{i_m-1}}{x_{i_m}-x_{i_m-1}}\tilde{\alpha}_i\right)\frac{1}{x_{i+1}-x_i}. \tag{A.14}$$

applied explicitly.

Applying the boundary condition implicitly is slightly different than the explicit application because the solution of the equation A.4 is not for $\boldsymbol{\phi}^{n+1}$ (as it would be for the CN method) but for the residual at each iteration. The same interpolation equations (A.9 and A.10) are used but they will need to be in residual form by substituting $\boldsymbol{\phi}^{k,n+1}$ and $\boldsymbol{\phi}^{k+1,n+1}$ for $\boldsymbol{\phi}$. The resulting equations are then subtracted from each other, eliminating the boundary condition, and giving, on the left hand boundary,

$$\boldsymbol{\phi}_{i_m-1}^{k+1,n+1}-\boldsymbol{\phi}_{i_m-1}^{k,n+1}=-\left(\boldsymbol{\phi}_{i_m}^{k+1,n+1}-\boldsymbol{\phi}_{i_m}^{k,n+1}\right), \tag{A.15}$$

and on the right boundary,

$$\boldsymbol{\phi}_{i_m+1}^{k+1,n+1}-\boldsymbol{\phi}_{i_m+1}^{k,n+1}=-\left(\boldsymbol{\phi}_{i_m}^{k+1,n+1}-\boldsymbol{\phi}_{i_m}^{k,n+1}\right). \tag{A.16}$$

Substituting equations A.15 and A.16 into equation A.5 gives the left hand boundary condition as,

$$\left(b_i-a_i\right)\boldsymbol{\phi}_{i_m}^{k+1,n+1}+c_i\boldsymbol{\phi}_{i_m+1}^{k+1,n+1}=RHS, \tag{A.17}$$

and the right hand side boundary as,

$$a_i\boldsymbol{\phi}_{i_m-1}^{k+1,n+1}+\left(b_i-c_i\right)\boldsymbol{\phi}_{i_m}^{k+1,n+1}=RHS. \tag{A.18}$$

In tridiagonal form for Nx nodes from $x = 0$ to $x = 1$ the system is,

$$\begin{bmatrix} a_{i=1} & c_{i=1} & 0 & \cdots & 0 \\ a_i & b_i & c_i & & \vdots \\ 0 & \ddots & \ddots & \ddots & 0 \\ \vdots & & a_{N_x-1} & b_{N_x-1} & c_{N_x-1} \\ 0 & \cdots & 0 & a_{i=N_x} & C_{i=N_x} \end{bmatrix} \begin{Bmatrix} \boldsymbol{\phi}_{i_m=1}^{k+1,n+1} \\ \boldsymbol{\phi}_{i_m}^{k+1,n+1} \\ \vdots \\ \boldsymbol{\phi}_{i_m=N_x-1}^{k+1,n+1} \\ \boldsymbol{\phi}_{i_m=N_x}^{k+1,n+1} \end{Bmatrix} = \begin{Bmatrix} \boldsymbol{\phi}_{i_m=1}^{k=0,n} - \boldsymbol{\phi}_{i_m}^{k,n+1} + \Delta t f\left(\boldsymbol{\Phi}\left(x_{i=0}=0\right)\right) \\ \boldsymbol{\phi}_{i_m}^{k=0,n} - \boldsymbol{\phi}_{i_m}^{k,n+1} + \Delta t f\left(\boldsymbol{\Phi}\left(x_i\right)\right) \\ \vdots \\ \boldsymbol{\phi}_{i_m=N_x-1}^{k=0,n} - \boldsymbol{\phi}_{i_m=N_x-1}^{k,n+1} + \Delta t f\left(\boldsymbol{\Phi}\left(x_{i=Nx-1}\right)\right) \\ \boldsymbol{\phi}_{i_m=N_x}^{k=0,n} - \boldsymbol{\phi}_{i_m=N_x}^{k,n+1} + \Delta t f\left(\boldsymbol{\Phi}\left(x_{i=Nx}=Lx\right)\right) \end{Bmatrix} \tag{A.19}$$

where $A_{i=1} = b_{i=1} - a_{i=1}$, $C_{i=N_x} = b_{i=N_x} - c_{i=N_x}$. The system in equation A.19 can be solved with the Thomas algorithm [167].

A.1.3 Neumann Boundary Conditions

For this work all Neumann boundary conditions are zero flux, or in the case of temperature, adiabatic, $\nabla(\cdot) = 0$, where $(\cdot)$ is any transported quantity at the boundary. Implementation of Neumann boundary conditions is less complicated than dirichlet conditions on a staggered grid because the boundary derivative is collocated at the face of a computational cell. This removes the need to interpolate boundary quantities and keeps the difference scheme's boundary conditions $O\left(\Delta x^2\right)$. Again, this procedure is used only when the PDE solved with equation A.19 is linear, the non-linear version will have a much more complicated Jacobian, $\partial f/\partial\phi$, and is addressed by the explicit, in time, sub steps in a Runge-Kutta, or Newton-Raphson (see appendix B), time stepping method.

The boundary flux, using the ghost points from figures A.1 and A.2, for the left

hand boundary is,

$$\tilde{\alpha}_i \left(\nabla \boldsymbol{\phi}\right)_{ol} = \frac{\boldsymbol{\phi}_{i_m} - \boldsymbol{\phi}_{i_m-1}}{x_{i_m} - x_{i_m-1}} = 0 \quad \rightarrow \quad \boldsymbol{\phi}_{i_m} = \boldsymbol{\phi}_{i_m-1}, \tag{A.20}$$

and for the right hand boundary,

$$\tilde{\alpha}_{i+1} \left(\nabla \boldsymbol{\phi}\right)_{or} = \frac{\boldsymbol{\phi}_{i_m+1} - \boldsymbol{\phi}_{i_m}}{x_{i_m+1} - x_{i_m s}} = 0 \quad \rightarrow \quad \boldsymbol{\phi}_{i_m} = \boldsymbol{\phi}_{i_m+1}. \tag{A.21}$$

To apply the boundary conditions to the explicit side of equation A.3 the same procedure is used as was used for the dirichlet boundary conditions in section A.1.2. Substitution $\boldsymbol{\phi}^{k=0,n}$ and $\boldsymbol{\phi}^{k+1,n+1}$ in for $\boldsymbol{\phi}$ in equations A.20 and A.21, adding them an dividing by two gives the boundaries in mid point form. For the left hand boundary,

$$\frac{1}{2}\left(\boldsymbol{\phi}_{i_m}^{k,n+1} + \boldsymbol{\phi}_{i_m}^{k=0,n}\right) = \frac{1}{2}\left(\boldsymbol{\phi}_{i_m-1}^{k,n+1} + \boldsymbol{\phi}_{i_m-1}^{k=0,n}\right) \quad \rightarrow \quad \boldsymbol{\Phi}_{i_m} = \boldsymbol{\Phi}_{i_m-1}, \tag{A.22}$$

and the right handed boundary,

$$\frac{1}{2}\left(\boldsymbol{\phi}_{i_m}^{k,n+1} + \boldsymbol{\phi}_{i_m}^{k=0,n}\right) = \frac{1}{2}\left(\boldsymbol{\phi}_{i_m+1}^{k,n+1} + \boldsymbol{\phi}_{i_m+1}^{k=0,n}\right) \quad \rightarrow \quad \boldsymbol{\Phi}_{i_m} = \boldsymbol{\Phi}_{i_m+1}. \tag{A.23}$$

Substituting equations A.22 and A.23 into equation A.4 using the boundary ghost points from figures A.1 and A.2, gives the left hand boundary condition, applied explicitly,

$$f\left(\boldsymbol{\Phi}\left(x=0\right)\right) = \boldsymbol{\nabla}\cdot\mathbf{F} = \left(\frac{\boldsymbol{\Phi}_{i_m+1} - \boldsymbol{\Phi}_{i_m}}{x_{i_m+1} - x_{i_m}}\tilde{\alpha}_{i+1}\right)\frac{1}{x_{i+1} - x_i}, \tag{A.24}$$

and the right hand boundary,

$$f\left(\boldsymbol{\Phi}\left(x=Lx\right)\right) = \boldsymbol{\nabla}\cdot\mathbf{F} = \left(-\frac{\boldsymbol{\Phi}_{i_m} - \boldsymbol{\Phi}_{i_m-1}}{x_{i_m} - x_{i_m-1}}\tilde{\alpha}_{i}\right)\frac{1}{x_{i+1} - x_i}. \tag{A.25}$$

Again, following the implicit procedure from section A.1.2 equations A.20 and A.21 can be put in residual form. For the left hand boundary this is,

$$\boldsymbol{\phi}_{i_m-1}^{k+1,n+1} - \boldsymbol{\phi}_{i_m-1}^{k,n+1} = \left(\boldsymbol{\phi}_{i_m}^{k+1,n+1} - \boldsymbol{\phi}_{i_m}^{k,n+1}\right), \tag{A.26}$$

and for the right hand boundary,

$$\boldsymbol{\phi}_{i_m+1}^{k+1,n+1} - \boldsymbol{\phi}_{i_m+1}^{k,n+1} = \left(\boldsymbol{\phi}_{i_m}^{k+1,n+1} - \boldsymbol{\phi}_{i_m}^{k,n+1}\right). \tag{A.27}$$

The boundaries are the applied implicitly changing equation A.5 to,

$$\left(b_i + a_i\right) \boldsymbol{\phi}_{i_m}^{k+1,n+1} + c_i \boldsymbol{\phi}_{i_m+1}^{k+1,n+1} = RHS, \tag{A.28}$$

for the left hand boundary and,

$$a_i \boldsymbol{\phi}_{i_m-1}^{k+1,n+1} + \left(b_i + c_i\right) \boldsymbol{\phi}_{i_m}^{k+1,n+1} = RHS. \tag{A.29}$$

for the right hand boundary. The system formed by in equations A.28 and A.29 can be solved with the Thomas algorithm, and is unchanged in form from equation A.19 except for the coefficients from equation A.19 which are $A_{i=1} = b_{i=1} + a_{i=1}$ and $C_{i=N_x} = b_{i=1} + c_{i=1}$ for Neumann conditions.

Appendix B

B.1 Time Discretization of A General Transport Equation

B.1.1 Time Evolution

The conservative transport equation (equation B.1) can be discretized in time to second order accuracy ($O\left(\Delta t^2\right)$), by a series of taylor expansions of the transported vector quantity ($\boldsymbol{\phi}$). The transport equation is then linearized in time through a Taylor expansion of its general function, f, which is some mixture of convective and diffusive terms. The final time integration for the general transport equation is done through Newton-Raphson iterations.

A general conservative transport equation, in one spacial dimension (x), and time (t), can be given as,

$$\partial_t \boldsymbol{\phi}\left(x,t\right) = \frac{\partial \boldsymbol{\phi}}{\partial t} = f\left(\boldsymbol{\Phi}\left(x,t\right)\right) \tag{B.1}$$

where $\boldsymbol{\phi}$ is any vector quantity, the function f is the discretizeation or solution to the transport PDE, and $\boldsymbol{\Phi} = \left(\boldsymbol{\phi}^{n+1} + \boldsymbol{\phi}^{n}\right)/2$ is the midpoint value of $\boldsymbol{\phi}$ in the time steps from $n \rightarrow n+1$ from chapter 3 and appendix A.

B.1.2 Taylor Expansion of a GTE

A Taylor series expansion, about t, of $\boldsymbol{\phi}$ from equation B.1 results in,

$$\boldsymbol{\phi}\left(x,t+\Delta t\right)=\boldsymbol{\phi}\left(x,t\right)+\Delta t\left.\frac{\partial\boldsymbol{\phi}}{\partial t}\right|_{x,t}+\frac{\Delta t^{2}}{2!}\left.\frac{\partial^{2}\boldsymbol{\phi}}{\partial t^{2}}\right|_{x,t}+O\left(\Delta t^{3}\right), \tag{B.2}$$

and about $t+\Delta t$,

$$\boldsymbol{\phi}\left(x,t\right)=\boldsymbol{\phi}\left(x,t+\Delta t\right)-\Delta t\left.\frac{\partial\boldsymbol{\phi}}{\partial t}\right|_{x,+\Delta t}+\frac{\Delta t^{2}}{2!}\left.\frac{\partial^{2}\boldsymbol{\phi}}{\partial t^{2}}\right|_{x,+\Delta t}+O\left(\Delta t^{3}\right). \tag{B.3}$$

Subtracting equation B.3 from equation B.2 yields,

$$\begin{aligned}&2\boldsymbol{\phi}\left(x,t+\Delta t\right)=\\&\quad 2\boldsymbol{\phi}\left(x,t\right)+\Delta t\left.\frac{\partial\boldsymbol{\phi}}{\partial t}\right|_{x,t}+\Delta t\left.\frac{\partial\boldsymbol{\phi}}{\partial t}\right|_{x,t+\Delta t}\\&\qquad+\frac{\Delta t^{2}}{2!}\left.\frac{\partial^{2}\boldsymbol{\phi}}{\partial t^{2}}\right|_{x,t}-\frac{\Delta t^{2}}{2!}\left.\frac{\partial^{2}\boldsymbol{\phi}}{\partial t^{2}}\right|_{x,t+\Delta t}+O\left(\Delta t^{3}\right).\end{aligned} \tag{B.4}$$

In terms of the indices in time and space, n and i respectively, equation B.4 is,

$$\begin{aligned}&\boldsymbol{\phi}_{i}^{n+1}=\\&\quad\boldsymbol{\phi}_{i}^{n}+\frac{\Delta t}{2}\left[\left(\frac{\partial\boldsymbol{\phi}}{\partial t}\right)_{i}^{n}+\left(\frac{\partial\boldsymbol{\phi}}{\partial t}\right)_{i}^{n+1}\right]\\&\qquad+\frac{\Delta t^{2}}{2!}\left[\left(\frac{\partial^{2}\boldsymbol{\phi}}{\partial t^{2}}\right)_{i}^{n}-\left(\frac{\partial^{2}\boldsymbol{\phi}}{\partial t^{2}}\right)_{i}^{n+1}\right]\frac{1}{2}+O\left(\Delta t^{3}\right).\end{aligned} \tag{B.5}$$

Substituting the Taylor series expansion,

$$\left(\frac{\partial^{2}\boldsymbol{\phi}}{\partial t^{2}}\right)_{i}^{n+1}=\left(\frac{\partial^{2}\boldsymbol{\phi}}{\partial t^{2}}\right)_{i}^{n}+\frac{\partial}{\partial t}\left(\frac{\partial^{2}\boldsymbol{\phi}}{\partial t^{2}}\right)_{i}^{n}\Delta t+...+O\left(\Delta t^{3}\right) \tag{B.6}$$

into equation B.5, and disregarding the third order derivatives, gives,

$$\frac{\boldsymbol{\phi}_{i}^{n+1}-\boldsymbol{\phi}_{i}^{n}}{\Delta t}=\frac{1}{2}\left[\left(\frac{\partial\boldsymbol{\phi}}{\partial t}\right)_{i}^{n}+\left(\frac{\partial\boldsymbol{\phi}}{\partial t}\right)_{i}^{n+1}\right]+O\left(\Delta t^{2}\right). \tag{B.7}$$

Substitution of equation B.1 into equation B.7,

$$\frac{\boldsymbol{\phi}_{i}^{n+1}-\boldsymbol{\phi}_{i}^{n}}{\Delta t}=\frac{1}{2}\left[f\left(\boldsymbol{\Phi}\right)_{i}^{n}+f\left(\boldsymbol{\Phi}\right)_{i}^{n+1}\right]+O\left(\Delta t^{2}\right), \tag{B.8}$$

indicates second order accuracy, of the time discretization, of equation B.1 [168]. The Taylor expansion of the RHS of equation B.1 is given as,

$$f\left(\mathbf{\Phi}\left(x,t+\Delta t\right)\right)=f\left(\mathbf{\Phi}\left(x,t\right)\right)+\Delta t\frac{\partial f\left(\mathbf{\Phi}\right)}{\partial t}\bigg|_{x,t}\rightarrow f\left(\mathbf{\Phi}\right)_{i}^{n+1}=f\left(\mathbf{\Phi}\right)_{i}^{n}+\Delta t\frac{\partial f}{\partial\boldsymbol{\phi}}\frac{\partial\boldsymbol{\phi}}{\partial t} \quad \text{(B.9)}$$

Rearranging equation B.8 as,

$$f\left(\mathbf{\Phi}\right)_{i}^{n+1}=2\frac{\boldsymbol{\phi}_{i}^{n+1}-\boldsymbol{\phi}_{i}^{n}}{\Delta t}-f\left(\boldsymbol{\phi}\right)_{i}^{n} \quad \text{(B.10)}$$

and combining equation B.10 with equation B.9 gives,

$$\frac{\boldsymbol{\phi}_{i}^{n+1}-\boldsymbol{\phi}_{i}^{n}}{\Delta t}=\frac{1}{2}\left[f\left(\mathbf{\Phi}\right)_{i}^{n}+f\left(\mathbf{\Phi}\right)_{i}^{n}+\Delta t\frac{\partial f}{\partial\mathbf{\Phi}}\frac{\boldsymbol{\phi}_{i}^{n+1}-\boldsymbol{\phi}_{i}^{n}}{\Delta t}\right]=f\left(\mathbf{\Phi}\right)_{i}^{n}+\frac{\partial f}{\partial\boldsymbol{\phi}}\frac{\boldsymbol{\phi}_{i}^{n+1}-\boldsymbol{\phi}_{i}^{n}}{2}, \quad \text{(B.11)}$$

which is the time evolution of a linear GTE in residual form.

B.1.3 Linearization of a Non-linear GTE

Equation B.11 is in the form of a general Newton-Raphson iteration equation,

$$f\left(\boldsymbol{\phi}^{k=0}+\Delta\boldsymbol{\phi}\right)\approx f\left(\boldsymbol{\phi}^{k=0}\right)+\Delta\boldsymbol{\phi}[f\left(\boldsymbol{\phi}^{k=0}\right)], \quad \text{(B.12)}$$

if $\boldsymbol{\phi}$ is a general vector quantity. Writing equation B.11 in the form of equation B.12 gives,

$$\frac{\boldsymbol{\phi}^{k+1,n+1}-\boldsymbol{\phi}^{k=0,n}}{\Delta t}=f\left[\frac{1}{2}\left(\boldsymbol{\phi}^{k=0,n}+\boldsymbol{\phi}^{k,n+1}\right)\right]+\frac{\Delta\boldsymbol{\phi}}{2}\frac{\partial f\left[\frac{1}{2}\left(\boldsymbol{\phi}^{k=0,n}+\boldsymbol{\phi}^{k,n+1}\right)\right]}{\partial\boldsymbol{\phi}} \quad \text{(B.13)}$$

where k is the current iteration, and $k=0$ is the initial approximation (usually the starting value of the vector field at the initial time step n). Using the relationship $\Delta\boldsymbol{\phi}+\boldsymbol{\phi}^{k,n+1}=\boldsymbol{\phi}^{k+1,n+1}$ and substituting it into equation B.13 gives the final version of the time advancement scheme, in residual form,

$$\left(\boldsymbol{\phi}^{k+1,n+1}-\boldsymbol{\phi}^{k,n+1}\right)\left[1-\frac{\Delta t}{2}\frac{\partial f}{\partial\boldsymbol{\phi}}\right]=\boldsymbol{\phi}^{k=0,n}-\boldsymbol{\phi}^{k,n+1}+\Delta tf\left[\frac{1}{2}\left(\boldsymbol{\phi}^{k=0,n}+\boldsymbol{\phi}_{k}^{n+1}\right)\right], \quad \text{(B.14)}$$

which is the time evolution equation for a non-linear GTE.

Appendix C

C.1 Natural Convection

Convection flows can be caused by variation in density in the presence of a gravity field. If the variations in the density of the working fluid are produced by thermal gradients, causing thermal expansion and contraction, it is called natural convection. This type of flow is also called a buoyancy-driven flow, where fluid is heated, becomes less dense and rises. The addition of a buoyancy forcing term, $\Theta_{\mathbf{u}} = \mathbf{g}\rho$, to equation 2.2 gives

$$\begin{aligned}\frac{D\mathbf{u}}{Dt} &= \partial_t(\rho\mathbf{u}) + \boldsymbol{\nabla}\cdot(\rho\mathbf{u}\otimes\mathbf{u}) = \\ &-\boldsymbol{\nabla}\cdot\mathbb{I}P + \boldsymbol{\nabla}\cdot\underbrace{\left[\mu(\boldsymbol{\nabla}\mathbf{u}+\boldsymbol{\nabla}^{\intercal}\mathbf{u}) - \frac{2}{3}\mu(\boldsymbol{\nabla}\cdot\mathbf{u})\,\mathbb{I}\right]}_{\text{deviatoric stress tensor, }\sigma} + \mathbf{g}\cdot\mathbb{I}\rho,\end{aligned} \tag{C.1}$$

where $\mathbf{g} = g_x\hat{\boldsymbol{\imath}} + g_y\hat{\boldsymbol{\jmath}} + g_z\hat{\mathbf{k}}$ is the gravity field. The addition of a gravity field and variable density can cause strong feedback into momentum transport equations through the pressure term. The first assumption to make is that the pressure, $P = P_{st} + P_d$, is made up of static, subscript st, and dynamic, subscript d, pressures. The dynamic pressure, P_d, is the pressure resulting in the fluid motion, and the hydrostatic pressure, $P_{st} = P_o - G_y\int_{A_c}\int_{y_o}^{L_y}\rho_o dy dA/A_c$ where $(\cdot)_o$ denots a reference value, A_c is the area under the hydrostatic column, and $P_o = 0$ is the pressure resulting from the fluid column above the a current height in the fluid field, y_o, or the piezometric pressure. The second assumption is that the anelastic approximation

$(\boldsymbol{\nabla} \cdot (\rho_o \mathbf{u}) = 0)$ is used in equation 2.1 giving a fluid that is not compressible. The density is not a function of the pressure and is only a function of the temperature field. This second assumption, for buoyancy-driven flows, is also know as the Boussinesq approximation, and it's effect is two fold. It gives a relationship between the temperature and the density in the linearized form,

$$\frac{\rho_o}{\rho} = 1 - \beta \left(\phi - \phi_o\right), \tag{C.2}$$

and it removes the variability of the density from the momentum and pressure terms in equation C.1. The Boussinesq approximation is allowable if the the variation of the density, due to the temperature, is small, $\rho_o/\rho << 1$. Substituting equation C.2, $\mathbf{g} = 0\hat{\boldsymbol{\imath}} - G_y\hat{\boldsymbol{\jmath}} + 0\hat{\mathbf{k}}$, $P = P_{st} + P_d \rightarrow \boldsymbol{\nabla} \cdot P_{st} = \mathbf{g}\rho_o$ into equation C.1 yields,

$$\rho_o \left[\partial_t \left(\mathbf{u}\right) + \boldsymbol{\nabla} \cdot \left(\mathbf{u} \otimes \mathbf{u}\right)\right] = \boldsymbol{\nabla} \cdot \left(\mu \boldsymbol{\nabla} \mathbf{u}\right) - \boldsymbol{\nabla} \cdot \mathbb{I} P_d + \mathbb{I} \cdot \mathbf{g}\rho_o \beta \Delta\phi. \tag{C.3}$$

For the cases discussed here the viscosity is not variable which gives the governing equation for natural convection with the Boussinesq approximation as,

$$\partial_t \mathbf{u} = \underbrace{\nu \boldsymbol{\nabla} \cdot \boldsymbol{\nabla} \mathbf{u} - \boldsymbol{\nabla} \cdot \left(\mathbf{u} \otimes \mathbf{u}\right) - \frac{1}{\rho_o} \boldsymbol{\nabla} \cdot \mathbb{I} P_d}_{\mathbf{F} \text{ from the FV method}} - \mathbb{I} \cdot \hat{\boldsymbol{\jmath}} G_y \beta \Delta\phi. \tag{C.4}$$

C.1.1 Rayleigh-Bénard Convection

To adequately simulate all the relevant physics and scales of a buoyancy-driven flows equation C.4 can be properly normalized and non-dimensionalized by $\mathbf{g}$, the scaling inherent in the Boussinesq approximation (equation C.2), and the characteristic length in the computational domain. The non-dimensional groups used for equation C.4 are determined by the characteristics of a specific type of buoyancy-driven flow, Rayleigh-Bénard convection (see figure C.1),

$$\begin{aligned}
\mathbf{u}^* &= \mathbf{u}\left[\frac{1}{U_c}\right] & \mathbf{x}^* &= \mathbf{x}\left[\frac{1}{L_y}\right] & t^* &= t\left[\frac{U_c}{L_y}\right] \\
P^* &= P\left[\frac{1}{\rho o U_c^2}\right] & \phi^* &= \frac{\phi - \phi_o}{\phi_\infty - \phi_o} & Ra &= \frac{G_y L_y^3 \beta \Delta\phi}{\nu \alpha_f},
\end{aligned} \tag{C.5}$$

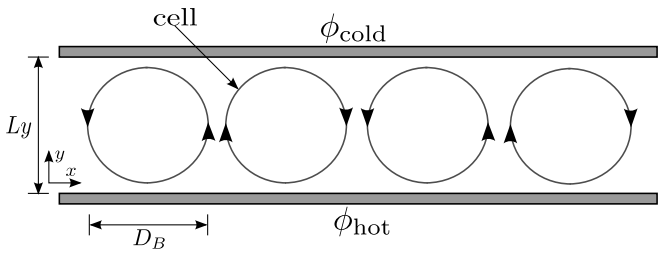

Figure C.1: Rayleigh-Bénard convection showing the rotational convection cells that develop causing hot plumes moving toward the cold top and cold plumes moving toward the hot bottom, where D_B is the characteristic width of each convection cell

where Ra is the Rayleigh number a ratio of convective forces to momentum diffusive forces, and U_c is the convection velocity, $U_c = \sqrt{G_y L_y \beta \Delta\phi}$. The Rayleigh number with the Prandtl number, $Pr = \nu/\alpha_f$, gives $Re = Ra^{\frac{1}{2}} Pr^{-\frac{1}{2}}$ as the effective Reynolds number for natural convection. Integrating equation C.4,about the C.V. (see section 3.1), applying the dimensionless groups from equation C.5 (omitting the $*$'s), taking the volumetric average of the temperature, and using the relationship for dimensionless pressure, $P^* = P^*_{st} + P^*_d$, gives the FV formulation for equation C.4,

$$\partial_t \overline{\mathbf{u}} = \frac{1}{V} \oint_V \Bigg[\underbrace{\frac{1}{Re}\boldsymbol{\nabla}^2 \mathbf{u} - \boldsymbol{\nabla}\cdot(\mathbf{u}\otimes\mathbf{u}) - \boldsymbol{\nabla}\cdot\mathbb{I}P_d}_{\text{FV method non-linear flux}\rightarrow \oint_V \boldsymbol{\nabla}\cdot\mathbf{F}dV} - \underbrace{\mathbb{I}\cdot\hat{\boldsymbol{\jmath}} G_y V \overline{\phi}}_{\text{Source term}\rightarrow \mathbf{f}_B} \Bigg] dV \tag{C.6}$$

The scalar transport is non-dimensionalized with the same dimensionless groups, equation C.5, used with equation C.6 and substituting them into equation 3.12 gives,

$$\partial_t \overline{\phi} = \frac{1}{V} \oint_V \left[\frac{1}{RePr} \boldsymbol{\nabla}^2 \phi - \boldsymbol{\nabla}\cdot(\mathbf{u}\phi) \right] dV, \tag{C.7}$$

for the fluid domain and,

$$\partial_t \overline{\phi} = \frac{1}{V} \oint_V \left[\frac{1}{RePr} \frac{\alpha_s}{\alpha_f} \boldsymbol{\nabla}^2 \phi \right] dV, \tag{C.8}$$

for the solid domain [169].

References

[1] Gau, C. & Viskanta, R. Melting and solidification of a pure metal on a vertical wall. *Journal of Heat Transfer* **108**, 174–181 (1986).

[2] Jana, S., b, S. R. & Durst, F. A numerical method to compute solidification and melting processes. *Applied Mathematical Modelling* **13**, 93119 (2007).

[3] Joulin, A., Younsi, Z., Zalewski, L., Rousse, D. R. & Lassue, S. A numerical study of the melting of phase change material heated from a vertical wall of a rectangular enclosure. *International Journal of Computational Fluid Dynamics* **23**, 553–566 (2009).

[4] Hoather, W. The density and coefficient of expansion of liquid gallium over a wide range of temperature. *Proceedings of the Physical Society* **48**, 699 (1936).

[5] for Metals, A. S. & Davis, J. R. *ASM handbook. 2. Properties and selection: nonferrous alloys and special-purpose materials* (ASM international, 2009).

[6] Hannoun, N., Alexiades, V. & Mai, T. Z. Resolving the controversy over tin and gallium melting in a rectangular cavity heated from the side. *Numerical Heat Transfer: Part B: Fundamentals* **44**, 253–276 (2003).

[7] Velghe, A. *Modélisation de l'interaction entre un écoulement turbulent et une paroi ablatable*. Ph.D. thesis, University of Vermont (2007).

[8] Velghe, A., Nguyen-Bui, N. & Chassaing, P. Direct numerical simulation of reacting turbulent flow on ablatable surface. *AIAA Paper* **4400** (2007).

[9] Desjardins Research Group. Nga-arts flow solver from the computational thermo-fluids laboratory, cornell university (2015). URL `http://ctflab.mae.cornell.edu/nga.html`.

[10] Lange, C., Durst, F. & Breuer, M. Momentum and heat transfer from cylinders in laminar crossflow at 10- 4 re 200. *International Journal of Heat and Mass Transfer* **41**, 3409–3430 (1998).

[11] Zhang, N., Zheng, Z. & Eckels, S. Study of heat-transfer on the surface of a circular cylinder in flow using an immersed-boundary method. *International Journal of Heat and Fluid Flow* **29**, 1558–1566 (2008).

[12] Nagendra, K., Tafti, D. K. & Viswanath, K. A new approach for conjugate heat transfer problems using immersed boundary method for curvilinear grid based solvers. *Journal of Computational Physics* **267**, 225–246 (2014).

[13] Churchill, S. & Bernstein, M. A correlating equation for forced convection from gases and liquids to a circular cylinder in crossflow. *Journal of Heat Transfer* **99**, 300–306 (1977).

[14] Kim, J. & Choi, H. An immersed-boundary finite-volume method for simulation of heat transfer in complex geometries. *KSME International Journal* **18**, 1026–1035 (2004).

[15] Gau, C. & Viskanta, R. Melting and solidificaiton of a metal system in a rectangular cavity. *International J. of Heat and Mass Transfer* **27**, 113–123 (1984).

[16] Frisch, U. *Turbulence: the legacy of AN Kolmogorov* (Cambridge university press, 1995).

[17] Jiménez, J. & Moin, P. Minimal flow unit in near-wall turbulence. *J. Fluid Mech.* **225**, 213–240 (1991).

[18] Turner, R. K., Adger, N. & Doktor, P. Assessing the economic costs of sea level rise. *Environment and Planning A* **27**, 1777–1796 (1995).

[19] Roebeling, P., Coelho, C. & Reis, E. Coastal erosion and coastal defense interventions: a cost-benefit analysis. *Journal of Coastal Research* **64**, 1415–1419 (2011).

[20] Turner, R. K., Burgess, D., Hadley, D., Coombes, E. & Jackson, N. A cost–benefit appraisal of coastal managed realignment policy. *Global Environmental Change* **17**, 397–407 (2007).

[21] Pérez-Maqueo, O., Intralawan, A. & Martínez, M. Coastal disasters from the perspective of ecological economics. *Ecological Economics* **63**, 273–284 (2007).

[22] Gaddis, E. B., Miles, B., Morse, S. & Lewis, D. Full-cost accounting of coastal disasters in the united states: implications for planning and preparedness. *Ecological Economics* **63**, 307–318 (2007).

[23] Venkatapathy, E. *et al.* Thermal protection system development, testing, and qualification for atmospheric probes and sample return missions: Examples for saturn, titan and stardust-type sample return. *Advances in Space Research* **44**, 138–150 (2009).

[24] Lyle, K. H. & Fasanella, E. L. Permanent set of the space shuttle thermal protection system reinforced carbon–carbon material. *Composites Part A: Applied Science and Manufacturing* **40**, 702–708 (2009).

[25] Olynick, D., Chen, Y. & Tauber, M. E. Forebody tps sizing with radiation and ablation for the stardust sample return capsule. *AIAA Paper* **2474**, 1997 (1997).

[26] Dougherty, M. *Numerical Simulations of reacting Flow in an Inductively Coupled Plasma Torch*. Ph.D. thesis, University of Vermont (2015).

[27] Owens, W. *Aero-Thermal Characterization Of Silicon Carbide Flexible Tps Using A 30kw Icp Torch*. Ph.D. thesis, University of Vermont (2015).

[28] Moin, P. & Mahesh, K. Direct numerical simulation: A tool in turbulence research.

Annu. Rev. Fluid Mech. **30**, 539–578 (1998).

[29] Kim, J., Moin, P. & Moser, R. Turbulence statistics in fully developed channel flow at low Reynolds number. *J. Fluid Mech.* **177**, 133–166 (1987).

[30] Moser, R. D., Kim, J. & Mansour, N. N. Direct numerical simulation of turbulent channel flow up to Re_τ=590. *Physics of Fluids* **11**, 943–945 (1999).

[31] Khabakhpasheva, Y. M. Experimental Investigation of Turbulent Momentum and Heat Transfer in the Proximity of the Wall. *Heat Transfer 1986, Proceedings of The 8th International Heat Transfer Conference* (1987).

[32] Teitel, M. & Antonia, R. Heat transfer in fully developed turbulent channel flow: comparison between experiment and direct numerical simulations. *International Journal of Heat and Mass Transfer* **36**, 17011706 (1993).

[33] Sinai, Y. A wall function for the temperature variance in turbulent flow adjacent to a diabatic wall. *Journal of heat transfer* **109**, 861–865 (1987).

[34] Kawamura, H., Ohsaka, K., Abe, H. & Yamamoto, K. Dns of turbulent heat transfer in channel flow with low to medium-high prandtl number fluid. *International Journal of Heat and Fluid Flow* **19**, 482–491 (1998).

[35] Kasagi, N., Kuroda, A. & Hirata, M. Numerical Investigation of Near- Wall Turbulent Heat Transfer Taking Into Account the Unsteady Heat Conduction in the Solid Wall. *Journal of Heat Transfer* **111**, 385–392 (1989).

[36] Kasagi, N., Tomita, Y. & Kuroda, A. Direct numerical simulation of passive scalar field in a turbulent channel flow. *Journal of heat transfer* **114**, 598–606 (1992).

[37] Kim, J. & Moin, P. Transport of passive scalars in a turbulent channel flow. *Turbulent Shear Flows 6* 85–96 (1989).

[38] Deardorff, J. W. Preliminary results from numerical integrations of the unstable planetary boundary layer. *Journal of the Atmospheric Sciences* **27**, 1209–1211 (1970).

[39] Mahesh, K., Constantinescu, G. & Moin, P. A numerical method for large-eddy simulation in complex geometries. *Journal of Computational Physics* **197**, 215–240 (2004).

[40] Mahesh, K. *et al.* Large-eddy simulation of reacting turbulent flows in complex geometries. *Journal of Applied Mechanics* **73**, 374–381 (2006).

[41] Peskin, C. Flow patterns around heart valves: A digital computer method for solving the equations of motion. *PhD Thesis, Albert Einstein College of Medicine* (1972).

[42] Mohd-Yusof, J. Combined immersed boundaries/B-splines methods for simulations of flows in complex geometries. *Center for Turbulence Research Annual Research Briefs* **NASA Ames/Stanford University** (1997).

[43] Jung Hee Seo, R., Mittal. A sharp-interface immesed boundary method with improved mass conservation and reduced spurious pressure oscillations. *Journal of Computational Physics* **230**, 7347–7363 (2011).

[44] Jongho Lee, J., Kim, Choi, H. & Yang, K. Sources of spurious force oscillations from an immersed boundary method for moving-body problems. *Journal of Computational Physics* **230** (2011).

[45] Ye, T., Mittal, R., HS, U. & Shyy, W. An accurate Cartesian grid method for viscous incompressible flows with complex immersed boundaries. *J. Comp. Phys.* **156**, 209–240 (1999).

[46] Mittal, R. *et al.* A versatile sharp interface immersed boundary method for incompressible flows with complex boundaries. *J. Comp. Phys.* **227**, 4825–4852 (2008).

[47] Kirkpatrick, M., Armfield, S. & Kent, J. A representation of curved boundaries for the solution of the navier–stokes equations on a staggered three-dimensional cartesian grid. *Journal of Computational Physics* **184**, 1–36 (2003).

[48] Meyer, M., Devesa, A., Hickel, S., Hu, X. & Adams, N. A conservative immersed interface method for large-eddy simulation of incompressible flows. *Journal of Computational Physics* **229**, 63006317 (2010).

[49] Brady, P. & Desjardins, O. A sharp, robust, discretely conservative cut-cell immersed boundary technique for complex three dimensional geometries. *J. Comput. Phys* (2014).

[50] Kang, S., Iaccarino, G. & Ham, F. DNS of buoyancy-dominated turbulent flows on a bluff body using the immersed boundary method. *J. Comp. Phys.* **228**, 3189–3208 (2009).

[51] Kang, S. *An Improved Immersed Boundary Method for Computation of Turbulent Flows with Heat Transfer*. Ph.D. thesis, Stanford University (2008).

[52] Osher, S. & Sethian, J. Fronts Propagating with Curvature Dependent Speed: Algorithms Based on Hamilton-Jacobi Formulations. *J. Comput. Phys.* **79**, 12–49 (1988).

[53] Shao, H., Chan, T., Merriman, B. & Osher, S. A Variational level set approach to multiphase motion. *Journal of Computational Physics* **127**, 179–195 (1996).

[54] Owkes, M. & Desjardins, O. A computational framework for conservative, three-dimensional, unsplit, geometric transport with application to the volume-of-fluid (vof) method. *Journal of Computational Physics* **270**, 587–612 (2014).

[55] Sethian, J. A fast marching level set method for monotonically advancing fronts. *Proc. Natl. Acad. Sci.* **93**, 1591–1595 (1996).

[56] Desjardins, O., Blanquart, G., Balarac, G. & Pitsch, H. High order conservative finite difference scheme for variable density low Mach number turbulent flows. *J. Comp. Phys.* **227**, 71257159 (2008).

[57] Pierce, C. & Moin, P. Progress-variable approach for large-eddy simulation of non-premixed turbulent combustion. *J. Fluid Mech.* **504**, 73–97 (2004).

[58] Osher, S. & Fedkiw, R. Level Set Methods: An Overview and Some Recent Results. *J. Comp. Phys.* **169**, 463–502 (2001).

[59] Chang, Y. C., Hou, T. Y., Merriman, B. & Osher, S. A Level Set Formulation of

Eulerian Interface Capturing Methods for Incompressible Fluid Flows. *J. Comput. Phys.* **124**, 449–464 (1996).

[60] Osher, S. & Fedkiw, R. *Level Set Methods and Dynamic Implicit Surfaces* (Springer, 2003).

[61] M.G. Crandall, L. L. Two approximations of solutions of HamiltonJacobi equations. *Math. Comput.* **43**, 1–19 (1984).

[62] M. Sussman P., S. O., Smereka. A level set approach for computing solutions to incompressible two-phase flow. *J. Comp. Phys.* **114**, 146–159 (1994).

[63] Min, C. On reinitializing level set functions. *J. Comp. Phys.* **229**, 2764–2772 (2009).

[64] Sussman, M., Fatemi, E., Smereka, P. & Osher, S. An Improved level set methog for incompressible two-phse flows. *Computer and Fluids* **27**, 663–680 (1998).

[65] Peng, D., Merriman, B., Osher, S., Zhao, H. & Kang, K. A PDE-Based Fast Local Level Set Method. *J. Comp. Phys.* **155**, 410–438 (1999).

[66] Sussman, M. & Fatemi, E. An efficient interface-preserving level set redistancing algorithm and its application to interfacial incompressible fluid flow. *SIAM J. Sci. Comput* **20**, 1165–1191 (1999).

[67] Sethian, J. *Level Set Methods and Fast Marching Methods Evolving Interfaces in Computational Geometry, Fluid Mechanics, Computer Vision, and Materials Science* (Cambridge University Pres, 1999).

[68] Chang, Y., Hou, T., Merriman, B. & S.J., O. A level set formulation of Eulerian interface capturing methods for incompressible fluid flows. *Journal of Computational Physics* **124**, 449–464 (1996).

[69] Adalsteinsson, D. & Sethian, J. A. The Fast Construction of Extension Velocities in Level Set Methods. *Journal of Computational Physics* **148**, 2–22 (1998).

[70] Dorfman, A. S. *Conjugate Problems in Convective Heat Transfer* (CRC Press, 2009).

[71] Kang, S., Iaccarino, G. & Ham, F. DNS of a buoyancy-dominated turbulent flow using an immersed boundary method. *Stanford Center for Turbulence Research Annual Research Briefs* **14**, 231–244 (2008).

[72] Iaccarino, G. & Moreau, S. Natural and Forced Conjugate Heat Transfer in Complex Geometries on Cartesian Adapted Grids. *J. Fluids Eng.* **128**, 838–846 (2006).

[73] Šarler, B. Stefan's work on solid-liquid phase changes. *Engineering Analysis with Boundary Elements* **16**, 83–92 (1995).

[74] Jiji, L. M. *Heat convection* (Springer, 2006).

[75] Willcockson, W. H. Stardust sample return capsule design experience. *Journal of Spacecraft and Rockets* **36**, 470–474 (1999).

[76] Dean, A., Kontinos, D. & Stackpoole, M. Post-flight analysis of the stardust sample return capsule earth entry. In *46th Aerospace Sciences Meeting and Exhibit, Reno, Nevada* (2008).

[77] Stackpoole, M., Sepka, S., Cozmuta, I. & Kontinos, D. Post-flight evaluation of stardust sample return capsule forebody heatshield material. In *46th AIAA Aerospace Sciences Meeting and Exhibit, Reno, Nevada* (2008).

[78] Kim, J. & Moin, P. Application of a fractional-step method to incompressible Navier-Stokes equations. *J. Comp. Phys.* **59**, 308–323 (1985).

[79] Morinishi, Y., Lund, T. S., Vasilyev, O. V. & Moin, P. Fully Conservative Higher Order Finite Difference Schemes for Incompressible Flow. *J. Comp. Phys.* **143**, 90124 (1998).

[80] Chung, T. *Computational Fluid Dynamics* (Cambridge University Press, 2002).

[81] Crank, J. & Nicolson, P. A practical method for numerical evaluation of solutions of partial differential equations of the heat-conduction type. *Advances in Computational Mathematics* **6**, 207–226 (1996reprint).

[82] H. Choi, P. M. Effects of the computational time step on numerical solutions of turbulent flow. *J. Comp. Phys.* **113**, 1–4 (1994).

[83] Stone, H. S. An efficient parallel algorithm for the solution of a tridiagonal linear system of equations. *Journal of the ACM (JACM)* **20**, 27–38 (1973).

[84] Pierce, C. *Progress-variable approach for large eddy simulation of turbulent combustion*. Ph.D. thesis, Flow Physics and Computation Division, Dept. Mech. Eng., Stanford Univ (2001).

[85] Henson, V. E. & Yang, U. M. BoomerAMG: a parallel Multigrid solver and preconditioner. *Applied Numerical Mathematics* **41**, 155–177 (2002).

[86] Iaccarino, G. & Moreau, S. A generalized minimal residual algorithm for solving nonsymmetric linear systems. *SIAM J. Sci. Stat. Comput* **7**, 856–869 (1986).

[87] LLNL. Hypre Suite of Solvers from Lawrence Livermore National Laboratory. `http://acts.nersc.gov/hypre/` (2015).

[88] Osher, S. & Solomon, F. Upwind difference schemes for hyperbolic systems of conservation laws. *Mathematics of Computation* **158**, 339–374 (1982).

[89] Nourgaliev, R. R. & Theofanous, T. G. High-fidelity interface tracking in compressible flows: Unlimited anchored adaptive level set. *Journal of Computational Physics* **224**, 836–866 (2007).

[90] Desjardins, O., Blanquart, G., Balarac, G. & Pitsch, H. High order conservative finite difference scheme for variable density low mach number turbulent flows. *Journal of Computational Physics* **227**, 7125–7159 (2008).

[91] Leonard, B. P. A stable and accurate convective modelling procedure based on

quadratic upstream interpolation. *Computer methods in applied mechanics and engineering* **19**, 59–98 (1979).

[92] Henrick, K., Aslam, T. & Powers, J. Mapped weighted essentially non-oscillatory schemes: Achieving optimal order near critical points. *J. Comp. Phys.* **207**, 542–567 (2005).

[93] Tan, L. & Zabaras, N. A level set simulation of dendritic solidification with combined features of front-tracking and fixed-domain methods. *J. Comp. Phys.* **211**, 36–63 (2006).

[94] Jiang, G.-S. & Peng, D. Weighted eno schemes for hamilton jacobi equations. *J. Sci. Comput.* **21**, 2126–2143 (2000).

[95] Liu, X.-D., Osher, S. & Chan, T. Weighted essentially non-oscillatory schemes. *Journal of Computational Physics* **115**, 200 – 212 (1994).

[96] Sethian, J. Evolution, Implementation, and Application of Level Set and Fast Marching Methods for Advancing Fronts. *J. Comput. Phys.* **169**, 503–555 (2000).

[97] Lorensen, W. E. & Cline, H. E. Marching cubes: A high resolution 3d surface construction algorithm. In *ACM siggraph computer graphics*, vol. 21, 163–169 (ACM, 1987).

[98] Guéziec, A. & Hummel, R. Exploiting triangulated surface extraction using tetrahedral decomposition. *Visualization and Computer Graphics, IEEE Transactions on* **1**, 328–342 (1995).

[99] Bloomenthal, J. Polygonization of implicit surfaces. *Computer Aided Geometric Design* **5**, 341–355 (1988).

[100] Ning, P. & Bloomenthal, J. An evaluation of implicit surface tilers. *Computer Graphics and Applications, IEEE* **13**, 33–41 (1993).

[101] Treece, G. M., Prager, R. W. & Gee, A. H. Regularised marching tetrahedra: im-

proved iso-surface extraction. *Computers & Graphics* **23**, 583–598 (1999).

[102] Ye, T., Mittal, R., Udaykumar, H. & Shyy, W. An accurate Cartesian grid method for viscous incompressible flows with complex immersed boundaries. *Journal of Computational Physics* **156**, 209–240 (1999).

[103] Hu, X., Khoo, B., Adams, N. & Huang, F. A conservative interface method for compressible flows. *J. Comput. Phys* **219**, 553578 (2006).

[104] Seo, J. H. & Mittal, R. A sharp-interface immersed boundary method with improved mass conservation and reduced spurious pressure oscillations. *Journal of computational physics* **230**, 7347–7363 (2011).

[105] Tseng, F., Y. Ferzinger. A ghost-cell immersed boundary method for ow in a complex geometry. *J. Comp. Phys.* **192**, 593–623 (2003).

[106] Sanitjai, S. & Goldstein, R. Forced convection heat transfer from a circular cylinder in crossflow to air and liquids. *International journal of heat and mass transfer* **47**, 4795–4805 (2004).

[107] Bharti, R. P., Chhabra, R. & Eswaran, V. A numerical study of the steady forced convection heat transfer from an unconfined circular cylinder. *Heat and Mass Transfer* **43**, 639–648 (2007).

[108] Ameen, F., Coney, J. & Sheppard, C. Experimental study of melting ice cylinders in a warm air cross-flow. *International Journal of Refrigeration* **14**, 168–175 (1991).

[109] Kravchenko, A. G. & Moin, P. Numerical studies of flow over a circular cylinder at red= 3900. *Physics of Fluids (1994-present)* **12**, 403–417 (2000).

[110] Dong, S., Karniadakis, G., Ekmekci, A. & Rockwell, D. A combined direct numerical simulation–particle image velocimetry study of the turbulent near wake. *Journal of Fluid Mechanics* **569**, 185–207 (2006).

[111] Catalano, P., Wang, M., Iaccarino, G. & Moin, P. Numerical simulation of the flow

around a circular cylinder at high reynolds numbers. *International Journal of Heat and Fluid Flow* **24**, 463–469 (2003).

[112] Dantzig, J. A. Modelling liquid–solid phase changes with melt convection. *International Journal for Numerical Methods in Engineering* **28**, 1769–1785 (1989).

[113] Richardson, L. F. The supply of energy from and to atmospheric eddies. *Proceedings of the Royal Society of London. Series A, Containing Papers of a Mathematical and Physical Character* 354–373 (1920).

[114] Hunt, J., Wray, A. & Moin, P. Eddies, streams, and convergence zones in turbulent flows. *Center for Trubulence Research Proceedings of the Summer Program* **Center for Turbulence Research**, 193 – 208 (1988).

[115] Jeong, J. & Hussain, F. On the identification of a vortex. *Journal of Fluid Mechanics* **285**, 69–94 (1995).

[116] Reynolds, O. On the dynamical theory of incompressible viscous fluids and the determination of the criterion. *Proceedings of the Royal Society of London* **56**, 40–45 (1894).

[117] Hoyas, S. & Jiménez, J. Velocity statistics in turbulent channel flow up to $Re_\tau = 4000$. *Center for Turbulence Research Annual Research Briefs* 351–356 (2005).

[118] Bernardini, M., Pirozzoli, S. & Orlandi, P. Scaling of the velocity fluctuations in turbulent channels up to $Re_\tau = 2003$. *Under consideration for publication in J. Fluid Mech.* (2014).

[119] Kolmogorov, A. N. The local structure of turbulence in incompressible viscous fluid for very large reynolds numbers. *Dokl. Akad. Nauk SSSR* **30**, 301305 (1941). Proc. R. Soc. London, Ser. A 434, 913 (1991).

[120] Obukhov, A. M. On the distribution of energy in the spectrum of turbulent flow. *Dokl. Akad. Nauk SSSR* **32**, 2224 (1941).

[121] Jiménez, J. & Hoyas, S. Turbulent fluctuations above the buffer layer of wall-bounded flows. *Journal of Fluid Mechanics* **611**, 215–236 (2008).

[122] Klebanoff, P., Tidstrom, K. & Sargent, L. The three-dimensional nature of boundary-layer instability. *Journal of Fluid Mechanics* **12**, 1–34 (1962).

[123] Kline, S., Reynolds, W., Schraub, F. & Runstadler, P. The structure of turbulent boundary layers. *Journal of Fluid Mechanics* **30**, 741–773 (1967).

[124] Kim, H., Kline, S. & Reynolds, W. The production of turbulence near a smooth wall in a turbulent boundary layer. *Journal of Fluid Mechanics* **50**, 133–160 (1971).

[125] Blackwelder, R. F. & Eckelmann, H. Streamwise vortices associated with the bursting phenomenon. *J. Fluid Mech.* **94**, 577–594 (1979).

[126] Orlandi, P. & Jiménez, J. On the generation of turbulent wall friction. *Physics of Fluids* **6**, 634–641 (1994).

[127] Kravchenko, A. G., Choi, H. & Moin, P. On the relation of near-wall streamwise vortices to wall skin friction in turbulent boundary layers. *Phys. Fluids* **A 5**, 3307–3309 (1993).

[128] Jimenez, J. On the structure and control of near wall turbulence. *Physics of Fluids* **6**, 944–953 (1994).

[129] Sendstad, O. *The near wall mechanics of three-dimensional turbulent boundary layers.* Ph.D. thesis, Stanford University (1992).

[130] Jiménez, J. & Moin, P. The minimal flow unit in near-wall turbulence. *J. Fluid Mech.* **225**, 213–240 (1991).

[131] Robinson, S. K. Coherent motions in the turbulent boundary layer. *Annual Review of Fluid Mechanics* **23**, 601–639 (1991).

[132] Smith, C. & Metzler, S. The characteristics of low-speed streaks in the near-wall region of a turbulent boundary layer. *Journal of Fluid Mechanics* **129**, 27–54 (1983).

[133] Österlund, J. M., Johansson, A. V., Nagib, H. M. & Hites, M. H. A note on the overlap region in turbulent boundary layers. *Physics of Fluids (1994-present)* **12**, 1–4 (2000).

[134] Jiménez, J. Recent developments on wall-bounded turbulence. *Revista de la Real Academia de Ciencias Exactas, Físicas y Naturales. Serie A: Matemáticas (RACSAM)* **101**, 187–203 (2007).

[135] Swearingen, J. D. & Blackwelder, R. F. The growth and breakdown of streamwise vortices in the presence of a wall. *Journal of Fluid Mechanics* **182**, 255–290 (1987).

[136] Kawahara, G., Jiménez, J., Uhlmann, M. & Pinelli, A. Linear instability of a corrugated vortex sheet–a model for streak instability. *Journal of Fluid Mechanics* **483**, 315–342 (2003).

[137] Reddy, S. C., Schmid, P. J., Baggett, J. S. & Henningson, D. S. On stability of streamwise streaks and transition thresholds in plane channel flows. *Journal of Fluid Mechanics* **365**, 269–303 (1998).

[138] Waleffe, F. On a self-sustaining process in shear flows. *Physics of Fluids (1994-present)* **9**, 883–900 (1997).

[139] Schoppa, W. & Hussain, F. Coherent structure generation in near-wall turbulence. *Journal of fluid Mechanics* **453**, 57–108 (2002).

[140] Jiménez, J. & Pinelli, A. The autonomous cycle of near-wall turbulence. *J. Fluid Mech.* **389**, 335–359 (1999).

[141] Townsend, A. A. *The structure of turbulent shear flow* (Cambridge university press, 1980).

[142] Millikan, C. B. A critical discussion of turbulent flows in channels and circular tubes.

In *Proc. 5th Int. Congr. Appl. Mech*, vol. 386 (1938).

[143] Afzal, N. & Yajnik, K. Analysis of turbulent pipe and channel flows at moderately large reynolds number. *Journal of Fluid Mechanics* **61**, 23–31 (1973).

[144] Jiménez, J. & Moser, R. D. What are we learning from simulating wall turbulence? *Philosophical Transactions of the Royal Society A: Mathematical, Physical and Engineering Sciences* **365**, 715–732 (2007).

[145] Del Alamo, J. C., Jiménez, J., Zandonade, P. & Moser, R. D. Scaling of the energy spectra of turbulent channels. *Journal of Fluid Mechanics* **500**, 135–144 (2004).

[146] Lozano-Durán, A. & Jiménez, J. Time-resolved evolution of coherent structures in turbulent channels: characterization of eddies and cascades. *Journal of Fluid Mechanics* **759**, 432–471 (2014).

[147] Hoyas, S. & Jiménez, J. Scaling of the velocity fluctuations in turbulent channels up to $re_\tau = 2003$. *Physics of Fluids (1994-present)* **18**, 011702 (2006).

[148] Kreplin, H. & Eckelmann, H. Behavior of the three fluctuating velocity components in the wall region of a turbulent channel flow. *Phys. Fluids* **22**, 1233 (1979).

[149] Mansour, N. N., Kim, J. & Moin, P. Reynolds-stress and dissipation-rate budgets in a turbulent channel flow. *J. of Fluid Mech.* **194**, 1544 (1988).

[150] Pope, S. B. *Turbulent Flows* (Cambridge University Press, 2000).

[151] Moser, R. & Moin, P. Direct numerical simulation of curved turbulent channel flow. *NASA TM* **85974**, 1–158 (1984).

[152] Moin, P. & Kim, J. Numerical investigation of turbulent channel flow. *Journal of Fluid Mechanics* **118**, 341– 377 (1982).

[153] Lesieur, M. *Turbulence in Fluids* (Springer, 2008).

[154] Comte, P., Silvestrini, J. & Begou, P. Streamwise vortices in large eddy simulation of mixing layers. *Eur. J. Mech. B* **17**, 615–637 (1998).

[155] Robinson, K. S. The kinematics of turbulent boundary layer structure. *TM 103859 NASA* (1991).

[156] Dubief, Y. & Delcayre, F. On coherent-vortex identification in turbulence. *J. of Turbulence* **1**, 1–22 (2000).

[157] Jiménez, J. & Pinelli, A. The autonomous cycle of near-wall turbulence. *J. Fluid Mech.* **389**, 335–359 (1999).

[158] Kim, J. & Moin, P. *Transport of Passive Scalars in Turbulent Channel Flow* (National Aeronautics and Space Administration, Ames Research Center, 1987).

[159] Kawamura, H., Ohsaka, K., Abe, H. & Yamamoto, K. Dns of turbulent heat transfer in channel flow with low to medium-high prandtl number fluid. *International Journal of Heat and Fluid Flow* **19**, 482–491 (1998).

[160] Kawamura, H., Abe, H. & Matsuo, Y. Dns of turbulent heat transfer in channel flow with respect to reynolds and prandtl number effects. *International Journal of Heat and Fluid Flow* **20**, 196–207 (1999).

[161] Papavassiliou, D. V. & Hanratty, T. J. Transport of a passive scalar in a turbulent channel flow. *International journal of heat and mass transfer* **40**, 1303–1311 (1997).

[162] Dubief, Y., Uhl, J. & Crocker, R. C. Direct numerical simulation of ablation from an internally heated turbulent flow. In *19th AIAA Computational Fluid Dynamics*, 4149 (AIAA, 2009).

[163] Crocker, R. & Dubief, Y. Numerical study of turbulence over a receding wall by controlled and thermal ablation. In *Proceedings of the Summer Program*, 395 (2010).

[164] Jeong, J., Hussain, J., Schoppa, W. & Kim, J. Coherent structures near the wall in a turbulent channel flow. *J. Fluid Mech.* **332**, 185–214 (1997).

[165] Beam, R. M. & Warming, R. An implicit factored scheme for the compressible navier-stokes equations. *AIAA journal* **16**, 393–402 (1978).

[166] Beam, R. M. & Warming, R. Alternating direction implicit methods for parabolic equations with a mixed derivative. *SIAM Journal on Scientific and Statistical Computing* **1**, 131–159 (1980).

[167] Thomas, L. H. Elliptic problems in linear difference equations over a network. *Watson Sci. Comput. Lab. Rept., Columbia University, New York* 1 (1949).

[168] Tannehill, J., Anderson, D. & Pletcher, R. *Computational Fluid Dynamics and Heat Transfer* (Taylor and Francis, 1997).

[169] Dubief, Y. Heat transfer enhancement and reduction by poylmer additives in turbulent rayleigh benard convection. *arXiv preprint arXiv:1009.0493* (2010).